Université de Nice–Sophia Antipolis
École Doctorale Sciences Fondamentales et Appliquées

Thèse d'Habilitation à Diriger des Recherches

Marcel Carbillet

Modélisation d'Optique Adaptative et Imagerie Post-Optique Adaptative en Astronomie

Thèse soutenue devant le jury composé de :

M. Claude Aime	Président
M. Marc Ferrari	Rapporteur
M. Roberto Ragazzoni	Rapporteur
M. Farrokh Vakili	Rapporteur
M. Mario Bertero	Examinateur
M. André Ferrari	Examinateur
M. Gérard Rousset	Examinateur

(Nice, Parc Valrose, 11 décembre 2013, 10h30)

Modélisation d'optique adaptative et imagerie post-optique adaptative en astronomie

Marcel Carbillet

Unité Mixte de Recherche 7293 J.-L. Lagrange
(Université de Nice–Sophia Antipolis, Centre National de la Recherche Scientifique, Observatoire de la Côte d'Azur)

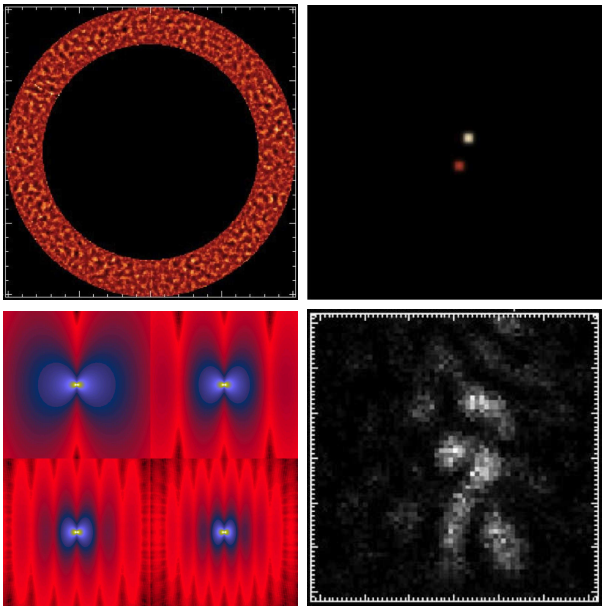

Table des matières

Chapitre 1

Vue (CAOS-tique) d'ensemble

[« Tout est chaos », Ben Vautier, 2007, Galerie Eva Vautier, Nice.]

Je vous le dis : il faut encore porter en soi un chaos
pour pouvoir mettre au monde une étoile dansante.
Je vous le dis : vous portez un chaos en vous.
Friedrich Nietzsche, in *Ainsi parlait Zarathoustra*, 1883–1885,
Trad. H. Albert, éd. Soc. du Mercure de France, 1898,
Partie 1, *Prologue de Zarathoustra*, 5, p. 14.

1.1 Introduction générale

Cette thèse, écrite en vue d'obtenir l'habilitation à diriger des recherches, constitue un condensé du travail de recherche que j'ai effectué depuis la présentation de ma thèse de doctorat le 6 décembre 1996. Une sélection d'articles accompagne le fil conducteur de la thèse tout le long de son déroulement, déroulement tentant lui-même de traduire de manière raisonnée le mouvement d'ensemble qu'a constitué cette (un peu plus que) quinzaine d'années.

La soutenance devant se dérouler début décembre 2013, il s'agira même à vrai dire de dix-sept années de recherche résumées dans ce document. Dix-sept années dont les neuf premiers mois, ceux de mon premier stage post-doctoral, à l'Université de Genève, ne figurent cependant pas dans ce document car relevants d'un domaine de recherche assez orthogonal au reste du travail présenté. Le reste de ces dix-sept années ne se sont par contre déroulées que dans deux autres lieux : l'*Osservatorio Astrofisico di Arcetri* de l'*Istituto Nazionale di AstroFisica* (INAF–OAA), à Florence (sept ans), puis le laboratoire LUAN (Laboratoire Universitaire d'Astrophysique de Nice), Unité Mixte de Recherche (UMR) n° 6525 de l'Université de Nice–Sophia Antipolis (UNS) et du Centre National de la Recherche Scientifique (CNRS), devenu UMR 6525 Hyppolite Fizeau (avec les deux mêmes tutelles précédentes plus l'Observatoire de la Côte d'Azur – OCA), puis finalement devenu UMR 7293 Joseph-Louis Lagrange (UNS/CNRS/OCA toujours), au gré des évolutions structurelles de ces dernières années.

Ces presque sept années dans le groupe de l'INAF–OAA, s'occupant de l'élaboration, entre autres choses, mais de manière essentielle, du système d'optique adaptative (OA) de première lumière du *Large Binocular Telescope* (LBT) [1], m'ont mis le pied à l'étrier dans le domaine de la modélisation détaillée des systèmes optiques pour l'astronomie. Elles m'ont permis d'aborder des thèmes variés, allant de celui déjà en partie dans mes cordes de la turbulence atmosphérique, à celui des analyseurs de surface d'onde (ASO) innovants que sont les pyramides, des miroirs correcteurs ambitieux que sont les *miroirs secondaires adaptatifs*, et, contextuellement et de manière liée au domaine de l'imagerie qui était déjà celui de ma thèse de doctorat, de la recombinaison interférométrique de type Fizeau que permettent les deux ouvertures du LBT. C'est donc dès le début de ma permanence à l'observatoire d'Arcetri (en tant que post-doctorant européen, puis post-doctorant financé par le projet LBT, puis sous contrat de recherche toujours lié au LBT) que j'ai pu développer cette bicéphalité modélisation instrumentale/traitements d'image qui constitue le nerf de ma recherche.

À mon arrivée à Nice, j'ai pu ainsi me consacrer d'une part à la modélisation instrumentale de l'instrument SPHERE (*Spectro-Polarimetric High-*

1. Le système d'OA à une seule étoile naturelle le plus innovateur alors, et le plus indéniablement performant aujourd'hui.

contrast Explonet REsearch) pour le *Very Large Telescope* (VLT) et d'autre part à la partie imagerie de cet instrument que constitue le coronographe de Lyot apodisé, développé localement, et de la détection d'exoplanètes, le thème phare de SPHERE. En parallèle, j'ai pu aussi finaliser un certain nombre des sujets abordés à Arcetri, où l'ambiance alors foisonnante d'innovations continues n'était pas en pratique toujours très compatible avec le temps et le recul nécessaires à chaque (tentative de) publication autres que celles liées aux conférences récurrentes des communautés OA et interférométrie. J'ai également pu développer, pour le côté modélisation et à titre d'exemple, de nouvelles applications telle que celle liée à l'astronomie optique au Dôme C. Pour le côté imagerie, j'ai pu mettre en pratique de nouvelles techniques par déconvolution d'image telles que la déconvolution myope avec contrainte de Strehl ou la super-résolution par déconvolution permettant d'aller encore plus loin en haute résolution angulaire (HRA). Il me semble intéressant de remarquer ici que, par exemple, la déconvolution myope avec contrainte de Strehl permet de lier plus intimement encore les performances de l'instrument, se situant plutôt du côté du plan pupille, aux images obtenues puis traitées, avec une finalité, la seule valable, astrophysique, se situant par contre du côté du plan image.

Le présent chapitre va illustrer cette vue d'ensemble du travail accompli, à travers le prisme de l'outil logiciel utilisé pour l'ensemble des applications présentées et de ces deux composantes premières : le `Software Package CAOS` et le `Software Package AIRY`. C'est donc, momentanément et à la section suivante, le flacon qui va l'emporter sur l'ivresse – mais ce n'est que pour mieux appuyer le discours global qui reprendra dès la dernière section de ce chapitre pour nous livrer le menu de la suite de cette thèse, se concentrant par contre sur les résultats obtenus *à l'aide* de ces deux outils et de ceux développés par la suite au sein du même écrin.

On verra donc s'illustrer d'elles-mêmes les deux grandes lignes présentées distinctement au sein d'une part du Chap. 2 et d'autre part du Chap. 3, mais totalement indissociables à mon sens : la modélisation numérique détaillée de systèmes d'OA d'une part, et l'imagerie post-OA nécessaire à l'optimisation des résultats obtenus par un télescope optique moderne d'autre part.

En effet, dans un soucis de reproductibilité et de transparence des résultats, le travail de modélisation a tout-de-suite été pensé pour être distribué sous forme de code(s) accessible(s) à tous. Il en est allé tout naturellement de même pour tout ce qui a concerné la partie « imagerie post-OA » développée en parallèle.

La thèse est organisée de la façon suivante. La section suivante va compléter les présentations concernant l'ensemble des outils développés en parallèle des différents travaux abordés plus tard dans ce document. La suite de la thèse sera ensuite organisée en deux chapitres distincts, l'un concernant la modélisation numérique de systèmes d'OA, l'autre dédié à l'imagerie post-OA. Un chapitre final qui fera le sommaire des principaux résultats obtenus, et sera également porteur des perspectives liées à ce travail, concluera alors l'ensemble.

On trouvera également en annexe une brève introduction à la problématique des observations astronomiques à travers l'atmosphère turbulente, problématique globale dans laquelle s'inscrit cette thèse, ainsi qu'une reproduction d'une part mon curriculum vitæ actuel et d'autre part de ma liste de publications (le lecteur intéressé par ce dernier point pourra ainsi facilement la trouver en toute fin d'ouvrage, pages xxv).

1.2 *Code for Adaptive Optics Systems (CAOS)*

1.2.1 Présentation(s)

Il s'agit là de l'outil que je développe donc depuis plus d'une quinzaine d'années, même si à ses prémices, à la fin du siècle dernier (!), il ne portait pas encore ce nom qui lui sied si bien : `CAOS`, ou plus précisément : le *problem-solving environment* (PSE) `CAOS`, et même si au tout début on ne parlait que de sa composante (son *package* originel et homonyme) de simulation de systèmes d'OA : le `Software Package CAOS`.

Le `PSE CAOS` [71, 93, 125, 127] s'est depuis lors enrichi de plusieurs autres *sofware packages*, tant dans le domaine de la modélisation numérique en OA que dans le domaine de l'imagerie post-OA. Pour ce qui est de la modélisation, abordée en détail au chapitre suivant, ceci s'est matérialisé par de nombreux développements du `Software Package CAOS` [81], par l'intégration de l'outil analytique `PAOLA` [97, 135] sous la forme du spécifique `Software Package PAOLAC` (pour `PAOLA` *within* `C`*aos*) [127], ou par le développement du `Software Package MAOS` de modélisation/simulation de systèmes d'OA multi-références (OA multi-conjuguée, OA couche limite). Pour ce qui est par contre de l'imagerie post-OA, le `Software Package AIRY` [58, 151] s'est lui aussi enrichi de nombreux développements en ce qui concerne la déconvolution d'images (éventuellement multiples dans le cas d'images interférométriques de Fizeau). Mais il faut également signaler sa version spécialisée à l'instrument LINC-NIRVANA du LBT, le `Software Package AIRY-LN` [108], ainsi que l'outil de simulation numérique détaillé de l'instrument SPHERE : l'homonyme `Software Package SPHERE` [105].

La Fig. 1.1 montre l'interface globale du `PSE CAOS`, le `CAOS Application Builder` [54, 65], avec la liste des *software packages* installés (ici, tous ceux existants ou actuellement en développement), visible à partir du bouton de menu *Modules*. Pour chaque *software package*, la liste de modules le composant peut être rendue visible à son tour, et chacun de ces modules peut alors être sélectionné pour être disposé sur la feuille de travail du `CAOS Application Builder` afin de définir le flux de données entre chacun et constituer ainsi un projet de simulation destiné à simuler un cas précis (à l'aide des modules du `Software Package CAOS` et/ou du `Software Package PAOLAC` et/ou du `Software Package MAOS` et/ou du `Software Package SPHERE`), ou bien à traiter un certain type de données grâce aux modules du `Software Package`

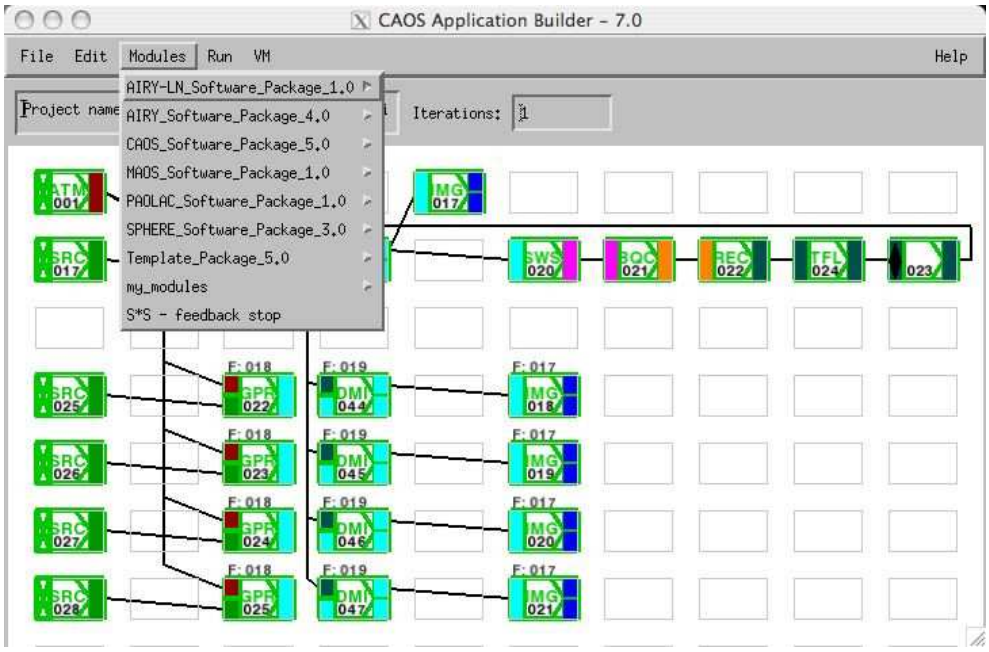

FIGURE 1.1: Le `CAOS Application Builder`, version 7.0, faisant apparaître la liste des *software packages* installés via le bouton `Modules`. En image de fond, un projet de simulation faisant appel aux modules du `Software Package CAOS`.

`AIRY` et/ou du `Software Package AIRY-LN`, ou bien d'autres modules encore construits en local par l'utilisateur.

L'avantage principal d'une telle structure, profondément modulaire, est de pratiquement imposer, par exemple lors de la modélisation d'un instrument ou de la simulation d'une observation, la séparation des différents phénomènes physiques successifs. En guise d'exemple : le modèle décrivant l'ASO ne doit pas « connaître » les caractéristiques physiques de l'atmosphère turbulente, mais simplement son résultat sur la pupille d'entrée du télescope : un front d'onde perturbé.

Ainsi, une modélisation donnée est construite en connectant simplement les occurrences nécessaires des différents modules entre elles, en ne respectant qu'une seule logique : celle de la compatibilité entre entrée(s) d'un module et sortie(s) du/des précédent(s). Cette contrainte est aisément reconnaissable grâce au code couleur adopté : à chaque type pré-défini (au niveau du `PSE CAOS` lui-même) d'entrée/sortie correspond une couleur donnée – les fronts d'onde en jaune, les images en bleu, etc. Cette caractéristique du `CAOS Application Builder` permet à l'utilisateur de se concentrer pleinement sur les aspects scientifiques de sa modélisation, tout en laissant la gestion des aspects mondains du codage à l'interface globale de l'outil.

De plus, chaque module est accompagné de sa propre *graphical user interface* (GUI) au travers de laquelle peuvent être choisis les paramètres physiques et numériques qui lui sont propres (et –surtout !– rien d'autre), durant la phase de définition du flux de données (i.e. de la modélisation/simulation visée) ou de manière équivalente plus tard. Chaque module est en pratique défini par un ensemble standard de fonctions/routines, une collection de paramètres qui lui est propre et des entrée(s)/sortie(s) bien déterminées.

1.2.2 *Modelling astronomical adaptive optics – I. The Software Package CAOS*

L'article suivant, publié par *Monthly Notices of the Royal Astronomical Society* en 2005, présente en détail le `Software Package CAOS` ; suivant de nombreuses publications de conférence présentant depuis 1998 aussi bien l'outil [37, 39, 50] que les résultats obtenus à partir de celui-ci [40, 47, 46, 53, 61, 62, 67, 60, 66, 74, 70, 72]. Le `Software Package CAOS` y est décrit comme un ensemble de modules conçus pour des simulations fines [2] de systèmes d'OA génériques. On passe ainsi de la modélisation de l'atmosphère turbulente à celle de la propagation de l'étoile laser à travers cette même atmosphère, en passant par la caractérisation de l'objet observé, la modélisation détaillée aussi bien d'un Shack-Hartmann que d'une pyramide, la reconstruction du front d'onde, le contrôle de la boucle et la correction à travers différentes technologies de miroirs déformables, mais aussi la formation d'image, l'interférométrie de Fizeau, la coronographie, etc. Étant donnée la grande variété de modélisations physiques le composant, l'outil se montre ainsi finalement être autant adapté à des études détaillées en optique astronomique (ou en astronomie optique), qu'à la simulation d'un instrument en particulier. Ça a d'ailleurs longtemps été le cas pour le système d'OA de première lumière du LBT ou la formation de franges en utilisant le LBT dans sa modalité binoculaire (i.e. avec LINC-NIRVANA, le recombineur Fizeau LINC assisté du système d'OA multi-conjugué *layer-oriented* NIRVANA).

L'utilisation du `Software Package CAOS` est ensuite illustrée par la résolution de la question concernant la possibilité d'utiliser un analyseur dédié pour la mesure du basculement (ou tip-tilt) pour un système d'OA à base de pyramide sur un télescope de la classe 8 mètres. La simulation présentée dans cet article montre très clairement que le gain serait dans le cas de la pyramide très faible et de plus très contraignant au niveau du pourcentage de lumière à envoyer d'un côté (pour la mesure des deux basculements, en x et en y) et de l'autre (pour la mesure des plus hauts ordres) de la boucle du système d'OA.

2. Ou *end-to-end* en anglais – ce qui décrit peut-être mieux le caractère détaillé, au sens pratiquement boucher du terme, de cette approche qui est aussi, précisons-le, de type Monte-Carlo.

Mon. Not. R. Astron. Soc. **356,** 1263–1275 (2005) doi:10.1111/j.1365-2966.2004.08524.x

Modelling astronomical adaptive optics – I. The software package CAOS

M. Carbillet,[1⋆] C. Vérinaud,[2] B. Femenía,[3] A. Riccardi[4] and L. Fini[4]

[1] *Laboratoire Universitaire Astrophysique de Nice–UMR 6525, Parc Valrose, 06108 Nice Cedex 02, France*
[2] *European Southern Observatory, Karl-Schwarzschild-str. 2, 85748 Garching-bei-München, Germany*
[3] *GTC Project, Instituto de Astrofísica de Canarias, C/ vía Láctea s/n, 38200 La Laguna, Spain*
[4] *INAF–Osservatorio Astrofisico di Arcetri, Largo Enrico Fermi 5, 50125 Firenze, Italy*

Accepted 2004 October 18. Received 2004 October 15; in original form 2004 July 2

ABSTRACT

The software package CAOS (code for adaptive optics systems) described in this paper is a software ensemble of modules designed for end-to-end simulation of generic astronomical adaptive optics (AO) systems, including a complete atmosphere turbulence model, sodium laser-guide star upward and downward propagation, observed object definition, Shack–Hartmann and novel pyramid wave-front sensors detailed modelling, wave-front reconstruction and subsequent time-filtering tools, and wave-front correction via different kinds of correctors; but also image formation, Fizeau interferometry, coronagraphy, etc. Consequently, it is more likely to be used as a tool dedicated to detailed optical astronomy studies than as an instrument simulator, as it is based on a wide range of unprecedented physical modelling. After a brief but global description, with particular emphasis on the most interesting physical modelling features, its use is illustrated through a chosen application, namely the question concerning the opportunity of having a tip–tilt-dedicated sensor in a 8-m class telescope pyramid-based AO system.

Key words: instrumentation: adaptive optics – instrumentation: high angular resolution – methods: numerical – telescopes.

1 INTRODUCTION

Adaptive optics (AO) is now a mature technology widely used in optical astronomy, and is part of every new optical telescope project. A number of impressive results, for example, with the NAOS AO system on board one of the Very Large Telescopes (VLT) (see, e.g., Gendron et al. 2004; Lacombe et al. 2004; Lagrange et al. 2004) has already been obtained, and a number of novel AO concepts are being studied for cutting-edge applications, such as extrasolar planet searching (e.g within the framework of the VLT-Planet Finder) or wide-field high-angular-resolution astronomy [the European Southern Observatory, ESO, multiconjugate, MC, AO demonstrator MAD for VLT, the interferometric MCAO system LINC-NIRVANA for the Large Binocular Telescope (LBT), the Gemini laser-based system, etc.], pushing the limits of the original concept.

Within this framework, and due to the complexity of this kind of system, the performance analysis has a number of problems that are not open to analytical solution. In fact, this kind of study involves the complex nature of the turbulent atmosphere, and also the fact that a number of competitive instrumental concepts are often to be deeply analysed and compared (e.g. pyramid wave-front sensors versus Shack–Hartmann ones, piezo-stacked mirrors versus adaptive secondaries, different reconstruction strategies, etc.). Consequently, Monte Carlo-based numerical simulations are necessary, not always end-to-end but often extremely detailed at least for a particular physical process or piece of hardware behaviour to be studied. Moreover, studies concerning the coupling of AO systems with the subsequent instrumentation (interferometry, coronagraphy, spectroscopy, etc.), are also of fundamental importance.

Some numerical tools have already been presented, though not always as widely distributed and developed as CAOS, and often strictly limited to a given type of AO. Among them we can cite the following: PAOLA, an IDL-written semi-analytical code dedicated to extremely large-aperture AO (Jolissaint & Véran 2002); LOST, also IDL-based and dedicated to layer-oriented MCAO simulations (Arcidiacono et al. 2004); and the ESO parallel C codes, dedicated to extremely large-aperture MCAO (Le Louarn et al. 2004).

In this paper we present a generic numerical tool for AO and AO-related studies: the software package CAOS, which integrates state-of-the-art physical and numerical modelling developments and is already distributed among a large community of AO-concerned astronomers/researchers. As a matter of fact, it has to be noted that a number of studies using the tool in its successive versions have already been, or are currently being, performed. Among them we can cite the following: a first evaluation of the performance of the first-light AO system of LBT (Carbillet et al. 2003); studies concerning the impact of partial AO correction on the interferometric imaging capabilities of LBT (Carbillet et al. 2002a); optimization of the deformable mirrors conjugation altitude in MCAO (Femenía & Devaney 2003); the proved possibility of sensing the differential piston using a pyramid sensor (Vérinaud & Esposito 2002); and simulation studies concerning the ESO MCAO demonstrator MAD (Carbillet et al. 2002b; Vérinaud et al. 2003). Moreover, it

⋆E-mail: marcel.carbillet@unice.fr

can also be used to provide a precise estimate of the astrophysical performance, in terms of the signal-to-noise ratio and exposure times, and/or as a solid preparation for observations with existing AO-equipped instruments (see, for instance, Habart et al. 2004), and for the preparation of the near future observations with, for instance, the LBT first-light AO system.

Our tool also represents a first necessary building block for further scientific studies of fundamental importance to optical astronomy (and especially AO), such as the crucial problem of very-high dynamic range imaging (as planned for the VLT-Planet Finder project, and more generally for exoplanets and protoplanetary discs observations). A number of definitive answers have to be found regarding the type of AO system that has to be used, the observing conditions (magnitude, wavelength, atmospheric turbulence, etc.) and the coupling/propagation of error when coronagraphy is contemplated.[1] The promise of wide-field optical astronomy, using MCAO for which a number of concepts have been proposed, is also another important area for which our tool can contribute.

The software package CAOS is essentially a set of modules designed to be used within a graphical programming environment – the CAOS application builder (Fini, Carbillet & Riccardi 2001; Fini & Carbillet 2003), where the data flow between modules can be defined, and the parameters of each module can be set. The present version of the software package CAOS is 5.0, and it is the result of six years of work involving considerable effort in the modelling of a number of the physical processes involved, and in the numerical writing and distribution of the tool. The graphical part of our software 'system', the CAOS application builder, has now reached version 4.1, and also accommodates the (somewhat more recently developed) software package AIRY (Correia et al. 2002), dedicated to Fizeau interferometric image restoration studies. The software package CAOS has now reached a very high level of maturity, and it is time to present it to the whole astronomical community.

The scope of this paper is not just the presentation of the software package CAOS, but also a description of its most interesting and novel features, together with an illustration of its use through a chosen example. Therefore, the paper is organized as follows. In Section 2 we briefly describe the global structure and main features of our programming environment, while in Section 3 we highlight the most interesting features of the various modules that have been developed. In particular, we give some details concerning the detailed modelling of the novel pyramid wave-front sensor for which there is wide interest. Section 4 is then dedicated to a case study concerning the utility of a typical tip–tilt sensing device in addition to pyramid wave-front sensing, within the framework of an 8-m class telescope. Finally, our concluding remarks are given in Section 5.

2 THE CAOS SYSTEM AND ITS RELATED PROGRAMMING ENVIRONMENT

The structure under the CAOS 'system' is modular. This means that each elementary physical process of a given simulation is modelled within a specific module; for example, in the AO case, the turbulence in each atmospheric layer, the propagation of light from an object to the observing telescope and through the turbulent layers, the physical characterization of the object itself, the wave-front sensing, the wave-front reconstruction, the time-filtering of the resulting deformable mirror commands, the wave-front correction, etc. Taking advantage of the CAOS application builder, a simulation can be built by connecting together the required occurrences of the desired modules, respecting only the logical constraints given by their formalized input/output types. Complex simulation applications are thus simply created by assembling the elementary building blocks (representing the modules) in a straightforward manner, so that the user can concentrate on the scientific aspects of her/his problem, while mundane coding problems are managed by some automatic tools.

Each module comes with an individual graphical user interface (GUI) in order to set its own physical and numerical parameters, during the design step or independently at a later moment. In practice, each module is defined by a standard group of function calls, a collection of parameters, and a typed definition of input(s) and output(s). It can support up to two inputs and two outputs, and it is represented within the application builder as a rectangular box with coloured input handles (on its left-hand side), and output ones (on its right-hand side). Each colour describes one of the pre-defined types of input/output: wave-front, image, commands, etc. The software package CAOS also contains a library of utilities, and a detailed hypertext help which can be called from each individual module GUI, and a set of examples of typical simulation projects that can be used as a starting point for new applications.

After the simulation design step is completed, the block diagram is analysed by the application builder and the IDL code implementing the simulation program is generated. It can be modified 'by hand' in order to complete some additional task not strictly provided using the existing modules. The whole structure of the simulation can be saved as a project that can be restored for later modifications and/or parameter upgrading. Beside the main simulation project one or more calibration project(s) might be previously designed and run.

Fig. 1 shows the CAOS application builder (background), together with the automatically generated code (foreground): two IDL-written routines, one for the calls to the various modules required, and the other one for the general administration of the simulation project (graphical representation and global parameters). As already mentioned, this code is generated at the end of the design phase for the simulation, a phase during which each required module is picked up from the 'module' menu in which all the modules of all the installed software packages are present, and then put in one of the pre-defined boxes within the application builder itself. The occurrence of a module is hence represented by a box with the name of the module (e.g. the turbulent atmosphere module is represented by the box named ATM in the figure) and with pre-defined inputs and outputs. By clicking on the occurrence of a module (e.g. the occurrence of module ATM we were evoking before was number 001), a GUI is opened in order to chose the various physical and numerical parameters related to the module itself (and only it). Global parameters (common to all modules) are limited to a strict minimum: only the total number of iterations and the current iterate number, and only if necessary.

It is clear from Fig. 1 how additional code can easily be implemented directly within the two automatically generated routines. Moreover, new modules can also be implemented very easily thanks to the template module included with the CAOS application builder distribution. Consequently, it has to be noted that new software packages (dedicated to a given thematics not treated by the existing software packages) are also easy to build up. Also note that

[1] A very detailed physical modelling of the instrumental response and the subsequent exact morphology of the resulting AO-corrected point spread function is fundamental here and is only achieved through the complete physical analysis provided by an end-to-end simulation tool such as the software package CAOS.

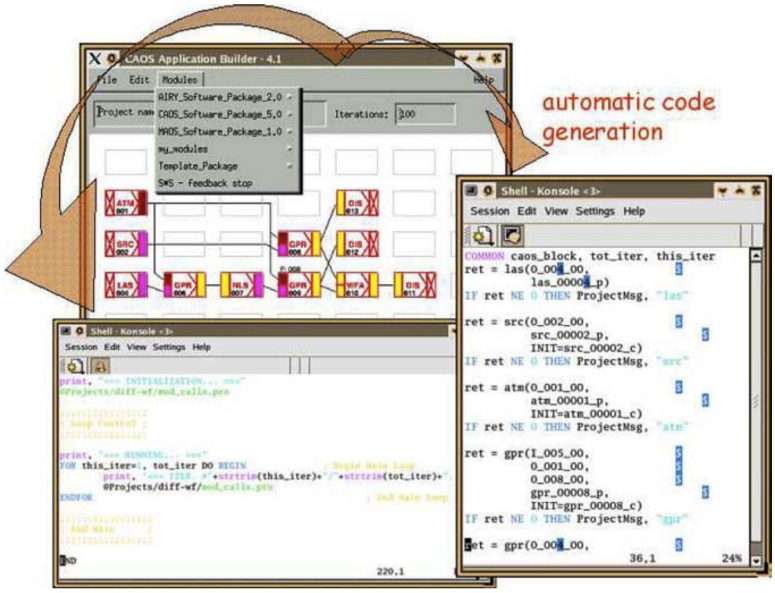

Figure 1. Background: the CAOS application builder showing a typical simulation design using the modules of the software package CAOS, and together with the list of software packages installed that appears when pushing the button 'modules'. Foreground: the two routines that are automatically generated at the end of the simulation design phase.

modules from different software packages can work together in a unique project, given the input/output structure type compatibility.

Everything, from the application builder to each of the software packages, is implemented in the IDL language, but efforts are being planned in order to port the whole code to the newly developed GDL language, which is supposed to reach complete equivalence to IDL version 6.0 soon (see http://sourceforge.net/projects/gnudatalanguage/).

3 DESCRIPTION OF THE MODULES OF THE SOFTWARE PACKAGE CAOS

In this section we describe the tasks of each module of the software package CAOS (version 5.0), going in detail for some of the features we believe to be most interesting. A complete and detailed description of each module can be found by directly looking at the hypertext help for each module given together with the package and downloadable from the CAOS web-page http://www.arcetri.astro.it/caos.

Table 1 shows a complete list, together with a very brief description, of the modules present in the modules library of the software package CAOS 5.0. Different classes of modules have been defined and details are given in the following subsections.

3.1 Wave-front perturbation

Module ATM (atmosphere building) generates the turbulent atmosphere that then produces the corrupted wave-fronts for the whole simulation through module GPR (geometrical propagation), which propagates the light from a given source/object modelled within module SRC (source definition) and through the modelled turbulent atmosphere.

Going into a bit more detail, we see that ATM is a module with no input except its parameters chosen via its GUI, and a unique output composed of a given number of turbulent layers together with their altitudes, wind velocities, etc. In fact, we assume that the turbulence is mainly located within a few relatively narrow layers – at least for good astronomical sites. The finite number of turbulent layers is a consequence of the modelling of the profile of the structure constant of the refraction index fluctuations, $C_N^2(h)$, as an ensemble of discrete values. Each of these values corresponds to a turbulent layer of the atmosphere, and each turbulent layer can be physically simulated as a random phase screen for which the power spectrum follows the von Kármán–Kolmogorov model.

The first step in building the turbulent atmosphere is to generate the phase screens that will simulate the behaviour of each turbulent layer. We have implemented, up to now, two methods: a fast Fourier transform- (FFT-) based method, with low-spatial-frequency boosting (also known as 'subharmonics adding'), and a Zernike-polynomials-based method, using an alternative definition of the Zernike polynomials for high orders. We refer to Carbillet & Riccardi (in preparation) for a detailed discussion concerning these two methods.

Once the phase screens have been generated, the turbulent atmosphere, that is the output of module ATM, is built by arranging the required number of phase screens/turbulent layers with their altitudes and taking into account the C_n^2 profile chosen by the user.

Table 1. Descriptive list of the modules of the software package CAOS, version 5.0.

Module	Purpose
Wave-front perturbation and image formation	
ATM, atmosphere building	– to build the turbulent atmosphere (see also utility PSG, phase screen generation)
SRC, source definition	– to characterize the guide star/observed object
GPR, geometrical propagator	– to geometrically propagate the light through the turbulence
IMG, imaging device	– to make an image of the observed object
LGS-oriented modules	
LAS, laser characterization	– to define the laser characteristics
NLS, Na-layer spot definition	– to characterize the sodium-layer behaviour
Wave-front sensing	
PYR, pyramid wave-front sensor	– to simulate the pyramid sensor behaviour
SLO, slope computation	– to compute the slopes from the pyramid signals
SHW, Shack–Hartmann wave-front sensor	– to simulate the Shack–Hartmann sensor behaviour
BQC, barycentre/quad-cell centroiding	– to compute the slopes from the SH spots centroiding
Wave-front reconstruction and correction	
REC, wave-front reconstruction	– to reconstruct the wave-front
TFL, time-filtering	– to apply time-filtering during wave-front reconstruction
DMI, deformable mirror	– to correct from the wave-front perturbations
Tip–tilt-specialized modules	
TCE, tip–tilt centroiding	– to compute and reconstruct the tip–tilt
TTM, tip–tilt mirror	– to correct from the tip–tilt
Calibration-oriented modules	
CFB, calibration fibre characterization	– to define a fibre to be used for calibration purpose
CSQ, command sequencer	– to generate a sequence of commands
MCA, make calibration	– to make and save the calibration matrix
MDS, mirror deformation sequencer	– to generate a sequence of mirror deformations
SCD, save calibration data	– to save the calibration data
Other modelling modules	
IBC, interferometric beam combiner	– to combine the light from two pupils
COR, coronagraphic module	– to simulate various coronagraphic concepts
AIC, achromatic interfero-coronagraph	– to simulate the achromatic interfero-coronagraph
BSP, beam splitter	– to split the light beam
Additional utilities	
WFA, wave-front adding	– to add or combine together wave-fronts
ATA, atmosphere adding	– to add or combine together atmospheres
IMA, image adding	– to add or combine together images
STF, structure function calculator	– to compute the structure function from propagated wave-fronts
SAV, save structure	– to save any type of input/output structure (XDR format) (see also utility RST, restore structure)
DIS, generic display	– to display any type of pre-defined input/output

If temporal evolution is needed, this is performed once (the first time), ATM will then just shift each of the layers by an ad hoc quantity taking into account the base-time (minimum atmosphere/turbulence evolution time defined within this module but imposed on all the subsequent simulation branches) and their associated velocity vectors. If no temporal evolution is needed, no base-time and no velocity vectors are asked for and each time ATM is called it outputs a statistically independent ensemble of turbulent layers.

In the case of a natural object, its angular coordinates (off-axis, position angle), photometric and spectroscopic characteristics (magnitudes in the various Johnson bands from U to M, spectral type – assuming the blackbody approximation), and its morphology can be set within module SRC. In addition, background magnitudes are also set for further computation during the process of image formation and/or wave-front sensing. Objects with a given morphology can also be defined, by either choosing one of the existing options or by loading a previously computed model resulting in a two-dimensional map. A finite distance can also be set; in such a case it is assumed to be a laser guide star (LGS) at such a distance from the telescope pupil.

The propagation of light is performed by the module GPR, taking into account the positioning of each part (telescope, projector, possibly a sodium layer, turbulent layers) and the time evolution. The propagation is performed in a geometrical way, and the so-called pixel magnification is taken into account in the LGS case in order to simulate the cone effect.

A module permitting Fresnel propagation instead of a geometrical one, and hence capable of simulating the scintillation effects on the subsequent physical processes (e.g. wave-front sensing and/or very high-contrast imaging) is being written, but will be part of a forthcoming release.

3.1.1 The LGS case

When the use of a laser guide star is contemplated, it can be modelled at different levels of detail. A first level of detail is achieved by taking into account the finite distance of the LGS only (i.e. defining a point

source at a finite distance within the module SRC). A deeper analysis also takes into account the two-dimensional morphology of the LGS (also using module SRC). And a complete end-to-end analysis considers the whole process of propagation of the laser beam from a telescope projector (using module LAS), through the turbulence, and to the sodium layer (modelling the three-dimensional resulting spot using module NLS, which can integrate a physical-model-based or an on-site-measurement-based profile), and then propagating the light from the sodium layer to the observing telescope and through the turbulent atmosphere again. The example project given in Fig. 1 is also an illustration of the difference between the latter case (whole modelling of a sodium LGS with modules LAS and NLS) and either simple downward propagation from a natural guide star or a simpler modelling of the LGS (considering only downward propagation with or without a two-dimensional morphology for the LGS using only module SRC). Note that one occurrence of module GPR (number 006 in the figure) is for the upward propagation of the laser beam through the turbulence to the sodium layer (hence the associated parameters denote the position, size and shape of the projector telescope), while the other one (number 009 in the figure) is for downward propagation of it (hence the associated parameters concern the observing telescope and are the same as GPR number 008). As a result, the simulation project in Fig. 1 (thanks also to module WFA, which can perform a difference between two propagated wave-fronts) permits the study of all the effects on the LGS AO system, and in particular the cone effect and the tip–tilt indetermination problem.

3.2 Imaging process

Module IMG (imaging device) performs the simulation of the image formation process on a square array detector (e.g. a CCD or an infrared detector array). Module IMG requires no information concerning the actual optical layout of the camera as explicit use of the aberration-free thin-lens approximation is made and its diameter is assumed to be large enough not to become the element defining the pupil of the optical system. Consequently, the intensity pattern on the focal plane (i.e. on the detector array) is computed using monochromatic Fraunhofer diffraction theory (Goodman 1968) involving a FFT operation when evaluating the point spread function (PSF) of the optical system telescope+atmosphere, and two additional FFT operations in order to perform the convolution between the PSF and the object distribution when imaging extended two- or three-dimensional sources. Both the aberration phase function used to compute the PSF and the object brightness distribution are fed to module IMG via its single input. Three-dimensional LGS spots are discretized in a set of two-dimensional arrays (each of them referred to as sublayers) and module IMG proceeds as if each sublayer were an extended two-dimensional source, so that for each sublayer we compute a PSF aberrated by atmospheric turbulence plus the defocus aberration caused by the fact that the detector is conjugated at a given plane, while the source spans behind and beyond such a plane. Each layer PSF is convolved with its corresponding LGS slice giving a two-dimensional image per LGS slice. The final image is obtained by a weighted average of all the LGS slice images, where the LGS slice intensities have been used as weights.

The sampling of the images obtained with FFTs will depend on the size of the array storing the input aberrated wave-front; let us denote this resolution by $\Delta_{\rm FFT}$. In general $\Delta_{\rm FFT} \neq \Delta_{\rm CCD}$, where $\Delta_{\rm CCD}$ is the detector pixel size. To avoid interpolation routines, the original wave-front array is padded with zeros in such a way that when performing the FFTs the resolution that we arrive at is $\Delta_{\rm CCD} = n\ \Delta'_{\rm FFT}$, where n is an integer greater than or equal to 1. When dealing with two- and three-dimensional sources the object brightness functions are bilinearly interpolated to the same resolution $\Delta'_{\rm FFT}$ (here we are implicitly assuming that object brightness functions are very smooth compared with PSFs). After convolution the image at resolution $\Delta'_{\rm FFT}$ is easily rebinned to yield an image of resolution $\Delta_{\rm CCD}$. The resulting field stop of the imaging system is assumed to be the detector itself, so that the field of view (FoV) is obtained as the number of pixels times the angle subtended by each pixel.

The parameters set by the IMG GUI are the linear number of pixels in the detector, the detector pixel size $\Delta_{\rm CCD}$, the distance from the entrance pupil to the height the detector is conjugated at, the integration and delay times, the observing band, the average quantum efficiency in the observing band and a selection of noise sources. If an even number of pixels is chosen, the optical axis is assumed to be at the junction of the four central pixels, while in the case of an odd number of pixels the optical axis is coincident with the central pixel. The sky background contribution is added to the resulting image before considering the different noise sources, the information on the background value in the observing band having been previously chosen within module SRC or any equivalent module. The noise sources considered by module IMG are Poisson photon noise, Gaussian dark-current and read-out noise (RON). All of them are assumed to be spatially white as zero correlation between pixels is assumed. The user is prompted to supply the seeds (for random number generation) for each noise source and the rms values for the Gaussian statistics describing the read-out and dark-current noise. Note that the Poisson noise processes are indeed modelled via a Monte Carlo approach. It is up to the user to decide if the image on the detector array takes into account any of the above sources of noise. Repeatability of noise is guaranteed using the same user-defined initial seed values.

3.3 Wave-front sensing

Two types of wave-front sensors have been widely modelled and developed within the software package CAOS, namely the well-known Shack–Hartmann sensor, and the relatively novel pyramid sensor. In the following we detail both of them, though with closer attention being paid to the physical modelling of the more interesting case of the latter.

3.3.1 Shack–Hartmann wave-front sensing

The basic scope of an end-to-end Shack–Hartmann module within CAOS is to compute the guide object image under each subaperture of the Shack–Hartmann array, combine them into a full sensor image, resize it to the CCD scale, integrate the image over the integration time, consider the various noise contributions, and, after waiting for a possible time delay, deliver/output the resulting noisy sensor images from which the slopes under each subaperture will be calculated.

With respect to previous versions, our present Shack–Hartmann module (SHW) – limited to square subapertures in a grid arrangement – is faster and its formal implementation is closer to that of module IMG, permitting easier understanding and maintenance of the whole package. Module SHW delivers a single output consisting of an array of images, one per lens in the lenslet array. This array of images is referred to as the Shack–Hartmann spots and will normally be fed to a barycentre quad-cell centroiding (BQC) module, which will compute the local slopes from the Shack–Hartmann spots by employing either a barycentre or a quad-cell algorithm (for further details see Section 3.5).

The parameters set by the SHW GUI are the distance from the entrance pupil to the height the CCD is conjugated at, the number of subapertures along the pupil diameter (i.e. the linear number of subapertures), the minimum illuminance required for a subaperture to be considered active, the FoV seen by each subaperture, the number of pixels per subaperture side (i.e. the linear number of pixels), the CCD plate scale (i.e. the pixel size $\Delta_{\rm CCD}$), the observing band, the average CCD quantum efficiency on this band and selection of noise sources as in module IMG. Moreover, as with module IMG, SHW assumes the optical axis of each subaperture to be at the junction of its four central pixels if an even number of pixels is used, while the optical axis is taken on the centre of the central pixel when the linear number of pixels per subaperture is odd. Note, however, that the use of an odd number of pixels per subaperture is not considered to be the most favourable arrangement (Hardy 1998).

Module SHW uses the same ideas as module IMG in order to avoid interpolations when going from the resolution obtained with the FFT operations ($\Delta_{\rm FFT}$) to the resolution imposed by the sensor CCD pixel size $\Delta_{\rm CCD}$. In fact, module SHW can be viewed as a generalization of module IMG, the only important difference being the fact that IMG outputs both the image and the PSF, while SHW delivers only the image from the lenslet array. An important implementation difference with respect to IMG occurs when the simulation is designed so that the linear number of pixels along a pupil diameter is not an integer multiple of the number of subapertures along the diameter (for instance, 256 wave-front pixels and 10 subapertures along the pupil diameter). In such cases module SHW is forced to perform a bilinear interpolation of the wave-front which will have an impact on the computation time and could slightly change the actual statistics of the assumed turbulence model. When this occurs a warning message is then triggered without stopping the simulation. Another difference with respect to the IMG module occurs when using a three-dimensional LGS. In this case SHW computes the projected two-dimensional map as seen from each subaperture. The spot produced by a given subaperture is then obtained as the convolution of the PSF for this subaperture with the corresponding LGS two-dimensional map projection as seen by this subaperture.

3.3.2 *Pyramid wave-front sensing*

The pyramid wave-front sensor, invented by Ragazzoni (1996), is based on the Foucault test method for optical systems. The main difference with respect to the original Foucault test is the replacement of the knife edge by a glass pyramidal optical element where the function is to emulate two knife edges in two perpendicular directions placed in the focal plane. Fig. 2 describes the set-up of a pyramid sensor: the pyramid is located in an image plane and the four pupils, corresponding to each of the four pyramid facets, are imaged by a relay lens on the pupil plane detector. A dynamic modulation of the beam (following either a circular or a square path) is applied by means for example of a tip–tilt mirror placed in a pupil plane. On the same figure the main steps of the algorithms implemented in module PYR are represented, which gives the final image on the detector. The modulation path is discretized by the user. The first step consists in computing the electric fields Ic_m on the pyramid for each point of the modulation of index m. This is performed by a simple Fourier transform (FT) of the complex amplitude that corresponds to the incoming wave-front φ to which is added the tilt $tilt_m$ corresponding to the position on the modulation path:

$$Ic_m(u, v) = \mathrm{FT}(\exp[-\mathrm{i}(\varphi + tilt_m)]). \quad (1)$$

The second output of module PYR is the resulting image on the top of the pyramid during one modulation cycle, represented by a discretized circle in Fig. 2. It is computed by summing up the squared modulus of all Ic_m values. The computation of the final four pupil images on the detector can be obtained in two ways, summarized in Fig. 3.

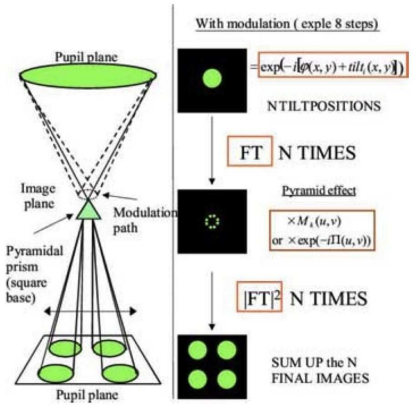

Figure 2. The pyramid wave-front sensor set-up (left) and algorithms (right) for simulating the modulation with N discretized points: the pupil plane image corresponding to each modulation point is computed independently from the others and the whole set of images are then finally summed.

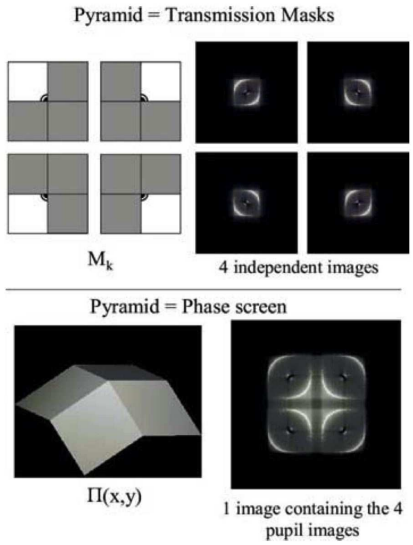

Figure 3. The two methods for computing the pyramid signals. Top, each facet of the pyramid is equivalent to a binary transmission mask and four independent pupil images are computed. Bottom, the pyramid is considered as a phase mask and only one image containing the four pupils is computed.

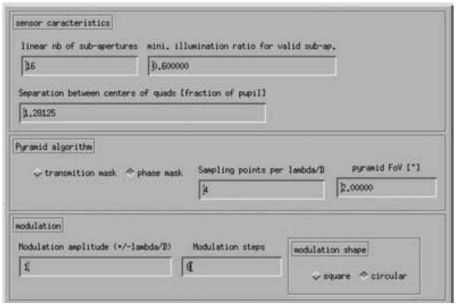

Figure 4. Part of the GUI of module PYR, showing the main relevant parameters. The other physical and numerical parameters (concerning the various noises, the spectral sensitivity, the time integration and delay, etc.) are not shown here.

The first method, already described in Esposito & Riccardi (2001), considers the pyramid as four independent transmission masks $M_k(u, v)$. Each of the four pupil images $Iccd_k(u, v)$ is then computed by summing the results for each modulation points:

$$Iccd_k(u, v) = \sum_m |\mathrm{FT}(Ic_m(u, v) \times M_k(u, v))|^2. \quad (2)$$

The second method, which is fairly new, considers the pyramid as a single phase mask $\Pi(u, v)$. Thus all the four pupils are computed in one step on one image $Iccd$ from which the $Iccd_k$ needs to be extracted for signal computation:

$$Iccd(u, v) = \sum_m |\mathrm{FT}(Ic_m(u, v) \times \exp[-\mathrm{i}\Pi(u, v)])|^2. \quad (3)$$

The latter method permits one to take into account the interference between the four pupil images, which depend on the separation between them. While in the first method, this interference is neglected as if the four images were infinitely distant from each other. After the computation of the $Iccd_k$ images, these are pixelized according to the number of subapertures defined, and the noise is computed as in module IMG. The measurements are then computed within module SLO:[2]

$$S_x(x, y) = [(I_1(x, y) + I_2(x, y)) - (I_3(x, y) + I_4(x, y))]/I_0,$$
$$S_y(x, y) = [(I_1(x, y) + I_4(x, y)) - (I_2(x, y) + I_3(x, y))]/I_0, \quad (4)$$

where $I_i(x, y)$ is the intensity in the subaperture located at (x, y) in the quadrant i, integrated during a modulation cycle and I_0 is either the average intensity per subaperture of the incoming beam or the total intensity in the subapertures in the four quadrants.

The user can choose one or other algorithm and set other parameters in the pyramid parameters GUI (part of it is shown in Fig. 4): the separation between the four pupils (centre to centre) in the case of the phase mask algorithm, the modulation angle and the number of modulation points[3] and the PSF sampling parameter. The value of this last parameter fixes the size of the array on which the FTs are computed, which is simply the PSF sampling parameter times the number of simulation pixels in the pupil. As its name indicates, it is also equal to the number of points sampling the Airy spot.

[2] SLO denotes SLOpe computation, even though the exact nature of pyramid sensor measurements can be significantly different from wave-front slopes (see Vérinaud 2004).

[3] A typical value for the number of steps in circular modulation in order to obtain a rather uniform path is 8 points per λ/D of modulation angle.

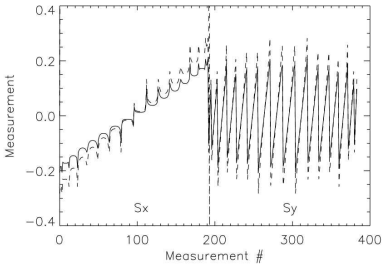

Figure 5. Measurements vector due to interference for a null incoming phase for a centre-to-centre pupil separation of 1.3. Solid line, PSF sampling = 32; dashed line, PSF sampling = 4.

The advantage of using the phase mask algorithm is twofold. At first, at a given PSF sampling it is nearly four times faster than the amplitude mask algorithm. It also permits one to take into account interference between light diffracted from one pupil to the others. Diffracted light is mainly present when no beam modulation is used and when residuals at the sensing wavelength are low. In this case, interference produces an enhancement of the light towards the centre of the image containing the four pupils (see Fig. 3, bottom part) such that even when the incoming phase is perfectly flat the measurement is not null, and can even reach rather high values, as can be seen in Fig. 5. In this figure the null measurement vector for two different values of the PSF sampling parameter is plotted. Note that the shape of the plot has no particular physical meaning and depends on the chosen arrangement of the measurement vector. However, by chance it is close to a measurement vector produced by a defocus which produces a similar enhancement of light towards the centre. On this plot we can see that when the sampling is too poor the interference is overestimated, because of aliasing in the FT. The relative error in the function of the PSF sampling is given in Fig. 6. From this result we can deduce that in order to obtain a 1 per cent accuracy for the interference modelling, the PSF sampling value should be at least 16. Thus when simulating high Strehl-ratio systems, for which

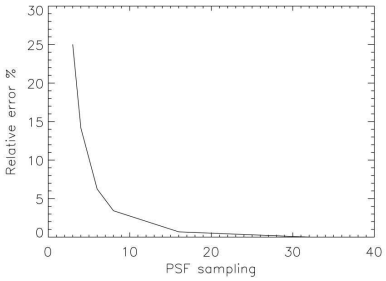

Figure 6. Error on the null measurements in function of the PSF sampling parameter. The reference measurement used to estimate the error has been computed for a PSF sampling value of 32.

interference may affect the signal, one may use a rather high PSF sampling (8–16), while for moderate-size systems with lower Strehl ratios, a PSF sampling value of 4 is generally sufficient.

3.4 Wave-front reconstruction and correction

3.4.1 Wave-front reconstruction

After measuring of the wave-front perturbations from the wave-front sensor, the computed slopes (either in the Shack–Hartmann or in the pyramid case) are sent to a wave-front reconstructor that must translate them into a series of mirror commands where the aim is to compensate for atmospheric deformations. These commands are obtained from both the wave-front sensor slope measurements and the interaction matrix that has been obtained previously by calibrating the system. Such a calibration is obtained by applying each elementary mirror deformation considered (by pushing up the actuators one by one or by applying combined modes one by one), and recording the slope measurements obtained: thus an interaction matrix is built (see Section 3.6).

A standard truncated singular-value decomposition (SVD) is implemented within the module REC in its present release, but other more refined strategies are being investigated, such as the optimal modal gain integrator (Gendron & Léna 1994) and a Kalman kind of control (Le Roux et al. 2004).

3.4.2 Time filtering

Module TFL (time filtering) implements a recursive digital filter in the time domain. Because AO systems work in a closed-loop regime, module TFL can be used as a servo control law to temporally filter the instantaneous estimation of the wave-front error to be compensated, before applying it to the wave-front corrector. The design of the servo control law is crucial in order to ensure stability of the loop and optimal performance for a given system, atmospheric conditions and reference source (Gendron & Léna 1994; Ellerbroek & Rhoadarmer 1997). The use of module TFL, however, is not limited to simulating a control law in servo configurations, it can be used whenever a time filtering is needed, such as in the case of noise filtering or to simulate the dynamical response of a deformable mirror, for instance.

Module TFL implements a traditional approach for the design of a digital recursive infinite impulse response (IIR) filter of the form

$$y_k = b_0 x_k + b_1 x_{k-1} + \cdots + b_M x_{k-M} - a_1 y_{k-1} - \cdots - a_N y_{k-N}, \tag{5}$$

using the bilinear approximation (Tustin transform, Oppenheim & Shafer 1989) of a rational analogue filter $H(s)$, defined in Laplace space, used as prototype. In equation (5) y_k and x_k are the output and input variables at the kth step, b_i and a_j are the weights of the digital filter. The bilinear transformation corresponds to the application of the trapezoidal integration rule to the differential equation associated to the analogue rational filter $H(s)$.

The prototype transfer function $H(s = \sigma + \mathrm{i}\omega)$ for the digital filter design, can be chosen from one of the following.

(i) A generic analogue filter in terms of gain G, zeros z_m and poles p_n of the form

$$H(s) = G \frac{\prod_{m=1}^{M}(s + z_m)}{\prod_{n=1}^{N}(s + p_n)}, \tag{6}$$

where the gain is a real positive number and the zeros and poles can be real or complex. In the latter case the zeros (or poles) are forced to be entered as complex conjugate couples in order to ensure real coefficients for the digital filter.

(ii) A single pole at zero frequency with a user-defined gain G, i.e. a pure integrator with $H(s) = G/s$. This is a simplified input modality with respect to the previous one.

(iii) A proportional–integrator–derivative (PID) filter given by $H(s) = K_\mathrm{p} + \frac{K_\mathrm{i}}{s} + K_\mathrm{d}\frac{\omega_0}{s+\omega_0}s$, where K_p, K_i and K_d are the gains for the proportional, integral and derivative component of the filter, respectively. A low-pass correction $\frac{\omega_0}{s+\omega_0}$ with cutting frequency ω_0 is introduced to filter out the contribution of the high-frequency noise in the derivative component.

Because the sampling frequency $\omega_\mathrm{s} = 1/T$ of the digital filter is unknown when the parameters for module TFL are chosen, the zero and pole frequencies are entered normalized to ω_s. In addition, for each of the three previous cases, the corresponding digital filter is computed and the recurrence relationship is shown. Nevertheless, the user can plot the Bode diagram (amplitude and phase versus frequency) of the prototype analogue filter. In the Bode diagram it is also possible to show the contribution of the effective delay and amplitude attenuation that is introduced by the finite frequency of the digital loop and the wavefront signal smoothing due to the non-zero CCD integration time.

3.4.3 Wave-front correction

Wave-front correction is performed by module DMI, which corrects the incident wave-front given the commands usually computed by the reconstructor REC and the time-filtering module TFL. Thus, it has two inputs: the incident wave-front to be corrected, and the commands coming from REC through TFL. It also has two outputs: the corrected wave-front that results from the difference between the two inputs (and considering the defined mirror stroke and mirror deformation series – mirror modes or influence functions), and the correction mirror shape itself (useful in order to duplicate the correction for wave-fronts coming from different objects observed together). As the mirror is mainly defined by its modes or influence functions computed elsewhere (during the calibration stage by module MDS or in any other manner, including laboratory measures), any kind of mirror can be considered here: piezo-stacked actuator mirrors, piezo-electric bimorph mirrors, electromagnetic actuated adaptive secondary mirrors, or simply ideal mirrors defined by Zernike or Karhunen–Loeve polynomials. Modelling of hysteresis is not implemented.

3.5 The tip–tilt case

Hereafter we will describe the dedicated modules TCE (tip–tilt centroid) and TTM (tip–tilt mirror) to estimate and correct from the overall tip–tilt on the entrance pupil.

When high-order sensing is performed with a LGS the use of a dedicated tip–tilt becomes nearly mandatory because of the LGS position indeterminacy (see, e.g., Rigaut & Gendron 1992). Such indeterminacy arises from the partial cancellation of the turbulence-induced motion when the laser propagates upwards from the launching telescope to the LGS altitude (i.e. focusing distance) and then downwards to the observing telescope. Several methods (see, e.g., Foy et al. 1995; Esposito 1998) have been proposed to sense the tip–tilt modes from the LGS by somehow determining the absolute LGS position, but note that even so there would be a remaining error in the tip–tilt determination because the LGS samples a cone turbulence volume (i.e. the same concept as the cone effect but applied to the tip–tilt modes). In view of these difficulties most (if not all) current LGS-based AO systems resort to determining the tip–tilt modes from an NGS. In systems with a dedicated tip–tilt sensor, a detector

placed at an alternative AO focal plane toward which some fraction of the light is diverted by a beamsplitter (module BSP in CAOS) is assumed. Given the use of a fraction of the precious natural guide star (NGS) light by the tip–tilt sensor, it is therefore a major issue to check on the necessity of such dedicated sensors when the NGS is also used to sense high-order modes. This will be the subject of the example application in Section 4.

In CAOS a dedicated tip–tilt sensor is modelled by module IMG coupled with module TCE. TCE takes the image from IMG and applies either a barycentre or a quad-cell algorithm to compute the centroid of the image as a measure of the overall tip–tilt on the entrance pupil. The barycentre algorithm estimates the x-centroid displacement $\theta_{x,\mathrm{C}}$ (equivalently for the y-centroid displacement $\theta_{y,\mathrm{C}}$ by replacing x by y) from

$$\theta_{x,\mathrm{C}} = \frac{\sum_{i=1}^{N_\mathrm{p}^2} I_i \theta_{x,i}}{\sum_{i=1}^{N_\mathrm{p}^2} I_i}, \tag{7}$$

where the sum extends to all pixels of the CCD detector and I_i, $\theta_{x,i}(\theta_{y,i}$ for the y centroid) correspond to the intensity, angular x coordinate (angular y coordinate) of pixel i of CCD, respectively. This diffraction approach is equivalent to the geometrical optics result for the centroid, provided that scintillation effects are negligible (Voitsekhovich, Orlov & Sánchez 2001). One should also bear in mind that pixelization effects and atmospheric coma-induced terms cause a loss of correlation between the centroid estimator and the actual tip–tilt, resulting in additional error sources (the latter effect commonly being referred to in the literature as centroid anisoplanatism). Equation (7) corresponds to the discrete case of the centroid position vector on the image plane, defined as

$$\boldsymbol{\Theta}_\mathrm{C} = \frac{\int I(\boldsymbol{\Theta})\boldsymbol{\Theta}\,\mathrm{d}^2\theta}{\int I(\boldsymbol{\Theta})\,\mathrm{d}^2\theta}. \tag{8}$$

If the quad-cell detector has been chosen, then module TCE estimates the image displacement according to the expressions

$$x_Q = \frac{I_\mathrm{r} - I_\mathrm{l}}{I_\mathrm{r} + I_\mathrm{l}} \quad \text{and} \quad y_Q = \frac{I_\mathrm{t} - I_\mathrm{d}}{I_\mathrm{t} + I_\mathrm{d}}, \tag{9}$$

where I_r and I_l are the total intensities to the right and left of detector centre, respectively, and I_t and I_d are the intensities on top and down from the detector centre, respectively. As shown by Tyler & Fried (1982) the quantities $I_\mathrm{r} - I_\mathrm{l}$ and $I_\mathrm{t} - I_\mathrm{d}$ are proportional to the tilt angles along the x and y axes, respectively. The denominators in x_Q and y_Q are the total intensity on the image plane, acting as normalizing factors that yield quadrant-cell measurements as estimators of relative tip–tilt angles. A calibration process is needed in order to obtain the required scaling factor, which allows the recovery of estimates of absolute tip–tilt from relative tip–tilt angle measurements. This calibration is performed by feeding a plane wave with the tip–tilt mirror at different known tilt angles. A curve of tilt angle versus TCE output is built and the required calibration constant Q is the slope of the curve in the region where a linear fit is suitable. It is possible to find an analytic estimate for Q under the assumption that the image on the detector is a Gaussian with a full-width at half maximum (FWHM) equal to the seeing angle:

$$Q = \frac{1}{4}\sqrt{\frac{\pi}{\ln 2}}\left\{\frac{\mathrm{Erf}(2\sqrt{\ln 2}\,x)}{1 - \exp[-(2\sqrt{\ln 2}\,x)^2]}\right\}\frac{\lambda}{r_0}, \tag{10}$$

where $\mathrm{Erf}(z) \equiv \frac{2}{\sqrt{\pi}}\int_0^z \mathrm{e}^{-t^2}\,\mathrm{d}t$ is the error function and x is the ratio of pixel size to the seeing angle (i.e. $x \equiv \frac{\Delta_\mathrm{CCD}}{\lambda/r_0}$). In the TCE GUI one has to either provide the file storing the calibration curve or the value of the Q-constant.

Finally, the tip–tilt correction can be operated using module TTM in exactly the same way as for module DMI, as we will also see in Section 4.

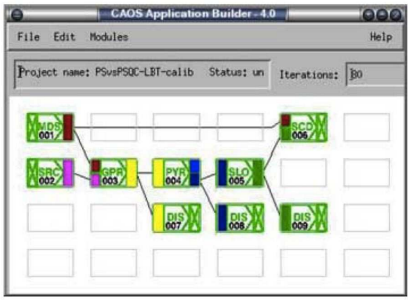

Figure 7. Project representing the calibration of a pyramid-based AO system; within the CAOS application builder and using the modules of the software package CAOS.

3.6 Modelling of the AO system calibration

Fig. 7 shows a typical calibration project within the CAOS application builder and using the modules of the software package CAOS. The case represented actually concerns the calibration of a pyramid-based AO system, the one that will then be used in Section 4.

During calibration of an AO system, typically a series of mirror deformations are sent by module MDS to the wave-front sensor module. The signals corresponding to each deformation are then sent to the module in charge of computing the resulting series of x and y slopes (from each equivalent subaperture), and then to module SCD (save calibration data), to which the mirror deformation series from module MDS also arrives. At the end of the simulated calibration, SCD saves the mirror deformations on one hand and the obtained interaction matrix on the other hand, in two separated files that will then be used by the deformable mirror and the wave-front reconstructor.

Pseudo-inversion of the interaction matrix by means of SVD, with the possibility of filtering out undesired modes, can then be operated during the very first iteration (the initialization iteration) of the subsequent actual simulation.

3.7 Other modelling modules

3.7.1 Fizeau interferometry

Fizeau interferometry has been implemented within module IBC, which permits one to combine the light beams from two telescopes which respective positions as a part of the wave-front input/output structure from the corresponding modules GPR. IBC is implemented in the simplest manner: it forms a new diluted (and atmospherically perturbed) pupil by positioning the two incoming wave-fronts. It also permits one to partially correct from the residual differential piston by selecting which percentage of it has to be maintained in the final diluted pupil. By cascading different modules IBC it is possible to combine more than two telescopes together.

This module has been used for a wide series of simulation studies concerning the Fizeau interferometer LBT (see Carbillet et al. 2002a; Correia et al. 2002; Anconelli et al. 2004), and, thanks to the multiple interferometric stage, for the VLTI (see Lardière et al. 2004).

3.7.2 Coronagraphy

Two coronagraphic modules have recently been implemented within the software package CAOS, namely module COR and module AIC.

Following the common formalism of Lyot (1939) coronagraphy and Roddier & Roddier (1997) phase mask coronagraphy introduced by Aime & Soummer (2003), who basically remark that the main difference between the two techniques resides in the coronagraphic mask present in the first focal plane (in between the first and the second pupil plane where a Lyot stop is put). Such a mask is opaque for Lyot while it is π-dephasing for Roddier & Roddier. It is then easy to model both coronagraphs by a series of three FTs: the first one translates the passage from the first pupil plane to the first focal plane (where the mask applies), the second one then goes to the second pupil plane (where the Lyot stop applies), and hence the third one goes to the second (and final) focal plane. By generalizing this concept to the four-quadrant phase mask (4QPM) technique (Rouan et al. 2000) – with the only difference being that no Lyot stop has to be applied – we have simply modelled all the three coronagraphs within module COR.

The case of the achromatic interfero-coronagraph (AIC) is different because of its interferential nature. Its implementation within CAOS was already presented in Vérinaud & Carbillet (2003), adapted from Gay & Rabbia (1996) and Baudoz, Rabbia & Gay (2000). The input, the numerical parameters, the physical parameters related to the companion star, and the output are similar to the previous case (module COR), except for the reflection and transmission factors.

More details concerning these two implementations can be found in Carbillet (2004).

3.7.3 Additional utilities

As can be noted from Table 1, a number of utilities have been developed: a generic display (module DIS) of all the kinds of input/output data used within the software package CAOS, a structure function calculator module (STF) that permits one to compute the structure function of the simulated wavefronts (or other types of obtained wavefronts) and compare the result with the theoretical formula from a Kolmogorov or von Kármán model, some modules that permit one to add/combine together wavefronts (module WFA), images (module IMA) or atmospheres (module ATA), and a couple of modules for saving (module SAV) and reading (utility RST) any kind of input/output data. Note that RST is not a proper module as it is not used through a dedicated GUI, as is also the case for utility PSG, made for generating phase screens that can be fed to module ATM later.

4 EXAMPLE APPLICATION: IS A TIP–TILT-DEDICATED SENSOR NECESSARY WHEN CONSIDERING A PYRAMID-BASED SYSTEM?

In this section we present a study based on the software package CAOS, and made within the framework of a modern 8-m class telescope. The question we want to address here is the gain we could achieve by implementing an additional dedicated RON-free quad-cell (QC) tip–tilt sensor, when already considering a system based on the pyramid sensor (PS) using a standard CCD. We first give some simple preliminary considerations, and the actual performance is then evaluated by means of end-to-end CAOS simulations, taking into account an ensemble of effects that cannot be completely modelled analytically, and thus need detailed numerical simulations. The practical parameters taken into account here are that of the LBT first-light AO system (Carbillet et al. 2003; Esposito et al. 2003).

4.1 Preliminary considerations

The main source of limitations when considering AO correction are the uncorrected atmosphere residuals, the photon starving, and the RON. For photon noise and also the contribution of RON, the total corresponding phase residual error variance $\sigma^2_{\rm noise}$ can be expressed as (Rousset 1999)

$$\sigma^2_{\rm noise} = \left(\frac{\pi\theta d}{\lambda_{\rm s}}\right)^2 \left(\frac{1}{n_{\rm ph}} + \frac{4\sigma_{\rm e}^2}{n_{\rm ph}^2}\right) [\mathrm{rad}^2], \tag{11}$$

where θ is the angular spot size on the sensor, $n_{\rm ph}$ is the number of photons per integration time and per subaperture, $\sigma_{\rm e}$ is the RON expressed in e^- rms, $\lambda_{\rm s}$ is the sensing wavelength, rad stands for radians, and the term proportional to $1/n_{\rm ph}$ is due to photon noise and the term proportional to $4\,\sigma_{\rm e}^2/n_{\rm ph}^2$ is due to the RON. Dark-current and background noise contributions are neglected here. Note that by considering this model in our case, we thus clearly assume that the pyramid roughly acts as a Shack–Hartmann sensor with 2×2 pixel under each subaperture. This is far from the physical actual situation, but it permits a couple of useful preliminary considerations.

The main consideration concerns RON. As we wish to consider a RON-free QC for measuring tip–tilt, it is clear that the corresponding measurement will only be affected by photon noise, while it will also be affected by RON when using the PS. This simple consideration implies that, if only tip–tilt were to be measured, the QC would be the best solution. However, as a portion of light must also be sent to the PS in order to measure the higher-order modes, this obviously does not apply straightforwardly. Let us call β the fraction of light sent to the QC, and let us re-write equation (11) for the specific cases of the QC and the PS, we have

$$\begin{aligned} \sigma^2_{\rm QC} &= \left(\frac{\pi\theta d}{\lambda_{\rm s}}\right)^2 \frac{1}{\beta n_{\rm ph}}, \\ \sigma^2_{\rm PS} &= \left(\frac{\pi\theta d}{\lambda_{\rm s}}\right)^2 \left(\frac{1}{n_{\rm ph}} + \frac{4\sigma_{\rm e}^2}{n_{\rm ph}^2}\right). \end{aligned} \tag{12}$$

Note for the QC expression that $d = D$ and $n_{\rm ph} = N$, where N is the total number of available photons and D is the telescope diameter. From equation (12), and stating that the scope is $\sigma^2_{\rm QC} < \sigma^2_{\rm PS}$ in order to have a better correction of the tip–tilt when using the QC, a minimum value of β respecting this condition can be calculated. Naturally the value found would not be rigorous, as here we are neglecting a large number of physically important processes/factors. For example the fact that we are interested in closed-loop operation during which different gains will be applied to the QC and the PS, and especially that the responses of both sensors are different a priori. This is sufficient to assess the existence of a minimum value of β for which a better correction of the tip–tilt is performed.

Nevertheless, β cannot reach any value, as from the higher-order modes sensing front, a minimum number of photons are also necessary in order to have an overall estimation (tip–tilt+higher orders) which is still better when using the 'PS+QC' configuration than when using the 'PS alone' configuration. Hence a trade-off between

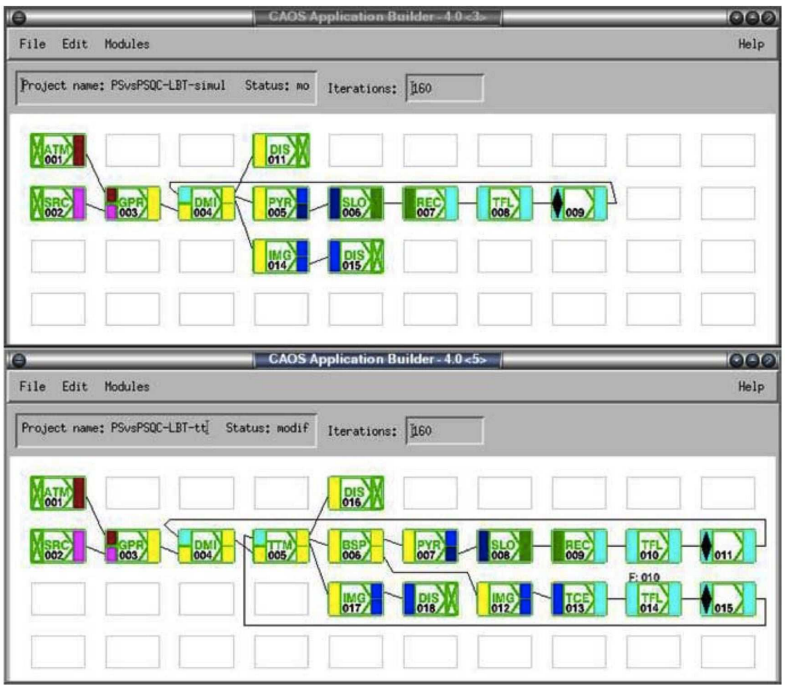

Figure 8. Projects representing the complete end-to-end simulations of the 'PS alone' case (top), and the 'PS+QC' case (bottom); within the CAOS application builder and using the modules of the software package CAOS.

those two conditions has to be found, leading to a range of values of β for which this trade-off is realized.

In the next section we will verify the existence of this range of values, also trying to find an optimal value for β, by performing complete end-to-end simulations. Thus we will compare the results obtained with that obtained when no tip–tilt separated sensor is used.

4.2 End-to-end simulation using CAOS

Fig. 8 shows the two main simulation projects that were used in order to compare the two system configurations considered here. A third project (not shown here but similar to that shown in Fig. 7) is necessary in order to calibrate the system, as already described in Section 3.6. The main difference between the two simulation projects of Fig. 8 resides in the tip–tilt branch present in the bottom part of Fig. 8: a beamsplitter (module BSP) is introduced just after the two correcting mirrors (module DMI for the higher-order modes and module TTM for the tip and tilt), sending part of the light to the tip–tilt sensor (modelled within module IMG). Hence the resulting image is sent to module TCE for measuring the corresponding tip–tilt and computation of the necessary tip–tilt commands. Module TFL is then used to filter these commands, the loop is closed thanks to the dedicated special module (part of the application builder), and the resulting correction is applied by TTM. Note that the latter could not be present in a real-life situation, as the higher-order deformable mirror could manage both types of commands, but it is clearer at least from the simulation and analysis point of view.

The main parameters of the simulation performed are reported in Table 2, and they correspond to one of the optimized situations for the first-light AO system of LBT (see Carbillet et al. 2003). Note that these optimized situations (in terms of sensor configuration, exposure time, number of modes corrected, etc.) were determined with respect to the AO guide star magnitude, the average expected atmospheric conditions, and the detailed characteristics of the system that is actually being built.

4.3 CAOS results and discussion

Fig. 9 shows the final result of our series of simulations in terms of wave-front rms residual error obtained after boot-strapping of the AO system, and hence during its stable regime. The rms plot as function of the different simulated values of β clearly shows the lower error value obtained for $\beta = 0.1$, confirming the existence of the trade-off foreseen previously.

Nevertheless, it also indicates that the achieved gain is rather modest. We have run a number of simulations with different standard conditions leading to the same conclusion, hence suggesting that a dedicated tip–tilt sensor when considering an 8-m class telescope pyramid-based AO system such as the one of LBT, does not yield

Table 2. Main parameters of the end-to-end CAOS simulations.

Turbulent atmosphere parameters	
Fried parameter r_0 (at 500 nm)	15 cm
Number of turbulent layers	2
Ground layer velocity	$\sim$8 m s^{-1}
Ground layer C_N^2 profile relative percentage	70 per cent
High layer velocity	$\sim$16.5 m s^{-1}
High layer C_N^2 profile relative percentage	30 per cent
Wave-front outer-scale L_0	20 m
Telescope parameters	
Effective diameter	8.22 m
Obstruction ratio	0.11
AO guide star parameters	
Spectral type	K5
R-magnitude	14
Deformable mirror parameters	
Type of adaptive mirror	Secondary mirror
Number of actuators	672
Wave-front reconstruction parameters	
Number of modes reconstructed	80
Time-filter type	Pure integration
Closed-loop gain	0.5
Wave-front sensing parameters	
Central sensing wavelength	750 nm
Bandwidth	300 nm
Total average transmission	0.41
Sensor configuration	15 $\times$15 (176 subap.)
Exposure time (ms)	2.5
$\Rightarrow$ corresponding $n_{\rm ph}$	$\simeq$18
Pyramid RON (e$^-$ rms)	4.5
Pyramid simulation method	Transmission mask
Pyramid modulation (λ/D)	4

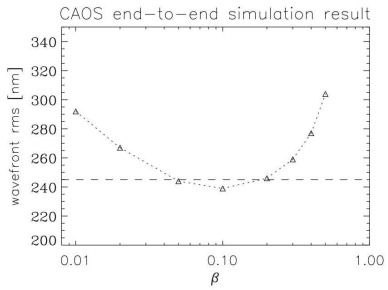

Figure 9. Wave-front rms residual resulting from the complete CAOS end-to-end simulation, in function of β. Note that the optimum value is reached for $\beta \simeq 0.1$.

a great improvement of the global system performance. Performing the same study but considering a Shack–Hartmann-based AO system would probably lead to a different conclusion, but this goes beyond the scope of this paper.

5 SUMMARY AND CONCLUDING REMARKS

In this paper we have presented the latest release of the software package CAOS, a numerical tool capable of simulating a wide range of astronomical optics problems, especially for AO and AO-related astronomy.

We have presented an example application of our tool concerning the opportunity of adding a tip–tilt sensing branch to an existing 8-m class telescope pyramid-based AO system. We have proved the existence of an optimum value of the distribution of light between the higher-order branch and the tip–tilt branch, by means of complete end-to-end numerical simulations using the modules of the software package CAOS. Moreover, we have arrived at the conclusion that the gain achievable is rather modest, suggesting that the addition of a tip–tilt branch, at least in the particular case considered here, does not lead to a significant improvement of the system performance.

The software package CAOS, version 5.0, is downloadable from the dedicated web site http://www.arcetri.astro.it/caos. It is presently delivered together with the CAOS application builder (version 4.1): the IDL-based graphical environment within which it was developed. Subscription to the dedicated mailing list is appreciated for new users. Note that the compatibility of the CAOS application builder has been extended (from present version 4.1) to Windows XP and Mac OS X platforms, in addition to native Unix/Linux.

Finally, let us note that parallel strategies are studied for CAOS (actually for all the software packages developed, with some parallel tools at a global level, i.e. at the level of the application builder itself). Some of the parallelization tools that are being developed within this framework could, in the future, be used by any existing IDL-based code.

ACKNOWLEDGMENTS

The authors wish to acknowledge the people who have contributed to early versions of the software package CAOS, namely Élise Vernet-Viard, Françoise Delplancke and Simone Esposito, but also to the people from which preliminary versions of the code benefited from their own, namely Enrico Marchetti on one hand and François Rigaut on the other hand. Serge Correia is acknowledged for his contribution to the interferometric module IBC, and Olivier Lardière for his contribution to the coronagraphic module COR. The authors also wish to thank users who gave feedback and contributions in fixing the code: Miska Le Louarn, Jeff Clifford, Stefan Hippler, Lyu Abe, Malcolm Smith, Brice Le Roux and Doug Looze. Finally, thanks are due to an anonymous referee for constructive comments on the original manuscript.

REFERENCES

Aime C., Soummer R., 2003, in Aime C., Soummer R., eds, EAS Publ. Ser. Vol. 8, Astronomy with high-contrast imaging. EDP Sciences, Les Ulis, p. 79
Anconelli B., Bertero M., Boccacci P., Carbillet M., 2004, A&A, in press
Arcidiacono C., Diolaiti E., Tordi M., Ragazzoni R., Farinato J., Vernet É., Marchetti E., 2004, Appl. Opt., 43, 4288
Baudoz P., Rabbia Y., Gay J., 2000, A&AS, 141, 319
Carbillet M., 2004, in Aime C., Soummer R., eds, EAS Publ. Ser., Vol. 12, Astronomy with high-contrast imaging. EDP Sciences, Les Ulis, p. 137
Carbillet M., Correia S., Boccacci P., Bertero M., 2002a, A&A, 387, 744
Carbillet M., Femenía B., Esposito S., Brusa G., Correira S., 2002b, in Vernet É., Ragazzoni R., Esposito S., Hubin N., eds, ESO Conf. Workshop Proc. 58, Beyond conventional adaptive optics. ESO, Garching-bei-munchen, p. 259
Carbillet M., Vérinaud C., Esposito S., Riccardi A., Puglisi A., Femenía B., Fini L., 2003, in Wizinowich P. L., Bonaccini D., eds, SPIE Proc. 4839, 131

Correia S., Carbillet M., Boccacci P., Bertero M., Fini L., 2002, A&A, 387, 733
Ellerbroek B. L., Rhoadarmer T. A., 1997, J. Opt. Soc. Am. A, 14, 1975
Esposito S., 1998, in Bonaccini D., Tyson R. K., eds, SPIE Proc. 3353, 468
Esposito S., Riccardi A., 2001, A&A, 369, L9
Esposito S. et al., 2003, in Wizinowich P. L., Bonaccini D., eds, SPIE Proc. 4839, 164
Femenía B., Devaney N., 2003, A&A, 404, 1165
Fini L., Carbillet M., 2003, in Payne H. E., Jedrzejewski R. I., Hook R. N., eds, ASP Conf. Ser. Vol. 295. Astron. Soc. Pac., San Francisco, p. 347
Fini L., Carbillet M., Riccardi A., 2001, in Primini F. A., Harnden F. R., eds, ASP Conf. Ser., Vol. 238, Astronomical data analysis software and systems X. Astron. Soc. Pac., San Francisco, p. 253
Foy R., Migus A., Biraben F., Grynberg G., McCulloch P. R., Tallon M., 1995, A&AS, 111, 569
Gay J., Rabbia Y., 1996, C. R. Acad. Sci. Paris, 332 (IIb), 265
Gendron É., Léna P., 1994, A&A, 291, 337
Gendron É. et al., 2004, A&A, 417, L21
Goodman J. W., 1968, Introduction to Fourier Optics. McGraw-Hill, New York
Habart É., Natta A., Testi L., Boulanger F., Carbillet M., Dartois E., d'Hendecourt L., 2004, VLT + NACO observing time proposal #072.C-178, 2004, VLT+NACO proposition #072.C-178, Carbon Dust in Protoplanetary Discs
Hardy J. W., 1998, Adaptive Optics for Astronomical Telescopes. Oxford Univ. Press, Oxford
Jolissaint L., Véran J.-P., 2002, in Vernet É., Ragazzoni R., Esposito S., Hubin N., eds, ESO Conf. and Workshop Proc. 58, 201
Lacombe F. et al., 2004, A&A, 417, L5
Lagrange A.-M. et al., 2004, A&A, 417, L11
Lardière O., Mourard D., Patru F., Carbillet M., 2004, in Traub W. A., Monnier J. D., Schöller M., eds, SPIE Proc. 5491, p. 415
Le Louarn M., Vérinaud C., Korkiaskoski V., Fedrigo E., 2004, in Bonaccini D., Ellerbroek B. L., Ragazzoni R., eds, SPIE Proc. 5490, p. 705
Le Roux B., Conan J.-M., Kulcsár C., Raynaud H.-F., Mugnier L. M., Fusco T., 2004, J. Opt. Soc. Am. A, 21, 1261
Lyot B., 1939, MNRAS, 99, 580
Oppenheim A. V., Shafer R. W., 1989, Discrete Time Signal Processing. Prentice-Hall, Englewood Cliffs
Ragazzoni R., 1996, J. Mod. Opt., 43, 289
Rigaut F., Gendron É., 1992, A&A, 261, 677
Roddier F., Roddier C., 1997, PASP, 109, 815
Rouan D., Riaud P., Boccaletti A., Clénet Y., Labeyrie A., 2000, PASP, 112, 1479
Rousset G., 1999, in Adaptive Optics in Astronomy. Cambridge Univ. Press, Cambridge, p. 91
Tyler G. A., Fried D. L., 1982, J. Opt. Soc. Am., 72, 6
Vérinaud C., 2004, Opt. Commun., 233, 27
Vérinaud C., Carbillet M., 2003, in Aime C., Soummer R., eds, EAS Publ. Ser. 8, 209
Vérinaud C., Esposito S., 2002, Opt. Lett., 27, 470
Vérinaud C., Arcidiacono C., Carbillet M., Diolaiti E., Ragazzoni R., Vernet-Viard É., Esposito S., 2003, in Wizinowich P. L., Bonaccini D., eds, SPIE Proc. 4839, 524
Voitsekhovich V. V., Orlov V. G., Sánchez L. J., 2001, A&A, 368, 1133

This paper has been typeset from a TEX/LATEX file prepared by the author.

1.2.3 *Restoring of interferometric images – I. The Software Package* AIRY

L'article suivant, publié par *Astronomy & Astrophysics* en 2002, présente en détail le Software Package AIRY, conçu d'une part pour la simulation, mais aussi et surtout d'autre part pour la déconvolution (éventuellement multiple) d'images astronomiques (éventuellement interférométriques mais au sens de Fizeau), avec une focalisation initiale et contextuelle sur les applications liées au LBT.

Comme le Software Package CAOS, le Software Package AIRY est modulaire, et fonctionne bien entendu au sein du même écrin, qui ne s'appelait pas encore le PSE CAOS. Cette première version d'AIRY contient une version accélérée [3] de l'algorithme classique de déconvolution Lucy-Richardson/Richardson-Lucy.

Son utilisation est illustrée ici par une étude des limites intrinsèques de l'algorithme de déconvolution multiple intégré dès cette première version de l'outil, dans le cas d'une étoile binaire et dans celui d'un objet diffus, ainsi qu'une première tentative de super-résolution par déconvolution, sujet que nous verrons traité plus en détail au Chap. 3, Sec. 3.3.

Là aussi, quelques articles précèdent celui-ci, présentant soit une version préliminaire de l'outil [51], soit quelque application [48]. Et surtout, de nombreux articles y font suite, chacun présentant une extension/application spécifique, illustrée la plupart du temps par le biais du cas particulier du LBT utilisé dans son mode interférométrique de Fizeau [56, 63, 68, 69, 78, 79, 80, 87, 88, 89, 94, 102, 124, 143], mais pas seulement [73, 95, 96, 119, 155]. Ils seront évoqués, et même détaillés pour certains d'entre eux, également au Chap. 3.

Concernant l'outil lui-même, un article de conférence de 2012 [151], écrit à l'occasion de la sortie de la version 6.0 du Software Package AIRY, rend compte des plus importantes évolutions subies à une dizaine d'années de sa création. Celles-ci concernent notamment une version rénovée du module central de déconvolution DEC, incluant différents types de régularisations, d'accélérations, de critères d'arrêt d'algorithmes standards tels qu'OSEM (pour *Ordered Subset Expectation Maximisation*) et Richardson-Lucy. Plusieurs autres modules du Software Package AIRY ont également été ajoutés et améliorés au cours du temps, tel que le module PEX d'extraction et d'extrapolation de la réponse impulsionnelle ou le module CBD de déconvolution aveugle avec éventuelles contraintes (telle que celle de Strehl que nous verrons présentée en détail au Chap. 3, Sec. 3.4), ou encore le module utilitaire RTI permettant de faire subir (proprement !) une rotation (ou dérotation) aux images traitées.

3. Seulement dans le cas d'images multiples.

A&A 387, 733–743 (2002)
DOI: 10.1051/0004-6361:20020370

Astronomy & Astrophysics

Restoration of interferometric images

I. The software package AIRY

S. Correia[1,2], M. Carbillet[3], P. Boccacci[4], M. Bertero[4], and L. Fini[3]

[1] UMR 6525 Astrophysique, Université de Nice–Sophia Antipolis, Parc Valrose, 06108 Nice Cedex 2, France
[2] European Southern Observatory, Alonso de Cordova 3107, casilla 19001, Santiago 19, Chile
[3] Osservatorio Astrofisico di Arcetri, largo E. Fermi 5, 50125 Firenze, Italy
e-mail: marcel@arcetri.astro.it; lfini@arcetri.astro.it
[4] INFM and DISI, Università di Genova, via Dodecaneso 33, 16146 Genova, Italy
e-mail: boccacci@disi.unige.it; bertero@disi.unige.it

Received 15 January 2002 / Accepted 7 March 2002

Abstract. The Software Package AIRY (Astronomical Image Restoration in interferometrY) described in this paper is designed for simulation and/or multiple deconvolution of interferometric images. It was conceived for applications to the Large Binocular Telescope (LBT), but can also be used for future interferometers of the same class. AIRY is modular, IDL-based, and designed to be used together with the CAOS (Code for Adaptive Optics Systems) Application Builder. As concerns multiple deconvolution AIRY includes an implementation of the method OS-EM (Ordered Subsets-Expectation Maximization) which is an accelerated version of the Lucy-Richardson method. After a description of the structure and modules of the software package, its use is illustrated with a few applications. In particular the intrinsic performance of the implemented restoration method is explored in the case of binary stars of different angular separations and magnitude differences, as well as in the case of a diffuse object. The possibility of obtaining super-resolved images of unresolved binary stars is also demonstrated.

Key words. techniques: interferometric – techniques: image processing – methods: data analysis – methods: numerical – stars: imaging

1. Introduction

The Large Binocular Telescope (LBT) is the first example of interferometers of a new conception, designed to provide high-resolution imaging of a wide field in the near-infrared and visible wavelengths domain. The basic feature of LBT and of future LBT-like interferometers (as for example the 20/20 telescope project) is the possibility of getting a good coverage of the u–v spatial frequency plane by means of a few observations at different parallactic angles. Indeed LBT will consist of two 8.4 m pupils placed 14.4 m apart on a common alt-azimuthal mount. It is currently under construction on the top of Mount Graham in Arizona and first light is planned for early 2004. As a permanent part of LBT, the foreseen high-level Adaptive Optics (AO) system, including adaptive secondary mirrors, pyramid wavefront sensors, and multi-conjugate AO techniques, is intended to achieve a high-quality correction (up to ∼90% Strehl ratio in the near-infrared) on a large part of the field (typically 2 arcmin). However, in order to be able to produce high-resolution, possibly deep and wide-field, imaging from interferometric data, appropriate restoration methods must be used.

The basic feature of the restoration problem for an interferometer like LBT is that a unique high-resolution image must be extracted from different interferometric observations of the same target, obtained with different orientations of the baseline with respect to the sky (i.e. different parallactic angles). Such a problem is essentially a problem of multiple image deconvolution (Piana & Bertero 1996), and is an extension of the usual image restoration problem where only one observation of the target is available. Well-know methods for the solution of the latter can be generalized to the case of multiple images. For instance Correia & Richichi (2000) provide the first application of the extension of the Lucy-Richardson (LR) method to LBT-like data while validation and comparison of the extensions of some iterative and non-iterative restoration methods is discussed in Bertero & Boccacci (2000b).

The main difficulty of the LR method, at least from the computational point of view, is the slow convergence of the iterations. However the analogy between the

Send offprint requests to: S. Correia,
e-mail: scorreia@eso.org

LBT restoration problem and computerized tomography suggests to investigate the applicability to LBT of methods introduced in that field for the acceleration of the Expectation Maximization (EM) method, which is the version of LR used in tomography (Shepp & Vardi 1982). As a result of this analysis a version of the method Ordered Subsets – Expectation Maximization (OS-EM), suitable to the LBT problem, is introduced in Bertero & Boccacci (2000a). The new method provides, when compared with LR, a reduction of the number of iterations by a factor p (where p is the number of observations), with approximately the same computational cost per iteration. Since the processing time is approximately independent of the number of observations, this method is well suited for a quick look in the restoration of images from interferometric data as it will be required by LBT. A practical implementation of this technique is included in the Software Package AIRY presented in this paper. However it is important to point out that, thanks to the particular modular structure of AIRY, it is easy to add to the package other modules implementing other restoration methods as those considered in Bertero & Boccacci (2000b), or blind deconvolution methods as those presented by Hege et al. (1999).

The acronym AIRY (Astronomical Image Restoration in interferometrY) was first introduced for describing the activity of a group of astronomers and mathematicians collaborating on the restoration of interferometric images (see the related WEB page: `http://dirac.disi.unige.it`). The first result of this collaboration is just the Software Package AIRY, which is based on IDL and designed to be used together with the CAOS (Code for Adaptive Optics Systems) Application Builder (Fini et al. 2001). It can be used for simulating optical and near-infrared interferometric observations, and to perform subsequent image restoration, with application to LBT or LBT-like interferometers.

The purpose of this paper is not only a description of the Software Package AIRY but also a demonstration of its use in the simulation and restoration of LBT images. Therefore the paper is organized as follows. In Sect. 2 we recall the restoration method we have implemented and we discuss the structure of AIRY. In Sect. 3 we give a detailed description of the modules of the present version of AIRY and of their tasks. In Sect. 4 we demonstrate the use of AIRY by a few applications to LBT. The topics considered in this last part concern the limits of the restoration method in evaluating astrometric and photometric parameters of binary stars with different values of angular separation and magnitude difference, the possibility of using OS-EM as a super-resolving method in the case of unresolved binary stars, and the imaging of a diffuse and extended object. In all these cases we assume perfectly co-phased and corrected point-spread functions (PSFs) as well as a declination of the object such that LBT can assure a complete coverage of the u–v plane. The effects on imaging due to partial angular coverage and to partial AO correction are investigated in the subsequent paper (Carbillet et al. 2002). We finally summarize the paper and give some conclusions and perspectives in Sect. 5.

2. Structure of the software package AIRY

We first give a brief description of the OS-EM method which is the restoration method implemented in the present version of AIRY. As already mentioned in the Introduction it is basically an accelerated version of the LR method, when applied to multiple images deconvolution, and therefore provides the same results as LR when the iterations are suitably stopped.

We denote by $\boldsymbol{f}$ the array $N \times N$ which represents the astronomical target to be recovered and by $\boldsymbol{g}_j$, $j = 1, 2, ..., p$, the arrays $N \times N$ corresponding to p observations of the target, performed with p different orientations of the baseline of the interferometer. The PSFs related to the observations $\boldsymbol{g}_j$ are denoted as $\boldsymbol{K}_j$ and, in this paper, are supposed to be space-invariant. Therefore we assume the following model for image formation:

$$\boldsymbol{g}_j = \boldsymbol{K}_j * \boldsymbol{f} + \boldsymbol{b}_j + \boldsymbol{w}_j, \tag{1}$$

where the symbol $*$ denotes convolution, the quantities $\boldsymbol{b}_j$ are the average backgrounds due to sky emission and the quantities $\boldsymbol{w}_j$ are the noise terms. We point out that, even if we write the noise as an additive contribution to the images, this does not imply that we are only considering signal-independent noise. Indeed, in our simulations we introduce both read-out and Poisson noise.

This model of image formation is that used in the generation of LBT images by AIRY. As concerns the image restoration problem, it consists in estimating the astronomical target $\boldsymbol{f}$ from the knowledge of the p observations $\boldsymbol{g}_j$, of the p corresponding PSFs $\boldsymbol{K}_j$ and of the p average backgrounds $\boldsymbol{b}_j$. Therefore it is the problem of deconvolving multiple images of the same object in the presence of background and noise. As already mentioned in the Introduction, a few methods for the solution of this problem are proposed and compared in Bertero & Boccacci (2000b). As a result of this comparison, we have found convenient to implement only one method in the first version of AIRY, i.e. OS-EM.

If we denote by $\boldsymbol{K}_j^{(-)}$ the PSF obtained by reflecting $\boldsymbol{K}_j$ with respect to the center of the array then the proposed version of the OS-EM iterative method is as follows:

- initialize with $\boldsymbol{f}^{(0)}$ positive (for instance a uniform image);
- given $\boldsymbol{f}^{(k)}$ set $\boldsymbol{h}^{(0)} = \boldsymbol{f}^{(k)}$ and, for $j = 1, 2, ..., p$, compute

$$\boldsymbol{h}^{(j)} = \boldsymbol{h}^{(j-1)} \boldsymbol{K}_j^{(-)} * \frac{\boldsymbol{g}_j}{\boldsymbol{K}_j * \boldsymbol{h}^{(j-1)} + \boldsymbol{b}_j}; \tag{2}$$

- set $\boldsymbol{f}^{(k+1)} = \boldsymbol{h}^{(p)}$,

where, as usual, products and quotients of images have to be intended as products and quotients pixel by pixel and the index k characterizes the iterations. Each iteration

consists of a cycle over the p observations. We also point out that this version of the method applies to the case where *each PSF is normalized in such a way that the sum of all its values is one.*

After these preliminary remarks, we describe now the structure of the Software Package AIRY which is modular and designed to simulate optical and near-infrared interferometric observations and/or to perform subsequent image restoration/deconvolution, using the model of image formation and the method of image deconvolution described above.

The Software Package AIRY can be applied to a wide range of imaging problems, including the post-processing of real data. It is written in IDL, and consists of a set of specific modules, each representing a particular task, which are described in the next section. AIRY is conceived to be used together with the CAOS Application Builder, from version 2.0 onwards (current version is 3.0). CAOS has been designed to provide a graphical programming environment where elementary building blocks can be assembled together to create complex simulation applications in a straightforward manner, so that the user can concentrate on the scientific aspects of her/his problem, while mundane coding problems are managed by some automatic tool. It basically allows a user to build a simulation program (a *project*) by putting together the needed elementary building blocks (the *modules*) and specifying the data flow between each block. When the project has been defined to the user's satisfaction the IDL code which implements the program is automatically generated. See Fini et al. (2001) for a more detailed description of the CAOS Application Builder.

As a CAOS-compatible software package, AIRY permits to build different applications by linking the modules together and setting their parameters through their own graphical user interfaces (GUIs). The concept of the Software Package AIRY is identical to that of the already existing Software Package CAOS (the original software package associated to the CAOS Application Builder – see Carbillet et al. 2001 – and devoted to adaptive optics systems simulations). In particular new modules can be easily implemented by the user for her/his particular needs. The Software Package AIRY also includes a library of ideal and AO-corrected LBT PSFs (produced using the Software Package CAOS), a library of useful routines (in addition to those related to each module), a hyper-text help which can be called from the individual GUI of each module, and a set of examples of typical simulation projects.

Table 1 shows a complete list, together with a very brief description, of the modules of the current version 1.0 of the Software Package AIRY. A more detailed description will be given in the next section. Nevertheless it may be important to remark that any module can have a number of inputs/outputs varying from zero to two and that only two types of input/output are defined within the present version of AIRY: the *object* type and the *image* type. Since AIRY is an image-oriented package, almost all modules have inputs and outputs of the type *image*, except the module `OBJ` (no input, and only one output of type *object*), and the module `CNV` (one input of type *object*, and one of type *image*, and only one output of type *image*). Finally the utility module `DSP` can display both types of input.

However, in order to clarify the role of each module, it is convenient to refer to a few typical applications. Two examples of projects are represented in Fig. 1. Both are essentially composed of three parts: a data modeling part, a data processing part, and a data analysis part.

The first project (left side of Fig. 1) is an example of treatment of real data in the case of the observation of a binary star. The data modeling part of this application is very simple because it is reduced to read the files containing the observed data and the corresponding PSFs obtained, for instance, from observations of a reference star. Therefore data modeling consists of two occurrences of the module `RFT` (one for the interferometric images and one for the PSFs), followed by a data processing part which in turns consists of a pre-processing stage (module `PRE`), and the subsequent multiple deconvolution (module `DEC`). Last part concerns the analysis of the deconvolved images, and in particular the detection and characterization of the retrieved binary star parameters with the help of the module `ANB`.

The second project (right side of Fig. 1) is the simulation of the observation, image restoration, and data analysis of a star cluster. Here the data modeling part is clearly more advanced because the object is first modeled within module `OBJ`, and then convolved with PSFs taken, for example, from the PSF library present in the package. To this purpose the modules `RFT` and `CNV` are used. Both the object data and reference data are then treated within module `ADN` in order to add the different kinds of noise contributions. The data processing part is then similar to that of the previous example (pre-processing of the data followed by multiple deconvolution), while the data analysis part consists of the analysis of the reconstructed star cluster by the module `FSM`.

In each application, utility modules allow to display and save the data at each stage of the data flow and at each iteration of the process.

As clarified by the previous examples, we use the following classification of the modules of AIRY: data modeling modules, data processing modules, data analysis modules, and utility modules. The next section describes in detail the tasks of the modules of these different classes.

It must also be stressed that, since the Software Package AIRY is fully modular, the possible applications are not limited to the previous two cases. The output of each module can be linked to the (compatible) input of another one, and ad hoc modules proper to the needs of the user can be easily added to AIRY, thanks to the template module given along with the package. Moreover, and thanks again to its modular structure, we believe the Software Package AIRY to be an ideal tool for fair comparison of different methods for image reconstruction, data pre-processing, etc.

Table 1. Descriptive list of the modules of the Software Package AIRY (version 1.0).

Module	Purpose
Data simulation modules	
OBJ - OBJect definition	-to define the object characteristics
CNV - object-PSF CoNVolution	-to perform convolution
ADN - ADd Noise to image	-to add read-out and Poisson noise
Data processing modules	
PRE - PRE-processing	-to perform image pre-processing
DEC - DEConvolution process	-to perform deconvolution (OS-EM method)
Data analysis modules	
ANB - ANalysis of Binary	-to analyse reconstructed images of binary objects
FSM - Find Star Module	-to detect stars in the reconstructed images
Other modules and utilities	
RFT - Read FiTs file format	-to read FITS images
WFT - Write FiTs file format	-to write FITS images
RSC - Restore im. Struct. Cubes	-to restore image structure cubes (XDR or FITS format)
SIM - Save IMage struct.	-to save image structure cubes (XDR or FITS format)
DSP - data DiSPlay	-to display images

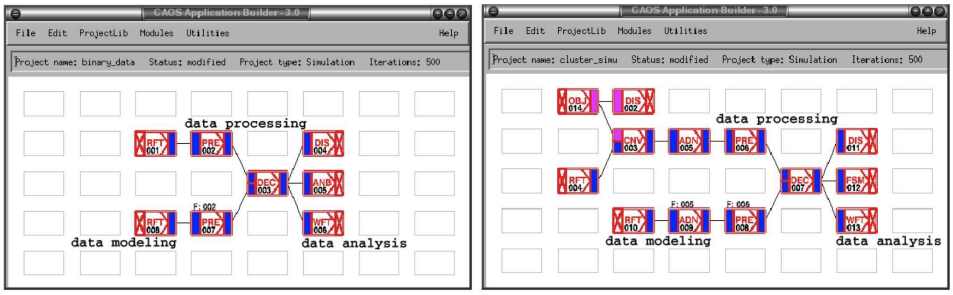

Fig. 1. Two examples of projects using the Software Package AIRY. Left: restoration and data analysis in the case of real observations of binary stars. Right: simulation of star cluster observations, followed by image restoration and data analysis.

3. Description of the AIRY modules

In this section we describe in detail the tasks of the modules of each one of the four classes indicated above.

3.1. Data modeling modules

This class contains the modules OBJ (OBJect definition), CNV (object-psf CoNVolution) and ADN (ADd Noise to image).

The module OBJ is designed to define the characteristics of an object chosen among several pre-defined types (binary object, open cluster, planetary nebula, Super Novae remnant, spiral galaxy, Young Stellar Object, stellar surface), or modeled by the user. For each object it is possible to adjust the corresponding relevant parameters. For instance planetary nebulae or Super Novae remnants modeling allows to enter emission-lines fluxes, which are subsequently converted into the flux within the observed bandwidth. Another example is provided by stellar surface modeling which allows to create maps of uniform elliptical disks with possibly the presence and characterization of a bright spot feature. Figure 2 shows the GUI corresponding to this module, with the main interface in the upper part, and the auxiliary interface corresponding to the particular case of a Young Stellar Object (YSO) in the bottom part. The whole set of available parameters is visible in this particular example, which is just the example of diffuse object considered in Sect. 4.

The module CNV performs an FFT-based convolution of the two inputs, typically the object map and a PSF cube (where usually each element of the cube represents the PSF at a given parallactic angle). The module CNV sets also the telescope- and detector-dependent parameters such as the overall efficiency, the integration time, and the telescope collecting surface. Moreover the module CNV rebins the object map with the pixel size of the PSF and puts each frame of these two inputs into an array with a dimension equal to the closest power of 2.

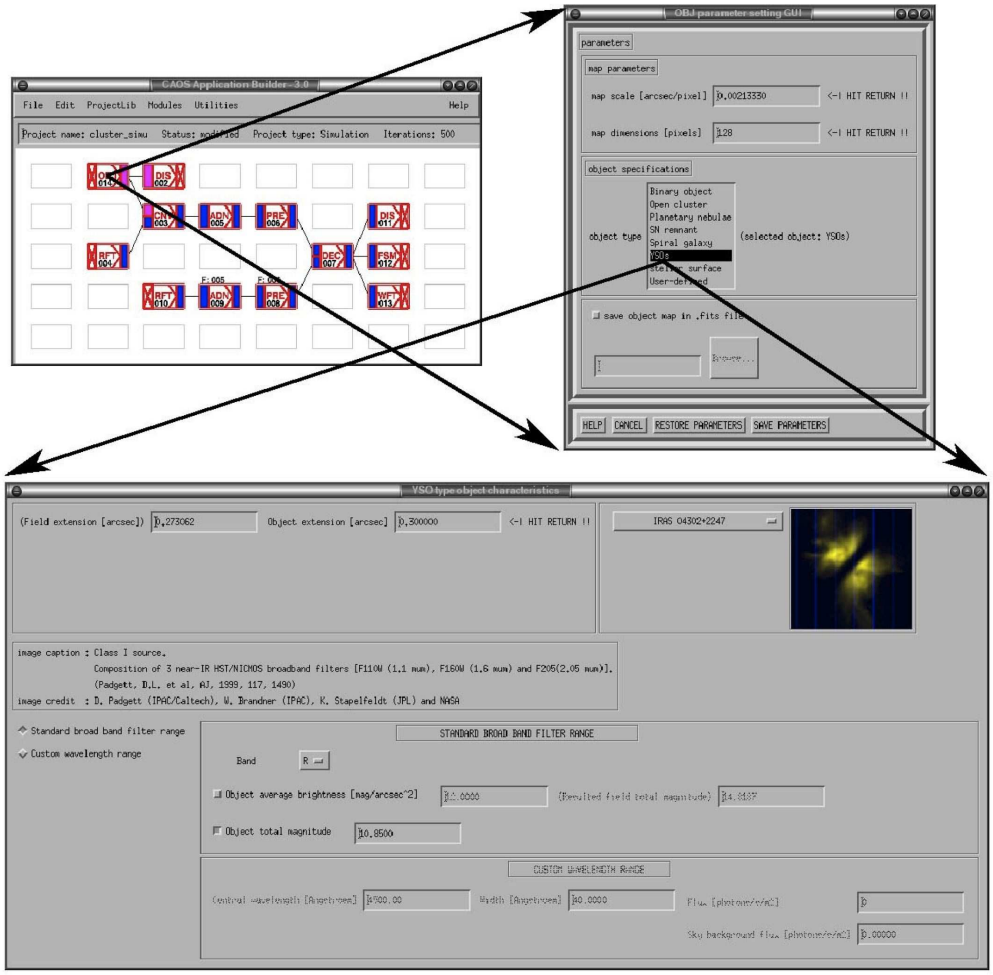

Fig. 2. Example of a module of the Software Package AIRY: the module OBJ (OBJect definition).

Finally the module ADN adds a defined sky background contribution to the outputs of the module CNV and provides a Poisson noise realization of the results. It can also add a computed contribution of the detector Read-Out Noise (RON).

3.2. Data processing modules

This class contains the modules PRE (data PREprocessing) and DEC (DEConvolution process).

The module PRE performs all the operations to be done on the data before applying the deconvolution process. For instance it evaluates the value of the sky background, a fundamental parameter which must be accurately measured in order to fully exploit the positivity constraint assured by the implemented deconvolution method. This operation is performed using the so-called MMM algorithm taken from the astrolib library. The module makes also possible to enter the value of the background if this value has been estimated outside AIRY. Moreover the module PRE computes the peak Signal-to-Noise Ratio (SNR), defined as the ratio between the peak value and the rms of the noise contribution, and allows to re-center the frames of a data cube in order to correct for misalignment of the object from frame to frame. This operation is performed by means of an FFT-shift technique. The module PRE also

includes the possibility of performing a border apodization which can be used in order to minimize "ripples" effects in the restored image. The filter used in this first version is a 2-D square function convolved with a Gaussian one of given $FWHM$, in order to smooth the borders.

The module DEC implements the OS-EM multiple deconvolution method, shortly described in Sect. 2. Its two inputs are the cube of the observations and that of the corresponding PSFs (in general different from those used in the module CNV). Both inputs include not only the observed images and PSFs but also an evaluation of the background contributions to them, obtained by means of the module PRE. As concerns the number of iterations its optimal value depends on the object and noise. Automatic criteria for stopping the iterations are under investigation. In the present version (1.0) of the Software Package AIRY the number of iterations has to be chosen by the user as a global parameter of the simulation project.

3.3. Data analysis modules

This class contains the modules ANB (ANalysis of Binary) and FSM (Find Star Module).

The module ANB performs the detection of a binary object, computes its photometric and astrometric parameters, and possibly compares them with entered binary model parameters. The detection of each component is achieved by an ad hoc routine, which detects in the input frame the peak location over a user-supplied threshold (expressed in rms background noise unit) and masks the pixels inside a disk of user-supplied detection radius, centered on the peak, before continuing. Centroid calculations are carried out with box size of user-supplied dimensions centered on the peak pixel of each detected star, yielding separation and position angle (PA) of the binary. Difference of magnitude is measured by using aperture photometry with a set of apertures of given diameters centered on the measured centroid location. The flux zero-point can be supplied by the user (when dealing with real data for instance) or can be computed.

The module FSM provides the detection of all the stars contained in an image, computing their location and aperture photometry. The module uses the astrolib routine findstar. Input parameters are the detection threshold (in rms background), the flux zero-points and the set of aperture photometry diameters.

3.4. Utility modules

The utility modules are the following: RFT (Read FiTs file format), WFT (Write FiTs file format), RSC (Restore image Structure Cubes), SIM (Save IMage structure) and DSP (data DiSPlay). The first four modules listed above are designed for saving and restoring data of different formats (images, image cubes, XDR format, FITS format) within a given project and possibly at each deconvolution iteration, while the module DSP allows to display the output of any module contained in the package.

4. Examples of application

The purpose of this section is to simulate high-resolution interferometric observations of astronomical objects of interest with LBT, and to evaluate the scientific parameters of these objects as retrieved by the deconvolution method implemented in AIRY. From this point of view the present work is to be considered as the continuation of preliminary studies already presented elsewhere (Correia et al. 2000; Carbillet et al. 2000; Correia et al. 2001).

As a relevant first example of application we treat the fundamental case of binary stars with different angular separations and magnitude differences, looking also at the possibility of achieving super-resolution with OS-EM. The second example of application concerns a diffuse stellar object. Indeed these two classes of objects have a different behaviour as concerns deconvolution because they correspond to two different spatial-frequency bands to be retrieved by the implemented method.

We restrict ourselves to the case of perfectly co-phased and AO-corrected PSFs, as well as to a complete coverage of the u–v plane. Therefore we first describe the set of the PSFs we are using in our simulations, assuming that they correspond to the observation of an object with a suitable declination.

4.1. The interferometric PSFs and other parameters

We consider a set of LBT interferometric PSFs corresponding to the observation of an object with a declination of $+80°$, assuming that observation is limited to airmass <2. More precisely we assume 6 observations equispaced in time in the allowed range of hour angles, that is between -5 h and $+5$ h. This corresponds to a range of parallactic angle of $\sim 200°$, thus providing a complete u–v plane coverage. Indeed, due to the alt-az mount of the telescope, the projection of the baseline onto the observed object in the sky plane rotates and this position angle is what one calls the "parallactic angle", which is a function of time (hour angle) and coordinates of the object on the sky (declination).

We assume an integration time per baseline of about 20 min. During this integration time and for the declination we are considering, the average rotation of the baseline is of about $5°$ in parallactic angle. This effect is taken into account in the computation of the PSFs by integrating over the interval of parallactic angles indicated above. The filter used is the K broad-band filter and we correct for the spectral width of the filter ($\Delta\lambda = 400$ nm) by integrating also over λ.

The spatial sampling adopted for all the interferometric PSFs used in this paper (except when we mention explicitly a different one) is 3 pixels per Full-Width at Half-Maximum ($FWHM$) of the fringes, where the $FWHM$ is equal to λ/L, with L the total baseline length (22.65 m

since the effective diameter of each mirror is 8.25 m due to the adaptive secondary mirror of LBT) and λ the filter central wavelength (here 2.2 μm).

Other parameters used in our simulations are: a total efficiency (mirror+optics+detector) of 25%, a sky background brightness of 12.5 mag/arcsec^2 and a readout noise corresponding to the scientific imaging device of 2 e$^-$ rms.

4.2. Intrinsic limits in the restoration of the parameters of binary stars

We investigate the intrinsic limitations of our method in the reconstruction of binary stars with different values of angular separation ρ and difference in magnitude Δm. The observed images are simulated by means of the modules CNV and ADN.

We consider five binary stars as observed with LBT and presenting increasing values of separation and magnitude difference. The five cases we consider here are the following:

(1) the binary is poorly separated ($\rho = \lambda/L$), but has a reasonable magnitude difference ($\Delta m = 1$);
(2) the binary can be resolved by the maximum baseline ($\rho = 2\lambda/L$), but not by each single pupil with diameter $D = 8.25$ m (for LBT $L/D \simeq 2.75$), and has a reasonable magnitude difference ($\Delta m = 1$);
(3) the binary has the same separation ($\rho = 2\lambda/L$) as in (2), but a larger magnitude difference ($\Delta m = 5$);
(4) the binary is well separated ($\rho = 5\lambda/L$), but has a magnitude difference $\Delta m = 9$;
(5) the binary is even more separated ($\rho = 15\lambda/L$), but has a magnitude difference $\Delta m = 13$.

The first example is likely to be considered as a limiting case for astrometry (if super-resolution is not attempted – see Sect. 4.3), and the last three examples for photometry. We place ourselves in a case of high SNR (with the assumed 20 min integration time per baseline and a main component magnitude $K = 10$).

The results are shown in Fig. 3, where the errors in the retrieval of the three binary parameters (angular separation ρ, position angle PA and magnitude difference Δm) are plotted as functions of the number of iterations of OS-EM. We comment on these results.

As expected it is much more difficult to retrieve the parameters whenever the companion is closer to and/or much fainter than the main component. More precisely, in the first two cases (same magnitude difference but different angular separation), the accuracy is higher when the angular separation is larger even if in both cases results are quite good and the correct values are reached after a rather small number of iterations (very small in the second case, but we recall that we are considering a case with a large SNR value).

As concerns the second and third case (same angular separation but different magnitude difference), the increase in Δm implies that a higher number of iterations is required for distinguishing the weak companion from the remaining sparse energy of the main component. However, after detection, the retrieved binary parameters converge to rather accurate values. The effect increases for increasing magnitude difference. Indeed the detection of the right

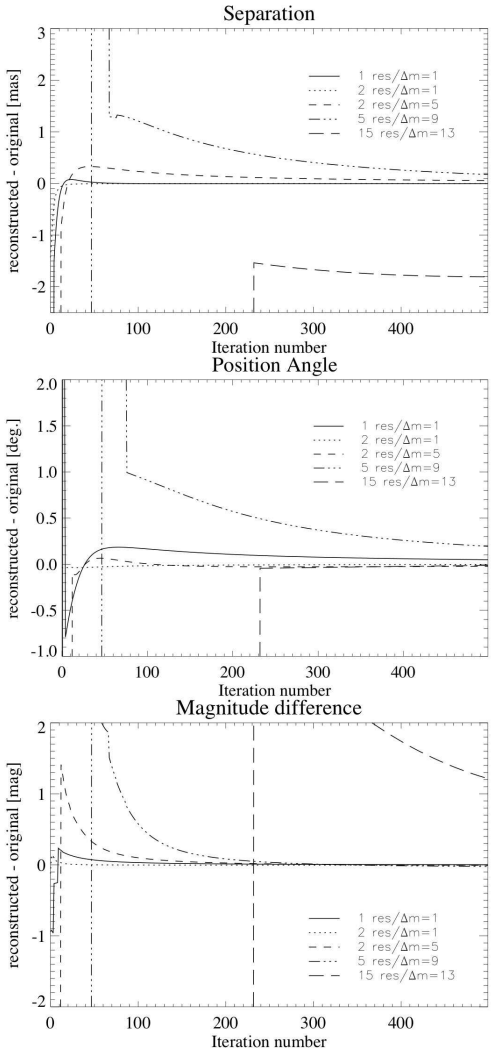

Fig. 3. Restoration of binary parameters in the case of ideal PSFs and complete coverage of the u–v plane: error plots of the angular separation ρ, position angle PA, and magnitude difference Δm, for the five cases defined in the text, versus the number of iterations of the OS-EM method. In the legends "res" stands for λ/L.

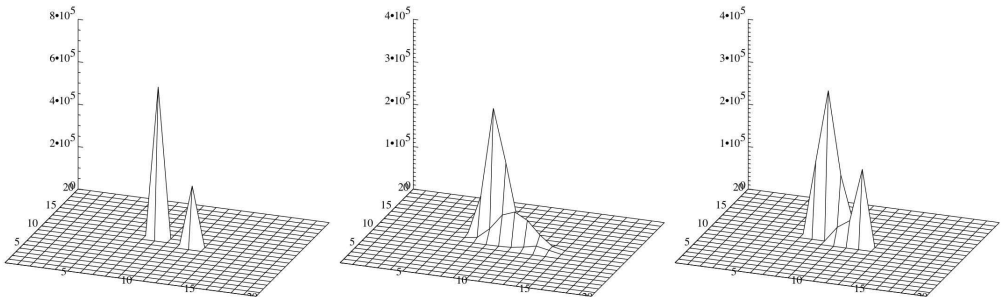

Fig. 4. Illustration of the possibility of super-resolution. From left to right: the original object; the non-resolved restored image obtained with 1000 iterations of OS-EM; the resolved restored image obtained with the use of the mask defining the object domain as deduced from the first restoration.

companion takes place after ∼50 iterations for the ($\rho = 5\lambda/L$, $\Delta m = 9$) binary and after ∼200 iterations for the ($\rho = 15\lambda/L$, $\Delta m = 13$) binary; then the parameters converge to the right values, with the exception of the angular separation of the ($\rho = 15\lambda/L$, $\Delta m = 13$) case.

In conclusion, for all binaries considered here except one (the last case), the parameters converge to the correct values, although with different convergence rates.

4.3. Super-resolution

In astronomy as well as in microscopy, super-resolution is a word used for denoting a method, in general a processing of the data, which allows to reach a resolution beyond the diffraction limit. Super-resolution requires an extrapolation of the object spectrum outside the band of the instrument and is possible in a limited number of situations. In problems of image deconvolution it can be obtained by the use of specific constraints, satisfied by the object to be restored, which must be implemented in the restoration method (for a tutorial see Bertero & De Mol 1996). In the case of astronomical objects these constraints are essentially positivity and the extent of the object, which must not be much greater than the angular resolution of the telescope. The LR method, and hence the OS-EM method, can be nicely used for such a task. Indeed positivity is automatically assured. As concerns the information about the angular extent of the object it can be easily inserted in the method by an appropriate initialization. Indeed if the result of one iteration is zero in a certain pixel, then it will be zero at that pixel for all subsequent iterations.

A possible application to the case of unresolved binary stars is the following. By means of OS-EM, initialized with a constant image, one first estimates the domain of the unresolved object, by taking for instance all pixels where the values of the restored object are greater than a certain threshold. Next the deconvolution based on OS-EM is repeated by initializing the method with a mask which is one over the estimated domain and zero elsewhere.

Table 2. Measured binary parameters of the restored super-resolved image compared with the true parameters. Measurements are performed by means of the module ANB.

	ρ(mas)	$\theta(^\circ)$	Δm
model	10.5	18.4	1.0
restoration	9.2	16.9	0.3

We present here the results of a simulation carried out in order to demonstrate the possibility of super-resolution. To this purpose we consider a binary star whose angular separation is about one half the resolution limit of LBT in K-band ($\rho = \lambda/2L$) while the magnitude difference is the same as in the first two cases of the previous section ($\Delta m = 1$). Since we are looking for super-resolution we assume that the sampling of the PSFs defined in Sect. 4.1 is increased by a factor two, so that a frequency which is twice the cut-off frequency of the telescope can be sampled. It is outside the scope of this paper to discuss how such an oversampling can be reached in practice. With a $K = 20$ primary and $\Delta m = 1$ the SNR of one baseline observation is ∼60.

To this example we apply the procedure outlined above by taking a threshold value of 10% of the peak value of the primary. The results are shown in Fig. 4. We can easily see that, as expected, the binary is not resolved by the first restoration while it is resolved by the second one when the object domain is provided as an input to the algorithm. The binary parameters of the super-resolved restoration are in a satisfactory agreement with the true ones (see Table 2), although they are obviously not so precise as in the case of a standard resolved binary.

In Fig. 5 we plot the power spectrum of the object together with those of the two restored images. The extrapolation of the power spectrum provided by the super-resolving method is clearly shown in this plot where the telescope cut-off frequency is located at $128/6 \sim 20$ pixels.

These results are preliminary and are given to demonstrate the feasibility of super-resolution. It is obvious that much more refined simulations are required and much

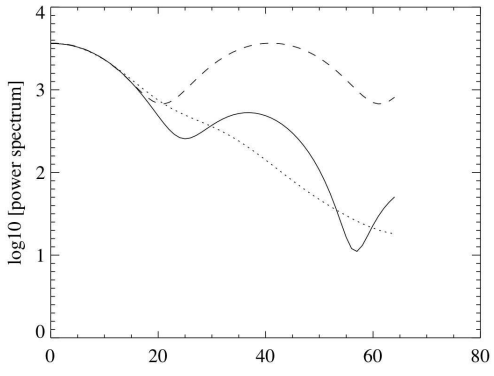

Fig. 5. Cuts of the power spectra along the binary axis. The dashed line corresponds to the original object, the dotted line to the result of the first restoration while the solid line to the result of the second restoration. The super-resolution effect is evident (the telescope cut-off is located at $128/6 \simeq 20$ pixels), but it is also evident that the magnitude difference is not correctly retrieved.

wider experimentation is needed in order to explore the limits of the method.

4.4. Restoration of a diffuse object

We test here our method in the case of an object with an extended and diffuse shape. To this purpose we consider an embedded young stellar object, also known as Class I object, derived from HST near-infrared observations of IRAS 04302 +2247. This is a remarkable object showing a bipolar scattered light nebulae and a totally opaque dust lane, probably featuring a large optically thick circumstellar disk seen edge-on (Padgett et al. 1999). We scale the image to have a $0\farcs85 \times 0\farcs85$ extension, so that our object is more distant by a factor $\sim$10 than the original one, i.e. about 1.4 kpc. With such a distance and the $K = 15$ mag that we set here, instead of the true $K = 10.9$ (Lucas & Roche 1997), our simulated object is intrinsically brighter by roughly 1 mag. With this brightness and the integration time considered in all our simulations (20 min), the single baseline image peak SNR is $\sim$180. Figure 6 shows the image of the object, as well as one of the observed images and the result of the restoration.

The accuracy of the restoration provided by the kth iteration can be measured by computing the relative rms error defined as follows:

$$R^{(k)} = \frac{\|\boldsymbol{f}^{(k)} - \boldsymbol{f}\|}{\|\boldsymbol{f}\|}, \tag{3}$$

where $\boldsymbol{f}^{(k)}$ is the result of the kth iteration (see Eq. (2)) and $\boldsymbol{f}$ is the original model (see Eq. (1)). The norm is the Euclidean one, i.e. the square root of the sum of the squares of the pixel values. In Fig. 7 we plot the restoration error $R^{(k)}$ as a function of the number of iterations k. The curve has a minimum at $k = 263$, with a minimum value of 5.6% (the restored image of Fig. 6 corresponds to this minimum). We observe however that in this example the minimum is rather flat so that after 70 iterations we already have a restoration error of about 7%. Such a restoration is not visually distinguishable from that given in Fig. 6.

The behaviour of the restoration error shown in Fig. 7 is typical of the regularizing iterative methods and is known as *semiconvergence* – see, for instance, Bertero & Boccacci (1998). The first iterations improve the accuracy of the approximation of the unknown object but after a certain number of iterations the amplification of the noise increases and the quality of the restoration is degraded. In some cases the effect is much stronger than in our example; in these cases the choice of the number of iterations may be critical.

Another way for checking the quality of the restored image may consist in comparing its power spectrum with that of the object. This is shown in Fig. 8, where the profiles of the azimuthaly averaged power spectra of both images are plotted. The two curves match fairly well up to the telescope cut-off frequency located at about 40 pixels.

5. Summary and concluding remarks

In this paper we have presented the first release of the image restoration and simulation package AIRY (Astronomical Image Restoration in interferometrY). After a description of the restoration method OS-EM implemented in the package, we discuss the modular structure of AIRY and the tasks of the modules available in the present version 1.0. Next we investigate the intrinsic capabilities of the implemented restoration method in the particular case of LBT. To this purpose we consider the ideal situation of perfectly co-phased and AO-corrected PSFs and we apply the method both to the restoration of binary objects and to the restoration of diffuse objects. In the first case resolution and detection are analysed both for angularly close objects and for high brightness ratios.

Our simulations indicate that the fundamental limit of the OS-EM method, at least as concerns the restoration of binary stars, is essentially a limit in the estimation of the brightness ratio which can be larger in the case of wider angular separation. Indeed the difference of magnitude can be as high as $\Delta m = 5$ for a separation of only two resolution limits and $\Delta m = 13$ for 15 resolution limits. The upper limit in brightness ratio for more separated objects is essentially given by the detection limit of the companion star alone. This is similar to the limitation imposed by the uncorrelated speckle noise, present in the halo of the PSFs in classical AO, for the detection of faint companions (see e.g. Racine et al. 1999). We have also found that the higher is the brightness ratio between the companion and the primary, the larger is the number of iterations required to actually detect it. But, even if the convergence of the parameters is slower, the bias in their estimation tends to decrease systematically with the number of iterations.

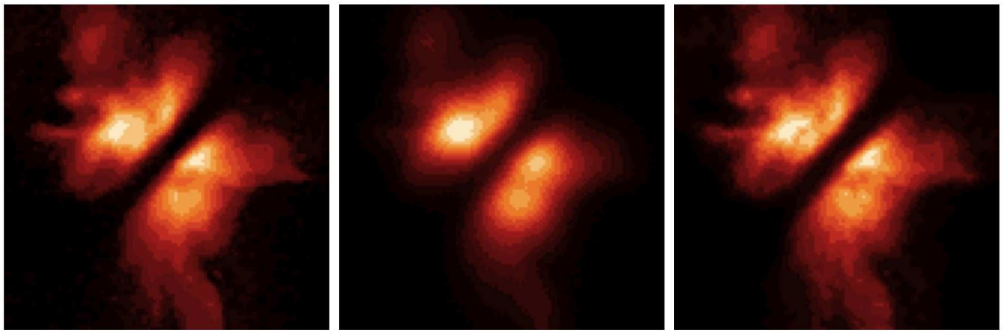

Fig. 6. From left to right: the original object; the image corresponding to a parallactic angle of ∼60°; the restored image. The image extension is about 0.″7. The grey scale is square root.

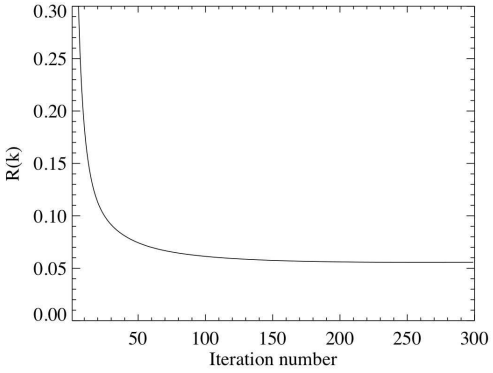

Fig. 7. Restoration error $R^{(k)}$ as a function of the number of iterations. The convergence occurs at iteration number 263, with $R^{(263)} = 5.6\%$.

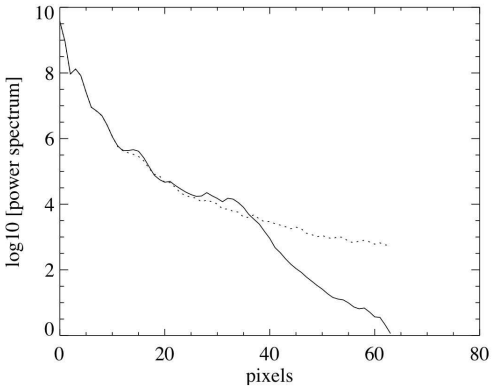

Fig. 8. Profiles of the azimuthaly averaged power spectra. Solid line corresponds to the restored image ($k = 263$), dotted-line to the object. The telescope cut-off frequency is located at $128/3 \simeq 40$ pixels.

Such a conclusion obviously holds true only in the case of high SNR, assuming that it is possible to calibrate exactly the PSFs of the system (in time and space). In real life it would hardly be the case, except for very good seeing conditions and/or with the help of techniques such as multi-conjugate AO which should be able to approach this limit.

We have also demonstrated the possibility of obtaining super-resolution for this kind of objects, at least in the case of a reasonable magnitude difference. Such a result, which might open very promising future developments, can be obtained without modifying the deconvolution algorithm implemented in AIRY; it is only necessary to use a suitable initialization of the iteration process. Of course such a remarkable property holds true not only in the case of OS-EM but also in the case of LR and, more generally, of any multiplicative iterative method.

In the case of a realistic diffuse object we have shown that it is possible to obtain quite accurate restorations up to the cut-off frequency of the telescope, if the amplification of the noise is not limiting.

All the results presented in this paper have been obtained by assuming ideal PSFs and complete coverage of the spatial frequency plane. The study of the effects of partial angular coverage and partial AO correction is the subject of the subsequent paper (Carbillet et al. 2002). However we believe that we have already demonstrated that OS-EM can be conveniently used at least for a quick look of the observations with LBT.

Obviously if some specific object, with a structure more complex than that of the examples considered in this paper, requires a more refined analysis, that can be done outside AIRY with methods more sophisticated than OS-EM or also using future modules of AIRY implementing those methods.

Indeed new modules can be easily implemented by any user, depending on his/her specific need, and can be included and distributed in future versions of AIRY. From our part, we are currently studying the possibility of implementing improved versions of existing deconvolution methods, including criteria for stopping the iterations or for choosing regularization parameters, as well as blind deconvolution methods.

The Software Package AIRY, version 1.0, is obtainable under request and subscription to its dedicated mailing-list by visiting the web site `http://dirac.disi.it/airy`. It is delivered together with the CAOS Application Builder (version 3.0): the IDL-based graphical environment within which it was developed.

Acknowledgements. We would like to acknowledge Piero Ranfagni for his help in astrometry, as well as Piero Salinari for useful discussions. Thanks are also due to Alfio Puglisi and Armando Riccardi for their help in modifying the original manuscript, and finally to the referee Isabelle Percheron for her constructive remarks. This work was partially funded by CNAA (Consorzio Nazionale per l'Astronomia e l'Astrofisica) under the contract No. 16/97.

References

Bertero, M., & De Mol, C. 1996, in Progress in Optics, vol. XXXVI, ed. E. Wolf, 129

Bertero, M., & Boccacci, P. 1998, Introduction to Inverse Problems in Imaging (IOP Publishing, Bristol)

Bertero, M., & Boccacci, P. 2000a, A&AS, 144, 181

Bertero, M., & Boccacci, P. 2000b, A&AS, 147, 323

Carbillet, M., Correia, S., Femenía, B., & Riccardi, A. 2000, in SPIE Conf. Ser. 4007, Adaptive Optical Systems Technology, ed. P. L. Wizinowich, 155

Carbillet, M., Fini, L., Femenía, B., et al. 2001, in ASP Conf. Ser. ADASS X, ed. F. A. Primini, & F. R. Harnden, 249

Carbillet, M., Correia, S., Boccacci, P., & Bertero, M. 2002, A&A, 387, 744

Correia, S., & Richichi, A. 2000, A&AS, 141, 301

Correia, S., Carbillet, M., Richichi, A., Bertero, M., & Boccacci, P. 2000, in SPIE Conf. Ser. 4006, Interferometry in Optical Astronomy, ed. P. J. Léna, & A. Quirrenbach, 650

Correia, S., Carbillet, M., Fini, L., et al. 2001, in ASP Conf. Ser. ADASS X, ed. F. A. Primini, & F. R. Harnden, 404

Fini, L., Carbillet, M., & Riccardi, A. 2001, in ASP Conf. Ser. ADASS X, ed. F. A. Primini, & F. R. Harnden, 253

Hege, E. K., Christou, J. C., Jefferies, S. M., & Cheselka, M. 1999, J. Opt. Soc. Am. A, 16(7), 1745

Lucas, P. W., & Roche, P. F. 1997, MNRAS, 286, 895

Padgett, D. L., Brandner, W., Stapelfeldt, K. R., et al. 1999, AJ, 117, 1490

Piana, M., & Bertero, M. 1996, J. Opt. Soc. Am. A, 13, 1516

Racine, R., Walker, G. A. H., Nadeau, D., Doyon, R., & Marois, C. 1999, PASP, 111, 587

Shepp, L. A., & Vardi, Y. 1982, IEEE Trans. Med. Imaging MI-1, 113

1.2.4 Autres développements CAOS-tiques

Outre tout ce qui concerne les deux outils principaux, le Software Package CAOS et le Software Package AIRY, et les développements de l'interface globale elle-même, que nous ne détaillerons pas ici, le PSE CAOS a profité d'un certain nombre d'autres développements, notamment sous la forme de nouveaux outils dédiés à des problématiques ciblées.

Ces nouveaux *software packages* ont déjà été listés au tout début de cette section. Nous allons maintenant présenter l'intérêt de chacun plus en détail.

Le Software Package PAOLAC Le Software Package PAOLAC est pratiquement une intégration de l'outil de simulation semi-analytique PAOLA [97, 135] au sein du PSE CAOS. Pour ce faire sans la moindre altération pour PAOLA, et permettre ainsi son développement indépendamment du PSE CAOS, ceci a été réalisé sous la forme d'un simple « habillage » de PAOLA dans le PSE CAOS : les fonctions/routines originales de PAOLA sont appelées depuis des modules ad hoc sous le PSE CAOS.

Ce simple habillage trouve tout son intérêt par le double fait qu'il force d'une part une totale compatibilité entre les deux codes et leurs hypothèses (parfois cachées), et qu'il permet d'autre part de mettre en place des simulations mélant des modules des deux outils, en augmentant ainsi également la compatibilité formelle des résultats délivrés par ces codes.

En effet, le but scientifique est ici avant tout de permettre la comparaison la plus directe possible entre simulations analytiques, extrêmement rapides mais issues d'une modélisation basée sur des hypothèses très fortes, et simulations Monte-Carlo détaillées (ou end-to-end), basées au contraire sur une modélisation complète des phénomènes physiques mis en jeu mais par conséquent particulièrement lentes et gourmandes en mémoire vive pour des sujets tels que les ELTs, les très grands champs ou la très haute dynamique, comme nous le verrons plus en détails à la Sous-sec. 2.5.2.

Le Software Package MAOS Le développement du Software Package MAOS a été malheureusement quelque peu mis de côté ces dernières années. Bien qu'actuellement pratiquement en *stand-by*, il présenterait l'avantage certain, s'il était exhumé et effectivement distribué dans une forme utilisable pour la communauté, de permettre une application formelle plus aisée des outils du Software Package CAOS au cas de l'OA multi-références, de l'OA couche-limite (ou *ground-layer* en anglais) ou différentes formes d'OA multi-conjuguée (MC). Un certain nombre de modules le composent [4], permettant la définition simultanée de plusieurs étoiles guides, ainsi que l'analyse simultanée des fronts d'onde correspondants, selon un schéma de type *layer-oriented* ou bien *star-oriented*.

4. Mais à l'état de versions β.

Le Software Package SPHERE Le Software Package SPHERE fut développé dans le cadre du projet homonyme SPHERE (*Spectro-Polarimetric High-contrast Exoplanet REsearch*) d'instrument de seconde génération du VLT dédié principalement à la détection directe et la caractérisation d'exoplanètes. Le Software Package SPHERE est quant à lui dédié à la simulation complète et détaillée de l'instrument dans son ensemble. Il inclut donc une modélisation instrumentale détaillée du système d'OA extrême SAXO, de la caméra/spectromètre proche-infrarouge et éventuellement double-bande IRDIS, du spectromètre à intégrale de champ proche-infrarouge IFS et du polarimètre imageur visible ZIMPOL.

Cet outil a été développé afin d'affronter différentes tâches liées au projet, en commençant par une analyse extrêmement détaillée du système complet incluant le test de points jugés critiques dans le concept opto-mécanique de l'instrument, ainsi qu'une évaluation des performances de l'instrument pour quelques cibles astrophysiques réalistes pour différents modes d'observation. La simulation de données typiques pour les tests d'algorithmes de détection d'exoplanètes a également fait partie des tâches affrontées. Certaines des études détaillées menées à bien grâce à cet outil sont présentées à la Sec. 3.5.

Au final, l'outil en soi est composé d'une partie « diffractive », mise sous forme de modules utilisables avec le CAOS Application Builder (voir la modélisation du sous-instrument IRDIS en mode DBI montrée Fig. 1.2), et d'un ensemble de routines constituant la partie « photométrique » du *software package*. Les modules du Software Package SPHERE sont au nombre de sept. Cinq de ceux-ci modélisent les différents sous-systèmes physiques. Le module AOC globalise l'atmosphère turbulente *et* le système d'OA extrême SAXO, délivrant les fronts d'onde corrigés par l'OA et se propageant au sein du reste de l'instrument. Le module COP ajoute à ces fronts d'onde les aberrations dues au chemin optique commun à l'ensemble des trois sous-instruments qui suivent : IRDIS (modélisée par IRD), IFS (modélisé par IFS) et ZIMPOL (modélisé par ZIM). Enfin, les deux modules restant s'occupent des mondanités d'usage : affichage (DDT – *Display DaTa*) et sauvegarde des données (WID – *Write Image Data*).

La partie photométrique du *software package* prend en charge à l'issue de l'un des trois sous-instruments la modélisation des effets dus au détecteur, à l'éventuelle rotation de champ, et, bien entendu, aux caractéristiques astrophysiques de l'objet observé.

Le Software Package AIRY-LN Le Software Package AIRY-LN est quant à lui développé dans le cadre du projet LINC-NIRVANA (LN), le recombineur Fizeau germano-italien du LBT. Du point de vue de l'imagerie, cet instrument délivrera des images multiples du même objet astrophysique, c'est-à-dire des images avec différentes orientations de la base de 22.8 m du LBT composé de deux ouvertures de 8.4 m (8.22 m en diamètre effectif). Le Software Package

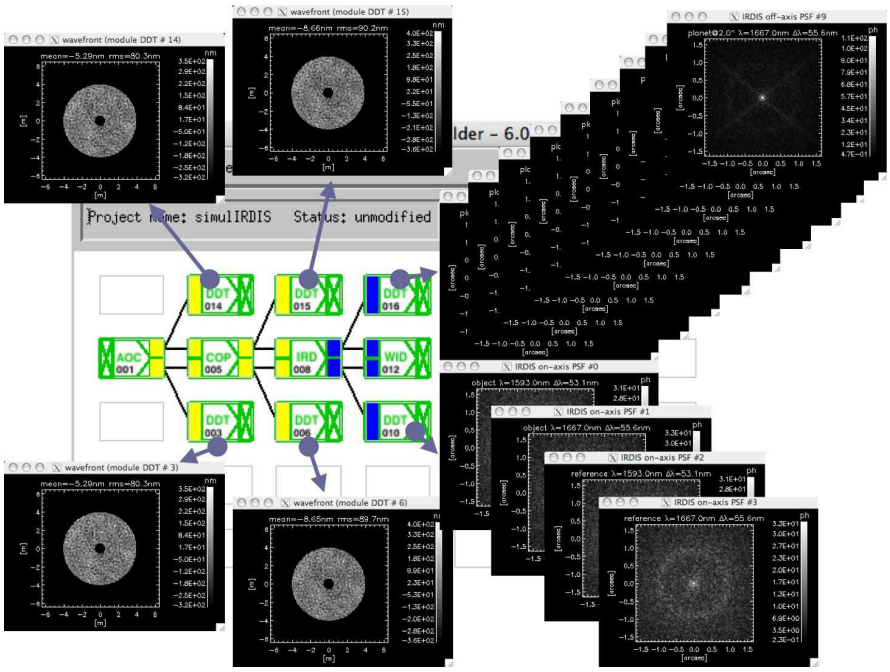

FIGURE 1.2: Projet de simulation du sous-instrument IRDIS en mode DBI (pour *Double-Band Imaging*) au sein du `CAOS Application Builder` et en utilisant les modules ad hoc regroupés dans le `Software Package SPHERE`. Les résultats des affichages effectués par les diverses occurences du module `DDT` correspondent à, de gauche à droite : les fronts d'onde post-SAXO de l'objet (en bas) et de l'étoile de référence (en haut), les mêmes fronts d'onde mais après les aberrations ajoutées par `COP`, les réponses impulsionnelles post-coronographe en axe correspondant à l'objet et à la référence et dans deux longueurs d'onde (en bas), les réponses impulsionnelles post-coronographe hors-axe selon plusieurs angles (allant de $0''.1$ – très près de l'axe – à $2''$– pratiquement hors de portée des effets du coronographe) et dans les deux mêmes longueurs d'onde.

`AIRY-LN` est très largement inspiré du `Software Package AIRY`, mais, contrairement à ce dernier qui est resté très général malgré ses nombreuses applications pratiques aux données simulées de LN, `AIRY-LN` est complètement dédié à LN et au format particulier de ses données.

En phase de test, les modules des deux *software packages* ont cependant été utilisés ensemble. En effet, le `Software Package AIRY-LN`, étant dédié au traitement de données réelles, il est dépourvu de modules de simulation de ces données, modules qui font par contre partie intégrante du `Software Package AIRY`.

1.3 Plan de la suite de la thèse

Après avoir présenté en détail les deux outils principaux constituant le `CAOS PSE` et, rapidement, les différents développements qui ont eu lieu à partir de ceux-ci, la suite de cette thèse va se concentrer sur les résultats scientifiques principaux qui ont pu être obtenus grâce à l'utilisation intensive de ces outils.

Le chapitre suivant est ainsi dédié à la modélisation numérique d'OA. Dans un premier temps, j'exposerai le contexte global, sous forme d'un rapide rappel des concepts qui nous permettront d'aborder les applications spécifiques exposées dans la suite du chapitre. Ensuite, je détaillerai tout d'abord la simulation de l'atmosphère turbulente au travers du prisme de l'amélioration des méthodes classiques de simulation basées sur la transformée de Fourier rapide d'une part et les polynômes de Zernike d'autre part. Les perspectives et les problèmes ouverts liés à cette problématique de la modélisation numérique de l'atmosphère turbulente sont ensuite exposés. Puis, je présenterai un rapide historique concernant deux des principaux ASO employés classiquement en OA astronomique, ainsi qu'une évaluation de l'amélioration possible due à l'emploi de détecteur de type EMCCD (pour *Electron-Multiplying Charge-Coupled Device*) pour un ASO de type pyramidal et un télescope de la classe 8 mètres. Le cas du correcteur est ensuite détaillé au travers des études menées pour le miroir adaptatif M4 du projet de télescope extrêmement grand européen E-ELT. La section suivante est consacrée à la présentation d'une étude de performance globale effectuée pour le système d'OA de première lumière du LBT, suivie d'une discussion sur la dualité modélisation analytique/modélisation end-to-end assortie de quelques résultats obtenus dans ce cadre, puis d'une section consacrée à l'étude d'un système d'OA possible pour le très intéressant site du Dôme C en Antarctique.

Le troisième chapitre est quant à lui dédié à l'imagerie post-OA. Après une rapide présentation du contexte, j'aborderai le thème de l'imagerie interférométrique de Fizeau par le biais d'une étude de cas correspondant au LBT (et plus précisément de LN). Les études successives menées par la suite autour du même instrument seront également résumées. Je proposerai ensuite une possibilité de super-résolution dans le cas plus général de l'imagerie astronomique, possibilité prouvée sur des données réelles obtenues avec le système d'OA NAOS du VLT. Puis, je présenterai une proposition de déconvolution aveugle sous contrainte de Strehl, particulièrement adaptée aux données partiellement corrigée. Enfin, je m'intéresserai au sujet de l'imagerie à très haute dynamique, en exposant les études menées pour la définition du coronographe de Lyot apodisé prévu pour l'instrument de seconde génération SPHERE du VLT, ainsi que pour les tests d'algorithmes de détection d'exoplanètes et la préparation des observations d'autres types d'objets avec cet instrument.

La thèse se terminera par un chapitre de conclusions et perspectives. Et/mais une introduction à la problématique de la formation d'images astronomiques en dépit de l'atmosphère turbulente se trouve en annexe, ainsi

qu'une reproduction de mon curriculum vitæ actuel d'une part et de la liste de mes publications d'autre part.

Chapitre 2

Modélisation numérique d'optique adaptative

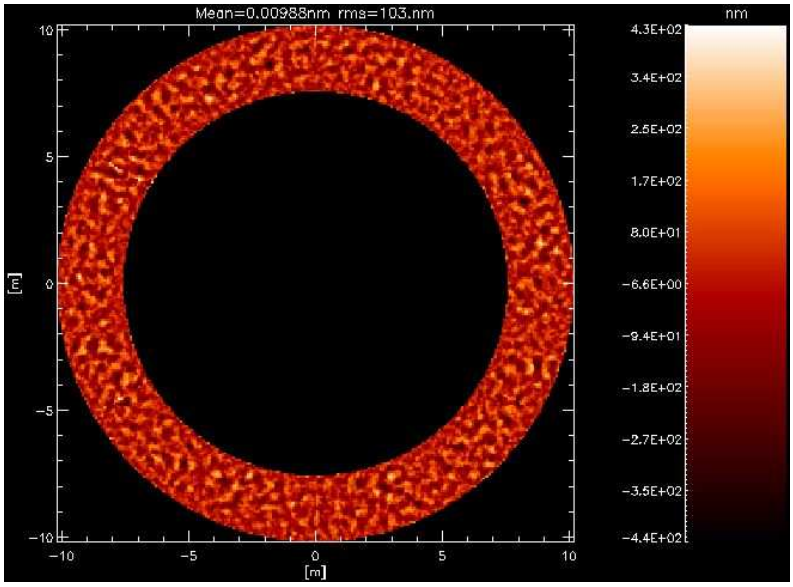

Le simulacre n'est jamais ce qui cache la vérité – c'est la vérité qui cache qu'il n'y en a pas. Le simulacre est vrai.
Jean Baudrillard, in *Simulacres et simulation*, Galilée, Paris, 1981, p. 9.

2.1 Contexte et sommaire

2.1.1 Budget d'erreur post-OA et PSF résultante

On a déjà abordé à la Sec. 1.2 la modélisation détaillée de la turbulence atmosphérique et des systèmes d'OA conçus pour en corriger les effets délétères sur la phase de l'onde incidente. D'un point de vue plus analytique et global, l'erreur résiduelle (ici exprimée en termes de variance notée σ^2) qui en résulte sur le front d'onde corrigé peut être modélisée de la façon suivante :

$$\sigma^2_{\text{post-OA}} = \sigma^2_{\text{atm.}} + \sigma^2_{\text{sys.OA}} + \sigma^2_{\text{autres}} \ , \tag{2.1}$$

et où trois ingrédients de base sont présents : l'erreur atmosphérique non-considérée par le système d'OA ($\sigma^2_{\text{atm.}}$), l'erreur résiduelle du système d'OA lui-même ($\sigma^2_{\text{sys.OA}}$), et l'ensemble des autres erreurs qui ne sont dues ni à l'atmosphère ni au système d'OA (σ^2_{autres}).

Ce dernier terme d'erreur est principalement lié aux aberrations au sein du chemin optique non-vu par le système OA, ainsi qu'à d'éventuelles erreurs d'étalonnage.

Le premier terme ($\sigma^2_{\text{atm.}}$) est quant à lui principalement dû (si l'on néglige bien entendu scintillation, effets de diffraction et effets chromatiques) à l'anisoplanétisme, principal ennemi lorsqu'il s'agit de vouloir obtenir des images grand-champs à HRA ou des données d'objets faibles relativement éloignés d'une étoile guide assez brillante pour le système d'OA.

En ce qui concerne l'erreur du système d'OA lui-même, un certain nombre de sources sont classiquement identifiées, selon l'expression suivante :

$$\sigma^2_{\text{sys.OA}} = \sigma^2_{\text{fit.}} + \sigma^2_{\text{alias.}} + \sigma^2_{\text{mes.}} + \sigma^2_{\text{temp.}} + \sigma^2_{\text{spec.}} \ . \tag{2.2}$$

Le dernier terme relève d'un système d'OA induisant éventuellement des erreurs spécifiques, tel qu'un système à base d'étoile laser ou d'OAMC. Nous allons plutôt ici nous concentrer sur un système générique, et donc sur les quatre autres types d'erreur.

Erreur de sous-échantillonnage spatial Le premier terme de l'Éq. 2.2 concerne la correction elle-même : $\sigma^2_{\text{fit.}}$. Ceci traduit le fait qu'une gamme limitée de fréquences spatiales, et donc un nombre limité de modes de la turbulence atmosphérique, peuvent être physiquement corrigés par le miroir. La raison en est évidente : c'est simplement dû au nombre limité d'actionneurs constituant le miroir déformable considéré. L'erreur est par conséquent exprimée en fonction du rapport entre la distance inter-actionneurs $d_{\text{act.}}$ et le paramètre de Fried r_0 (défini dans la bande d'observation considérée) :

$$\sigma^2_{\text{fit.}} \propto \left(\frac{d_{\text{act.}}}{r_0} \right)^{\frac{5}{3}} \ . \tag{2.3}$$

Le facteur devant $(d_{\text{act.}}/r_0)^{\frac{5}{3}}$ dépend des détails mécaniques du miroir et est raisonnablement compris entre 0.25 et 0.7. Typiquement et pour des miroirs non-segmentés, il est proche de 0.3.

Notons tout-de-suite qu'il s'agit là de l'erreur ultime d'un système d'OA donné (au sens au moins du dimensionnement de celui-ci). Ainsi, même dans des conditions idéales de mesure des perturbations de la phase de la part de l'ASO ($\sigma^2_{\text{mes.}}$ et $\sigma^2_{\text{alias.}}$ pratiquement nulles) et de rapidité extrême de la boucle dans son ensemble ($\sigma^2_{\text{temp.}} \simeq 0$), un système d'OA sera de toute façon limité par cette erreur de sous-échantillonnage spatial.

D'un point de vue pratique, notons également qu'un système pour lequel $d_{\text{act.}} = r_0$ ne donnera pas de rapport de Strehl [1] meilleur que, dans la bande où r_0 est ici défini et en considérant l'approximation de Maréchal :

$$S_+ \simeq \exp\left\{-\sigma^2_{\text{fit.}}\right\} \simeq 0.74 \ . \tag{2.4}$$

À raison de $2\,r_0$ par $d_{\text{act.}}$, typique d'un système d'OA extrême, nous arrivons par contre, toujours avec un coefficient de 0.3, à $S_+ \simeq 0.91$.

Notons finalement qu'il peut aussi se révéler utile de considérer la distribution spatiale de cette erreur (en particulier d'ailleurs pour des miroirs segmentés). La Sec. 2.4 montre plus loin une étude détaillée de cette erreur pour le miroir adaptatif M4 de l'*European-Extremely Large Telescope* (E-ELT).

Erreur de repliement de spectre Le second terme d'erreur de l'Éq. 2.2 concerne l'erreur de repliement de spectre due à l'ASO. De la même manière que le miroir déformable est limité par son nombre fini d'actionneurs, l'ASO est limité par son nombre fini d'éléments d'analyse (qui peut être aussi bien le nombre de micro-lentilles dans le cas d'un Shack-Hartmann que le nombre de pixels analysant chacune des quatre images de pupilles à l'issue d'une pyramide). Cette erreur de repliement de spectre (ou *aliasing* en anglais) apparait à cause des hautes fréquences spatiales forcément mal échantillonnées et par conséquent possiblement interprétées comme des fréquences beaucoup plus basses. En posant une taille physique des éléments d'analyse d_{ASO}, on a ici [42] :

$$\sigma^2_{\text{alias.}} \propto \left(\frac{d_{\text{ASO}}}{r_0}\right)^{\frac{5}{3}} \ . \tag{2.5}$$

Notons enfin que très souvent $d_{\text{ASO}} \simeq d_{\text{act.}}$, mais aussi que les configurations géométriques de l'un et de l'autre composant peuvent être complètement différentes (e.g. circulaire pour le miroir déformable et carrée pour l'ASO). Cette erreur sera discutée plus en détails à la Sec. 2.3.

Erreur de mesure Le troisième terme de l'Éq. 2.2 est aussi liée à l'ASO, et plus précisément à la mesure effectuée par celui-ci. C'est un problème classique de détection de la lumière par une caméra CCD, où $\sigma^2_{\text{mes.}}$ peut être écrit :

$$\sigma^2_{\text{mes.}} = \sigma^2_{\text{phot.}} + \sigma^2_{\text{lect.}} + \sigma^2_{\text{obsc.}} + \dots \ , \tag{2.6}$$

où le classique $\sigma^2_{\text{phot.}}$, dû au bruit de photon, est inversement proportionnel au nombre de photons disponibles $N_{\text{phot.}}$:

$$\sigma^2_{\text{phot.}} \propto \left(\frac{1}{N_{\text{phot.}}} \right) \ , \tag{2.7}$$

et où l'erreur de lecture $\sigma^2_{\text{lect.}}$ est quant à elle telle que :

$$\sigma^2_{\text{lect}} \propto \left(\frac{\sigma_e^2}{N^2_{\text{phot.}}} \right) \ . \tag{2.8}$$

avec σ_e exprimée en électrons/pixel/lecture et dépendant des détails électroniques du CCD utilisé (et fortement de la cadence des lectures). D'autres termes d'erreur tels que celui lié au courant d'obscurité ($\sigma^2_{\text{obsc.}}$) peuvent être considérés également. Rappelons-nous enfin que des détecteurs pratiquement libérés du bruit de lecture existent également, les EMCCD. Mais ces derniers présentent en contre-partie un bruit « exotique » caractérisé par une distribution Gamma (de la même façon que l'on a à faire à une distribution de Poisson pour le bruit de photons et à une distribution de Gauss pour le bruit de lecture). L'article présenté à la Sec. 2.3 donne plus de détails sur ce dernier point, et surtout opère une comparaison directe entre un détecteur de type EMCCD et un CCD classique.

Erreur temporelle Le dernier terme invoqué dans l'Éq. 2.2 est celui relatif à l'erreur temporelle globale du système OA, dû au simple fait qu'entre l'instant auquel un front d'onde donné est réfléchi sur le miroir déformable et celui auquel il peut être effectivement corrigé (après mesure par l'ASO, calcul des commandes par le reconstructeur, contrôle de ces mêmes commandes et application par le miroir), un laps de temps (typiquement de l'ordre de quelques petites millisecondes) s'est nécessairement écoulé. Cette erreur est bien entendu dépendante du temps de cohérence de la turbulence atmosphérique τ_0 et du temps total mis par la boucle OA (Δt_{OA}), incluant le temps d'intégration de l'ASO et le délai avant application effective des commandes. Elle est modélisée telle que :

$$\sigma^2_{\text{temp.}} \propto \left(\frac{\Delta t_{\text{OA}}}{\tau_0} \right)^{\frac{5}{3}} . \tag{2.9}$$

Équilibrer le budget Il est clair à la lecture de ce rapide bilan d'erreurs et de leurs dépendances, qu'augmenter l'efficacité d'un système d'OA va, au premier abord, être une question d'essayer de minimiser par le biais technologique les différents termes d'erreur. Il est également clair qu'un certain

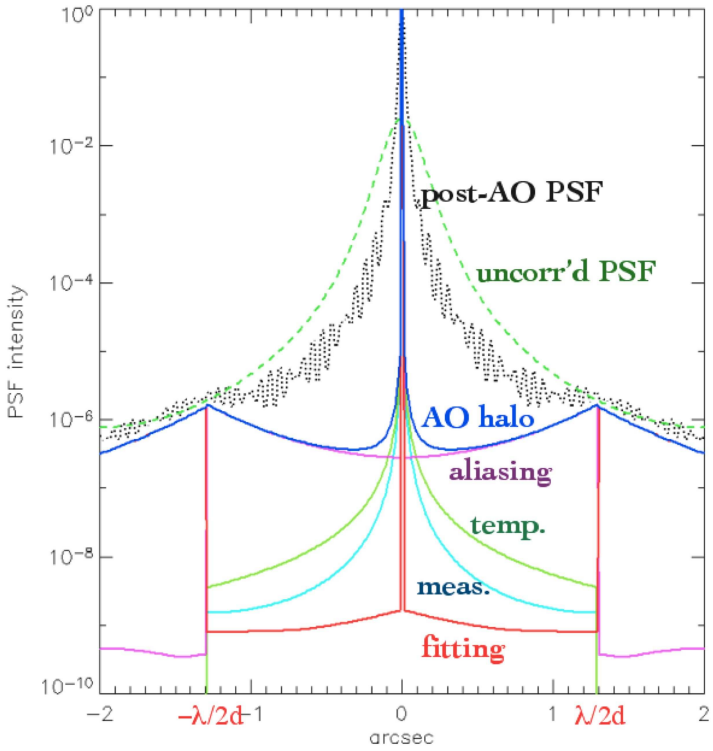

FIGURE 2.1: Distribution spatiale/angulaire des différentes erreurs post-OA au sein du halo de la PSF. *(Figure tirée de Lardière et al. [74].)*

nombre de compromis vont devoir être affrontés (et c'est même à dire vrai le pain quotidien de la modélisation numérique en OA).

Morphologie de la PSF résultante En séparant les effets dus aux différentes sources d'erreur, et en regardant également leurs distributions spatiales/angulaires dans le plan focal (comme par exemple dans Lardière et al. [74]), i.e. à l'intérieur de la PSF elle-même, on obtient ce qui est représenté Fig.2.1 (obtenue à l'aide de l'outil analytique `PAOLA`) :

Un effet particulièrement intéressant à observer Fig.2.1 est la morphologie de l'erreur de sous-échantillonnage spatial d'une part, et celle de l'erreur de repliement de spectre d'autre part (ici $d_{\text{ASO}} = d_{\text{act.}} = d$), en particulier autour de $\lambda/2d$, valeur après laquelle les anneaux d'Airy sont noyés dans les speckles, et donc à partir de laquelle les bénéfices de la correction due à l'OA ne sont plus présents.

Tout comme ces deux dernières, l'erreur de mesure et celle temporelle ($\sigma^2_{\text{mes.}}$ et $\sigma^2_{\text{temp.}}$) participent à la résolution angulaire et à la distribution de l'erreur à l'intérieur de la zone « nettoyée » de la PSF, de taille λ/d.

2.1.2 Sommaire des études numériques qui suivent

Dans la suite je vais m'attacher à détailler quelques travaux se concentrant sur quelques uns de ces termes d'erreur, par le biais d'une première étude sur la modélisation de l'atmosphère turbulente tout d'abord, puis sur une option intéressante afin d'améliorer l'erreur de mesure d'un ASO, puis encore sur l'évaluation de l'erreur ultime que constitue l'erreur de sous-échantillonnage spatial due au miroir M4 de l'E-ELT. Enfin, l'évaluation des performances globales d'un système d'OA complet tel que celui de « première lumière » équipant le LBT sera effectuée. La modélisation elle-même sera alors discutée (approche analytique vs. approche end-to-end), puis une application au site particulier du Dôme C sera également présentée.

2.2 L'atmosphère turbulente

2.2.1 *Numerical modeling of phase screens : new solutions for classical FFT and Zernike methods*

L'article suivant, publié par *Applied Optics* lors de son numéro spécial « Adaptive Optics » de fin 2010, présente la solution à deux problèmes rencontrés lors de la modélisation numérique des fronts d'onde perturbés par l'atmosphère turbulente.

Le premier problème ainsi abordé concerne le manque d'énergie constaté dans les basses fréquences spatiales des fronts d'onde générés par la méthode de transformée de Fourier rapide (ou *Fast Fourier Transform* en anglais, FFT). Des sous-harmoniques sont ainsi ajoutées, ce qui était déjà une solution connue dans son principe [20, 38, 77], mais aucun critère quantitatif précis n'existait dans la littérature pour définir le nombre de sous-harmoniques nécessaires pour un ensemble de caractéristiques physiques définissant un front d'onde. Via le calcul de la puissance intégrée sur toute la gamme de fréquences spatiales d'une part et de la fonction de structure pour une séparation donnée d'autre part, ce problème est ici résolu.

Le second problème présenté concerne l'« autre » méthode classique de simulation numérique de fronts d'onde perturbés, basée sur la projection des fronts d'onde sur une base de polynômes de Zernike, et son problème corollaire : l'instabilité numérique résidant cette fois-ci du côté des hautes fréquences spatiales. La solution est apportée par le biais d'une définition alternative des polynômes de Zernike basée sur les polynômes de Jacobi.

Numerical modeling of atmospherically perturbed phase screens: new solutions for classical fast Fourier transform and Zernike methods

Marcel Carbillet[1,*] and Armando Riccardi[2]

[1]UMR 6525 H. Fizeau, Université de Nice Sophia Antipolis/CNRS/Observatoire de la Côte d'Azur, Parc Valrose, 06108 Nice, Cedex 2, France

[2]INAF—Osservatorio Astrofisico di Arcetri, Largo E. Fermi 5, 50125 Firenze, Italy (riccardi@arcetri.astro.it)

*Corresponding author: marcel.carbillet@unice.fr

Received 20 January 2010; accepted 14 May 2010;
posted 4 June 2010 (Doc. ID 122838); published 25 June 2010

We describe new solutions permitting us to overcome the well-known problems encountered when employing the two main classical methods for numerical modeling of atmospherically perturbed phase screens. The first method, the fast-Fourier-transform-based numerical method, suffers from a lack of low frequencies. Subharmonics adding is an already-known solution to this problem, but no criterion has been defined up to now in order to precisely determine how many subharmonics are necessary for each given case of physical and numerical characteristics. We define two criteria and show their practical efficiency. The second, Zernike-based, method suffers, *a contrario*, from bad behavior of the phase screens at high spatial frequencies. To overcome this problem, due to numerical instability, we developed an algorithm based on an alternative definition of the Zernike polynomials, involving the recurrence definition of the Jacobi polynomials, as well as the relationship between the Zernike and the Jacobi polynomials. The methods described and used in this paper have been implemented within the freely distributed software package CAOS. © 2010 Optical Society of America

OCIS codes: 010.1300, 010.1330, 070.7345, 350.1260.

1. Introduction

Turbulence is mainly located within a few relatively narrow layers, at least in good astronomical sites. The finite number of turbulent layers is a consequence of a modelization of the profile of the structure constant of the refraction index fluctuations, $C_n^2(h)$, where h is the altitude, to an ensemble of discrete values. Each of these values corresponds to a turbulent layer of the atmosphere, and each turbulent layer can be physically simulated as a random phase screen, whose power spectrum follows a von Karman/Kolmogorov model.

The first step for building a turbulent atmosphere is, hence, to generate the phase screens that will simulate the behavior of each turbulent layer. Two methods are usually considered:

1. the fast-Fourier-transform (FFT)-based method, suffering, however, from a lack of low frequencies;
2. the Zernike-polynomials-based method, suffering *a contrario* from possible bad behavior of the phase screens at high spatial frequencies.

An already-known solution to the first problem consists of boosting the low-spatial-frequencies [1,2] by adding subharmonics to the FFT-computed phase screens. But the number of low frequencies to be added is not actually defined in the literature. Section 2 details the two criteria we have defined for this scope and shows their efficiency.

In Section 3 we show how the second problem can be overcome by considering an alternative definition of the Zernike polynomials for high orders.

0003-6935/10/310G47-06$15.00/0

In fine, a brief summary and concluding remarks are given in Section 4.

2. Fast-Fourier-Transform-Based Method with Subharmonics Adding

The well-known FFT method allows us to generate phase screens $\varphi(\vec{r})$, where $\vec{r}$ is the two-dimensional position within the phase screen, assuming usually either a Kolmogorov or a von Karman spectrum $\Phi_\varphi(\vec{\nu})$, where $\vec{\nu}$ is the two-dimensional spatial frequency, from which is computed the modulus of $\tilde{\varphi}(\vec{\nu})$, the Fourier transform of $\varphi(\vec{r})$. Assuming the near-field approximation and small phase perturbation [3], the von Karman/Kolmogorov spectrum is given by

$$\Phi_\varphi(\vec{\nu}) = 0.0229 r_0^{-\frac{5}{3}} \left(\nu^2 + \frac{1}{\mathcal{L}_0^2}\right)^{-\frac{11}{6}}, \tag{1}$$

where r_0 is the Fried parameter and $\mathcal{L}_0$ is the wavefront outer scale (infinite for the Kolmogorov model). Within the framework of the classical FFT-based technique, a turbulent phase screen $\varphi_L(\vec{r})$ of physical length L is obtained by taking the inverse FFT of $\tilde{\varphi}_L(\vec{\nu})$, the modulus of which is obtained from Eq. (1) by applying the definition of the power spectrum, which is

$$\begin{aligned}\Phi_\varphi(\vec{\nu}) &= \lim_{L\to\infty}\left(\frac{\langle|\tilde{\varphi}_L(\nu)|^2\rangle}{L^2}\right)\\ &\Rightarrow |\tilde{\varphi}_L(\nu)| \simeq L r_0^{-\frac{5}{6}}\sqrt{0.0228}\left(\nu^2+\frac{1}{\mathcal{L}_0^2}\right)^{-\frac{11}{12}},\end{aligned} \tag{2}$$

and which phase is random and uniformly distributed.

The obtained phase screen is thus numerically written

$$\varphi_L(i,j) = \sqrt{2}\sqrt{0.0228}\left(\frac{L}{r_0}\right)^{\frac{5}{6}}\left\{\mathrm{FFT}^{-1}\left[\left(k^2+l^2 + \left(\frac{L}{\mathcal{L}_0}\right)^2\right)^{-\frac{11}{12}}\exp\{\imath\theta(k,l)\}\right]\right\}, \tag{3}$$

where i and j are the indices in the direct space, k and l are the indices in the FFT space, $\{\}$ stands for either *real part of* or *imaginary part of*, $\imath$ is the imaginary unit, and θ is the random uniformly distributed phase (between $-\pi$ and π). The factor $\sqrt{2}$ comes from the fact that here we use both the real and imaginary parts of the original complex generated FFT phase screens, which are independent one from the other [4]. This kind of phase screen suffers, however, from the lack of spatial frequencies lower than the inverse of the necessarily finite length L of the simulated array.

In order to compensate from this lack of low frequencies, the technique of subharmonics adding was proposed by Lane *et al.* [1]. This technique consists of generating additional low frequencies and adding their effects to the already-sampled frequencies. If one divides the lower unsampled spatial frequency content in three harmonics, thus adding the effect of $3\times 3 = 9$ bidimensional spatial frequencies at each step, the subharmonics screens are numerically written in this case as

$$\varphi_{3^n L}(i,j) = \sqrt{2}\sqrt{0.0228}\left(\frac{L}{r_0}\right)^{\frac{5}{6}}\frac{1}{3^n}\left\{\mathrm{DFT}^{-1}\left[\left(k_S^2+l_S^2 + \left(\frac{L}{\mathcal{L}_0}\right)^2\right)^{-\frac{11}{12}}\exp\{\imath\theta(k_S,l_S)\}\right]\right\}, \tag{4}$$

where k_S and l_S are the indices in the discrete Fourier transform (DFT) space and n is the number of subharmonics added.

A tricky point remains of defining when to stop the iterative process of subharmonics adding. In their original paper, Lane *et al.* [1] add 5 subharmonics for a Kolmogorov screen over a pupil of $1\ \mathrm{m}\times 1\ \mathrm{m}$ in order to match the theoretical structure function. Later on, Sedmak [2] adds 10 subharmonics to Kolmogorov screens and a number of subharmonics that gives a physical size comparable with, or a bit larger than, the outer scale of turbulence $\mathcal{L}_0$ in the case of von Karman screens. In a successive paper, Sedmak [5] also gives a thorough overview of the practical methods employable for adding subharmonics, with some refinement as well. Nevertheless, no real quantitative criterion for the number of subharmonics to be added has been defined in the literature, and we therefore treat this point hereafter.

A. Subharmonics-Adding Issue

We have investigated the question of how many subharmonics have to be added and defined two aid-to-decision criteria that are able to recommend a minimum number of subharmonics to be added in order to obtain a given precision.

Assuming that the number of computed phase screens is sufficiently large (ideally infinite), the decision criteria can be based on the computation of the ratio between theoretical relevant quantities and will-be-obtained quantities.

In the general case of von Karman turbulence, two candidates well fit the role of decision quantities: the integrated power over the whole range of frequencies and the structure function computed for a relevant space lag. In the case of an infinite wavefront outer scale (Kolmogorov model), the integrated power is infinite, so the only valid criterion becomes the structure function ratio.

1. *Integrated Power Ratio*

The total theoretical integrated power is obtained by integrating the power spectrum over the whole range of theoretically present frequencies, i.e., from 0 to infinity. This gives

$$\int_{-\infty}^{\infty}\int_{-\infty}^{\infty}\Phi_\varphi(\nu_x,\nu_y)\mathrm{d}\nu_x\mathrm{d}\nu_y = 2\pi\int_0^{\infty}\nu\Phi_\varphi(\nu)\mathrm{d}\nu$$
$$= 2\pi 0.0228 r_0^{-\frac{5}{3}} \times \int_0^{\infty}\nu\left(\nu^2+\frac{1}{\mathcal{L}_0^2}\right)^{-\frac{11}{6}}\mathrm{d}\nu$$
$$= \frac{6\pi}{5}0.0228\left(\frac{\mathcal{L}_0}{r_0}\right)^{\frac{5}{3}}. \quad (5)$$

While the will-be-obtained integrated power will not include frequencies lower than the lowest sampled one, which gives

$$\int_{\nu_{x,\mathrm{lim}}}^{\infty}\int_{\nu_{y,\mathrm{lim}}}^{\infty}\Phi_\varphi(\nu_x,\nu_y)\mathrm{d}\nu_x\mathrm{d}\nu_y = 2\pi 0.0228 r_0^{-\frac{5}{3}} \times \int_{\nu_{\mathrm{lim}}}^{\infty}\nu\left(\nu^2+\frac{1}{\mathcal{L}_0^2}\right)^{-\frac{11}{6}}\mathrm{d}\nu$$
$$= \frac{6\pi}{5}0.0228\left(\frac{\mathcal{L}_0}{r_0}\right)^{\frac{5}{3}} \times (1+\nu_{\mathrm{lim}}^2\mathcal{L}_0^2)^{-\frac{5}{6}}, \quad (6)$$

so that the integrated power ratio α_Φ obtained is simply

$$\alpha_\Phi = (1+\nu_{\mathrm{lim}}^2\mathcal{L}_0^2)^{-\frac{5}{6}}. \quad (7)$$

This already means that, because in the subharmonics-adding process $\nu_{\mathrm{lim}} = \frac{1}{3^n L}$, if the length of the screens L is chosen to be equal to the outer scale $\mathcal{L}_0$, this is not enough to guarantee that a sufficient number of low frequencies will be added. In fact, in that case $\alpha = 2^{-\frac{5}{6}} \simeq 0.561$, which is definitely smaller than 1.

Let us, hence, deduce a formula for the number of subharmonics to be added. From the last equation, one has

$$\alpha_\Phi^{-\frac{6}{5}} = 1+\left(\frac{\mathcal{L}_0}{3^n L}\right)^2 \Rightarrow n \geq \frac{1}{\ln 3}\ln\left[\frac{\mathcal{L}_0}{L}\left(\alpha_\Phi^{-\frac{6}{5}}-1\right)^{-\frac{1}{2}}\right], \quad (8)$$

from which we can immediately deduce that even by taking a phase screen length L equal to the outer scale $\mathcal{L}_0$, 1% accuracy is obtained only by adding at least two subharmonics (see Fig. 1).

2. *Structure Function Ratio*

Because the FFT-based phase screens are circularly periodic, the largest relevant structure function space lag ρ is equal to $L/2$. On the other hand, the definition of the structure function $D_\varphi(\vec{\rho})$ is

$$D_\varphi(\vec{\rho}) = 2\int\Phi_\varphi(\vec{\nu})[1-\cos(2\pi\vec{\nu}\vec{\rho})]\mathrm{d}\nu, \quad (9)$$

where the integral is made over the whole range of present frequencies, that means from 0 to infinity for the ideal case, and from ν_{lim} to infinity for the simulated case (assuming also an ideal frequency behavior).

In the Kolmogorov case ($\mathcal{L}_0$ infinite), the theoretical structure function is well known to be

$$D_\varphi(\vec{\rho}) = 6.88\left(\frac{\rho}{r_0}\right)^{\frac{5}{3}}, \quad (10)$$

while the will-be-obtained one is to be deduced from Eq. (9). The structure function ratio α_D is, thus, a function of n and L, the expression of which is

$$\alpha_D(n,L) = 0.0131 L^{-\frac{5}{3}}\int_{\frac{1}{3^n L}}^{\infty}\nu^{-\frac{8}{3}}[1-\cos(\pi L\nu)]\mathrm{d}\nu. \quad (11)$$

In the von Karman case, both structure functions are to be deduced from Eq. (9), and the resulting ratio α_D becomes a function of n and L, but also $\mathcal{L}_0$.

Figure 2 clearly shows the result of the computation of α_D for n ranging from 0 to 10, and L ranging

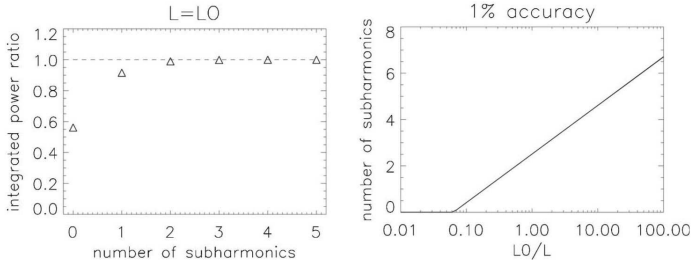

Fig. 1. Integrated power ratio α_Φ versus the number of subharmonics to be added n (left) and number of subharmonics to be added n versus the ratio $L/\mathcal{L}_0$ (right). The integrated power ratio α_Φ is computed for a screen length L equal to the wavefront outer scale $\mathcal{L}_0$. Note the values 0.561 for $n=0$ and 0.99 for $n=2$, reported in the text. The number of subharmonics to be added is computed for a requested accuracy of 1% ($\alpha_\Phi = 0.99$). Note that $n=0$ for $\mathcal{L}_0/L \leq 0.1$, and it becomes nearly 6 for $\mathcal{L}_0/L \simeq 100$.

from 0 m to 250 m for both models (Kolmogorov and von Karman with $\mathcal{L}_0 = 20$ m).

This result shows that Kolmogorov phase screens always need the same number of subharmonics for a given requested accuracy, whatever the screen length L. A good number seems to be 9, after which there is a saturation effect of the attainable accuracy. For von Karman screens, it is obviously dependent on $\mathcal{L}_0$, but it is also obvious that von Karman screens always need fewer subharmonics to be added for the same ratio α_D.

3. Zernike-Polynomials-Based Method Using Jacobi Polynomials

When the Zernike polynomials method is used, the phase screens $\varphi(r,\theta)$ are generated as the sum of the first $N = (j_{\max} - 1)$ Zernike polynomials $Z_j(\frac{r}{R},\theta)$:

$$\varphi(r,\theta) = \sum_{j=2}^{j_{\max}} c_j Z_j\left(\frac{r}{R},\theta\right), \tag{12}$$

where r and θ are the polar coordinates on the pupil of radius R. The Zernike polynomial is expressed as a multiplication between a radial component $R_n^m(\rho)$ and an azimuthal component $[\sin(m\theta)$ or $\cos(m\theta)]$, as described by Noll [6], where n and m represent the radial and azimuthal orders, respectively. The piston term $(j = 1)$ is not considered because the point-spread function is not depending on it.

For each phase screen realization, an independent set of the coefficients c_j has to be obtained with the correct statistics stated by the $N \times N$ covariance matrix [7]: $C_{jj'} = \langle c_j c_{j'} \rangle$. Only a small portion of the matrix has no zero elements, so sparse matrix algorithms can be used when implementing the method in order to allocate less memory and increase the code speed [8].

To obtain good behavior of the phase screens at high spatial frequencies, $j_{\max}$ must be large enough to take into account polynomials with a number of oscillations over the pupil diameter comparable to the chosen sample (usually at least two or three pixels per r_0). In these conditions, $j_{\max}$ can be as large as, for example, a few thousands in the visible for 8 m class telescopes.

The usual definition formula for the Zernike radial component $R_n^m(\rho)$ [6] fails when computing polynomials with high radial order, because the formula involves differences between large terms that should produce a result around the unit value. For instance, when double precision arithmetic is used, numerical instability starts to be evident for $j \gtrsim 1030$, when the largest coefficients of the radial component of the corresponding Zernike polynomial have values around 1×10^{15}, close to the inverse of the floating point precision.

To overcome this problem, we developed an algorithm based on an alternative definition for $Z_j(\rho,\theta)$, involving the relationship between the Zernike radial component $R_n^m(\rho)$ and the Jacobi polynomials $P_k^{\alpha,\beta}(x)$ [9] and using both the Jacobi polynomials definition and their recurrence relationship from Magnus *et al.* [10], as follows:

$$R_n^m(\rho) = \rho^m P_{(n-m)/2}^{(0,m)}(2\rho^2 - 1), \tag{13}$$

where

$$P_k^{\alpha,\beta}(x) = \frac{[C_1 P_{k-1}^{\alpha,\beta}(x) - C_2 P_{k-2}^{\alpha,\beta}(x)]}{C_0}, \tag{14}$$

$$P_0^{\alpha,\beta}(x) = 1, \tag{15}$$

$$P_1^{\alpha,\beta}(x) = (\alpha+\beta+2)/2x + (\alpha-\beta)/2, \tag{16}$$

$$C_0 = 2k(\alpha+\beta+k)(\alpha+\beta+2k-2), \tag{17}$$

$$C_1 = (2k+\alpha+\beta-2)(2k+\alpha+\beta-1)(2k+\alpha+\beta)x + (\alpha^2-\beta^2)(2k+\alpha+\beta-1), \tag{18}$$

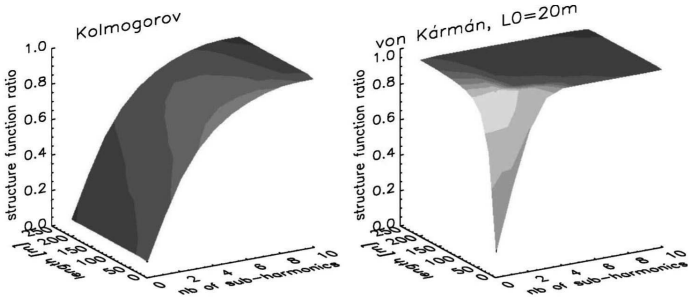

Fig. 2. Structure function ratio α_D versus the number of subharmonics to be added n and the screen physical length L, for the Kolmogorov model (left) and the von Karman model (right, with $\mathcal{L}_0 = 20$ m).

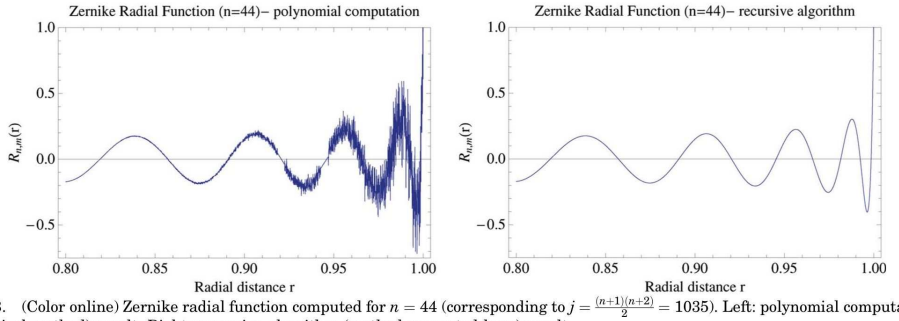

Fig. 3. (Color online) Zernike radial function computed for $n = 44$ (corresponding to $j = \frac{(n+1)(n+2)}{2} = 1035$). Left: polynomial computation (classical method) result. Right: recursive algorithm (method presented here) result.

$$C_2 = 2(k+\alpha-1)(2k+\alpha+\beta)(k+\beta-1). \qquad (19)$$

Figure 3 illustrates the problem of precision exposed above, showing the result of both methods (the classical method and the method proposed here) for $j = 1030$, as a function of the (normalized) radial distance, while Fig. 4 shows an example of phase screen generated using our method. The structure function (computed from 400 phase screens of 256×256 pixels, i.e., $8\ \text{m} \times 8\ \text{m}$, with $j_{\max} = 4186$ and $r_0 = 1$ m) is here, again, in very good agreement with the theoretical method (Kolmogorov here).

4. Summary and Concluding Remarks

We have described new solutions permitting to overcome the well-known problems encountered when employing the two main classical methods for numerical modeling of atmospherically perturbed phase screens, namely the FFT-based and the Zernike-based methods.

Concerning the FFT-based numerical method, we have defined two criteria permitting us to precisely chose the number of subharmonics needed in order to overcome the lack of low frequencies inherent to this method and show their practical efficiency.

Concerning the Zernike-based method, we have developed an algorithm based on an alternative definition of the Zernike polynomials, involving the recurrence definition of the Jacobi polynomials as well as the relationship between the Zernike polynomials and the Jacobi polynomials.

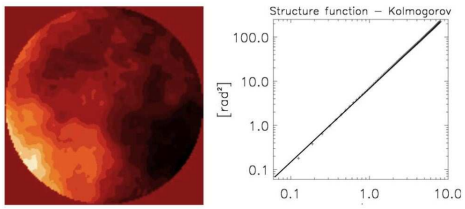

Fig. 4. (Color online) Left: example of a Kolmogorov/Zernike phase screen. Right: the associated theoretical (straight line) and simulated (crosses) structure functions, in logarithmic scale.

The whole code implemented for and used in this paper (the FFT-based method with subharmonics adding and aid-to-decision tools, making use of the two criteria defined in this paper and permitting us to choose the number of subharmonics to be added, and the Zernike-polynomials-based method with the use of Jacobi polynomials) has been implemented within the freely distributed software package CAOS [11] and, more precisely, within the ATM (which stands for "ATMosphere building") module of this AO-dedicated package. CAOS is itself developed within the homonymic CAOS problem-solving environment (PSE) [12]. Both CAOS and the CAOS PSE are downloadable from the dedicated website http://fizeau.unice.fr/caos.

The authors wish to acknowledge Enrico Marchetti, who implemented a preliminary version of the subharmonics-adding code. Thanks are also due to Simone Esposito for prolific discussions on the subject and to the two anonymous reviewers of this paper for their useful remarks.

References

1. R. G. Lane, A. Glindeman, and J. C. Dainty, "Simulation of a Kolmogorov phase screen," Waves Random Media **2**, 209–224 (1992).
2. G. Sedmak, "Performance analysis of and compensation for aspect-ratio of fast-Fourier-transform-based simulations of large atmospheric wavefronts," Appl. Opt. **37**, 4605–4613 (1998).
3. F. Roddier, "The effects of atmospheric turbulence in optical astronomy," Prog. Opt. **19**, 281–376 (1981).
4. P. N. Regagnón, "Bispectral imaging in astronomy," Ph.D. dissertation (Imperial College, 1995).
5. G. Sedmak, "Implementation of fast-Fourier-transform-based simulations of extra-large atmospheric phase and scintillation screens," Appl. Opt. **43**, 4527–4538 (2004).
6. R. Noll, "Zernike polynomials and atmospheric turbulence," J. Opt. Soc. Am. **66**, 207–211 (1976).
7. N. Roddier, "Atmospheric wavefront simulation using Zernike polynomials," Opt. Eng. **29**, 1174–1180 (1990).
8. R. W. Press, B. P. Flannery, S. A. Teutolsky, and W. T. Vetterling, *Numerical Recipes in C* (Cambridge U. Press, 1986).

9. M. Born and E. Wolf, *Principles of Optics* (Pergamon, 1985).
10. W. Magnus, F. Oberhettinger, and R. P. Soni, *Formulas and Theorems for the Special Functions of Mathematical Physics* (Springer-Verlag, 1966).
11. M. Carbillet, C. Vérinaud, B. Femenía, A. Riccardi, and L. Fini, "Modelling astronomical adaptive optics: I. the software package CAOS," Mon. Not. R. Astron. Soc. **356**, 1263–1275 (2005).
12. M. Carbillet, C. Vérinaud, M. Guarracino, L. Fini, O. Lardière, B. Le Roux, A. T. Puglisi, B. Femenía, A. Riccardi, B. Anconelli, M. Bertero, and P. Boccacci, "CAOS—a numerical simulation tool for astronomical adaptive optics (and beyond)," Proc. SPIE **5490**, 637–648 (2004).

2.2.2 Perspectives et questions ouvertes

Plusieurs perspectives et questions ouvertes peuvent être associées à l'activité de modélisation numérique de l'atmosphère turbulente dans le cadre des simulations à HRA.

Une première perspective concerne l'implémentation, en alternative de la propagation géométrique, d'un algorithme de propagation de Fresnel, pouvant permettre ainsi et par exemple, une modélisation de la scintillation, négligée jusqu'ici au sein du `Software Package CAOS` (et ailleurs !), mais pouvant se révéler utile, par exemple et non seulement, dans la perspective d'applications quittant le domaine actuel du proche infrarouge, où cet effet est plus facilement négligeable, pour aborder celui du visible. Un tel algorithme intégré au `Software Package CAOS` serait directement utile aussi pour des propagations à des échelles beaucoup plus petites : entre le plan pupille et le plan image d'un coronographe par exemple. Il existe des algorithmes dédiés à ce problème et déjà codés en `IDL`, tels que `PROPER` [1] ou `TurbuLenZ` [2], dont on peut s'inspirer, tout en sachant que ce type d'implémentation est connu pour ses difficultés numériques (voir e.g. Cruz et al. [64]).

Une seconde perspective concerne une autre *finesse* qui pourrait avoir son importance dans la perspective, cette fois-ci, des télescopes extrêmement grands (ou encore des interféromètres) : la prise en compte du profil de l'échelle externe (et pas seulement de sa valeur intégrée, dont la valeur médiane est toujours plus ou moins prise autour de 25 m pour un télescope de latitude moyenne – i.e. pratiquement partout sauf en Antarctique), qui peut être obtenu par un instrument dédié [109].

Une question ouverte, qui prend tout son sens également dans la perspective des télescopes extrêmement grands, concerne l'hypothèse de Taylor. Cette hypothèse, très largement utilisée, suppose que le front d'onde formé sur la pupille d'entrée du télescope à un instant t n'est, à un temps $t + \Delta t$, que le même front d'onde simplement décalé de $v\Delta t$ dans la direction et le sens de $\vec{v}$ (ou du moins sa composante horizontale). Pour un modèle d'atmosphère multi-couches, la même hypothèse est reproduite sur chacune des couches turbulentes. C'est une hypothèse forte qui néglige le phénomène de *boiling* due à la turbulence optique elle-même [103] [3]. Face aux échelles spatiales bien plus grandes mises en jeu dans le cadre des ELT (e.g. l'E-ELT sera cinq fois plus grand qu'un VLT), il est recommandable de caractériser les différentes couches turbulentes sur ces grandes échelles (voir e.g. Metti et al. [110]), et notamment en termes de temps de cohérence afin de pouvoir vérifier la validité de l'hypothèse de Taylor sur de grandes échelles spatiales.

1. Voir `http://www.openchannelsoftware.com/projects/PROPER`.
2. Voir `http://www.mpia-hd.mpg.de/ALFA/MENU/tlz.html`.
3. À différencier de l'effet de *speckle boiling* dû aux plusieurs couches superposées se déplaçant à des (vecteurs) vitesses $\vec{v}$ différents.

2.3 L'analyseur de surface d'onde

2.3.1 Quel ASO pour l'OA ?

Des introductions aux caractéristiques des ASO considérés en OA peuvent être trouvées dans Campbell & Greenaway [91] et dans Rousset [43], en particulier en ce qui concerne l'ASO basé sur le test de Hartmann modifié par Shack (le « Shack-Hartmann », SH) et l'analyseur de courbure proposé précédemment par Roddier [16], puis en complément dans Ragazzoni [32] pour ce qui est de l'ASO à base de prisme pyramidal (la « pyramide »). Je focaliserai plutôt ici sur l'émulation somme toute épique qui a tout particulièrement concerné le SH et la pyramide ces dernières années.

Après les premiers résultats astronomiques obtenus en 1989 à l'Observatoire de Haute-Provence avec le système COME-ON [4] [18] utilisant un SH 5×5 et un miroir déformable à 19 actionneurs, puis la proposition déjà citée ci-avant d'utilisation alternative d'une pyramide en 1996 [32], Ragazzoni & Farinato montrent en 1999 [41], à partir d'un raisonnement purement analytique, que la pyramide devrait permettre un gain de 2 magnitudes (en termes de magnitude limite) par rapport au SH. Le raisonnement analytique suivi était basé sur l'expression attendue de la variance de l'erreur de mesure liée à chaque composante de Zernike de la phase perturbée, expression dérivée du résultat obtenu au préalable par Rigaut & Gendron [22] pour le SH.

Ceci fut ensuite confirmé par Esposito & Riccardi [52] par le biais de simulations numériques modélisant la correction de l'OA, mais en régime de boucle ouverte et sans autres résidus atmosphériques que ceux correspondants aux modes (partiellement) corrigés eux-mêmes.

Des simulations end-to-end complètes ont ensuite été présentées dans Carbillet et al. [62] sur le cas d'étude constitué par le système d'OA de première lumière du LBT alors en phase de projet, en considérant cette fois l'erreur post-OA dans son ensemble, et donc en particulier l'erreur de mesure d'une part et l'erreur de repliement de spectre (*aliasing*) d'autre part. Un gain fut effectivement trouvé dans tous les cas considérés, et de manière remarquable d'une part en régime à faible flux (où l'erreur de mesure domine), et, à l'opposé, en régime de trés haute correction (où cette fois c'est l'erreur de repliement de spectre qui domine).

La Fig. 2.2, courbe de gauche, illustre bien ce point : le gain attendu en termes de magnitude limite y est d'une magnitude environ, autour de la magnitude 16 (définie en bande R), et un gain de quelques pourcents en termes de rapport de Strehl est clairement démontré également du côté des forts flux. Il est aussi intéressant de noter que cette comparaison est en fait celle d'une pyramide (avec ré-échantillonnage au niveau du détecteur CCD pour avoir 10×10, 15×15 ou 30×30 pixels au niveau de chacune des quatre images de la

4. Pour Cge - Observatoire de paris-Meudon - Eso - ONera, déclinant les noms des membres du consortium ayant développé l'instrument.

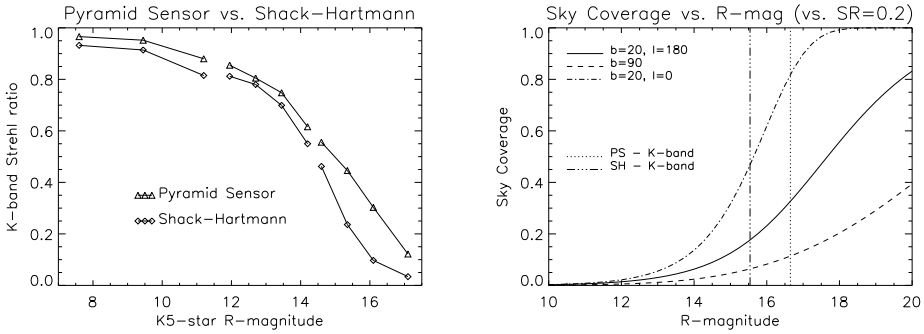

FIGURE 2.2: Comparaison entre les performances prévues pour le système d'OA de première lumière du LBT (à base de pyramide) et un système équivalent à base de SH, en termes de rapport de Strehl obtenu en bande K (à gauche) d'une part, et de couverture du ciel dans la même bande et pour différentes régions du ciel d'autre part (à droite). *(Figure de droite tirée de Carbillet et al. [62].)*

pupille vue au travers de la pyramide) contre trois SH (dans les configurations respectives correspondantes de 10×10, 15×15 et 30×30 sous-ouvertures).

En terme de couverture du ciel, ce gain est également visible dans la courbe de droite de la Fig. 2.2. Nous avons utilisé le modèle de distribution stellaire de Bahcall & Soneira [8] pour l'établir, avec une contrainte sur le rapport de Strehl qui doit être atteint. Un paramètre additionnel pris en compte ici est l'angle maximum de correction à considérer. Notons-le $\theta_{\rm max}$ et prenons-le ici égal à 30 arcsec en bande K. L'aire correspondante de ciel est alors $\pi\theta^2_{\rm max}$, et la couverture du ciel qui en découle $1-\exp\{-N\}$, avec N le nombre d'étoiles d'une magnitude donnée en R dans cette aire. Considérons maintenant un rapport de Strehl de 20% (qui décroîtrait d'environ 10% à 30 arcsec de l'étoile guide). Cette valeur de Strehl correspond à une magnitude en bande R de ~ 16.7 pour la pyramide et ~ 15.5 pour le SH, comme on peut le constater sur la courbe de gauche de la Fig. 2.2... En reportant ces valeurs sur la courbe de droite, on peut aisément en déduire que pour un cas médian ($b = 20$, $l = 180$), la couverture du ciel passe de $\sim 18\%$ pour le SH à $\sim 33\%$ pour la pyramide. De la même manière, la couverture du ciel passe de $\sim 6\%$ à $\sim 11\%$ pour un cas pessimiste ($b = 90$), et de $\sim 47\%$ à $\sim 82\%$ pour un cas plus optimiste ($b = 20$, $l = 0$). Le gain possible de la pyramide est alors clairement démontré, tant du côté des faibles flux en termes de magnitude limite et de couverture du ciel pour une qualité de correction donnée, que du côté des forts flux en termes de rapport de Strehl pour une magnitude donnée.

Mais le vent fit ensuite mine de tourner quand Poyneer & Machintosh [76] proposèrent de diminuer cette dernière erreur pour le SH en introduisant un filtrage spatial agissant sur la réponse impulsionnelle au niveau de l'ASO. De

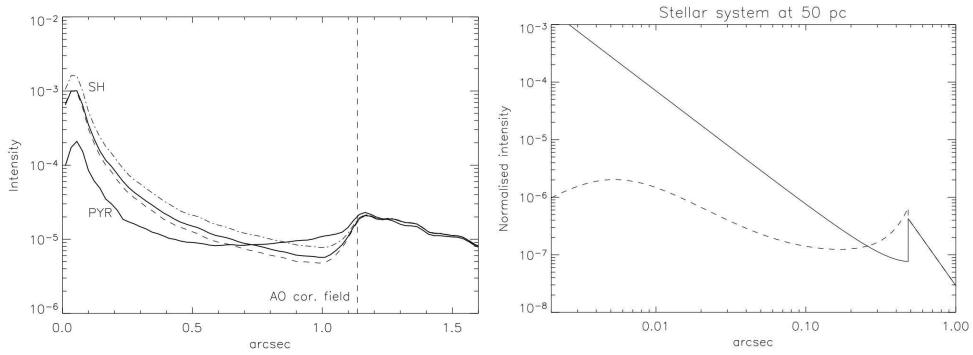

FIGURE 2.3: Comparaison entre les performances prévues pour un système d'OA extrême (D=8 m, d=40 cm, régime à fort flux, seeing$\simeq$0.″85, 1000 modes contrôlés à 2 kHz) à base de pyramide (notée ici PS) et un système équivalent à base de SH filtré spatialement, en termes de profil du halo résiduel (i.e. de la distribution spatiale/angulaire de l'erreur résiduelle post-OA dans le plan focal) de la PSF résultante en bande K (à gauche). Concernant le SH, le trait plein correspond à sa version avec filtrage spatial, les deux autres traits à sa version sans filtrage spatial (mais dans le cas plus avantageux avec un nombre supérieur de photons). La même comparaison est effectuée à droite, mais dans le cas d'un ELT (D=100 m, d=15 cm, bande R, seeing$\simeq$0.″7, 4 kHz). La modélisation est de type « end-to-end » à gauche et analytique à droite. *(Figures tirées de Vérinaud et al. [84].)*

plus, Nicolle et al. [75] proposèrent la même année de diminuer aussi l'erreur de mesure par le biais d'une optimisation du calcul du signal correspondant aux pentes effectué après le SH.

Finalement, c'est l'étude présentée dans Vérinaud et al. [84] qui aura le dernier mot, du moins du point de vue théorique/modélisation : alors que la pyramide est plus performante proche du centre de la tache de diffraction (i.e. proche du cœur-même de la réponse impulsionnelle de taille λ/D), le SH dans sa version filtrée spatialement donne de meilleurs résultats vers les bords de la zone corrigée autour du cœur de la réponse impulsionnelle (i.e. jusqu'à $\lambda/2d$). La Fig. 2.3 illustre cette dernière comparaison par modélisation.

Depuis lors, la pyramide a obtenu des résultats inégalés avec FLAO (*First-light AO*), le système de première lumière du LBT [133, 137]. La barre est placée très haute, mais on doit s'attendre à des résultats tout aussi spectaculaires en ce qui concerne le SH de la part de l'instrument SPHERE/VLT lors de sa prochaine mise en fonction sur le ciel.

Dans l'article qui suit, on s'attaque également à réduire l'erreur de mesure, grâce à la diminution de l'erreur de lecture du détecteur situé en bout de chaîne de l'ASO, pyramidal dans ce cas précis.

2.3.2 *Low-light-level CCDs for pyramid wavefront sensing on 8-m class telescopes : what actual gain ?*

L'article suivant, publié par *Applied Optics* lors de son numéro spécial « Adaptive Optics » de fin 2010, présente la comparaison entre un CCD standard et un EMCCD, ou LLLCCD pour *Low-Light Level* CCD) modélisés au sein d'un même ASO de manière totalement identique, aux paramètres spécifiques près, paramètres spécifiques définissant leurs bruits fondamentaux et caractéristiques physiques respectives.

L'EMCCD n'est pas ici modélisé par l'approximation usuelle qui consiste à considérer un bruit de lecture proche de $0.5\,e^-$, mais par la modélisation de tous les bruits réellement présents lors de l'acquisition d'image de la part des CCD, y compris l'étage de multiplication : bruit de photons (suivant une distribution de Poisson), bruit de lecture (distribution de Gauss), mais aussi bruit d'amplification suivant une distribution Gamma (établie au passage dans l'article) et bruit de courant d'obscurité « exotique » dans le cas des EMCCD.

Les résultats obtenus à faible flux montre un net avantage pour les EMCCD, surtout du point de vue de la magnitude limite atteignable ($+0.8$ mag.), tendant à les indiquer tout particulièrement pour des cas de correction plus faible (magnitudes élevées, domaine visible).

Low-light-level charge-coupled devices for pyramid wavefront sensing on 8 m class telescopes: what actual gain?

Marcel Carbillet[1,*] and Armando Riccardi[2,3]

[1]UMR 6525 H. Fizeau, Université de Nice Sophia-Antipolis/CNRS/Observatoire de la Côte d'Azur, Parc Valrose, 06108 Nice Cedex 2, France

[2]INAF, Osservatorio Astrofisico di Arcetri, Largo E. Fermi, 50125 Firenze, Italy

[3]riccardi@arcetri.astro.it

*Corresponding author: marcel.carbillet@unice.fr

Received 2 April 2010; revised 25 September 2010; accepted 7 October 2010; posted 7 October 2010 (Doc. ID 126427); published 21 October 2010

We present the results of a comparison made between standard charge-coupled devices (CCDs) and low-light-level (LLL) CCDs in the framework of pyramid wavefront sensing for astronomical adaptive optics (AO) systems on 8 m class telescopes. This comparison is based on detailed end-to-end numerical simulations of the first-light AO system of the Large Binocular Telescope, a relevant example of a pyramid-based AO system. While the model used for simulating the standard CCD is the usual well-established one, mainly based on the consideration of Poisson photon noise and Gaussian readout noise (RON), the model used for the LLLCCD is not only made through the simplistic consideration of a subelectron equivalent RON, but also through the establishment of a gamma distribution. Moreover, an additional dark current component, also resulting from the peculiar architecture of LLLCCDs, is considered. The results obtained clearly show a gain of roughly 0.8 magnitude when considering K-band Strehl ratios ranging from 15% to 60%, at least in the particular case study chosen (Fried parameter characterizing the turbulent atmosphere above the telescope $r_0 = 15$ cm and low light levels).

OCIS codes: 350.1260, 120.4820.

1. Introduction

A low-light-level charge-coupled device [(LLLCCD) also called L3CCD or EMCCD for electron multiplying CCD] [1–5], a kind of CCD that has the capability of giving a high internal gain, is here compared to a standard CCD within the framework of a pyramid-based adaptive optics (AO) system aboard an 8 m class telescope.

The main point of interest is the gain in magnitude limit that seems to be possible by using an LLLCCD instead of a standard CCD within the necessary wavefront sensor of an AO system. In fact, an LLLCCD is expected to attain subelectron readout noise (RON) levels, hence practically eliminating a significant noise source for wavefront sensing, because it permits amplification of the signal prior to readout.

A preliminary idea of the possible gain achievable within the framework of a given AO system can be very simply performed by assuming a subelectron RON (see, e.g., Petit *et al.* [6]) for simulating the behavior of the system (with typically 0.5 e^- rms), and then compare the resulting performance to the performance obtained when using a standard CCD. For example, roughly 1 magnitude of gain was predicted from numerical simulations in the specific case of the first-light AO system of the Large Binocular

0003-6935/10/31G167-07$15.00/0

Telescope (LBT), when considering a goal of a 30% Strehl ratio in the K band [7].

The necessity of more detailed simulations, in order to measure the precise impact of such a CCD on the final performance of an AO system, rises up mainly because of the essentially stochastic nature of the charge multiplication process of the LLLCCD, with respect to standard CCDs. In fact, within the LLLCCD, an extended serial register is used to allow electron avalanche multiplication that can permit a large mean gain (typically 1000) but at the following cost: the detailed process by which the signal is amplified is stochastic and hence introduces additional noise at the output. The (indirect) effect of this noise on the performance of the system has to be studied.

An additional concern rises for the specific, and interesting, case of a pyramid wavefront sensor. In fact, given the amplification of the signal and practical elimination of the RON, one would like to use the pyramid wavefront sensor in a way that uses the largest number of subapertures and the shortest time exposure. Having the maximum number of allowable subapertures (and hence the largest possible number of elements of analysis of the incoming perturbed wavefront) permits us to control a larger number of mirror modes for a given AO-guide-star magnitude, and therefore (*a priori*) enhance the correction. On the other hand, having the shortest possible time exposure would permit compensation of the wavefront temporal evolution due to the movement of the perturbed layers above the telescope more rapidly and, therefore, once again enhance the correction.

Hence we see that a decisive numerical simulation study concerning the issue of having an LLLCCD aboard a pyramid-based AO system, requires both a complete simulation of the multiplication process inside the LLLCCD and an *ad hoc* optimization of the relevant parameters that concerns the wavefront sensing and correction: the number of mirror modes corrected and the closed-loop gain.

In this paper we first recall, in Section 2, the expected advantage of the LLLCCD in terms of signal-to-noise ratio (SNR) with respect to RON and the excess noise factor that can be found in the literature. In Section 3 we describe the simulation procedure followed and the results found for a relevant example of pyramid-based AO systems: the first-light AO system of the LBT detailed as an example one of the cases of AO-guide-star magnitudes of interest. Finally, the results obtained are summarized in Section 4.

2. Pyramid Wavefront Sensing and LLLCCD

A. Pyramid Wavefront Sensor

The pyramid wavefront sensor, whose concept was first published by Ragazzoni in 1996 [8], is based on the Foucault test method for optical systems. The main difference with respect to the original Foucault test is the replacement of the knife edge by a glass pyramidal optical element whose function is to emulate two knife edges in two perpendicular directions placed in the focal plane. As described, for example, in Carbillet *et al.* [9], where the pyramid wavefront sensor setup is also described, the pyramid is located in an image plane and the four pupils, corresponding to each of the four pyramid facets, are imaged by a relay lens on the pupil plane detector. A dynamic modulation of the beam (following either a circular or a square path) is applied by means for example of a tip-tilt mirror placed in a pupil plane.

One main basic advantage of the concept, as announced by Ragazzoni [8], is that the sampling of the perturbed wavefront (and, hence, the size of the equivalent subaperture itself with respect to the Fried parameter r_0 characterizing the spatial coherence size of the incoming wavefront for a given wavelength) can be easily changed in a simple and continuous manner. Let us note that the latter also implies that the same pyramidal prism and subsequent CCD, i.e., the same wavefront sensor, can be used with different subaperture configurations (i.e., different linear number of subapertures per telescope diameter) by simply changing the binning of the CCD. Therefore, only one pyramid wavefront sensor with a given number of possible binning configurations of the CCD is equivalent to the same given number of different Shack–Hartmann wavefront sensors. For example, a pyramid wavefront sensor with 30×30, 15×15, and 10×10 (binned) pixels per pupil image after each pyramid facet is equivalent to three different Shack–Hartmann wavefront sensors with 30×30, 15×15, and 10×10 lenslets, respectively.

Further studies also show a better behavior with respect to the more classical and widely used Shack–Hartmann sensor, in terms of wavefront residuals, and hence the Strehl ratio, in particular in a photon-starving regime [7,10,11], due to its higher sensitivity, but also in a high-flux regime [7,12] because of its better behavior with respect to aliasing effects.

Moreover, the recent results on the sky presented by Esposito *et al.* [13] definitely show the unprecedented performance achievable on an 8 m class telescope with this kind of wavefront sensor.

B. LLLCCD (as Opposed to Standard CCDs)

The main difference between using one CCD or the other is the resulting noises, namely, the photon noise, RON, and dark current noise. In the case of an LLLCCD, the intrinsic noise involved by its peculiar amplification process also needs to be taken into account.

Because of the amplification factor of the order of 1000, possible with the LLLCCD, one could use it, unlike a standard CCD, with a faster read mode, and a larger configuration (in terms of number of equivalent subapertures) in the case of a pyramid-based AO system, allowing better performance thanks to the considerably reduced RON. But on the other hand, the dark current noise related to LLLCCDs has an additional component and the intrinsic noise involved by the amplification process when using an LLLCCD leads, in practice, to an excess noise factor.

We assume hereafter a negligible classical dark current noise. The standard expression for the SNR we are concerned with here will be in the form of $n/\sqrt{n+4\sigma_e^2}$, where n is the number of photons per subaperture per exposure time, and σ_e is the RON in terms of electron rms (note that four pixels are read for each wavefront measure). A first very simple reasoning would be to consider that because the large amplification factor, an image obtained with an LLLCCD would be dominated by photon noise, and hence be of the form $n/\sqrt{n}=\sqrt{n}$, the expression of a perfectly noiseless detector. In this case the LLLCCD is always a better detector.

But the amplification noise relative to the LLLCCD actually implies consideration of an excess noise factor (see, e.g., Basden *et al.* [3]) up to $\sqrt{2}$, leading to an SNR expression of the form $n/\sqrt{2n}=\sqrt{n/2}$, which is already an expression that can be compared with a standard CCD one (i.e., $n/\sqrt{n+4\sigma_e^2}$) to find in which regime a given case is placed.

Figure 1 gives an idea of what these expressions become for a given case and as a function of the number of incident photons n. Four cases are considered: an "ideal CCD" one (photon noise only), a first "actual CCD" case considering a RON of $3.5\,e^-$ rms, a second "actual CCD" case considering a RON of $4.5\,e^-$ rms, and an "actual LLLCCD" case considering the excess noise factor of $\sqrt{2}$.

These very simple plots already show that the LLLCCD should allow better performance at least at low light levels, i.e., until the excess noise factor $\sqrt{2}$ produces a worse effect than the RON.

But this simple result cannot be considered as a reliable quantitative result: first because the noise expressions are not that simple (and not that well established for the specific example of a pyramid wavefront sensor) and second because a different SNR value would imply a different set of parameters used during the closing of the AO loop (namely, the closed-loop gain itself, the number of modes corrected, the time integration, the sensor configuration, and so on), leading to performance that has to be simulated in detail. Moreover, the additional component of the dark current noise peculiar to the LLLCCD has to be taken into account as well. In the next section we describe the resulting simulations we have performed and the results obtained from them.

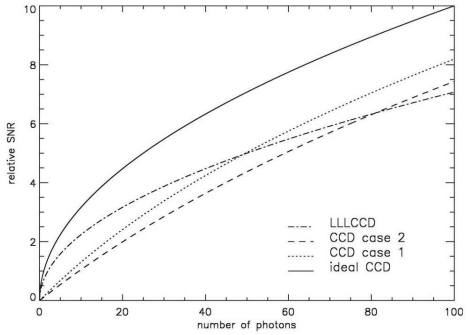

Fig. 1. (Relative) SNR: ideal CCD (photon noise only) versus CCD $+3.5\,e^-$ RON (case 1) versus CCD $+4.5\,e^-$ RON (case 2) versus LLLCCD (excess noise factor of $\sqrt{2}$, no dark current noise).

3. Numerical Simulations

A. Probability Distribution Model of the LLLCCD

As a first step, the model of probability distribution given by Basden *et al.* [3] has been verified by comparing the results with direct simulations of the avalanche of electrons through the stages. The latter method is extremely time consuming. In addition, it presents numerical problems when too many photons are considered (where "too many photons" here means only a few photons) because it rapidly involves a very large number of iterations. In contrast, the modelized probability distribution method gives faster results and permits any number of input photons.

Following Basden *et al.* [3], the theoretical distribution for such a multiplication process can be described in a similar way to a Poisson distribution, with slight changes. The probability of detecting an output number of electrons x is, in fact, given by

$$P(x)=\frac{m^{-nr}x^{n-1}e^{-xm^{-r}}}{(n-1)!}, \tag{1}$$

where m is the multiplication factor, e.g., 1.012 for a 1.2% chance of multiplication, r is the number of elements in the multiplication register (for example, 591), and n is the initial number of electrons (i.e., the number of incident photons).

By assuming $X=xm^{-r}$ and remarking that $(n-1)!=\Gamma(n)$, Eq. (1) becomes more readily

$$P(X)=\frac{X^{n-1}e^{-X}}{\Gamma(n)}, \tag{2}$$

which represents the well-known gamma distribution.

At this point it is straightforward to compare this model to direct simulations of the avalanche of photoelectrons through the stages. Figure 2 shows the resulting histogram when considering 128×128 incident photons (i.e., a 128×128 chip uniformly illuminated) and predicting the resulting output electrons with direct simulation of the avalanche process (rhombuses), with respect to a model-based simulation (squares). The two histograms clearly match.

B. Numerical Tool

Once verified, the modelization described in Subsection 3.A was implemented within the software package CAOS [9], developed within the homonymous CAOS problem-solving environment (see Carbillet *et al.* [14] and http://fizeau.unice.fr/caos). The whole numerical model used in the present paper [turbulent atmosphere generation (see also Carbillet and Riccardi [15] for details about this particular point),

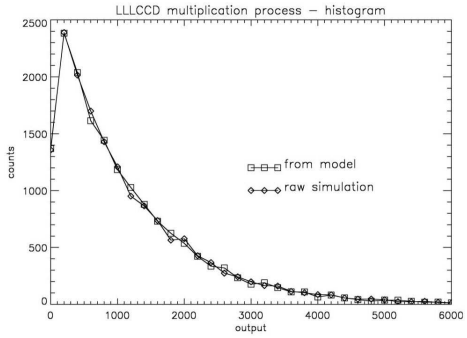

Fig. 2. Histograms of the number of output electrons when considering 128×128 incident photons (each pixel of the 128×128 pixel chip receives one incident photon) and predicting the resulting output electrons with direct simulation of the avalanche process (rhombuses), and model-based simulation (squares). Note that the number of elements in the multiplication register considered is 591 and the multiplication factor is 1.012, implying that the expected value for the output is $1.012^{591} \simeq 1150$ photoelectrons.

light propagation through the turbulent atmosphere, pyramid modeling, including the classical noises implementation, and image formation] is described in detail in Carbillet *et al.* [9] but for the LLLCCD case for which an adaptation of the module that simulates the pyramid wavefront sensing (module PYR) was performed. It now permits simulation, in addition to the usual photon noise, of RON and (standard) dark current noise, the additional dark noise particular to the LLLCCD, and especially the whole avalanche of photoevents through a given number of stages and with a given amplification factor.

Because the probability density function for multiplication of a single input electron has an exponential shape, it is also important here to be able to discriminate between the presence and the absence of a signal [3,4]. Hence, the possibility to work in the photon counting mode (or "clipping" mode) has also been implemented. In practice, a threshold (in number of outputs electrons) under which the signal is clipped can be defined.

The code developed and used here will be available with the next distributed version of the software package CAOS.

C. Simulation Procedure and Physical Parameters

Table 1 shows a list of the different physical parameters taken into account for the detailed simulations presented here.

The parameters considered for the turbulent and evolving atmosphere, as well as for the telescope, the AO guide star, the deformable mirror, and the "standard CCD" case of the pyramid wavefront sensor are similar to the set of parameters already taken elsewhere and for which a first characterization of the first-light AO system of LBT was performed [7].

Note that because we are rather interested in low-flux regimes, the "standard CCD" is used with the 10×10 and 15×15 configurations (in terms of equivalent subapertures of the pyramid sensor of the first-light AO system of LBT; see Carbillet *et al.* [7]), which correspond to an optimization of its use within these regimes. The time exposures also correspond to optimal values, and the RON values to the corresponding expected ones.

From its side, the "LLLCCD" case is mainly characterized by the fact that with this detector, the wavefront sensing is supposed to be done always at 500 Hz (i.e., at a 2 ms time exposure), and with

Table 1. Main Parameters of the Simulation

Turbulent Atmosphere		
Fried parameter (at 500 nm), wavefront outer scale	15 cm, 20 m	
Ground layer: velocity, $C_N^2(h)$ percentage	~8 m/s, 70%	
High layer: velocity, $C_N^2(h)$ percentage	~16.5 m/s, 30%	
Telescope		
Effective diameter, obstruction ratio	8.22 m, 11%	
AO guide star		
Spectral type, R-magnitude range	K5, 13–18	
Deformable mirror		
Number of actuators	672	
Wavefront sensing		
Central sensing wavelength, bandwidth	750 nm, 300 nm	
Standard dark current	none	
Type of CCD	standard CCD	LLLCCD
Total average transmission	0.41	0.36
Subaperture configuration	10×10, 15×15	30×30
Exposure time [ms]	2.5, 5, 10	2
RON [e^- rms]	3.5, 4.5	35
Additional dark current [e^-/px/frame]	—	0.1
Number of stages of the multiplication register	—	591
Amplification factor	—	1.012
Resulting total amplification factor	—	~1150
Threshold [e^-]	—	210

the largest configuration (in terms of equivalent subapertures of the pyramid sensor of the first-light AO system of LBT), i.e., 30×30. At this rate the RON is expected to be $35\,e^-$ rms.

With regard to the dark current noise, which is amplified together with the signal in the LLLCCD case but which classical thermal component can be kept negligible if the detector is operated at a very low temperature, we have to take into account an additional component that depends very weakly on the temperature and does not depend on the exposure time [1]. This effect is also known as "clock-induced charge" or "spurious charge" [1]. It is expected to be $\sim 0.1\,e^-$/pixel/frame (at -55°C and following the manufacturer data sheet—E2V Technologies, formerly Marconi Applied Technologies). The standard thermic component is roughly expected to be between $0.001\,e^-$/px/s and $1\,e^-$/px/s low temperatures [4]. Because most of the time the additional component is dominant in our case, we are neglecting the standard component in the present simulations, as for the standard CCD case.

We are here optimizing both the closed-loop gain and the number of modes to be reconstructed, the loop being closed using a simple pure integrator. We globally consider up to 671 modes to be reconstructed (all possible modes with the adaptive secondary mirror of LBT), with a variable step, and the following closed-loop gains: 1/4, 1/2, 1, 3/2, and 2. This work is done both for the standard CCD case, the LLLCCD case, and seven AO-guide-star R magnitudes (ranging from 13 to 18). The first two cases of magnitude (13 and 14) are optimal, with the standard CCD, when using the 15×15 equivalent subaperture configuration, while the last four cases of magnitude (15, 16, 17, and 18) are optimal when using the 10×10 equivalent subaperture configuration.

For each star magnitude, the various PSFs obtained (for the various numbers of modes corrected and the various values of loop gains applied) are computed. The optimum values of both the parameters (number of modes corrected and loop gain) are then found by searching for the maximum K-band Strehl ratio obtained. This is done both for the standard CCD and for the LLLCCD. Exploring the optimum value of the couple of parameters leads each time to a slightly different set of values for those parameters.

D. Example of Detailed Results: R magnitude = 15

Figure 3 (top) shows the optimization plots obtained for both the number of modes (left) and the loop gain (right), in the standard CCD case and for a 15th magnitude AO guide star. The bottom part of this figure shows the same quantities for the LLLCCD case. Note that the method employed to search for the minimum of these surfaces uses as a starting assumption the (observed from preliminary simulations) fact that the corresponding surfaces are convex, with a clear unique global minimum. An exhaustive search would

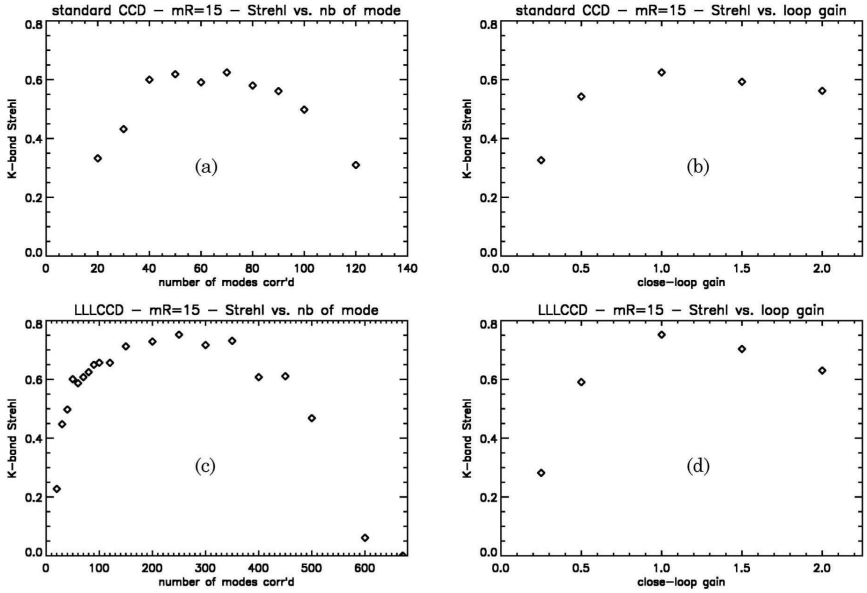

Fig. 3. (a) K-band Strehl values versus the number of modes corrected for the standard CCD case and an AO-guide-star R magnitude of 15, (b) Strehl values versus the (relative) loop gain for the same case, (c), (d) the same plots as in the LLLCCD case.

Table 2. Standard CCD Case Versus LLLCCD Case[a]

Standard CCD								
K5 Star R Magnitude	Best Configuration	Best Δt (ms)	⇒ Light Level	⇒ RON (e^- rms)	Pyramid Modulation	Best Gain	Best n_M	K-Band Strehl
13	15 × 15	2.5	∼170	4.5	$\pm 2\lambda/D$	∼0.5	∼100	∼0.69
14	15 × 15	2.5	∼70	4.5	$\pm 2\lambda/D$	∼0.5	∼80	∼0.66
15	10 × 10	5	∼25	3.5	$\pm 4\lambda/D$	∼1.0	∼70	∼0.62
16	10 × 10	5	∼10	3.5	$\pm 4\lambda/D$	∼1.0	∼60	∼0.44
17	10 × 10	10	∼8.0	3.5	$\pm 4\lambda/D$	∼1.0	∼40	∼0.14
18	10 × 10	10	∼3.2	3.5	$\pm 4\lambda/D$	∼0.5	∼30	∼0.07
LLLCCD								
K5 Star R Magnitude	One Configuration	One Δt (ms)	⇒ Light Level	⇒ RON (e^- rms)	Pyramid Modulation	Best Gain	Best n_M	K-Band Strehl
13	30 × 30	2	∼7.0	35	$\pm 2\lambda/D$	∼1.5	∼300	∼0.86
14	30 × 30	2	∼2.8	35	$\pm 2\lambda/D$	∼1.0	∼300	∼0.84
15	30 × 30	2	∼1.1	35	$\pm 4\lambda/D$	∼1.0	∼250	∼0.75
16	30 × 30	2	∼0.45	35	$\pm 4\lambda/D$	∼1.5	∼120	∼0.58
17	30 × 30	2	∼0.18	35	$\pm 4\lambda/D$	∼1.5	∼80	∼0.34
18	30 × 30	2	∼0.07	35	$\pm 4\lambda/D$	∼2.0	∼50	∼0.12

[a]Light levels are indicated in photons/subaperture/time exposure; n_M is the number of mirror modes corrected.

consider an important number of mostly improbable couples of values and would need an enormous amount of computational time (end-to-end simulations can be extremely time consuming) but would lead, as far as we observed from preliminary simulations, to the exact same result.

It is worth remarking from this figure that the LLLCCD has, in addition to the expected advantage of permitting a better Strehl value, the other advantage of permitting a relaxation on the choice of the right number of modes to be corrected in order to have an optimal operation of the AO system. In fact, while the K-band Strehl value rapidly drops down from ∼60% to ∼40% when controlling ∼30 modes or ∼110 modes instead of the optimum ∼60 modes in the standard CCD case, it remains around 70% when controlling from ∼150 modes to ∼350 modes in the LLLCCD case. The quantities given here are dependent on the fact that a simple pure integrator is used to control the mirror modes, but the relaxation noticed can most probably be extended to other command methods.

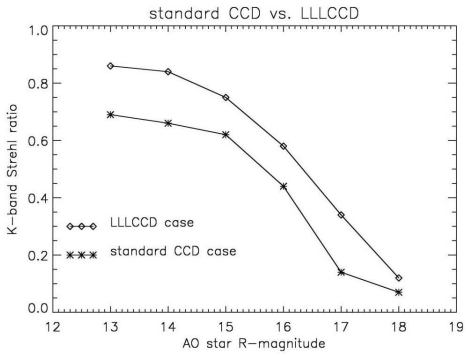

Fig. 4. Optimum K-band Strehl values versus the AO-guide-star R magnitude for both the standard CCD case and the LLLCCD case.

4. Conclusion

Table 2 and Fig. 4 are a résumé of the results obtained. The gain achieved thanks to the use of the LLLCCD is quite clear, and it can be easily estimated to lie within a 0.6–0.9 magnitude when considering K-band Strehl ratios of 15%–60%, with a gain of ∼0.9 ratio of 15%, 0.8 magnitude for both a Strehl ratio of 20% and a Strehl ratio of 60%, and ∼0.6 magnitude for a Strehl ratio of 40%–45%. For the few higher Strehl ratios presented here, the gain is even growing. It was not the main zone of interest for this study (where the goal was to push the magnitude limit of the system). But it is, nevertheless, an interesting result because it opens the possibility to actually maintain, when using an LLLCCD instead of a standard CCD, the same wavefront sensor configuration (in terms of number of subapertures used) for any AO-guide-star magnitude. In fact, it was already predicted for this particular system, in the standard CCD case, that, while the 15 × 15 configuration is optimal until a magnitude of ∼11.5 (where, by very simply extrapolating the curve of Fig. 4, it is likely that a gain when using an LLLCCD can be still expected), the 30 × 30 configuration becomes the optimal one when going for brighter guide stars (where no gain can be expected from the LLLCCD because, within the limit of very bright guide stars, the RON and all other noise sources must become insignificant) [7,16].

This possibility to not change wavefront sensor configuration for each AO-guide-star magnitude

(and the corresponding optimal time exposure) and having anyway a significant gain when using an LLLCCD could definitely be an excellent opportunity for future pyramid-based AO systems.

A last foreseen advantage concerns the relaxation on the choice of the right number of modes to be corrected in order to have an optimal closing of the AO loop, thanks to the fact that the maximum predicted in our simulation is much flatter when compared to the CCD case. This is to be verified when using smarter control laws than the simplistic one chosen here (pure integrator), but this could form an excellent opportunity, too.

Although the whole analysis presented in this paper was made for a pyramid-based particular AO system (the first-light AO system of LBT), the general trend presented here (better performance at low light levels and simplifications of the system operation) can be generalized to other pyramid-based systems and, even more straightforwardly, to other atmospheric conditions. Dedicated end-to-end detailed simulations are nevertheless difficult to circumvent in order to have a precise value of the achievable gain for other scenarios.

Thanks are due to Piero Salinari, Simone Esposito, and Italo Foppiani for prolific discussions on the subject. The authors are also indebted to Barbara Basalgète for proofreading the manuscript and to the two anonymous reviewers for important remarks that permitted us to significantly improve the article.

References

1. P. Jerram, P. Pool, D. J. Burt, S. Bowring, S. Spencer, M. Hazelwood, I. Moody, N. Catlett, and P. Heyes, "The LLLCCD: low light imaging without the need for an intensifier," Proc. SPIE **4306**, 178–186 (2001).
2. C. D. Mackay, R. N. Tubbs, R. Bell, D. J. Burt, P. Jerram, and I. Moody, "Sub-electron read noise at MHz pixel rates," Proc. SPIE **4306**, 289–298 (2001).
3. A. G. Basden, C. A. Haniff, and C. D. Mackay, "Photon counting strategies with low light level CCDs," Mon. Not. R. Astron. Soc. **345**, 985–991 (2003).
4. I. Foppiani, C. Baffa, V. Biliotti, G. Bregoli, G. Cosentino, E. Giani, S. Esposito, B. Marano, and P. Salinari, "Photon counting CCDs as wavefront sensors for AO," Proc. SPIE **4839**, 312–316 (2003).
5. A. G. Basden and C. A. Haniff, "Low light level CCDs and visibility parameter estimation," Mon. Not. R. Astron. Soc. **347**, 1187–1197 (2004).
6. C. Petit, Th. Fusco, J. Charton, D. Mouillet, P. Rabou, T. Buey, G. Rousset, J.-F. Sauvage, P. Baudoz, P. Gigan, M. Kasper, E. Fedrigo, N. Hubin, P. Feautrier, J.-L. Beuzit, and P. Puget, "The SPHERE XAO system: design and performance," Proc. SPIE **7015**, 70151D (2008).
7. M. Carbillet, C. Vérinaud, S. Esposito, A. Riccardi, A. Puglisi, B. Femenía, and L. Fini, "Performance of the first-light adaptive optics system of LBT by means of CAOS simulations," Proc. SPIE **4839**, 131–139 (2003).
8. R. Ragazzoni, "Pupil plane wavefront sensing with an oscillating prism," J. Mod. Opt. **43**, 289–293 (1996).
9. M. Carbillet, C. Vérinaud, B. Femenía, A. Riccardi, and L. Fini, "Modelling astronomical adaptive optics: I. the software package CAOS," Mon. Not. R. Astron. Soc. **356**, 1263–1275 (2005).
10. R. Ragazzoni and J. Farinato, "Sensitivity of a pyramidic wave-front sensor in closed loop adaptive optics," Astron. Astrophys. **350**, L23–L26 (1999).
11. S. Esposito and A. Riccardi, "Pyramid wavefront sensor behavior in partial correction adaptive optics systems," Astron. Astrophys. **369**, L9–L12 (2001).
12. C. Vérinaud, M. Le Louarn, V. Korkiakoski, and M. Carbillet, "Adaptive optics for high-contrast imaging: pyramid sensor versus Shack–Hartmann sensor," Mon. Not. R. Astron. Soc. **357**, L26–L30 (2005).
13. S. Esposito, A. Riccardi, L. Fini, A. T. Puglisi, E. Pinna, M. Xompero, R. Briguglio, F. Quirós Pacheco, P. Stefanini, J. C. Guerra, L. Busoni, A. Tozzi, F. Pieralli, G. Agapito, G. Brusa-Zappellini, R. Demers, J. G. Brynnel, and P. Salinari, "First-light AO (FLAO) system for LBT: final integration and acceptance tests in Europe," Proc. SPIE **7736**, 773609 (2010).
14. M. Carbillet, C. Vérinaud, M. Guarracino, L. Fini, O. Lardière, B. Le Roux, A. T. Puglisi, B. Femenía, A. Riccardi, B. Anconelli, M. Bertero, and P. Boccacci, "CAOS—a numerical simulation tool for astronomical adaptive optics (and beyond)," Proc. SPIE **5490**, 637–648 (2004).
15. M. Carbillet and A. Riccardi, "Numerical modeling of atmospherically perturbed phase screens: new solutions for classical fast Fourier transform and Zernike methods," Appl. Opt. **49**, G47–G52 (2010).
16. M. Carbillet, A. Riccardi, and S. Esposito, "Numerical simulation studies for the first-light adaptive optics system of the Large Binocular Telescope," Proc. SPIE **5490**, 731–732 (2004).

2.4 Le miroir déformable

2.4.1 Contexte

Nous allons ici aborder le problème spécifique des miroirs adaptatifs pour l'E-ELT. Ces miroirs requièrent l'augmentation de la surface correctrice d'au moins un ordre de grandeur (et d'autant en termes de nombre d'actionneurs), par rapport à la technologie actuelle utilisée avec les télescopes de la classe 8 mètres dans le cadre des miroirs secondaires adaptatifs [112]. L'augmentation drastique en complexité nécessite une modélisation détaillée des miroirs adaptatifs impliqués ainsi que du reste du système d'OA envisagé. Cette modélisation doit par la suite permettre d'analyser au mieux les problèmes spécifiques rencontrés avec cette classe particulière de miroirs adaptatifs (en termes de correction bien entendu mais également en amont de ceci en termes de reconstruction du front d'onde perturbée et en amont encore en termes d'analyse de celui-ci).

L'étude ainsi abordée s'appuie sur l'expérience acquise lors du développement du `PSE CAOS` et en particulier de l'homonyme `Software Package CAOS`, couplé à l'utilisation de codes spécifiques aux miroirs abordés, en partie développés lors d'études préliminaires, puis peaufinés et intégrés à l'ensemble logiciel en évolution au sein du `PSE CAOS` afin d'aborder au mieux les problèmes rencontrés avec ce type de miroirs pour l'E-ELT, i.e. :

- ⋆ La segmentation du miroir adaptatif, entraînant une erreur de sous-échantillonnage spatial due également aux bords des segments (en l'occurrence six pétales) ainsi que des problèmes pressentis de cophasage à étudier dans un second temps en termes d'interaction avec l'ASO.
- ⋆ La projection de la pupille sur le miroir, nécessitant de considérer la présence d'actionneurs *slaves* et *masters* dont la gestion, en termes de reconstruction du front d'onde, est en cours d'étude comparative.
- ⋆ La saturation des actionneurs de force, saturation qui devra là aussi être gérée au mieux.

Les premiers résultats obtenus et reportés dans l'article présenté à la sous-section suivante indiquent pour ce qui est du premier et du second point, pour un modèle réduit du miroir (un anneau de celui-ci, rendant plus maniable numériquement le problème qui implique autrement un très grand nombre d'actionneurs) qu'une reconstruction du front d'onde impliquant une hiérarchie des actionneurs entre masters et slaves, que ce soit en ne forçant pas les actionneurs slaves (*slaves non-forcés*) ou bien en ne leur faisant suivre que les modes appliqués par les masters (*slaves forcés*), ne modifie pas significativement l'erreur de sous-échantillonnage finale qui reste autour de 120 nm pour le cas turbulent médian considéré. La Fig. 2.4 illustre ce point.

Ces résultats sont cependant encore à confirmer vis-à-vis de la mesure effective des modes appliqués par ces actionneurs de la part d'un analyseur

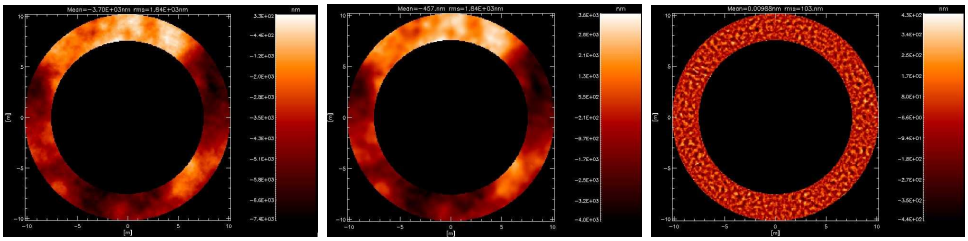

FIGURE 2.4: Exemples de distribution spatiale de l'erreur de sous-échantillonnage pour un modèle réduit du miroir M4 pour l'ELT. De gauche à droite : front d'onde d'entrée résultant de la perturbation atmosphérique, forme du miroir correcteur après application de ses modes et front d'onde corrigé en résultant.

pyramidal (intégration en cours), notamment, et comme précisé plus haut, en raison de la présence des bords des différents pétales du miroir. Le troisième point sera abordé plus avant et demandera possiblement l'intervention d'une loi de commande ad hoc dont les contours sont encore à préciser.

2.4.2 *Numerical modeling and simulation study for the M4 adaptive mirror of the E-ELT*

La communication suivante, présentée à la conférence « Adaptive Optics Systems III » lors de la meta-conférence bi-annuelle « Astronomical Telescopes and Instrumentation » de la SPIE, à Amsterdam en juin 2012, recueille les résultats obtenus jusqu'alors concernant les études numériques effectuées dans le cadre du miroir adaptatif M4 pour l'E-ELT et introduites ci-avant.

L'erreur de sous-échantillonnage spatial y est notamment déterminée pour les conditions de turbulence atmosphériques médianes du site, selon différentes stratégies de calcul. La nécessaire gestion des actionneurs de force, introduisant les notions d'actionneurs *slaves* et *masters*, y est également étudiée.

Numerical Modeling and Simulation Study for the M4 Adaptive Mirror of the E-ELT

Marcel Carbillet[a], Armando Riccardi[b], Marco Xompero[b]

[a] UMR 7293 Lagrange (Université de Nice Sophia-Antipolis/CNRS/Observatoire de la Côte d'Azur), Parc Valrose, 06108 Nice cedex 2, France;
[b] Osservatorio Astrofisico di Arcetri – Istituto Nazionale di AstroFisica, Largo Enrico Fermi 5, 50125 Firenze, Italy

ABSTRACT

We report in this paper on the progress of numerical modeling and simulation studies of the M4 adaptive mirror, a representative of the "adaptive secondary mirrors" technology, for the European Extremely Large Telescope (E-ELT). This is based on both dedicated routines and the existing code of the `Software Package CAOS`. The points approached are basically the specific problems encountered with this particular type of voice-coil adaptive mirrors on the E-ELT: ($\star$) the segmentation of the adaptive mirror, implying a fitting error due also to the edges of its six petals, as well as possible co-phasing problems to be evaluated in terms of interaction with the wavefront sensor (a pyramid here) ; ($\star\star$) the necessary presence of "master" and "slave" actuators which management, in terms of wavefront reconstruction, implies to consider different strategies. The on-going work being performed for the two above points is described in details, and some preliminary results are given.

Keywords: Adaptive Secondary Mirrors, E-ELT, Numerical Simulations, CAOS

1. FITTING ERROR PERFORMANCE

The adaptive mirror M4 of the European Extremely Large Telescope (E-ELT)[1] being a segmented mirror, it induces a priori both co-phasing error and fitting error. The best-fitting mirror shape is, with respect to the atmospherically-perturbed entrance wavefront, the curve that provides the smaller *rms* between the real shell shape and the desired one. The residual between the best-fitting shape of the mirror and the desired one can be defined as its fitting error. With this definition, the possible local jump at the edge of the segments is considered as part of the fitting error. The present fitting error analysis makes direct use of the influence functions (IF) simulated by an ad hoc finite-elements analysis (FEA) model provided by A.D.S. International s.r.l (Lecco, Italy).

Because the M4 mirror (represented by the black line in Fig. 1) is not the pupil of the telescope, the AO correction for a given direction towards the sky is performed by a subset of actuators (within green circle in Fig. 1 again). For sake of clarity the present work will analyze only the on-axis case (which correspond to the red circle in Fig. 1).

Because the M4 physical mirror is circular with regular triangular actuator pattern over its surface, the projection over the beam section is elliptical with a slightly different density between the x-axis and the y-axis. Moreover, because the available FEA for the M4 IFs have been provided for the old 42m-diameter E-ELT, the current 37m-diameter configuration (largest totally inscribed diameter over the M1 segment map) provides an excess of out-of-pupil actuators on the outer edge and a defect of actuators around the central hole. Let us finally note that we have considered here the same physical inter-actuator distance as the old M4 design (31.5 mm).

1.1 Atmospherically Perturbed Wave-Front Modeling

The atmospherically-perturbed wavefronts considered here are modeled by means of the `Software Package CAOS`,[2] developed within the `CAOS problem-solving environment` (`PSE`[3, 4]) with the main physical and numerical parameters reported in Table 1. The number of sub-harmonics added (three) is sufficient in this case (see Carbillet & Riccardi, 2010,[5] for details about sub-harmonics adding). Figure 2 shows the structure function obtained from 10000 wavefronts used for our simulations (black dots), showing a very good behavior with respect to theory (red line).

Further author information: (Send correspondence to M.C.): `marcel.carbillet@unice.fr`.

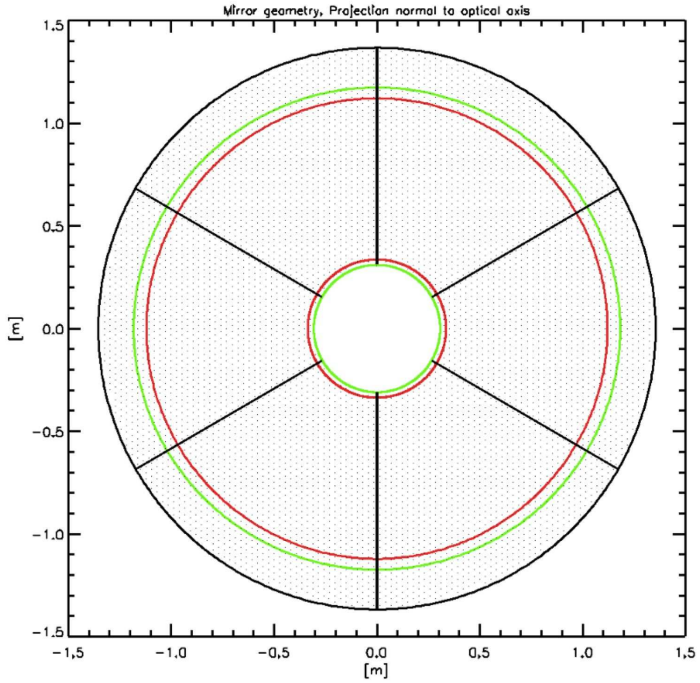

Figure 1. M4 geometry.

turbulent atmosphere parameters	
seeing (at 500 nm)	0.″85
⇒ Fried parameter r_0 (at 500 nm)	∼12.1 cm
number of turbulent layers considered	2
0 km-layer C_N^2 profile relative percentage	60%
10 km-layer C_N^2 profile relative percentage	40%
wavefront outer-scale $\mathcal{L}_0$	50 m
number of sub-harmonics added	3
telescope parameters	
mechanical projected outer diameter	42 m ≡ 512 px
optical projected outer diameter	37 m ≡ 476 px
optical projected inner diameter	11.1 m

Table 1. Main simulation parameters.

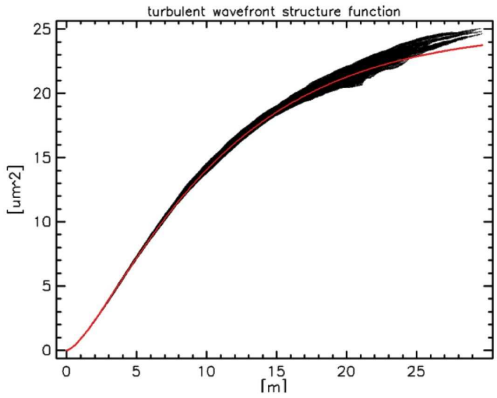

Figure 2. Structure function obtained for 10000 wavefronts used for the simulations presented in this paper (black dots), compared with the theoretical one (red line).

1.2 Actuator Management & Wave-Front Reconstruction

1.2.1 Masters and Slaves

Because of the on-axis projection of the pupil over mirror M4 (both smaller and elliptical), at least two classes of actuators have to be defined. We call "masters" the subset of them which have a significant contribution inside the pupil footprint, while the rest of them are called "slaves". The idea behind this classification is to avoid the possible introduction of sharp glass bending at the edge of the pupil (and subsequent excess of actuator forces) when controlling the whole set of modes deduced from the whole set of actuators for this particular type of voice-coil adaptive mirrors (the so-called "adaptive secondary mirrors", ASM[6]). Avoiding to control the modes induced by the slaves should permit to avoid this problem of excess of actuator forces.

The classification between masters and slaves is made by considering the corresponding IF contribution inside the pupil footprint, defined as the IF peak-to-valley inside the pupil footprint with respect to the IF value on the actuator location. Below a given threshold, the actuator is considered as a slave, and otherwise as a master. A large threshold should make lowering the number of masters, hence the number of modes corrected, and hence the fitting error performance. A small threshold, at the contrary, should make further actuators outside the edge trying to fit the wavefront disturbance inside the pupil with small correction but large expected force contribution. A threshold value of 0.8 has been found to be a satisfactory trade-off. Hence 4326 actuators over 6306 (6 petals of 1051 actuators each) are found to be masters, and the rest of them (1980) slaves.

1.2.2 Actuator Management/Wave-Front Reconstruction Strategies

Then two simple strategies can be considered:

- ⋆ the slaves do not apply any force, and hence just follow the global mirror shape produced by the masters only (see Riccardi, 2012,[7] for the relationship between master and slave position commands in this case).
- ⋆⋆ the slaves are forced to actuate the modes induced by the masters, and hence should help better correcting the input atmospherically-perturbed wavefronts, extrapolating a smooth shape of the shell outside the pupil.

We call the first case described above the "unforced-slaves" case, oppositely to the "forced-slaves" case. For sake of comparison, we also consider in our simulations the case, unfortunately impossible because of the applied forces that it would imply, where all the 6306 actuators are masters. The trend expected is that the performance, in terms of wavefront residuals *rms*, is larger in the unforced-slaves case than in the ideal all-masters one. But the forced-slaves case is expected to give a result closer to the latter.

1.3 Simulation Strategies & Some Preliminary Results

1.3.1 Numerical Simulation Strategies

In order to compare the two "masters and slaves" strategies between them and with respect to the ideal all-masters case, we compute the resulting mean fitting error over a set of 1000 to 10000 statically independent wavefronts with the physical and numerical parameters defined in Table 1. In addition, three simulation strategies are contemplated:

- ⋆ the fitting error is computed petal per petal, maintaining reasonable dimensions of arrays to manipulate and hence rapid times of execution.
- ⋆⋆ the fitting error is computed for the whole pupil at once, permitting to assess the previous result and prepare further simulations which will include an actual wavefront sensor for which the pupil must be seen as a whole.
- ⋆⋆⋆ the fitting error is computed on a subset of the whole pupil, i.e. a ring of it, in order to test this reduced model for the above cited simulations involving an actual wavefront sensor while attempting to avoid the huge amount of memory and computational time necessary for them.

The "whole-pupil" simulation strategy considers the whole set of 6306 actuators, from which 4326 masters. The "petal-per-petal" strategy consecutively deals with six petals of 1051 actuators, with an average of 721 masters per petal. The "reduced-ring" strategy considers a comparable number of masters: 734 here. A different reconstructor must be computed for each of the three actuator management cases (all-masters, unforced-slaves, and forced-slaves) and the three simulation strategies (whole-pupil, petal-per-petal, and reduced-ring).

For the whole-pupil simulation strategy the time (with an 8 dual core Opteron machine mounted with 48 GB of memory) involved for computing the reconstructor is ∼12 h, while tens of minutes for the two other simulation strategies. For all the three strategies, a few seconds or tens of seconds are then necessary for each iteration (for each independent wavefront to be projected onto the modal basis once the reconstructor is computed).

1.3.2 Preliminary Results

The left part of Fig. 3 shows the mean map of the residual *rms* wavefront inside the on-axis projection of the pupil, for the petal-per-petal case. Average (in quadrature) value is 120 nm rms and maximum value is ∼220 nm over the junctions between the petals. The middle part of Fig. 3 is the corresponding mean map of full-area mirror positions peak-to-valley. Maximum value is ∼1.6 μm adn is located outside the on-axis projection of the pupil due to the extrapolation on the slave actuators of the in-pupil shape generated by the master actuators. And the right part of Fig. 3 is the corresponding full-area mean map of absolute forces applied. Maximum value is 1.9 N. It can be noted that the slave actuators have here zero forces. We have not simulated here any clipping mechanism of the forces to reduce the force peak.

Figure 4, left part, represents the mean map of the residual *rms* wavefront for the whole-pupil case, while the right part of the same Figure is the mean map of the residual *rms* wavefront for the reduced-ring case. This two *rms* maps are to be compared with the one presented before in Fig. 3.

1.3.3 Discussion

The few *rms* values reported in Table 2 give a number of valuable informations. First of all, ∼120.4 nm is the quantity that indicates the fitting error expected for M4 for a median seeing of 0.″85, for the worse expected reconstruction strategy: the unforced-slaves one, confirmed by the convergence of both the whole-pupil and the petal-per-petal simulation strategies. This has anyway to be refined with a large number of independent realizations for the whole-pupil strategy.

A second important point is that the reduced-ring simulation strategy seems to converge as well to this performance number, indicating that it would be suitable for further simulation studies where the petal-per-petal strategy is not possible and the whole-pupil strategy would be extremely time consuming. This will be the case when considering a real wavefront sensor instead of an ideal one like we have done within this section.

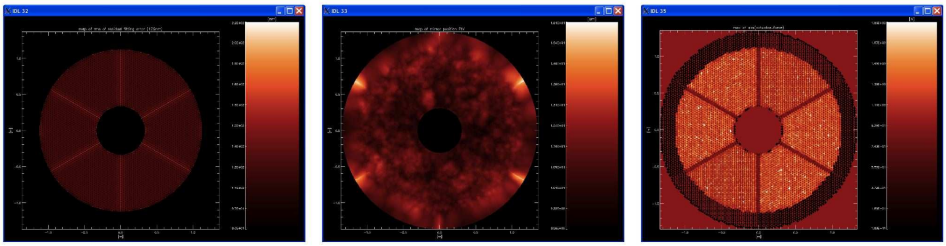

Figure 3. *rms* Results from the petal-per-petal simulation strategy code. From left to right: mean map of the residual *rms* wavefront ; corresponding mean map of mirror positions peak-to-valley ; corresponding mean map of absolute forces applied.

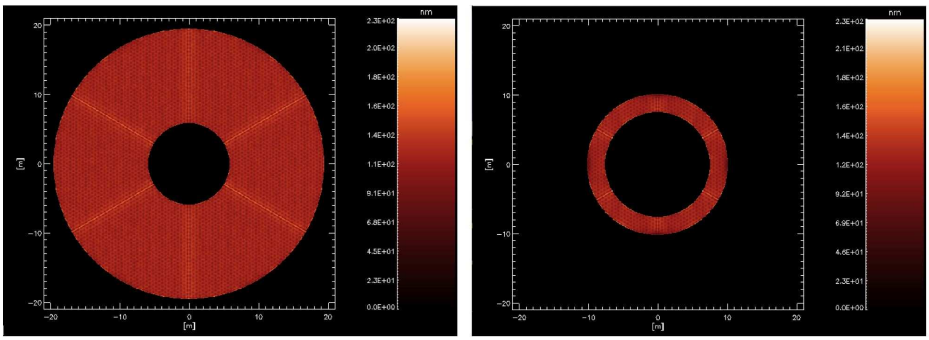

Figure 4. *rms* Mean map of the residual *rms* wavefront. From left to right: from the whole-pupil simulation strategy code ; from the reduced-ring simulation strategy code.

petal per petal (10000 wf)	whole pupil (1000 wf)	reduced ring (10000 wf)
∼120.2 nm	∼120.4 nm	∼120.5 nm

Table 2. Mean *rms* value obtained for the three simulation strategies used.

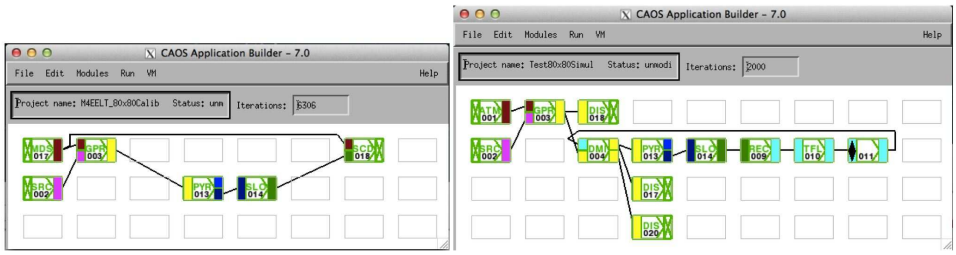

Figure 5. Complete numerical modeling including a pyramid wavefront sensor, within the `CAOS PSE` and by using the modules of the `Software Package CAOS`. From left to right: modeling of the whole AO system calibration ; modeling of the whole AO system running.

The optical design of the telescope has very recently evolved. Previous simulations, made in the framework of the 42m-diameter configuration, clearly indicated that by forcing the slaves it is possible to lose some nanometers on the residual fitting error with respect to not forcing them at all, in order to get as close as possible to the all-masters case. The numbers obtained where **117.9 nm** for the all-masters case, **120.4 nm** for the unforced-slaves case, and **118.2 nm** for the forced-slaves case. Given the similarity with the performance found with the present unforced-slaves case, we expect to find roughly the same performance with the new optical design.

The problem encountered here is clearly the forces applied to the actuators, which have to be limited. With the new optical design, we need to precisely define which actuator is a *forced* slave or an *unforced* slave, rather than considering the whole set of slaves as "forced" or "unforced". In fact, a number of them are actually too far from the pupil footprint and this implies a bad numerical inversion when projecting the input wavefronts onto the IF basis. The final optimal solution will probably imply a classification of the actuators in three classes, optimizing the fitting error.

2. COMPLETE MODELING FEAT. THE PYRAMID WAVE-FRONT SENSOR

After assessing the reduced-ring approach in the previous section, we now know that we will be able to tackle the problem of simulating the performance of M4 with a real wavefront sensor (or at least not an ideal one) with reasonable computation times. In fact, the computing time necessary when dealing with the whole-pupil simulations is for example 9–10 days for the calibration step of the AO system.

Figure 5, left part, shows the numerical simulation/modeling of the whole AO system calibration within the `CAOS PSE` and by using the modules of the `Software Package CAOS`, while the figure on the right shows the numerical simulation/modeling of the AO system running, where the atmospherically-perturbed wavefronts (from module `ATM`) are propagated to the pupil (thanks to module `GPR`), then corrected by the M4 mirror (within module `DMI`). The corrected wavefronts are then measured by modules `PYR` (simulating the pyramid wavefront sensor) and module `SLO` (which evaluates the slopes from the four sub-images of the pyramid). The wavefront reconstruction is then made by module `REC`, and a time-filtering (classically a pure integrator) is applied by module `TFL`. The resulting commands are then sent to module `DMI`, closing the loop.

3. FURTHER WORK AND A FINAL REMARK

Further work will include, first of all, a complete resuming of the simulations performed until now with the IFs established from the FEA corresponding to the current 37m-diameter configuration. The definition of the three classes of actuators (rather than only two with the previous 42m-diameter configuration) will then be performed in the framework of an optimization of the M4 fitting error.

After these two steps concerning the fundamental issue of detailed fitting error analysis, we will be able to tackle with the complete numerical modeling, via the reduced-ring model after re-assessment of it with respect to the whole-pupil model. A more refined definition of the modes of M4 will also probably be advantageous, with

respect to considering the set of modes coming as is from the pseudo-inverse calculus made during the wavefront reconstruction phase.

This study is being performed using the freely distributed `Software Package CAOS`, developed within the `CAOS problem-solving environment (PSE)`. See `http://lagrange.oca.eu/caos` for more details about the whole `CAOS` PSE.

REFERENCES

[1] É. Vernet, N. Hubin, M. Mueller, R. Biasi, D. Galieni, this conference (2012).

[2] M. Carbillet, C. Vérinaud, B. Femenía, A. Riccardi, L. Fini, *Mon. Not. R. Astron. Soc.* **356** (4), 1263 (2005).

[3] M. Carbillet, C. Vérinaud, M. Guarracino, L. Fini, O. Lardière, B. Le Roux, A. T. Puglisi, B. Femenía, A. Riccardi, B. Anconelli, M. Bertero, P. Boccacci, in *Advancements in Adaptive Optics*, D Bonaccini, B. Ellerbroek, & R. Ragazzoni Eds., *SPIE* Proc. **5490** (2), 550 (2004).

[4] M. Carbillet, G. Desiderà, E. Augier, A. La Camera, A. Riccardi, A. Boccaletti, L. Jolissaint, D. Ab Kadir, in *Adaptive Optics Systems II*, B. L. Ellerbroek, M. Hart, N. Hubin, & P. L. Wizinowich, Eds., *SPIE Proc.* **7736**, 773644 (2010).

[5] M. Carbillet. & A. Riccardi, App. Opt. **49** (31), G47 (2010).

[6] A. Riccardi, M. Xompero, D. Zanotti, L. Busoni, C. Del Vecchio, P. Salinari, P. Ranfagni, G. Brusa Zappellini, R. Biasi, M. Andrighettoni, D. Gallieni, E. Anaclerio, H. M. Martin, S. M. Miller, in *Adaptive Optics Systems*, N. Hubin, C. Max, & P. L. Winizowich Eds., *SPIE Proc.* **7015**, 12 (2008).

[7] A. Riccardi, *Arcetri Technical Report* **1-2012**, `http://www.arcetri.astro.it/pubblicazioni/Reports/12/1_12.html` (2012).

2.5 Systèmes complets

Remarquons tout-de-suite que quand on parle ici de *système complet*, il s'agit (pour bien faire) de considérer le système atmosphère⊕télescope⊕système d'OA, d'autant plus que les systèmes d'OA sont de plus en plus pensés comme une partie intégrante du télescope (dès sa conception) et que le choix-même de sa situation géographique (au télescope toujours) découle directement des études de site, et donc de l'atmosphère turbulente qui y règne.

L'étude numérique détaillée d'un système complet requiert donc une modélisation physique de chacun des composants impliqués, et dont les principaux, à part la partie commande/contrôle, ont fait l'objet d'études spécifiques dans les sections précédentes.

Nous allons voir à la sous-section suivante une étude complète concernant FLAO, étude exécutée au début de la construction du système en 2004. Ce système délivrera quelques années plus tard (en 2010) ses premiers résultats sur le ciel, résultats somme toute très proches des prévisions de l'étude présentée.

Nous allons ensuite imprudemment soulever le couvercle de la boîte de Pandore, en tentant une comparaison (ou un mariage possible) entre l'approche analytique « à la `PAOLA` » et celle end-to-end « à la `CAOS` ». Cette section sur les études de systèmes complets sera ensuite clôturée par un autre exemple d'application : celui du très particulier cas du site du Dôme C en Antarctique.

2.5.1 *Numerical simulation studies for the first-light adaptive optics system of the Large Binocular Telescope*

La communication suivante a été présentée à la conférence « Advancements in Adaptive Optics » lors de la meta-conférence bi-annuelle SPIE « Astronomical Telescopes and Instrumentation » à Glasgow en juin 2004. Elle contient des résultats d'évaluation de performance détaillés du système d'OA de première lumière du LBT (alors encore appelé WLBT, maintenant FLAO), dans les bandes de V à K en termes de rapports de Strehl, puis en termes plus scientifiquement parlant pour d'une part l'instrument LUCIFER dans le proche infrarouge (rapports signal-à-bruit et magnitudes limites attendus, dans le cas photométrique comme spectroscopique) et pour d'autre part l'instrumentation visible prévue alors en termes d'énergie encerclée.

Cet article fait suite à celui de 2003 [62] dont il a déjà été question à la Sous-sec. 2.3.1 à propos de la comparaison entre pyramide et SH.

Numerical simulation studies for the first-light adaptive optics system of the Large Binocular Telescope

Marcel Carbillet*, Armando Riccardi, Simone Esposito

INAF – Osservatorio Astrofisico di Arcetri (OAA), largo E. Fermi 5, 50125 Firenze, Italy

[marcel@arcetri.astro.it | riccardi@arcetri.astro.it | esposito@arcetri.astro.it]

ABSTRACT

We present our latest results concerning the simulation studies performed for the first-light adaptive optics (AO) system of the Large Binocular Telescope (LBT), namely WLBT. After a brief description of the "raw" performance evaluation results, in terms of Strehl ratios attained in the various considered bands (from V to K), we focus on the "scientific" performance that will be obtained when considering the subsequent instrumentation that will benefit from the correction given by the AO system WLBT and the adaptive secondary mirrors LBT 672. In particular, we discuss the performance of the coupling with the instrument LUCIFER, working at near-infrared bands, in terms of signal-to-noise values and limiting magnitudes, and in both the cases of spectroscopy and photometric detection. We also give the encircled energies that are expected in the visible bands, result relevant in one hand for the instrument PEPSI, and in other hand for the "technical viewer" that will be on board the WLBT system itself.

Keywords: Large Binocular Telescope, first-light adaptive optics system, performance evaluation

1. INTRODUCTION

The first-light adaptive optics (AO) system of the Large Binocular Telescope (LBT) is foreseen to operate at the end of 2004. It is a part of the acquisition, guiding and wavefront sensing (AGW) unit of LBT, and it is named WLBT. A complete description of the system is given in Esposito et al.,[3] while the LBT 672 adaptive secondary mirror features are described in Riccardi et al.[6] In this paper we focus on the latest numerical studies we have made in order to evaluate the performance of the whole system.

Those are given first in terms of Strehl ratios in the whole set of bands considered (from V to K), taking into account for the bands R and I to distribute 50% of the light between the wave-front sensor (working between 600 and 900 nm) and the scientific instrument. These "raw" results are given together with the optimal values found for the ensemble of system parameters (sensor configuration, exposure time, number of LBT 672 modes controlled, pyramid modulation) corresponding to each AO guide-star R-magnitude considered.

We have then computed the encircled energies that result from the point-spread functions (PSFs) obtained in each band and for each AO guide-star R-magnitude, showing the great improvement that can be obtained even at short wavelengths (hence relevant to the instrument PEPSI and the "technical viewer" foreseen on board the WLBT system itself).

Finally, we go in more details for the near-infrared performance, i.e. for what concerns the WLBT+LUCIFER performance, both in terms of photometric detection and spectroscopy. For this, we have computed the limiting magnitudes that are reached when considering a given signal-to-noise (SNR), namely 3, a given time exposure (1800 s), and a given spectral resolution.

The paper is hence organized as follows. In Sec. 2 we describe the numerical simulations performed by using the Software Package CAOS, while in Sec. 3 we expose the "raw" performance obtained for the system in terms of Strehl ratios in the whole ensemble of bands considered, together with the resulting optimized WLBT system parameters. Section 4 is then dedicated to the coupling of the WLBT system with the subsequent scientific instrumentation, namely LUCIFER (near-infrared bands), PEPSI (visible bands), and the "technical viewer" intended to work at the sensing wavelength. Finally, we give our conclusions in Sec. 5.

* On move from OAA to Laboratoire Universitaire d'Astrophysique de Nice, UMR 6525, Université de Nice–Sophia Antipolis, Parc Valrose, 06108 Nice Cedex 02, France – Correspondance e-mail: marcel.carbillet@unice.fr

2. SIMULATING THE WLBT SYSTEM WITH CAOS

The "Code for Adaptive Optics Systems"

The simulation tool used for the simulations presented here is the CAOS "system" (where CAOS stands fro Code for Adaptive Optics Systems). It is essentially composed of *Software Packages*, among them the original Software Package CAOS dedicated to AO systems modeling,[1] designed to be used within a graphical programming environment – the CAOS Application Builder[4,5] where the data flow and the parameters of each module can be set.

The structure of this numerical tool being modular, each physical elementary process of a given simulation is modeled within a specific module – like, in the AO case, the turbulence in each atmospheric layer, the propagation of the light from a source to the observing telescope and through the turbulent layers, the wavefront sensing, the wavefront reconstruction, time-filtering of the resulting deformable mirror commands, the wavefront correction, etc. Taking advantage from the CAOS Application Builder, a simulation can be built putting and connecting together the required occurrences of the desired modules, respecting the only logical constraint given by their formalized type of input/output. Each module comes with an individual GUI in order to set its own physical and numerical parameters, during the design step of a simulation or independently in a later moment. The whole structure of a simulation can be saved as a "project" that can be restored for later modifications and/or parameters upgrading. The IDL code, corresponding to the designed simulation, is written down during the saving of a project, and it can possibly be modified "by hand" in order to be completed with some additional task not provided by strictly using the Software Package CAOS.

More detailed informations about this numerical simulation tool and the already developed associated packages can be found from the dedicated web-site `http://www.arcetri.astro.it/caos`, and from the companion communication within these proceedings.[2]

Simulation procedure followed

Figure 1 shows the simulation procedure followed, within the CAOS Application Builder and using the modules of the Software Package CAOS, for simulating the WLBT system and the resulting PSF morphology for the various wavelength bands and off-axis values considered here.

The output of the module `ATM` simulating the atmosphere (made of two moving turbulent layers) is sent to module `ATA` that mimics the correction due to the deformable mirror (the adaptive secondary mirror LBT 672 in our case) into a "correction" layer (here conjugated to the ground). The resulting corrected wavefront is then computed by the module `GPR` that basically propagates the light between the guide star defined within module `SRC` and the telescope which characteristics are set by using the GUI of `GPR`. The resulting corrected wavefront is then taken into account by module `PYR` that simulates the behavior of the pyramid wavefront sensor, and the resulting signals are then sent to a slope calculator (`SLO`) that compute the slopes corresponding to each subaperture of the pyramid wavefront sensor, before sending the result to the wavefront reconstructor `RCC` that reconstruct the wavefront by using the LBT 672 computed modes. The loop is then closed by a special module (part of the Application Builder) that send the result to previously evoked module `ATA`. During each step of the simulation the resulting PSFs are computed within the occurrences of module `IMG` in the Johnson bands V, R, I, J, H, and K. These PSFs are here calculated with no background nor noise contributions in order to be used latter varying the object magnitude, time-exposures, and noise contributions (see next section). Note that, instead, the on-axis star (occurrence `#003` of module `SRC` in the figure) magnitude is fixed as it is also the AO guide star considered, and the series of system parameters are being varied accordingly in order to find the optimum set of them permitting the best AO correction.

A quite noticeable remark is that each process is simulated as close as possible to the real-life situation. For example the pyramid sensor, in which diffraction effects play a certain role on the performance of the system, is simulated following the following scheme: the electric field in the image plane is masked for each facet of the pyramid, resulting after diffraction computation in the four-pupil image of Fig. 1. The pyramid can also be simulated by simulating the pyramid as a phase mask. Still for the pyramid, we here consider a standard CCD device, but we could also consider an low-light-level CCD, for which the photon noise is not anymore Poisson-like, and an "exotic" dark current component has to be taken into account.

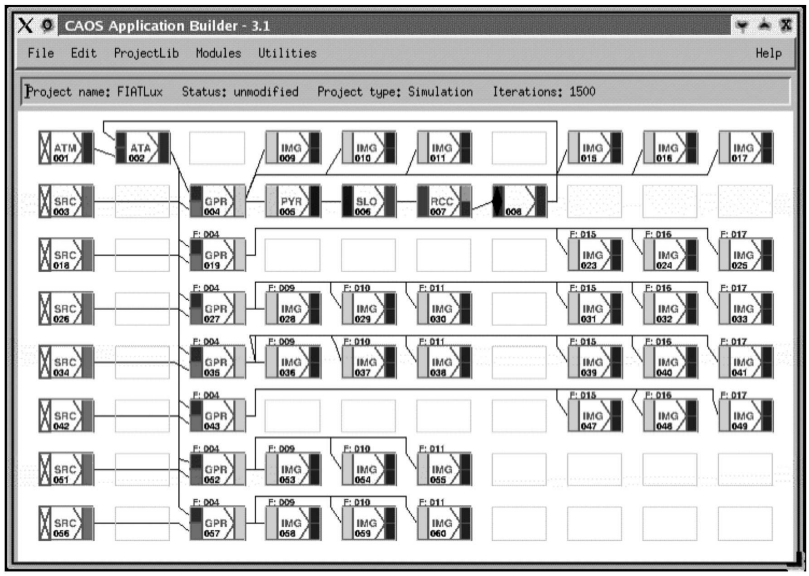

Figure 1. Simulation procedure followed for simulating the WLBT system by means of the CAOS Application Builder and the Software Package CAOS. The different occurrences of module `SRC` correspond to different off-axis values considered for the observed object, while the different occurrences of module `IMG` correspond to the various imaging bands considered (V,R,I,J,H,K) for each of the object off-axis values.

We have designed this typical simulation for the different configurations of the wavefront sensor and ran it for a wide range of parameters defining each consecutive process of the whole simulation, exploring so the hyper-space of parameters as extensively as possible, and finally finding the set of optimum values.

3. WLBT SYSTEM "RAW" PERFORMANCE EVALUATION

The performance of the WLBT system have been evaluated following the procedure exposed in previous section. The main parameters associated with this wide series of simulations are reported in Table 1, but concerning the read-out noise (RON) values corresponding to the CCD adopted, which are reported in Table 2.

The hyper-space of free parameters has been explored by different simulation realizations, and the result in terms of optimized system parameters is given in Table 3.

The final result is given in Fig. 2, in terms of terms of Strehl ratios in the various Johnson bands considered, namely V, R, I, J, H, and K. It has to be noted that while the light is well separated for the near-infrared bands (J,H,K), it has to be splitted between the wavefront sensor (working between 600 and 900 nm – basically band R and a part of band I) and the scientific channel for the visible bands R and I, while for band V the situation is equivalent to the near-infrared wavelength bands. As a consequence, the wavefront sensing more suffers from photon starving in the bands R and I (in addition to the poorer correction from the AO system), and this is directly propagated in the results shown in the figure. We have chosen to split the light as follows for the bands R and I: 50% to the wavefront sensing and 50% to the scientific channel.

Table 1. Main parameters concerning the simulations made for the WLBT performance evaluation.

turbulent atmosphere parameters	
Fried parameter r_0 (at 500 nm)	15 cm
number of turbulent layers	2
ground layer velocity	∼8 m/s
ground layer C_N^2 profile relative percentage	70%
high layer velocity	∼16.5 m/s
high layer C_N^2 profile relative percentage	30%
wavefront outer-scale $\mathcal{L}_0$	20 m
telescope parameters	
effective diameter	8.22 m
obstruction ratio	0.11%
AO guide star parameters	
spectral type	K5
R-magnitude	8—17
deformable mirror parameters	
type of adaptive mirror	secondary mirror
number of actuators	672
wavefront reconstruction parameters	
number of modes reconstructed	up to 672
time filter type	pure integration
pyramid sensor parameters	
central sensing wavelength	750 nm
bandwidth	300 nm
pyramid simulation method	transmission mask
standard dark current	none
total average transmission	0.41
configurations	10×10, 15×15, 30×30
exposure time [ms]	1, 1.67, 2.5, 5, 10
RON [e^- rms]	see Table 2
point-spread function forming - visible	
imaging bands	V, R, I
off-axis angles [″]	0, 2.5, 5, 10, 15
pixel size [mas]	5
dimension [px]	251×251
point-spread function forming - near-infrared	
imaging bands	J, H, K
off-axis angles [″]	0, 5, 10, 20, 30
pixel size [mas]	15
dimension [px]	251×251

Table 2. Read-out noise values in function of the exposure time and CCD binning.

Exposure time [ms] / CCD binning → pyramid config.	10	5	2.5	1.67	1
1×1 CCD px → 30×30 sub-ap.	4.5	4.5	5.8	8.4	8.4
2×2 CCD px → 15×15 sub-ap.	3.5	4.5	4.5	5.8	8.4
3×3 CCD px → 10×10 sub-ap.	3.5	3.5	2.5	4.5	5.8

Table 3. Performance evaluation optimized parameters.

K5 star R-mag.	pyramid configuration	Δt [ms]	$\Rightarrow$ RON [e^- rms]	number of modes	pyramid mod. [λ/D]
8	30×30	1.00	$\Rightarrow$ 8.4	671	±1
9	30×30	1.00	$\Rightarrow$ 8.4	500	±1
10	30×30	1.00	$\Rightarrow$ 8.4	450	±2
11	30×30	1.67	$\Rightarrow$ 8.4	400	±2
12	15×15	1.67	$\Rightarrow$ 5.8	150	±3
13	15×15	2.50	$\Rightarrow$ 4.5	130	±3
14	15×15	2.50	$\Rightarrow$ 4.5	105	±3
15	10×10	5.00	$\Rightarrow$ 3.5	60	±4
16	10×10	5.00	$\Rightarrow$ 3.5	55	±5
17	10×10	10.00	$\Rightarrow$ 3.5	45	±6

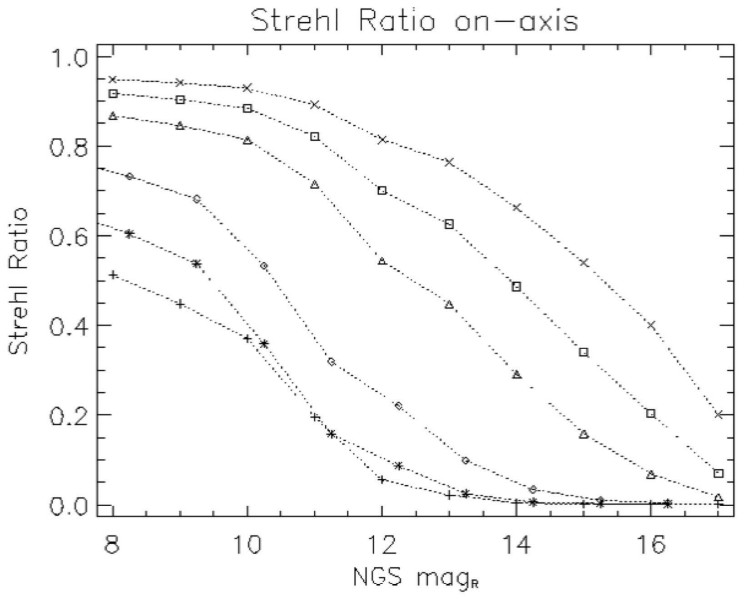

Figure 2. Strehl ratios in bands V (+), R (∗), I (rhombuses), J (triangles), H (squares), and K (×).

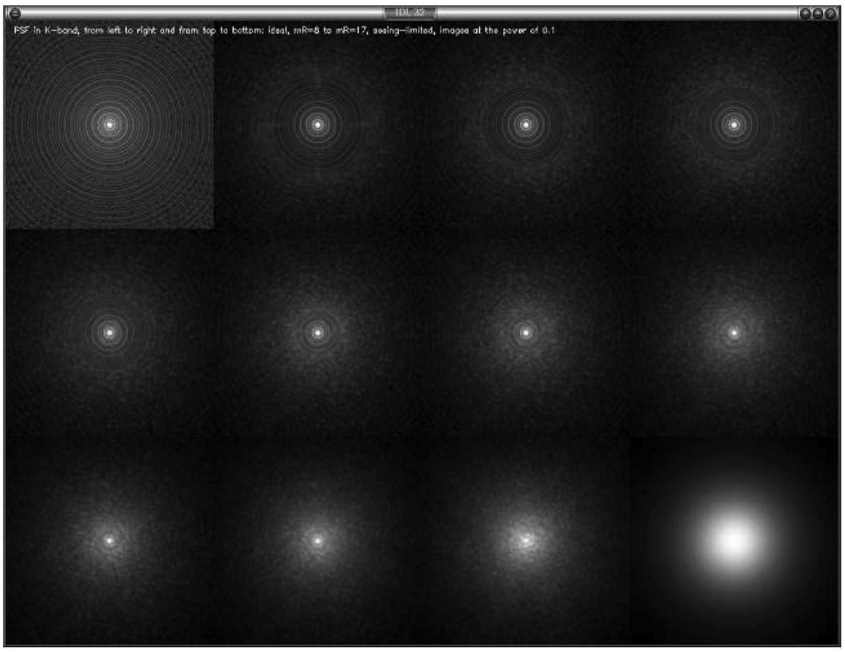

Figure 3. K-band PSFs as a function of the AO guide-star magnitude, represented at the power of 0.1 for sake of clarity. From top to bottom and from left to right: ideal case, R-magnitude cases from 8 to 17, seeing-limited case.

Figure 3 shows the K-band PSFs obtained in function of the R-magnitude of the K5 spectral type AO guide star, together with the diffraction-limited PSF (first figure in the top-left corner) and the seeing-limited one (last figure in the bottom-right corner). The corresponding AO guide star R-magnitudes (spectral type K5) are, from left to right and from top to bottom: 8, 9, 10, 11, 12, 13, 14, 15, 16, and 17.

Note the evolving shape of the resulting PSF. As classically known the Strehl ratio is decreasing with increasing of the AO guide star magnitude, because of the progressive lack of photons. Hence the optimal system parameters are also evolving, as it can be noticed from Table 3: the number of subapertures and the number of corrected modes are decreasing, while the exposure time and the pyramid modulation are increasing. Beside this Strehl ratio evolution the angular resolution is decreasing as well, even if it basically remains close to λ/D for the brightest cases. The global shape of the PSF is also strongly changing, with a speckle-ized halo which level grows with increasing of the AO guide star magnitude.

4. COUPLING WITH THE SUBSEQUENT SCIENTIFIC INSTRUMENTATION

In order to evaluate the actual performance the WLBT system will permit to the subsequent scientific instrumentation, after having completely optimized the AO system parameters for the median atmospheric conditions considered for LBT, and computed the "clean" (no background, no noises contribution) PSF corresponding to the various bands and off-axis values defined in previous section, it is necessary here to vary the object magnitude, background, and noise contributions, corresponding to each band and to a fixed exposure time. The exposure time has been fixed to 30 min (1800 s), and the others relevant parameters are reported in Table 4.

Table 4. Image formation parameters.

band	total average efficiency	Δt [s]	RON [e^-]	dark current [e^-/s]	sky background
V	0.204	1800	0.5	0.10	21.0 mag./$''^2$
R	0.204	1800	0.5	0.10	20.0 mag./$''^2$
I	0.204	1800	0.5	0.10	19.5 mag./$''^2$
J	0.204	1800	9.0	0.05	15.0 mag./$''^2$
H	0.204	1800	9.0	0.05	12.5 mag./$''^2$
K	0.204	1800	9.0	0.05	13.5 mag./$''^2$

All the subsequent computations, in terms first of the encircled energy, but then in a more interesting way in terms of signal-to-noise and limiting magnitudes obtained, are described hereafter.

Encircled energy

We have computed the encircled energy that results from the previously described PSF simulations. The results obtained, shown in Fig. 4, are clearly depending on the morphology itself of the resulting PSFs in the various bands of interest (visible and near-infrared) and, for the bands in common with the spectral sensing range (600–900 nm), i.e. R and I, on the 50% light distribution chosen (use of a beam-splitter).

From a first evaluation, we remark that, when taking benefit from the high-angular resolution given by the WLBT system, a great gain is achievable in all bands, even the less corrected ones (visible). For example at 50 mas and observing in R-band we have a gain of ∼150 going from the seeing-limited (no AO) situation to the case of best correction (AO guide-star of R-magnitude 8), and to ∼12.5 for an AO guide-star of R-magnitude 14.

In K-band, we reach a gain from ∼50 to ∼75 for the AO guide-star from an R-magnitude of 14 to 8, considering again to look at 50 mas. More generally, it is clear from these plots that the gain is impressive especially in the bands I to K from the level of correction given by an median AO guide-star of magnitude 14.

While bands V, R, and I are particularly relevant to the instrument PEPSI and to the "technical viewer" that will be on board the WLBT itself, the near-infrared bands J, H, and K are clearly relevant to the instrument LUCIFER. Next subsection deals with the latter case.

Signal-to-noise ratio and limiting magnitudes – LUCIFER case

In this subsection we go a step forward, evaluating the limiting magnitudes both in photometric detection and spectroscopic modes, starting from a given signal-to-noise (SNR) to be attained and concentrating, for sake of conciseness, on the near-infrared wavelengths. The latter directly corresponds to the instrument LUCIFER, a spectro-imager that will work together with the WLBT system as soon as possible.

Fixing the SNR to be reached, the limiting magnitudes writes:

$$\mathrm{mag_{lim}} = -2.5 \log N/N_0 \tag{1}$$

where N_0 is the number of photons per second for a star of magnitude 0 in the band considered, and:

$$N = \frac{-b + \sqrt{b^2 - 4\,a\,c}}{2\,a}, \text{ with :} \tag{2}$$

$$a = \Delta t^2\,\rho^2, \tag{3}$$

$$b = -\mathrm{SNR}^2\,\Delta t\,\rho,$$

$$c = -n_{\mathrm{px}}\left((N_{\mathrm{bg}} + N_{\mathrm{d}})\,\Delta t + {\sigma_{\mathrm{e}}}^2\right)\,\mathrm{SNR}^2,$$

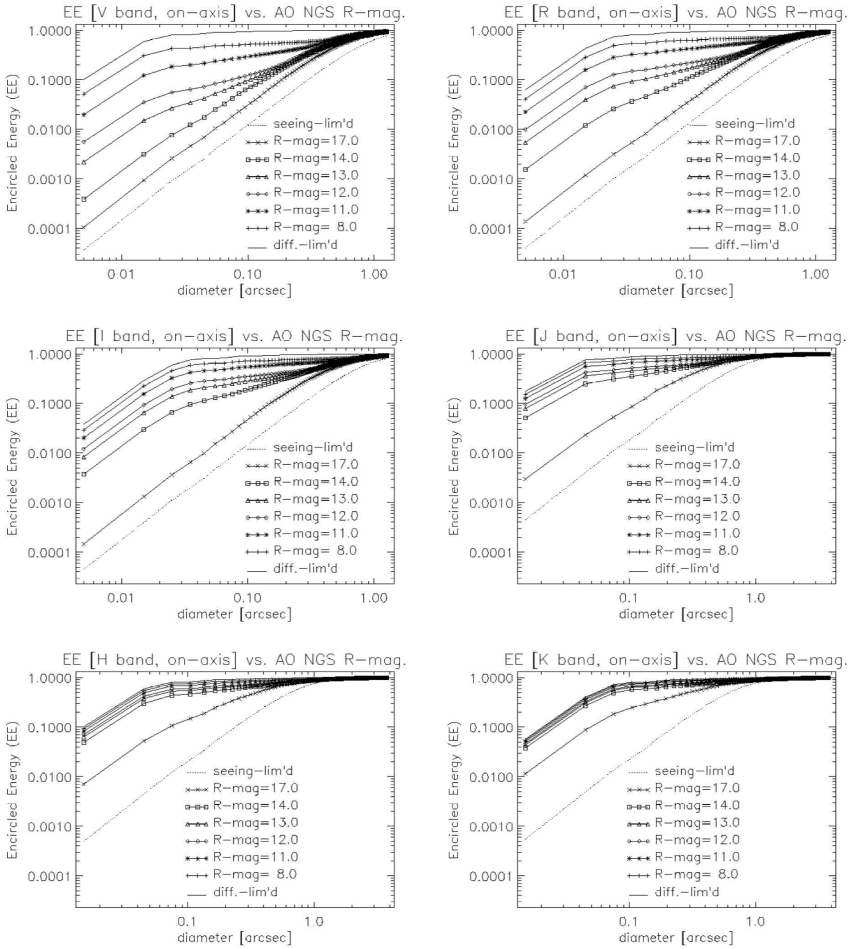

Figure 4. On-axis encircled energy in function of the observing band and the AO guide star R-magnitude. From top to bottom and from left to right: V band, R band, I band, J band, H band, K band.

and where Δt is the time exposure, ρ represents the weight due to the corrected AO-guide-star image morphology (which is consequently strongly dependent upon the off-axis angle), SNR is the signal-to-noise ratio to be attained, $n_{\rm px}$ is the number of pixels under the circular mask (photometric case) or the slit per spectral resolution element (spectroscopic case), $N_{\rm bg}$ is the number of photons per second from the sky background, $N_{\rm d}$ corresponds to the dark current noise contribution, and σ_e is the read-out-noise rms. Concerning $N_{\rm bg}$, the photons coming from the wings of the partially corrected AO guide star are also taken into account into it when considering a very close object observed (typically $0\farcs3$ here).

In Table 5 we have reported the parameters used for the limiting-magnitude calculations presented here.

Table 5. Limiting magnitudes computation parameters.

band	OH fraction	slit width	spectral resolution
J	0.93	$0.075''$	0.033 nm/slit ⇒ ∼37900
H	0.95	$0.105''$	0.060 nm/slit ⇒ ∼27500
K	0.50	$0.135''$	0.105 nm/slit ⇒ ∼21000

In practice, the coupling with the instrument LUCIFER has been studied by taking the output images obtained during the "raw" performance evaluation described in previous section, and performing a series of simulations made by varying the observed object magnitude and computing the resulting limiting magnitude considering the given exposure time and the desired SNR.

Two schemes have been then considered, reported in the following.

Photometric detection

The first scheme considered concerns the photometric detection performance. Basically, we evaluate here until which magnitude an object can be detected with a SNR of 3, a time-exposure of 1800 s, and in function of the angle separating the observed object (a star) from the AO guide-star. The obtained result are shown in Fig. 5.

A remarkable case is the one corresponding to an off-axis angle of $0\farcs3$ for which the limiting magnitude readily drops down. This is due to the morphology of the partial AO corrected image of the AO guide-star itself that is superimposed with the observed object image.

Spectroscopy

The second scheme deals with the spectroscopic performance, where a spectral resolution has been fixed (see Table 5). The result obtained are reported in Fig. 6, in terms of limiting magnitudes and optimal slit length.

5. CONCLUSION

We have reported our latest results concerning the performance evaluation of the first-light AO system of LBT, considering also here the subsequent scientific instrumentation (and especially LUCIFER). The results were given in all bands of interest (V, R, I, J, H, K) in terms of encircled energy, and detailed were given for the near-infrared wavelengths in terms of SNR and limiting magnitudes.

ACKNOWLEDGMENTS

Thanks are due to Christophe Vérinaud for the developments made for the physical modeling of the CAOS module `PYR`, that mimics the pyramid wave-front sensor, and for Bruno Femenía for the developments made for the CAOS module `IMG`, that permits to compute the resulting PSFs and images. Luca Fini is also thanked for the CAOS Application Builder maintaining, and Alfio Puglisi for the intensive computing support.

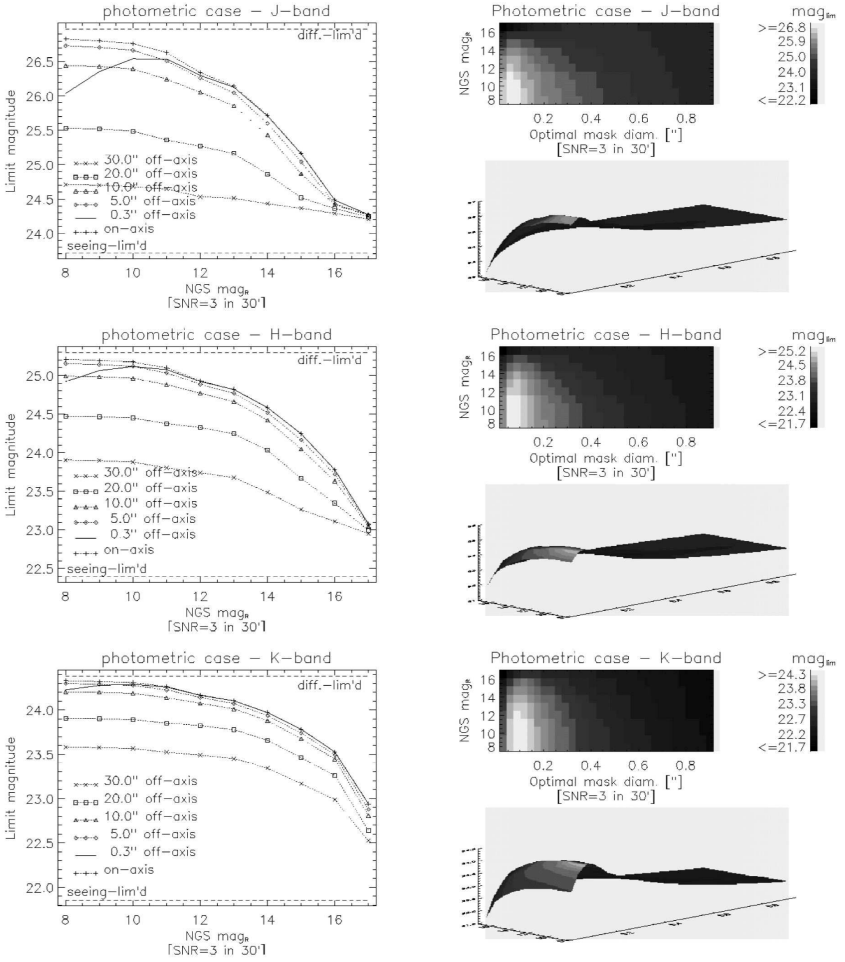

Figure 5. Photometric performance result in the bands J, H, and K, in terms of limiting magnitudes for the various off-axis angles considered (left-part plots), and in terms of optimal mask diameter (right-part plots).

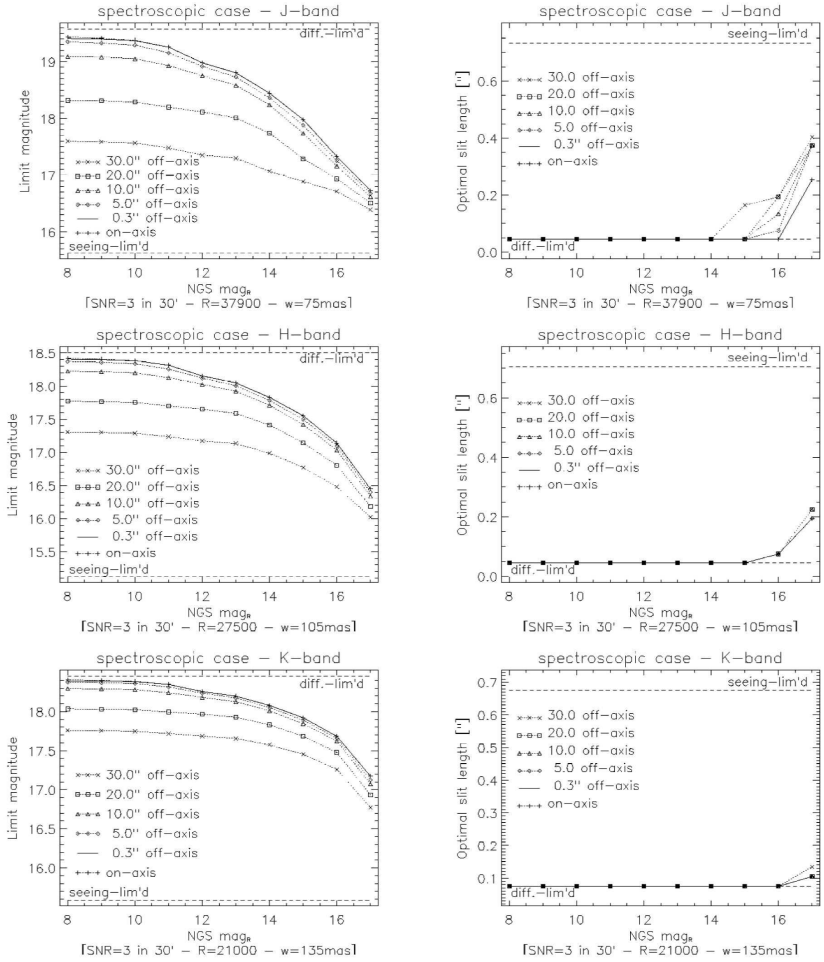

Figure 6. Spectroscopic performance result in the bands J, H, and K, in terms of limiting magnitudes for the various off-axis angles considered (left-part plots), and in terms of optimal slit length (right-part plots).

REFERENCES

1. M. Carbillet, C. Vérinaud, B. Femenía, A. Riccardi, L. Fini, submitted to MNRAS, 2004a.
2. M. Carbillet, C. Vérinaud, M. Guarracino, et al., these proceedings, 2004b.
3. S. Esposito, A. Tozzi, A. Puglisi, et al., these proceedings, 2004.
4. L. Fini, M. Carbillet, A. Riccardi, in *ASP Conf. Ser.* **238**, F. A. Primini & F. R. Harnden Eds, 253, 2001.
5. L. Fini & M. Carbillet, in *ASP Conf. Ser.* **295**, H. E. Payne, R. I. Jedrzejewski, and R. N. Hook Eds., 347, 2003.
6. A. Riccardi, G. Brusa, M. Xompero, et al., these proceedings, 2004.

2.5.2 Modélisation analytique vs. modélisation end-to-end

Ce point d'une portée plus globale concerne la comparaison entre simulations analytiques (extrêmement rapides mais issues d'une modélisation basée sur des hypothèses parfois très fortes) et simulations détaillées, basées au contraire sur une modélisation complète des phénomènes physiques mis en jeu (et donc particulièrement lentes et gourmandes en mémoire vive pour des sujets tels que les ELT, l'OA multi-références, ou la très haute dynamique).

Il s'agit en effet ici de comparer les deux approches par le biais de deux outils connus et utilisés dans la communauté astronomique : d'une part le `Software Package CAOS`, et d'autre part l'outil analytique `PAOLA` (ou sa version en cours d'intégration complète sous le `PSE CAOS`, le `Software Package PAOLAC`). Ce travail est naturellement effectué dans le but d'inter-valider les deux codes, mais également, et surtout, afin d'une part d'atténuer l'effet des hypothèses fortes de l'outil analytique en se nourrissant en partie de l'approche adoptée avec l'outil *end-to-end*, rendant ainsi l'outil analytique plus réaliste là où le besoin s'en ressent, et d'autre part, là où ceci ne sera pas possible, de trouver des compromis permettant ainsi d'affronter travaux de recherche exploratoires ou études instrumentales détaillées en combinant autant que faire se peut certitude et efficacité.

Un premier pas a déjà été effectué en ce sens, après une première phase de mise en accord des deux approches de modélisation, en testant les limites fondamentales que représentent l'erreur de sous-échantillonnage spatial et l'erreur d'anisoplanétisme (équivalente d'ailleurs dans nos tests à l'erreur due au retard temporel de la boucle). Une première comparaison de système complet « standard » sur un télescope de la classe 8 mètres a également été commencée en considérant le bruit de photon (contribuant au bruit de mesure lié à l'ASO), laissant apparaître un certain nombre de points de divergence à approfondir.

La Fig. 2.5 illustre en termes de rapport de Strehl la convergence obtenue concernant les erreurs de sous-échantillonnage spatial et d'anisoplanétisme. La Fig. 2.6 montre quant à elle le fossé restant à combler concernant la comparaison globale entre les deux approches. Les principaux paramètres physiques à la base de ces comparaisons sont les suivants : un vent de 8 m/s, un SH de 16×16 sous-ouvertures avec 8×8 px de $0''.128$ par sous-ouverture, une longueur d'onde d'analyse de 620 nm avec 245 nm de largeur de bande, pas de bruit de lecture ni de bruit de courant d'obscurité, D=8 m, modèle du miroir déformable : d=0.5 m en ce qui concerne le modèle analytique, 206 fonctions d'influence pour le modèle `CAOS` après filtrage post-pseudo-inversion de la matrice d'interaction (afin d'éliminer les modes possédant des valeurs propres en-dessous de la valeur correspondant à un conditionnement de 10), gain de la boucle (intégrateur simple) de 0.5.

Plusieurs remarques peuvent être effectuées au vu de cette différence dans l'erreur globale (voir pour les détails à ce sujet Carbillet & Jolissaint [148]), remarques qui peuvent se résumer au fait qu'une plus grande similitude des

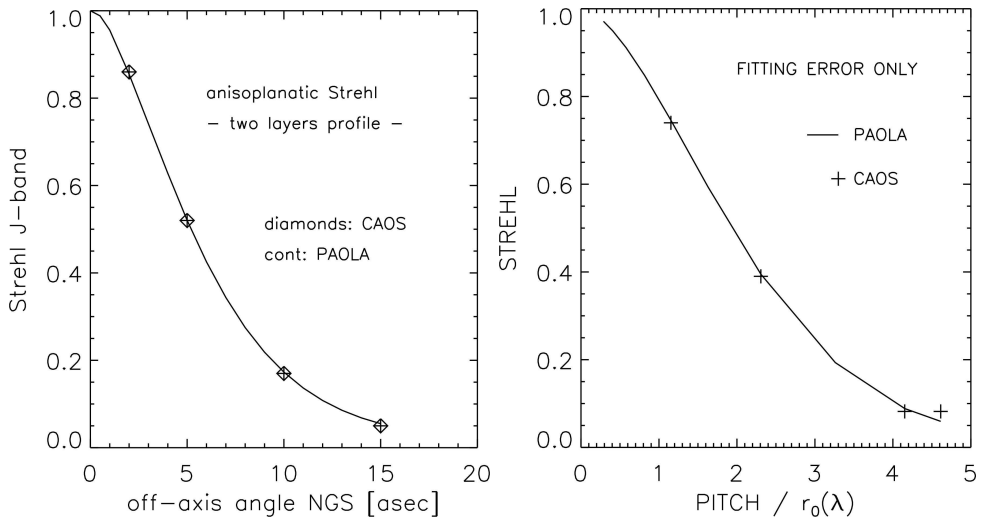

FIGURE 2.5: Premières comparaisons des modélisations analytiques et end-to-end en termes de rapport de Strehl pour un système d'OA « standard » monté sur un télescope de la classe 8 m. De gauche à droite : erreur d'anisoplanétisme, erreur de sous-échantillonnage spatial. *(Figures tirées de Carbillet & Jolissaint [148].)*

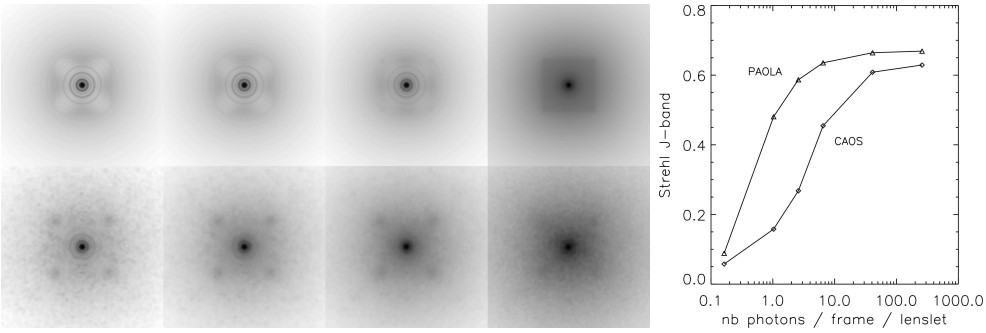

FIGURE 2.6: PSF (en haut pour `PAOLA`, en bas pour `CAOS`) obtenues pour la comparaison concernant l'erreur globale pour des magnitudes visuelles de l'étoile guide de magnitude, de gauche à droite, 14, 15, 16 et 18. À droite est également représenté la courbe résumant cette comparaison en termes de rapport de Strehl. *(Figures tirées de Carbillet & Jolissaint [148].)*

modes choisis pour le miroir déformable (l'équivalent de fonctions *sinc* sous `PAOLA`, des modèles plus proches des miroirs existants sous `CAOS`), une étude comparative plus poussée de la modélisation du bruit de mesure afin de vérifier la validité de la modélisation analytique dans certains cas limite, un plus grand échantillon de réalisations et une recherche d'optima (en termes de nombre de modes corrigés, de gain de la boucle et de temps de pose de l'ASO en fonction de la magnitude traitée) pour le modèle end-to-end, devrait amener à une meilleure correspondance et une meilleure compréhension de la complémentarité des deux approches.

2.5.3 Quelle OA pour le Dôme C ?

Cette application est la finalisation d'un travail d'exploitation des mesures de turbulence atmosphérique effectuées sur le très particulier [5] site du Dôme C en Antarctique. Cette exploitation est entendue ici du seul point de vue de l'OA et des performances en ce qui concerne l'OA grand champ [6] et, à l'autre bout de la zoologie de types de systèmes d'OA, l'OA pour la très haute dynamique.

Il s'agit ici très clairement de ne pas perdre l'opportunité d'exploiter au mieux les dernières mesures optiques provenant des campagnes de qualification de la turbulence au dessus du site du Dôme C afin d'en tirer toutes les conclusions nécessaires à l'étude ultérieure complète, du moins vis-à-vis de la turbulence atmosphérique, d'un possible futur télescope visible/proche-infrarouge à installer sur ce site si particulier (ou même d'un ensemble de télescopes interférant entre eux). Même si un tel projet est à voir dans un futur lointain, il est fondamental qu'une conclusion puisse être donnée du point de vue de l'OA au regard de l'ensemble des mesures atmosphériques qui ont été effectuées sur le site et desquelles il faut donc tirer la substantifique moelle.

La Fig. 2.7 montre des résultats publiés en 2010 [128] mais basés sur un profil médian de la turbulence [116] ne décrivant pas de manière suffisamment satisfaisante la bi-modalité depuis démontrée de la distribution du seeing au Dôme C [117]. Ceci étant, des informations intéressantes s'en dégagent déjà. L'on considère ici un système de GLAO avec champ de vue pour l'analyse de surface d'onde de $15'$ de diamètre et trois étoiles guides régulièrement distribuées sur un cercle. La stabilité de la réponse impulsionnelle est ici très claire, avec un rapport de Strehl en bande J ($1.25\,\mu$m) autour de 0.3 et une largeur à mi-hauteur de la PSF bien en-dessous de celle limitée par le seeing. La comparaison avec la valeur limitée par le seeing hors-couche-limite ($\sim 0''.3$) amène à conclure qu'un système GLAO, même à seulement 8 mètres du sol, permet de meilleures observations. Ceci, car le système aura de toute façon tendance à corriger non seulement la couche limite (bien qu'imparfaitement

5. Du point de vue géographique et climatologique, mais aussi et surtout ici du point de vue de la distribution verticale de la turbulence optique de son atmosphère.

6. A priori ici de type « couche limite » – Ground-Layer AO (GLAO) en anglais.

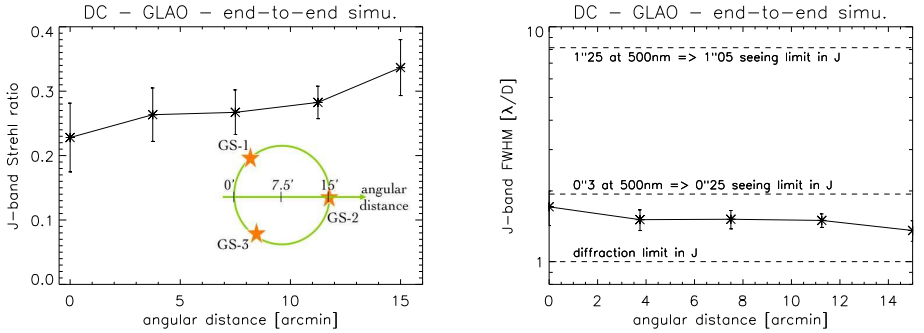

FIGURE 2.7: Résultats des simulations end-to-end pour un système de GLAO sur un télescope de 2 m au Dôme C, en termes de rapport de Strehl et de largeur à mi-hauteur en bande J. La géométrie de l'astérisme constitué des trois étoiles guides du système de GLAO considéré y est également représentée. *(Figures tirées de Carbillet et al. [128].)*

bien entendu), mais également les modes de plus bas ordres des couches hautes, puisque les bas ordres restent spatialement corrélés sur un champ plus grand que les hauts ordres.

Étant donnée la bi-modalité de la distribution du seeing, le vrai facteur discriminant est cependant celui du pourcentage de temps que le télescope étudié passera à l'intérieur ou complètement en dehors de la couche limite.

S'appuyant sur les mesures statistiques concernant la hauteur de cette couche limite [117], puis enfin sur les nouvelles mesures permettant une résolution en altitude bien supérieure et une meilleure statistique (mesures PML [7] depuis 2011 d'une part, avec une résolution de 100 m en altitude [160], mesures SSS [8] en 2006 et 2011 d'autre part, avec une résolution de 500 m [150]), une conclusion doit être donnée qui indique les conditions de fonctionnement optimal d'un système d'OA installé sur le site – hauteur de la tour recevant le télescope, pourcentage de temps dédié à l'astronomie grand champ et performances correspondantes, etc.

Notons finalement qu'étant donné le coût en calcul nécessaire à l'accomplissement exclusif de simulations de type end-to-end lorsqu'il s'agit de grand champ, un compromis entre modélisation end-to-end et modélisation analytique devra ici aussi être trouvé – ce qui entre incidemment aussi dans le cadre précédemment décrit de comparaison entre approche analytique « à la `PAOLA` » et approche end-to-end « à la `CAOS` ».

7. *Profiler of Moon Limb.*
8. *Single Star Scidar.*

2.6 Conclusion

Nous avons tout au long de ce chapitre examiné quelques uns des travaux que j'ai pu effectuer ces dernières années dans le domaine de la modélisation numérique en OA. Le budget d'erreur présenté en introduction a permis ensuite de présenter des travaux spécifiques aux différentes sources d'erreur à considérer, liées à autant de composantes physiques du problème :

- ⋆ L'atmosphère turbulente, par le biais de la résolution de problèmes liés à sa modélisation numérique détaillée.
- ⋆ L'ASO, par le biais d'une étude sur les détecteurs particuliers que sont les EMCCD, réduisant le bruit de lecture à pratiquement néant mais non sans une contre-partie qu'il convenait de considérer de manière attentive.
- ⋆ Le miroir déformable, par le biais d'un exemple d'étude détaillée de son erreur d'échantillonnage spatial sur le cas particulièrement intéressant constitué par le M4 de l'E-ELT.

Ensuite, les systèmes d'OA complets ont été abordés, tout d'abord par le biais du système d'OA de première lumière du LBT, le plus performant existant actuellement, puis au travers de la question du type de modélisation elle-même à considérer (analytique, end-to-end), et enfin par le biais de l'intéressant site du Dôme C.

Un certain nombre d'autres applications a été (nécessairement !) négligé au passage, applications qui ont touché notamment à l'étude d'autres systèmes existants tel que NACO et MACAO pour le VLT (voir par exemple Robbe et al. [122] en ce qui concerne MACAO et son importance pour les mesures AMBER/VLTI), ou en étude tel que le très prospectif système possible pour le télescope sud-africain SALT (voir Catala et al. [149]).

Le chapitre suivant aborde quant à lui un aspect complémentaire, et particulièrement indiqué, de la modélisation aussi précise que possible des systèmes d'OA : celui de l'imagerie, et plus généralement des traitements et instruments particuliers, qui vont tenter de profiter aussi pleinement que faire se peut de la correction apportée par les systèmes d'OA.

Chapitre 3

Imagerie post-optique adaptative

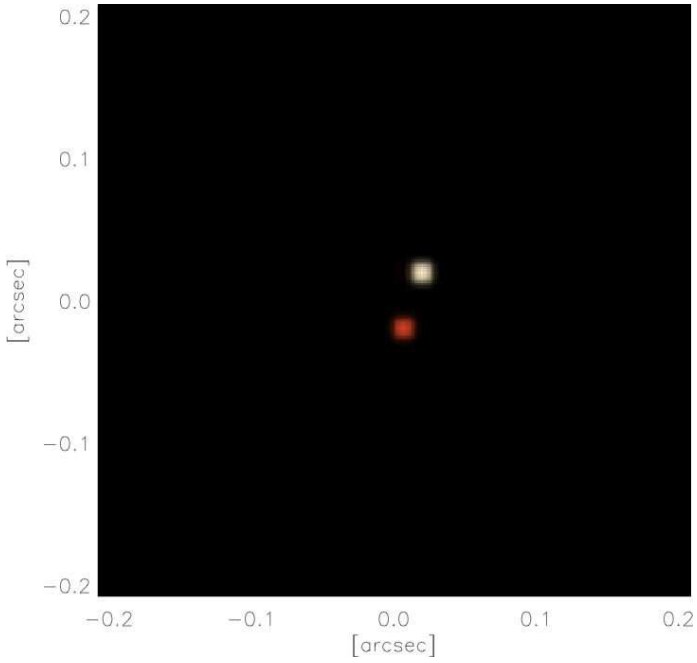

La semplicità è la sofisticazione finale.
(La simplicité est la sophistication ultime.)
Leonardo da Vinci.

Pourquoi faire simple quand on peut faire compliqué ?
Les Shadoks.

3.1 Contexte et sommaire

Cette seconde activité d'imagerie post-OA découle tout naturellement du travail que j'avais effectué durant mon stage de cinquième année universitaire puis ma thèse de doctorat, où il s'agissait de mettre en place des traitements efficaces et innovants de données speckle (et donc, pour le coup, sans apport a priori d'OA lors de l'observation), mais aussi bien entendu de ce dont il est question dans la partie précédente de modélisation en OA.

Après deux ans environ de post-doctorat durant lesquels je me suis intéressé exclusivement à la modélisation/simulation de systèmes d'OA j'ai donc entrepris de marier les deux expertises acquises en initiant le `Software Package AIRY` avec Serge Correia à l'Observatoire d'Arcetri (dans le cadre de sa thèse de doctorat) et le groupe du Prof. Bertero de l'*Università di Genova*, spécialiste de reconstruction d'image et déconvolution ; et surtout en réalisant les études que nous estimions nécessaires sur le mode d'imagerie interférométrique directe du LBT, télescope pour lequel je devais par ailleurs modéliser le système d'OA de première lumière, comme nous l'avons vu au chapitre précédent, Sous-sec. 2.5.1.

Cette collaboration, débutée peu avant la conférence SPIE/Astronomie de Münich en 2000, a tourné d'une part autour du développement de l'outil de déconvolution `AIRY`, présenté à la Sous-sec. 1.2.3 et d'une portée générale, et de l'outil `AIRY-LN`, vu à la Sous-sec. 1.2.4) et dédié à l'instrument LN, et d'autre part autour de la recherche d'algorithmes de reconstruction d'images et leurs tests en situations instrumentales réalistes (voir Sous-sec. 3.2.1 pour une étude de cas dédiée au LBT et Sous-sec. 3.2.2 pour celles successives). Elle a eu comme tout premier domaine d'application la reconstruction des images qui seront obtenues avec le LBT en mode de recombinaison interférométrique de Fizeau. Notons cependant qu'aussi bien du côté de la recherche d'algorithmes de reconstruction d'images que de celui de l'outil de déconvolution fourni en sus, le champ d'application est beaucoup plus large et applicable à n'importe quel instrument astronomique optique formant des images à HRA.

C'est également dans le cadre de cette collaboration que je suis en train d'approfondir deux des points abordés : l'un concernant l'application d'un algorithme de super-résolution, l'autre qui a pour sujet l'application d'un algorithme de déconvolution aveugle avec contrainte de Strehl. Dans les deux cas, l'application est visée autant aux données des grands télescopes optiques en cours de construction ou de modification (LBT aussi bien en mode monopupille qu'interférométrique, VLT avec la seconde génération d'instrument à haut Strehl) que des projets à plus long terme tels que l'E-ELT.

Outre le mode d'imagerie interférométrique directe du LBT, mon intérêt s'est propagé à l'imagerie post-OA en général, et à l'imagerie à très haute dynamique en particulier, dans le cadre des développements autour du coronographe de Lyot apodisé [55] pour l'instrument SPHERE et de sa modélisation, ainsi que des études qui en ont découlé.

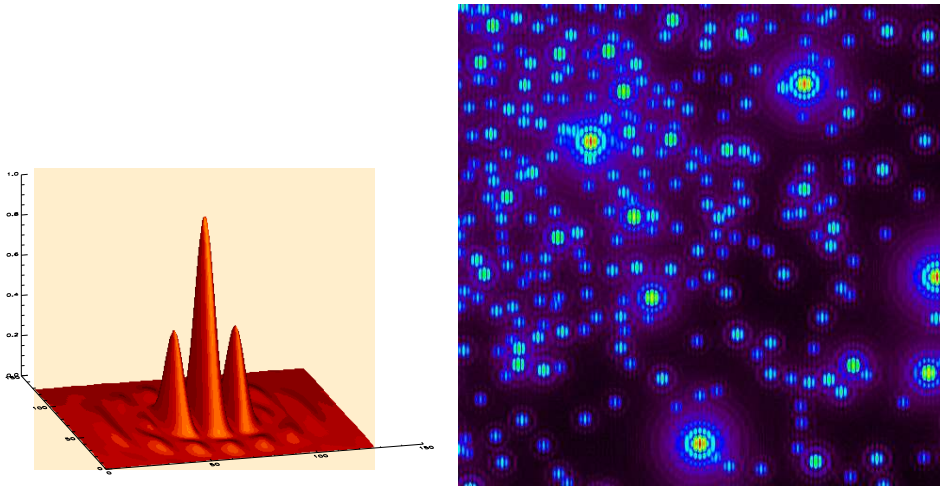

FIGURE 3.1: De gauche à droite : PSF interferométrique du LBT, image simulée d'une partie d'amas stellaire.

La suite de ce chapitre est organisée de la façon suivante. Je consacrerai tout d'abord la Sec. 3.2 à l'étude de cas de déconvolution multiple effectuée dans le cadre du LBT, étude qui met en avant les deux principaux facteurs physiques limitant identifiés : la couverture angulaire et la correction d'OA, toutes deux forcément partielles. Je clôturerai cette section par une rapide revue des nombreuses études effectuées qui en suivront. Dans la Sec. 3.3, j'appliquerai pour la première fois appliquée à des données réelles un algorithme de super-résolution, évoqué lors de cette revue, et j'en développerai les perspectives associées. Je proposerai ensuite, à la Sec. 3.4, un algorithme de déconvolution sous contrainte de Strehl, ainsi que les perspectives d'application associées. Enfin, je rappellerai à la Sec. 3.5 les différentes études effectuées dans le cadre de l'instrument à très haute dynamique SPHERE (étude du coronographe de Lyot apodisé, détection d'exoplanètes, préparation des observations d'autres types d'objets).

3.2 Imagerie interférométrique de Fizeau

La Fig. 3.1 montre la PSF typique correspondant au mode interférométrique du LBT, ainsi que l'image simulée d'une partie d'un amas stellaire. Une caractéristique intéressante d'un tel interféromètre est la possibilité d'avoir une bonne couverture du plan (u, v) des fréquences spatiales avec quelques observations à différentes orientations de la base par rapport au ciel (i.e. à différents angle parallactiques). Dans le cas du LBT ceci est obtenu simplement grâce à la rotation de la Terre, ce qui engendre non seulement une rotation du champ (d'où le besoin de dé-rotateur), mais aussi une rotation de la base

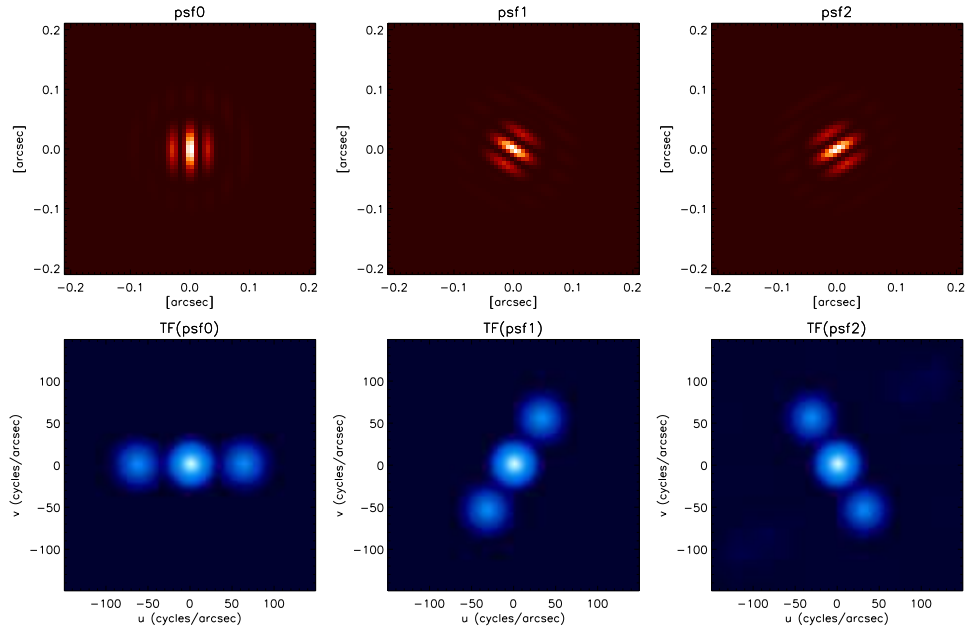

FIGURE 3.2: De haut en bas : PSF interférométrique du LBT pour différents angles parallactiques (0°, 60°et 120°), FTO correspondantes montrant la couverture (instantanée) du plan (u, v).

projetée sur l'objet. Ce dernier effet est mis à profit afin d'échantillonner le plan (u, v). La Fig. 3.2 présente un ensemble typique de PSFs obtenues à différents angles parallactiques relatifs (0°, 60°et 120°), ainsi que les fonctions de transfert optique (FTO) correspondantes, illustrant la couverture du plan (u, v).

Le problème de reconstruction qui en résulte en est qu'une unique image à HRA de l'objet astrophysique doit être restaurée à partir d'un ensemble d'observations interférométriques correspondant à différents angles parallactiques. Plusieurs méthodes peuvent alors être appliquées à ce problème [45]. Nous ne traiterons cependant ici que de la méthode itérative OSEM, proposée en premier lieu par Bertero & Boccacci [44] et implémentée comme nous l'avons déjà vu dans le `Software Package AIRY`.

Pour rappel et pour résumé, OSEM est une version accélérée de la méthode classique de Lucy-Richardson pour les images multiples telles que celles délivrées par un interféromètre de Fizeau. L'accélération apportée est d'un facteur p en nombre d'itérations pour p images (correspondant à d'autant d'orientations de la base par rapport à l'objet observé, et donc à d'autant de poses différentes pendant la nuit d'observation), mais chaque itération de OSEM recquiert $4p$ FFT, au lieu de $3p + 1$ dans le cas classique. Ce qui conduira typiquement à un gain de 2.5 (pour $p = 3$) à 4 (pour $p = 5$).

3.2.1 *Restoration of interferometric images – II. The case-study of the Large Binocular Telescope*

L'article suivant, publié par *Astronomy & Astrophysics* en 2002, propose, au travers de l'exemple précis du LBT en mode interférométrique de Fizeau et post-OA, une double étude à portée plus générale.

D'une part, c'est l'influence de la couverture angulaire sur la qualité de la reconstruction qui est considérée. D'autre part, l'influence du niveau de correction d'OA est étudiée en détail, notamment au regard de la différence éventuelle de correction entre l'objet observé et l'étoile de référence (supposée non-résolue et servant de source d'étalonnage de la PSF globale de l'ensemble atmosphère⊕télescope⊕instrument).

Ces deux études sont effectuées sur un objet intéressant à plusieurs titres, et au moins du point de vue de l'imagerie, puisqu'il est composé d'une binaire serrée encerclée d'un anneau diffus de poussière de magnitude beaucoup plus élevée. L'objet composite traité ici est totalement inspiré de l'objet observé et reconstruit par Roddier et al. en 1996 [33] : l'étoile binaire de type T-Tauri du système quadruple GG Tau, observée dans le proche infrarouge avec le *Canada-France-Hawaii Telescope* équipé du système d'OA de l'Université de Hawaii. Dans cette étude l'objet est repoussé plus loin dans l'espace, puisque la binaire centrale y possède une séparation de seulement 40 mas (pour *milli-arcseconds*, i.e. milli-secondes d'arc en anglais), soit deux fois la résolution du LBT en mode interférométrique en bande K.

La limitation en couverture angulaire a deux effets potentiels : la limitation de la couverture du plan (u, v) d'une part, et l'éventuelle rotation des franges pendant le temps d'intégration de l'image interférométrique d'autre part. L'article suivant montre cependant qu'une bonne reconstruction de l'objet peut être atteinte dans la plupart des cas.

La limitation due à la correction forcément limitée apportée par le système d'OA est étudiée aussi bien pour un système à une seule étoile guide que pour un système multi-références de type OAMC [1]. Cette étude démontre notamment que c'est plutôt l'uniformité de la correction de l'OA (i.e. un rapport de Strehl uniforme) sur le champ de vue, plus que simplement la qualité globale des images (i.e. un plus haut rapport de Strehl moyen), qui va déterminer la qualité de la reconstruction finale de l'objet observé.

Du point de vue de la conception d'un système d'OAMC, il s'agit là d'une information intéressante. Il a été par exemple montré dans Vérinaud et al. [67], juste après la publication de cet article, que dans le cadre de la technique d'OAMC *layer-oriented*, sa déclinaison à champ de vue multiple (*multiple-field-of-view layer-oriented MCAO*) permet une meilleure uniformité du rapport de Strehl à travers le champ de vue corrigé, au prix cependant d'un rapport de Strehl moyen plus bas...

1. Pour rappel : optique adaptative multi-conjuguée, MCAO en anglais.

A&A 387, 744–757 (2002)
DOI: 10.1051/0004-6361:20020389

Astronomy & Astrophysics

Restoration of interferometric images

II. The case-study of the Large Binocular Telescope

M. Carbillet[1], S. Correia[2,3], P. Boccacci[4], and M. Bertero[4]

[1] Osservatorio Astrofisico di Arcetri, largo E. Fermi 5, 50125 Firenze, Italy
[2] UMR 6525 Astrophysique, Université de Nice–Sophia Antipolis, Parc Valrose, 06108 Nice Cedex 2, France
[3] European Southern Observatory, Alonso de Cordova 3107, casilla 19001, Santiago 19, Chile
e-mail: scorreia@eso.org
[4] INFM and DISI, Università di Genova, via Dodecaneso 33, 16146 Genova, Italy
e-mail: boccacci@disi.unige.it; bertero@disi.unige.it

Received 13 February 2002 / Accepted 8 March 2002

Abstract. We present in this paper a study of the imaging properties of the Large Binocular Telescope interferometer, focusing our attention on what we believe to be the most relevant effects, namely the limited angular coverage and the partial adaptive optics (AO) correction. For this purpose we make use of the Software Package AIRY (Astronomical Image Restoration in interferometrY), designed for multiple deconvolution of interferometric images and presented in our previous paper. We also consider as our testing object a model of young binary star consisting of a core binary surrounded by a massive circumbinary ring seen in scattered light, similar to that of GG Tau. The effect of angular coverage, linked to the problem of time-averaging smearing of the interferometric images, is investigated for a number of cases corresponding to different declinations of the observed object. We find encouraging results showing that a good estimation of the relevant astronomical parameters of the object can be obtained even with an incomplete angular coverage. We then study the effect of partial AO-correction for both schemes of classical AO and multi-conjugate AO. We show that uniformity of the point-spread function over the field-of-view, rather than absolute global quality, is fundamental for the quality of the restored image.

Key words. instrumentation: interferometers – instrumentation: adaptive optics – techniques: interferometric – techniques: image processing – methods: numerical – stars: imaging

1. Introduction

In a previous paper, hereafter referred to as Paper I (Correia et al. 2002), we present the Software Package AIRY (Astronomical Image Restoration in interferometrY) designed for the simulation and restoration of the images of LBT (Large Binocular Telescope) and LBT-like interferometers (as for example the 20/20 telescope project). The main peculiarity of this kind of interferometers is the possibility of getting a good coverage of the u–v spatial frequency plane by means of a few observations at different orientations of the baseline with respect to the sky (i.e. different parallactic angles). Indeed LBT is a two 8.4 m pupils interferometer with a center-to-center baseline of 14.4 m, both pupils being placed on a common alt-azimuthal mount.

The associated restoration problem is that a unique high-resolution image of the astronomical target will have to be recovered from a set of interferometric observations corresponding to different parallactic angles. Several restoration methods can be applied to this problem (see, for instance, Bertero & Boccacci 2000b). In the present paper we use the iterative method known as OS-EM (Ordered Subsets – Expectation Maximization), proposed in Bertero & Boccacci (2000a), and implemented within the Software Package AIRY (see Paper I). It is an accelerated version of the EM (Expectation Maximization) method (Shepp & Vardi 1982), also known in astronomy as the LR (Lucy-Richardson) method.

The purpose of this paper is to study the peculiar interferometric imaging performance of LBT by means of numerical simulations. In particular, we study what we have identified to be the most relevant effects, namely the limitation in angular coverage, and the partial AO-correction.

As concerns the angular coverage, it must be observed that, due to the alt-azimuthal mount of the telescope, the effects of earth rotation during the night are both a rotation of the field and a rotation of the projection of the baseline onto the object. The first rotation is compensated by a hardware device (a field de-rotator), while the second one is used to sample the u–v plane.

Send offprint requests to: M. Carbillet,
e-mail: marcel@arcetri.astro.it

Since the variation of the parallactic angle with time is a non-uniform function of the object declination, the implication is twofold. First, the range of parallactic angles accessible during the night can be limited (i.e. less than 180°), depending on the object declination. The consequence is an incomplete coverage of the u–v plane. Second, and due to the variation of the fringe pattern rotation rate during the night, the variation of parallactic angle during the integration time is not negligible in some circumstances – when the object is close to the zenith for instance – so that, for a given integration time, it can induce significant differences in angular range for different baseline orientations.

As concerns partial AO-correction, we recall that, in the case of LBT, a high-level AO system is intended to correct for the atmospheric turbulence effects on each pupil, directly on the secondary mirror, and to cophase each beam before recombination. LBT first light, including an adaptive optics (AO) system based on adaptive secondary mirrors and pyramid wavefront sensors, is planned for early 2004. The final AO system will also include multi-conjugate (MC) AO features, intended to achieve high-quality correction on a wide field-of-view (FoV). A broad range of image quality can anyway be achieved, mainly due to variation of the seeing conditions, but also to a series of other factors as the number of photons that are allowed for wavefront sensing and the angular distance between the AO guide star and the astronomical target. Hence the study of such an effect on the restored image appears to be a fundamental issue.

The above mentioned effects are investigated by simulating high-resolution LBT interferometric observations of an astronomical object of interest, and comparing the scientific parameters of the restored object with the original ones. From this point of view the present work is to be considered as the continuation of preliminary studies already presented elsewhere (Correia et al. 2000; Carbillet et al. 2000; Correia et al. 2001), as well as in Paper I.

All along this study we use as astronomical object a model of young binary star consisting of a core binary surrounded by a dusty circumbinary ring. The model is directly inspired by near-infrared observations of the famous T-Tauri binary star of the quadruple system GG Tau and their consecutive data interpretation/modelization (Roddier et al. 1996; Wood et al. 1999). We believe that this type of object is challenging for any kind of restoration method because it combines point-like features (the core binary star) and a diffuse one (the circumbinary ring), with a high-dynamic range between them. For a better understanding of the capabilities of the restoration method as well as of the effects due to the above mentioned features, we also treat separately the two components of the object. We first look at the detectability of both the core binary star and the circumbinary ring, and then we quantify the quality of the reconstruction: for the core binary star we compute the error on the reconstruction of its astrometric and photometric parameters while, for the circumbinary ring we evaluate the error on some suitable morphological parameters.

The paper is organized as follows. In Sect. 2 we describe in detail the model of astronomical object considered for our study, as well as the general features of the sets of PSFs used and the associated imaging process. In Sect. 3 we describe our simulation of observations corresponding to different declinations of the astronomical object (and then to different amounts of angular coverage), and give the results obtained by applying the restoration method to the various sets of observations. The relevant scientific parameters are plotted as functions of the number of OS-EM iterations and the features of the restorations are discussed. The effect of the quality of the attained AO correction is studied in Sect. 3.3, for both cases of classical AO and MCAO. In Sect. 5 we summarize the results of the paper and give our conclusions.

2. The simulated data

2.1. The astronomical object: A model of young binary star

We assume as our astronomical object a young binary star with scattered light emission coming from the presence of a dusty circumbinary ring. The model is produced using observational parameters for the ring emission taken from observations of the close binary of the quadruple GG Tau system obtained in the near-infrared by Roddier et al. (1996), and reproduced afterwards in modelizations by Wood et al. (1999). According to the latter we assume that:

1. the light scattered by the circumbinary ring is mainly contained within two concentric ellipses with the same axial ratio $b/a = 0.82$ and with semi-major axes of, respectively, ∼10 and ∼20 times the binary angular separation ρ;
2. the ratio between scattered and direct light in K-band is 0.57×10^{-2} (corresponding to a difference of integrated magnitude between the core binary star and the circumbinary ring of ∼5.64 mag);
3. the ratio of scattered light between the near side and the far side of the ring is ∼2.

In addition, the ring inclination angle is set to 35° and lumpy features are included. As concerns the binary star lying in the core of the dynamically cleared region, we assume an angular separation ρ twice the angular resolution limit of LBT in K-band (i.e. ∼40 mas), and a position angle PA chosen in such a way that the position of the companion star *does not* coincide with a given pixel. We also assume a main component K-magnitude $m = 10$ and a difference of magnitude $\Delta m = 1$. We point out that the brightness of the central binary we consider here is sufficiently realistic for this type of object (see for instance Ghez et al. 1997) and leads to a ring integrated magnitude of ∼15.25 (i.e. 15.48 mag/arcsec^2). This model could

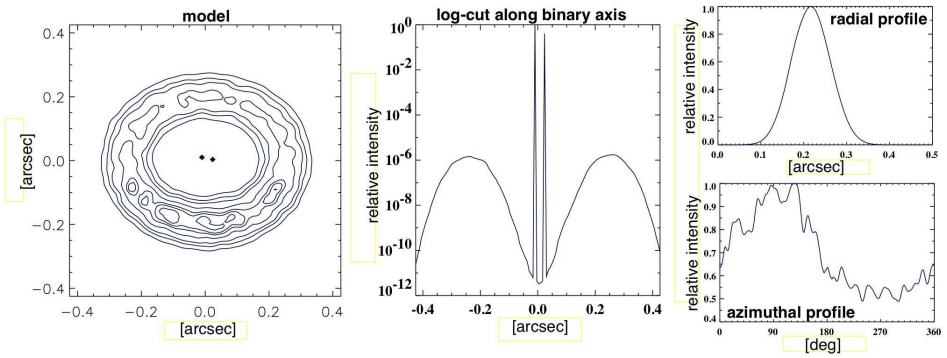

Fig. 1. The model of young binary star surrounded by its circumbinary ring used for our study. Left: contour plot of the model. The seven level lines correspond respectively to 0.1, 0.2, 0.3, 0.5, 0.7, 0.8 and 0.9 of the maximum value of the circumbinary ring (i.e. respectively 2.6×10^{-7}, 5.3×10^{-7}, 8.0×10^{-7}, 1.3×10^{-6}, 1.8×10^{-6}, 2.1×10^{-6}, and 2.4×10^{-6} of the maximum value of the whole object). Center: logarithmic plot of the cut along the binary axis. Up right: radial intensity profile $I_\theta(r)$ of the circumbinary ring. Bottom right: azimuthal intensity profile $I_r(\theta)$ of the circumbinary ring.

represent a young binary object located at a distance of about 2.5 times that of the Taurus-Auriga Complex.

Figure 1 shows different representations of our model. In order to characterize in detail the circumbinary ring we have plotted both its radial intensity profile $I_\theta(r)$, defined as the integration over the polar angle θ of the intensity map $I(\theta, r)$, and its azimuthal intensity profile $I_r(\theta)$, defined as the integration over the radius r of $I(\theta, r)$.

Let us point out that this combination of point-like and diffuse structures with a very high dynamic range between them is a severe test for imaging since, as a consequence of their vicinity, there will be a strong interaction between the image of the core binary star image and that of the circumbinary ring.

2.2. Interferometric PSFs

The spatial sampling adopted for all the interferometric PSFs used in this paper is 3 pixels per Full-Width at Half-Maximum ($FWHM$) of the fringes, where the $FWHM$ is equal to λ/L, with L the total baseline length (22.65 m = 8.25 m effective diameter of each pupil + 14.4 m baseline separation), and λ the filter central wavelength (2.2 μm all along this paper).

Since we intend to study separately the effects of partial angular coverage and partial AO-correction, we will consider different sets of PSFs for each case. When dealing with the angular coverage effect, we will assume perfectly coherenced and cophased PSFs (no optical aberration), while when dealing with the AO-correction effect, we will assume a good angular coverage. We refer to the corresponding sections for further details.

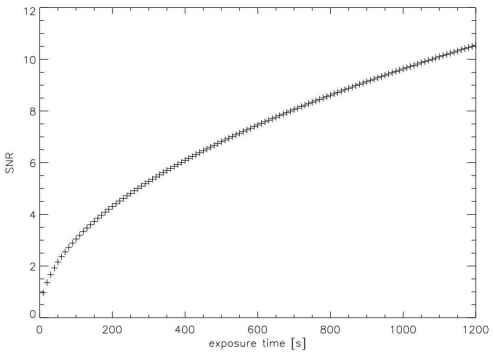

Fig. 2. SNR vs. integration time for the detection of the circumbinary ring.

2.3. Image formation process

Sets of interferometric images are formed by convolving the model with the PSFs of a given set (each PSF corresponding to a given parallactic angle). Sky background emission is added to the results which are eventually corrupted with Poisson and detector noise realizations. The following parameters are used all along this study: a total efficiency (mirror+optics+detector) of 25%, a sky background brightness of 12.5 mag/arcsec^2, and a read-out noise (RON) corresponding to the scientific imaging device of 2 e$^-$ rms.

From the above parameters and the characteristics of the circumbinary ring it is straightforward to compute the expected average SNR of the ring emission as a function of the integration time. Such a function is plotted in Fig. 2. We can in particular observe that 1 min integration time,

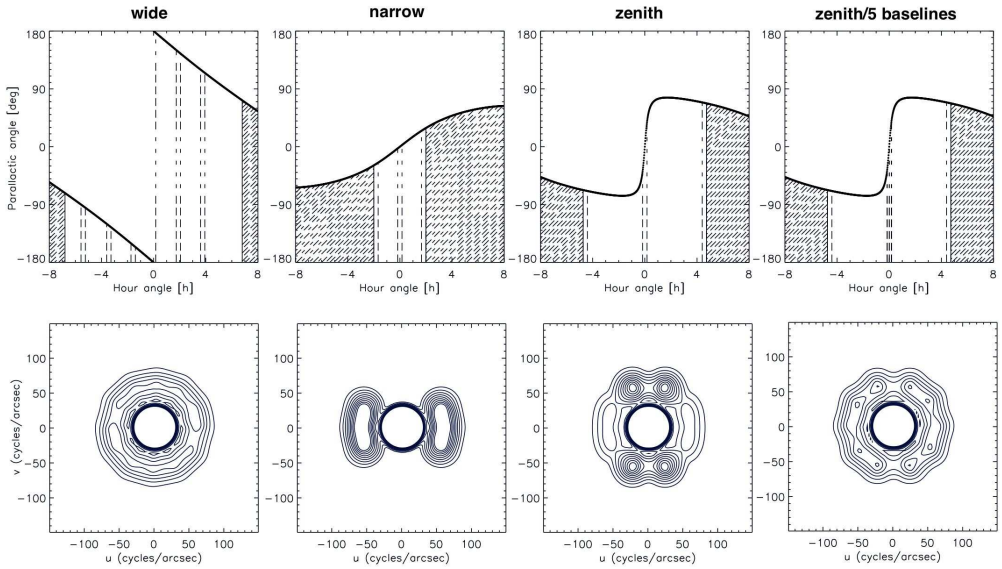

Fig. 3. The four cases of angular coverage considered. First row: plots of the parallactic angle q as a function of the hour angle H for an object of declination δ, from left to right: $+80°$ ("wide" case), $-20°$ ("narrow" case), $+30°$ with 3 baselines ("zenith" case), and $+30°$ with 5 baselines ("zenith/5 baselines" case). The filled regions, accessible only at airmass >2, are not considered in the present study. The intervals defined by the vertical dashed lines represent the variation of the parallactic angle during the considered integration time: 20 min in all cases, but 1 min only for the three central intervals of the "zenith/5 baselines" case. Second row: the corresponding angular coverages in the spatial frequency space represented by means of level lines of the sum of the power spectra of the corresponding PSFs. Ten levels (from 0.01 to 0.1 of the maximum value) are shown.

the shortest exposure-time we are considering, leads to an average SNR of $\sim$2.5, while 20 min, the longest exposure time, leads to an average SNR of $\sim$10.

3. Angular coverage effects

3.1. The cases considered

The parallactic angle q is defined as:

$$q = \arctan\left(\frac{\tan\phi\cos\delta - \sin\delta\cos H}{\sin H}\right), \qquad (1)$$

where ϕ is the latitude of the observatory ($+32.667°$ in the case of LBT), δ the declination of the object, and H the hour angle. Four different cases of variation of the parallactic angle q versus the hour angle H are shown in Fig. 3, each representative of a relevant situation in terms of accessible range of parallactic angle and field-rotation velocity.

The first case (the "wide" case – left-part of Fig. 3) gives the largest range of parallactic angle ($\sim$200°); it corresponds to an object with a declination of $+80°$. The second case (the "narrow" case) gives the smallest range of parallactic angle ($\sim$60°); it corresponds to the angular coverage of an object with a declination of $-20°$. In the two other cases (the "zenith" case and the "zenith/5 baselines" case) the range of parallactic angle ($\sim$135°) is intermediate when compared with the previous ones, but the corresponding field-rotation velocity around $H = 0$ is much higher, due to the fact that the object is much closer to the zenith ($\delta = +30°$).

In order to sample the covered regions of the u–v plane in a way which is approximately uniform for the four cases, we consider six equispaced parallactic angles for the "wide" case, three for the "narrow" case and the "zenith" case, and five for the "zenith/5 baselines" case, as represented in Fig. 3. This corresponds to an angular sampling of roughly one baseline each 30° of parallactic angle.

We consider an integration time of 20 min for each observation (each observation corresponding to one range of parallactic angle) of the first three cases. This corresponds to a variation of parallactic angle of $\sim$5° during each observation of the "wide" case and the "narrow" case (low field-rotation velocity). In the "zenith" case (fast field-rotation velocity) the integration time corresponds to a variation of $\sim$1.5° for the two extreme parallactic angles, and of $\sim$76° for the middle one. Therefore in the "zenith/5 baselines" case we split the latter wide angular-spanning observation into three angularly equispaced short exposures, each one of 1 min integration time (corresponding to a variation of

parallactic angle of $\sim 5°$). In such a way we aim to compare the effect of field-rotation averaging, typical of a long exposure, with the effect of noise increase, arising from the fact that the long exposure is splitted into three shorter ones.

In our simulations the effect of the rotation of the baseline during the integration time ("time-averaging") is taken into account by adding snapshot PSFs of different orientations with a temporal step of 1 min. In addition to this, we also include the width of the K broad-band filter ($\Delta\lambda = 400\,\mathrm{nm}$), by adding four monochromatic PSFs corresponding to wavelengths within the band. However it has to be noted that in our tests we do not find a significant effect of this kind of further refinement.

We also note that in the "zenith/5 baselines" case the fluxes of the images with different integration times are normalized in such a way that they have the same integrated value, as required by our image restoration algorithm (Bertero & Boccacci 2000a).

We obviously expect the best reconstruction in the first case, since the angular coverage is complete (greater than 180°) and there is no dramatic variation of the parallactic angle during the integration time. At the opposite, the second case corresponds to a limited range of spatial frequencies "seen" during the observations. The third case is characterized by a wide angular averaging due to the fast field-rotation when passing through the zero-hour angle. This phenomenon is reduced in the fourth case, but at the cost of a noise increase.

3.2. Reconstruction of the whole object and estimation of the parameters of the binary star

Figure 4 shows the restorations of the whole object obtained for the four cases of angular coverage we are considering.

Elongation of the small scale features, i.e. the lumpy features and the binary star components, are clearly visible, especially in the "narrow" case and in the "zenith" case. This is due to the incomplete coverage which implies orientations with different resolutions and therefore elongated shapes of the point-source objects. This elongation is, in the "narrow" case, in the direction where the parallactic angles are not sampled and, in the "zenith" case, in the direction where these angles are smeared. The noise amplification due to the three low-SNR baselines of the "zenith/5 baselines" case is also evident in the restored ring. We will return on this phenomenon when treating the restoration of the ring alone. However we observe that, in the "zenith/5 baselines" case, the binary is less elongated than in the "zenith" case. It is also better resolved, as it can be seen from the cuts of the restorations along the axis of the reconstructed core binary star. It is to be noted anyway that in all cases both the core binary star *and* the circumbinary ring are clearly detected.

Let us now investigate quantitatively the effect of the different angular coverages on the restoration of the parameters of the core binary star. In Fig. 5 the errors on these parameters are plotted as functions of the number of OS-EM iterations. We point out that in all cases the parameters converge to the correct values when the number of iterations increases, although in the "wide" case the convergence is globally faster than in the other ones.

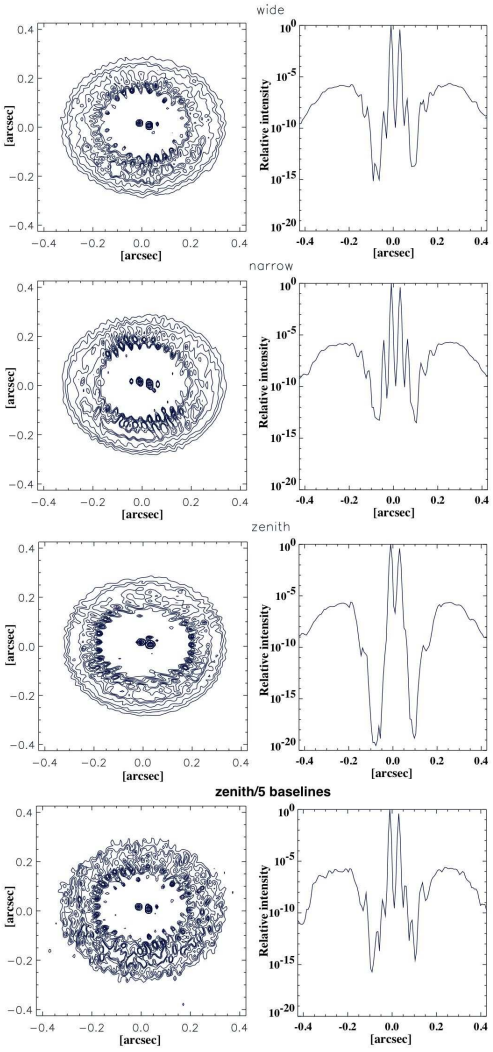

Fig. 4. Restoration of the model of young binary star for the four cases of angular coverage. The reconstructed images are represented with the same levels as in Fig. 1. The logarithmic plots of the cuts along the axis of the reconstructed binary star are also shown.

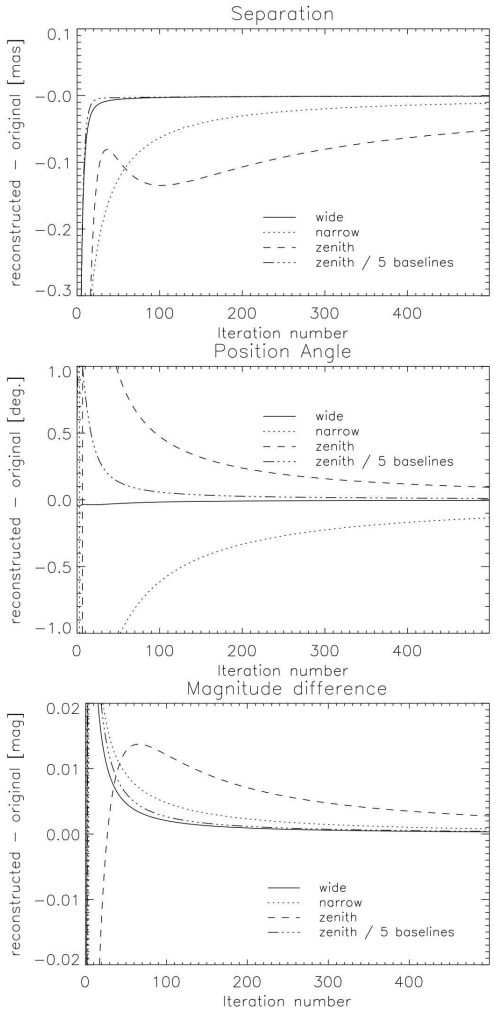

Fig. 5. Restoration of the parameters of the binary star: plots of the errors as functions of the number of OS-EM iterations for the restoration of the angular separation ρ, the position angle PA and the difference in magnitude Δm, and for the four cases of angular coverage.

In addition the accuracy in the retrieval both of the astrometric parameters (ρ and PA) and of the photometric parameter Δm is definitely better when the coverage is complete ("wide" case), or almost complete without wide time-averaging ("zenith/5 baselines" case). We also observe that the direction of the axis of the binary star falls in the "well-scanned" angular sector of the first two cases while it is within the angular smeared region of the third case. As a consequence in the "zenith" case the retrieved separation is smaller than the correct one (the elongation lies in the direction of separation).

Note that from the point of view of (relative) astrometry and photometry the absolute errors are remarkably small (error on $\rho \lesssim 0.05\,\mathrm{mas}$, error on $\Delta m \lesssim 0.005\,\mathrm{mag}$).

3.3. Circumbinary ring restoration

For the evaluation of the restoration of the circumbinary ring, we adopt the following approach: a masking of the central core is performed on the different reconstructed images so that the radial profile $I_\theta(r)$ and the azimuthal profile $I_r(\theta)$ can be easily computed; then, if we denote by $\boldsymbol{I}$ the vector formed by the samples of the radial or azimuthal profile of the original model and by $\boldsymbol{I}^{(k)}$ the corresponding vector obtained from the result of the kth iteration, the accuracy of the restoration provided by such an iteration is measured by computing the following relative distance:

$$R_I^{(k)} = \frac{\|\boldsymbol{I}^{(k)} - \boldsymbol{I}\|}{\|\boldsymbol{I}\|}, \tag{2}$$

where the norm is the Euclidean one, i.e. the square root of the sum of the squares of the sample values.

Besides the reconstruction of the whole model, we also consider a second approach which consists in applying the restoration method to data obtained after subtraction of the binary star contribution. A possible procedure could be the following: first perform a deconvolution of the complete data to estimate the binary parameters (as performed in Sect. 3.2); next subtract from the original data the binary images obtained by convolving the estimated binary with the PSFs; finally perform a second deconvolution of the circumbinary data alone. Even if this kind of procedure is routinely applied with success for probing the circumstellar environment of T-Tauri stars and possibly detecting disks emission (see e.g. Roddier et al. 1996; Krist et al. 2000), its practical implementation and validation are beyond the scope of this paper. Therefore we only consider a perfect subtraction of the binary contribution. In other words we perform the restoration of the circumbinary ring alone and then compute again $R_I^{(k)}$ on both the radial and azimuthal profiles. This last procedure has also the advantage that it provides further information on the behavior of our restoration method when applied to faint diffuse objects (see Paper I).

Figure 6 shows the results of the restoration of the ring alone, while the relative distances $R^{(k)}$ for the four cases of angular coverage and the two approaches considered (restoration of the complete object and of the ring alone) are shown in Fig. 7.

As concerns the maps of the restored ring, a simple visual analysis and comparison with the model of Fig. 1 makes already evident that when the angular coverage increases (from the "narrow" case to the "wide" case through the "zenith" case), the reconstructed features

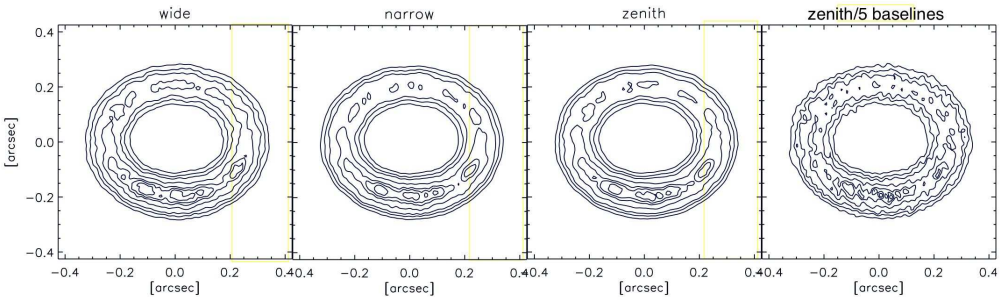

Fig. 6. Restoration of the circumbinary ring after binary subtraction for the four cases of angular coverage. The level lines correspond to 0.1, 0.2, 0.3, 0.5, 0.7, 0.8, and 0.9 of the maximum value of the model, and therefore are equivalent to the level lines of Fig. 1.

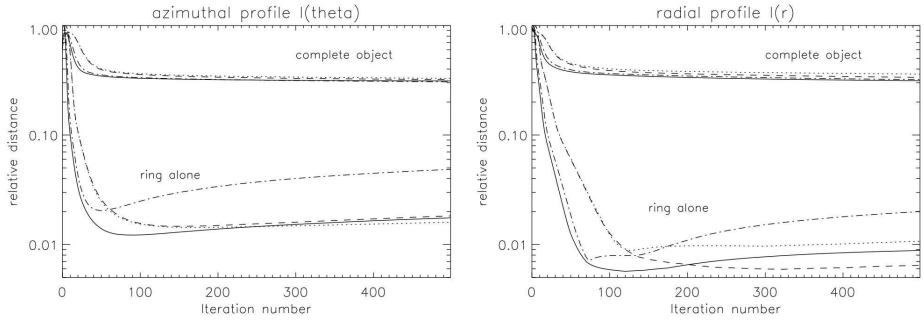

Fig. 7. Circumbinary ring restoration: logarithmic plot of the relative errors in the restoration of the azimuthal profile $I_r(\theta)$ (left) and of the radial profile $I_\theta(r)$ (right), in the four cases of angular coverage. Continuous line is for the "wide" case, dotted-line for the "narrow" case, dashed line for the "zenith" case, and dashed-dotted line for the "zenith/5 baselines" case. Two sets of results are represented: the upper set corresponds to the restoration of the complete object, while the lower set corresponds to the restoration of the ring alone.

become sharper. In addition, the "zenith/5 baselines" case clearly shows the expected effect of noise increase.

This is quantitatively confirmed by Fig. 7, where the common behavior of the various distance curves is a minimum around 100–200 iterations. This feature is known in the theory of iterative methods for image restoration as *semiconvergence* (see e.g. Bertero & Boccacci 1998, as well as Paper I), and is due to the phenomenon of *noise amplification* (see also White 1994). Moreover, as it is known, this phenomenon is stronger in the case of noisier data, in the sense that the optimal number of iterations decreases with increasing noise. This last point is evident here from Fig. 7 when comparing the "zenith" case with respect to the "zenith/5 baselines" case.

3.4. Discussion

A first result of our analysis is that, as expected, the restored image has a higher quality when a broader range of parallactic angles is accessible. However the influence on the extended part of our model is not dramatic: reliable results are obtained even in the case of incomplete angular coverage or smeared baselines.

The interpretation of this effect in the u–v plane is as follows: the spectrum of the extended part is mainly concentrated at low angular frequencies so that the information provided by a single mirror is fundamental while that coming from the long baseline provided by the interference between the two mirrors is not very relevant.

More critical is the effect on small features or on point objects such as the stars of the binary. Indeed their spectrum extends outside the disc in the u–v plane covered by a single mirror so that, in the case of incomplete coverage, the restorations exhibit elongated shapes in the directions not covered by the baselines. It is interesting to remark, however, that, as concerns the estimation of the binary parameters the main difference between the different cases consists essentially in different convergence rates. The final accuracy is always quite good even if we show that an improvement can be obtained by splitting a too large angular smearing into shorter exposures.

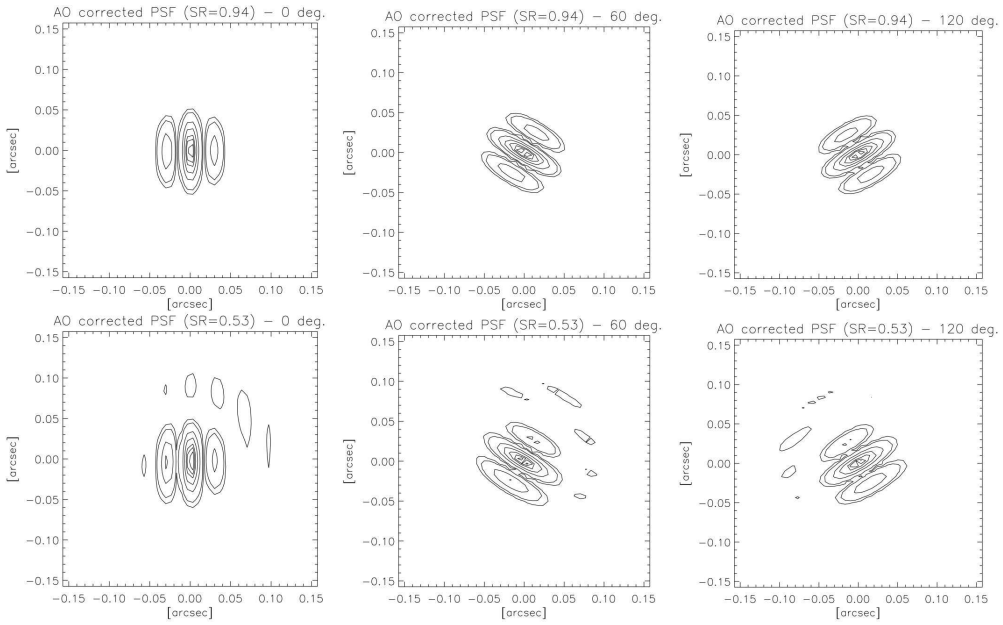

Fig. 8. Two examples of the sets of interferometric AO-corrected PSFs used in this study. Each set consists of three PSFs corresponding to three equispaced orientations of the baseline (0°, 60°, and 120°). The average SR of the upper set is 0.94, and 0.53 for the bottom set. Level lines correspond to 0.05, 0.1, 0.3, 0.5, 0.7, 0.8, and 0.9 of the maximum value.

The last strategy can be hardly applied to the faintest objects due to the need of finding a compromise between integration time and time-smearing. In particular we find that, if some images have poor SNR values, the result may be corrupted by the phenomenon of noise amplification. In such a case the choice of the number of iterations is more critical and we conclude that the definition of a reliable stopping-rule (see Lanteri et al. 1999a, 1999b) will be required when dealing with real data.

4. Partial AO-correction effects

Although the goal of AO is to correct the atmospheric degradations as perfectly as possible, it is obvious that residuals will always be present and have a relative destructive effect on image formation.

The effects of partial correction on each single pupil of an interferometer have the global consequence that the image of a point-source is not exactly an Airy disc, but consists of a central core surrounded by a halo, where typically the first Airy ring is visible but broken. The tip-tilt residual causes a residual global image motion, while the high-orders residuals tend to "speckle-ize" the image.

In the interferometric case, the dilution of the pupil implies that differential effects must also be considered. The residual of differential piston tends to produce a motion of the fringes pattern along the baseline axis. In addition to it, the differential tip-tilt, resulting from both the tip-tilt residuals of the single pupils, has the effect of a bad superimposition of the two single-pupil PSF envelopes: the envelopes from the two pupils combine in a deformed one. Hence the effect on the fringes is similar to that due to the differential piston, but with the main difference that the central fringe remains static, while in the case of differential piston the central fringe is moved.

For what concerns the high-orders residuals, and as in the case of single-pupil astronomy, they cause the interferometric PSF to be composed of a central fringed core together with a "speckle-ized" halo where each speckle-like feature is fringed as well. In the following of this section we consider the overall deformation of the PSFs due to the whole ensemble of perturbations.

4.1. The AO-corrected interferometric PSFs

When dealing with the deconvolution of post-AO images, an important issue is the good estimation of the PSF that best corresponds to the observed object. Mainly due to the anisoplanatism error that affects the AO correction of an object distant by a certain angle from the guide star (GS), its PSF can be very different from the GS one. By extension the PSF related to the formation of the image of the observed object (the "object PSF") can be very different

from the PSF related to the point-like reference star used for deconvolution (the "reference PSF"). Note that the reference point-like star is not a priori the GS used for the AO correction (or one of the GS' in the case of MCAO).

In the following of this paper we use five different sets of PSFs, obtained by simulating the behavior of the LBT AO system in its single-reference single-conjugate mode (i.e. classical AO), and using the Software Package CAOS (Carbillet et al. 2001a). Two typical examples of our sets of PSFs are shown in Fig. 8.

As in the case reported in details in Carbillet et al. (2000), we simulate our sets of AO-corrected interferometric PSFs for three parallactic angles: 0°, 60°, and 120°. Note that this angular coverage of the frequency plane is good enough to allow us to focus on the AO-correction effects only. The simulations are performed in closed-loop with an independent realization of the turbulent atmosphere for each parallactic angle. This will be the situation in real life since different parallactic angles correspond to different instant during the observation night (see Sect. 3). The scope of the present section being to study the effects due to the difference between the reference PSFs and the object PSFs, we simulate several sets of PSFs by taking point-like stars with different off-axis angles (the GS is considered on-axis), varying from 0 arcsec towards the isoplanatic angle corresponding to the simulated atmosphere (depending on the turbulence profile, the wavefront outerscale, and the speed of each turbulent layer). We then characterize the corresponding image quality by means of the resulting Strehl ratio (SR), defined as the ratio between the intensity of the AO-compensated PSF and the intensity of the ideal PSF, measured in the central point of the later. The resulting SR are respectively: 0.94 (on-axis PSF), 0.93, 0.88, 0.81, and 0.53 (farthest PSF).

All along this section we characterize the quality of the correction of a given set of PSFs by its SR only. Although a full description of each PSF would require also parameters such as its $FWHM$ and its encircled energy (both related to the attained resolution), as well as the main features of its morphology (mainly for what concerns the halo), we assume here that the SR is sufficient to characterize the PSFs, and that a different SR implies a different $FWHM$ and a different morphology. This assumption is reasonable also because we are dealing here with relatively high SR (>50%).

Our first application concerns classical AO. Therefore we assume in the following that the reference star used for deconvolution corresponds to the AO GS (and hence that the SR of the reference PSFs is 0.94), while we consider four cases of object PSFs corresponding to the SRs from 0.93 to 0.53. We have considered here anisoplanatism only, but other sources exists, such as anisopistonism (Esposito et al. 2000; Femenía et al. 2001), but also the geometry and magnitude map of the asterisms of the GSs when considering an MCAO scheme. Therefore we call the "general AO case" this first application, because it also includes MCAO when the correction is not perfectly uniform.

In addition to it, we also consider a second application concerning a uniform MCAO system. Indeed, the main attractive feature of this kind of system is its expected capability of maintaining the same level of correction all over the corrected FoV. In good conditions the PSFs are typically expected to be stable over a FoV of up ∼2 arcmin (see e.g. the recent results reported in Bello et al. 2001 or Carbillet et al. 2001b). Since the AO-correction quality depends, as in the classical case, on the atmospheric and system status during the single observation, our MCAO case study concerns different levels of correction over a FoV covering both the astronomical object and the reference star. For the sake of simplicity we limit our analysis to the best situation ($SR = 0.94$ for both the reference PSFs and the object PSFs), and to the worst one ($SR = 0.53$ for both sets). We call this second application the "uniform MCAO case".

4.2. General AO case

Four sets of LBT images are generated by convolving the model of Sect. 2.1 with the four sets of PSFs corresponding to the four SR values indicated before (object PSFs) and by adding to the results sky background emission and noises as defined in Sect. 2.3. Next the four sets of images are deconvolved using the reference PSFs. The restoration of the binary star is again evaluated in terms of the retrieval of its parameters ρ, PA, and Δm, after deconvolution of the whole object, while the restoration of the circumbinary ring is still evaluated in terms of the retrieval of its azimuthal profile $I_r(\theta)$ and its radial profile $I_\theta(r)$.

Figure 9 shows the results obtained for the binary parameters, in the four SR cases. A first conclusion which can be derived from these plots is that all parameters are remarkably retrieved, for all cases of SR. In particular, if we first consider the plots of the magnitude difference, we find that the different SR cases lead to different errors, from almost zero (case of $SR = 0.93$) to less than 0.07 mag. (case of $SR = 0.53$). The main difference between the four cases consists in different and slightly wrong estimated values of Δm rather than in different convergence rates. On the other hand, the PA plots show that in the cases with $SR = 0.53$, 0.81 and 0.88 the results converge toward the same value (with a final error of a few hundredth of degree only) but at very different rates. The case $SR = 0.93$ is again almost perfect here, converging to the right value in less than 100 iterations. Finally the separation plots show the same behavior as those for Δm, but with a difference between the cases with $SR = 0.81$ and $SR = 0.88$, more similar to the behavior of the PA plots. Note that the final error for ρ is at most ∼0.25 mas for the worst case scenario ($SR = 0.53$), which is still remarkably small.

As concerns the evaluation of the restoration of the circumbinary ring, we have adopted again the two different approaches mentioned in Sect. 3. As it is shown by the upper plots of Fig. 10, the reconstruction of the ring

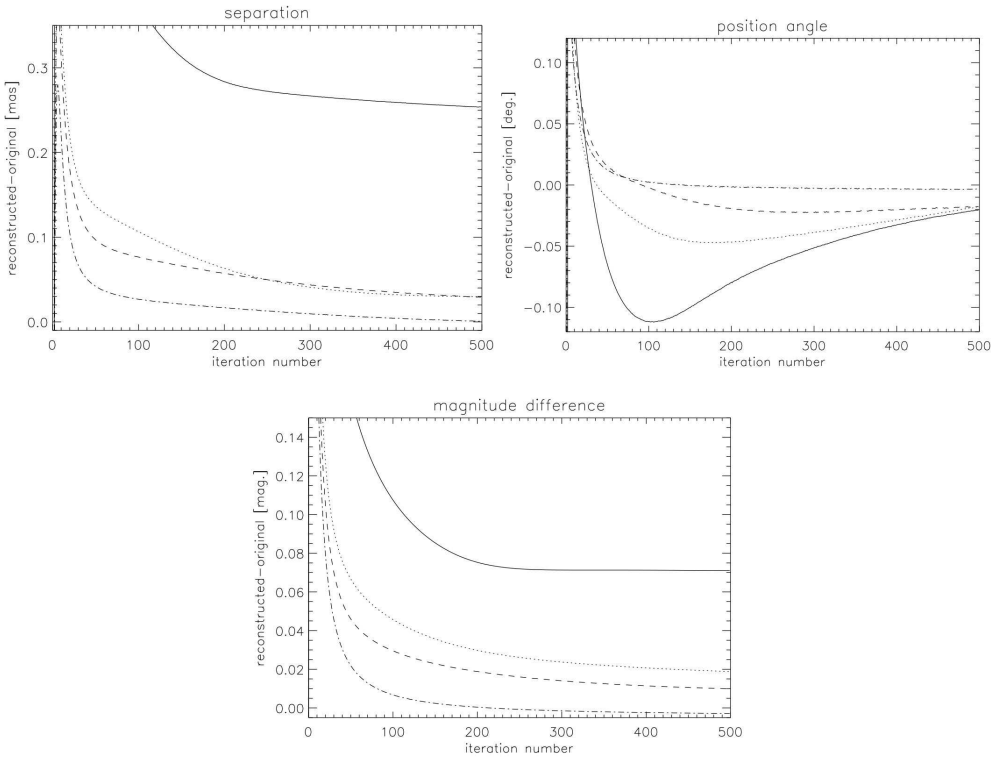

Fig. 9. Restoration of the binary parameters – general AO case: error plots for the separation ρ, position angle PA, and magnitude difference Δm, as functions of the number of OS-EM iterations for the four SR cases. Continuous line is for $SR = 0.53$, dotted line for $SR = 0.81$, dashed line for $SR = 0.88$, and dashed-dotted line for $SR = 0.93$.

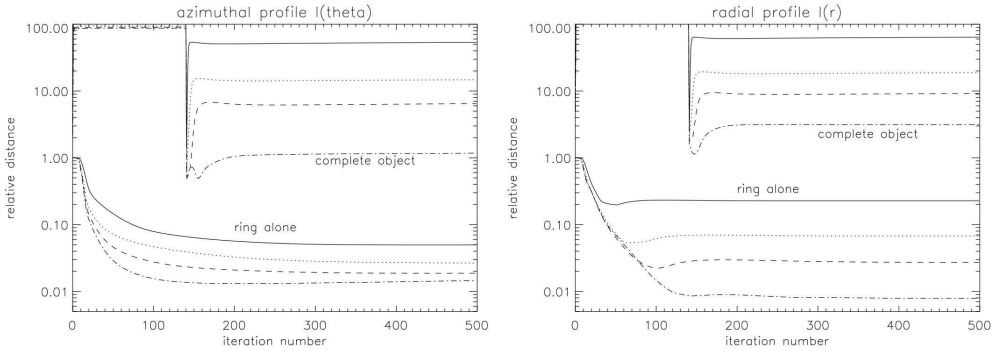

Fig. 10. Restoration of the circumbinary ring parameters – general AO case: logarithmic plots of the relative restoration error on the azimuthal profile $I_r(\theta)$ (left) and on the radial profile $I_\theta(r)$ (right), for the four SR cases. Continuous line is for $SR = 0.53$, dotted-line for $SR = 0.81$, dashed line for $SR = 0.88$, and dashed-dotted line for $SR = 0.93$. Two sets of results are represented: the upper set corresponds to the deconvolution of the data of the complete object, while the bottom set to the deconvolution of the ring data.

as obtained from the complete object data is not satisfactory, while the reconstruction process applied to the subtracted data provides good results. This result underlines the fact that a good PSF-subtraction method will be necessary when dealing with real data of this kind of object. The different values of SR clearly lead to different levels of precision in the restoration of the two profiles, even if the differences are more evident in the case of the radial profile $I_\theta(r)$. In this case, indeed, the final error ranges from ∼20% for the case of $SR = 0.53$, to less than 1% for the $SR = 0.93$ case. For $I_r(\theta)$ the range of error is smaller: from 5% to 1.5%. It is also interesting to point out that in all cases the algorithm converges after about 100–200 iterations.

The overall good accuracy in the reconstruction of the ring is confirmed by Fig. 11 where the reconstructed images are given. While in the case of $SR = 0.53$ the principal features of the ring are already recovered, in the other cases it is also possible to recognize almost all details of the model represented in Fig. 1.

4.3. Uniform MCAO case

In this second application we assume a MCAO system which allows an ideal uniformity of the PSFs over the whole reconstructed FoV. We point out that such a system would not only assure a remarkable similarity between the reference and object PSFs, but would also make easier the search for a suitable reference star since any star in the field can be used. Therefore we simulate such a situation by considering two of the sets of images generated in the previous section (and precisely those corresponding to $SR = 0.94$ and 0.53), and by deconvolving these sets by means of the same PSFs used for their generation.

Figure 12 shows the results obtained for the reconstruction of the binary parameters in the two MCAO cases considered. Note that, for an easier comparison, these plots have the same identical range as those of Fig. 9.

A comparison with the results obtained in the general AO case clearly shows that the possibility of having reference PSFs as similar as possible to the object PSFs greatly improves the precision of the results. No more significant offsets are visible in these curves that almost perfectly converge toward the correct solution, in the case of $SR = 0.94$ as well as in the case of $SR = 0.53$. Especially in this last case, the comparison with the plots of Fig. 9 shows that a better precision *and* a faster convergence are obtained when the similarity between the reference PSFs and the object PSFs is preferred with respect to the choice of a set of reference PSFs better corrected, but different from the object PSFs. The main difference due to a different quality of the global AO-correction consists in a different convergence rate, which is slower in the case of $SR = 0.53$ than in the case of $SR = 0.94$, with a final error which in all cases clearly tends to zero.

As concerns the restoration of the circumbinary ring, the error plots of Fig. 13 for the radial and azimuthal profiles have approximately the same behavior as those for the binary parameters. Here again the comparison with the general AO case shows the great advantage of PSF uniformity. Furthermore it is to be noted that even when deconvolving the whole object, with the already underlined problem of huge dynamic range between the ring and the core binary star, the results on the retrieval of $I_\theta(r)$ and $I_r(\theta)$ are better than those obtained in the general AO case, especially for what concerns the azimuthal profile.

Table 1. Relative distances between the profiles of the incoherent sums of images and those of the model.

Strehl case	rel. dist. on $I_\theta(r)$	rel. dist. on $I_r(\theta)$
0.53	0.33	0.062
0.94	0.19	0.034

It is interesting to compare also the retrieved parameters with those obtained by taking as ring image the incoherent sum of the three interferometric ring images (obtained at the three parallactic angles). In such a way we can directly evaluate the advantage of using the restoration method. The comparison is performed by computing the relative distance between the radial and azimuthal profiles of the incoherent sums and those of the original model. The results are reported in Table 1 and show that the use of the restoration algorithm provides a much better precision, and that this is already true after a few iterations (∼20 in all cases). A visual confirmation of such a result is shown in Fig. 14, where the reconstructed images are represented in both cases of MCAO correction, together with the corresponding incoherent sums. The great resolution achieved in the reconstructed images is evident.

4.4. Discussion

The results described in this section show the importance of having uniform PSFs over the field even with a lower SR, rather than reference PSFs with a high SR but different from the PSFs in other domains of the field. In other words, this means that when designing and/or using an MCAO system, the uniformity of the PSF seems to be more important than its mean value over the corrected FoV. We have shown in fact that, at least from the point of view of our restoration method, and for the range of relatively high SR values we have simulated, it is more convenient to have a SR of ∼50% stable over the FoV than a SR whose average value is higher but with significant variations over the FoV.

We should anyway mention that a possible solution to achieve the same level of precision and convergence rate in the general AO case could be the use of blind deconvolution techniques (see e.g. Jefferies & Christou 1993; Fusco et al. 1999).

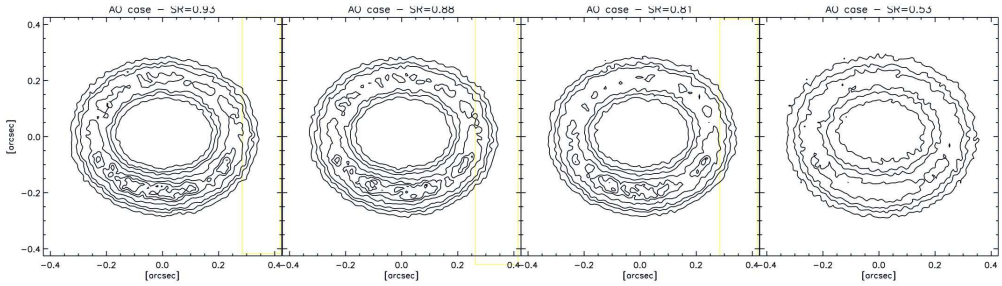

Fig. 11. Restoration of the circumbinary ring – general AO case. The level lines correspond to 0.1, 0.2, 0.3, 0.5, 0.7, 0.8 and 0.9 of the maximum value of the model, and therefore are equivalent to the the level lines of Fig. 1.

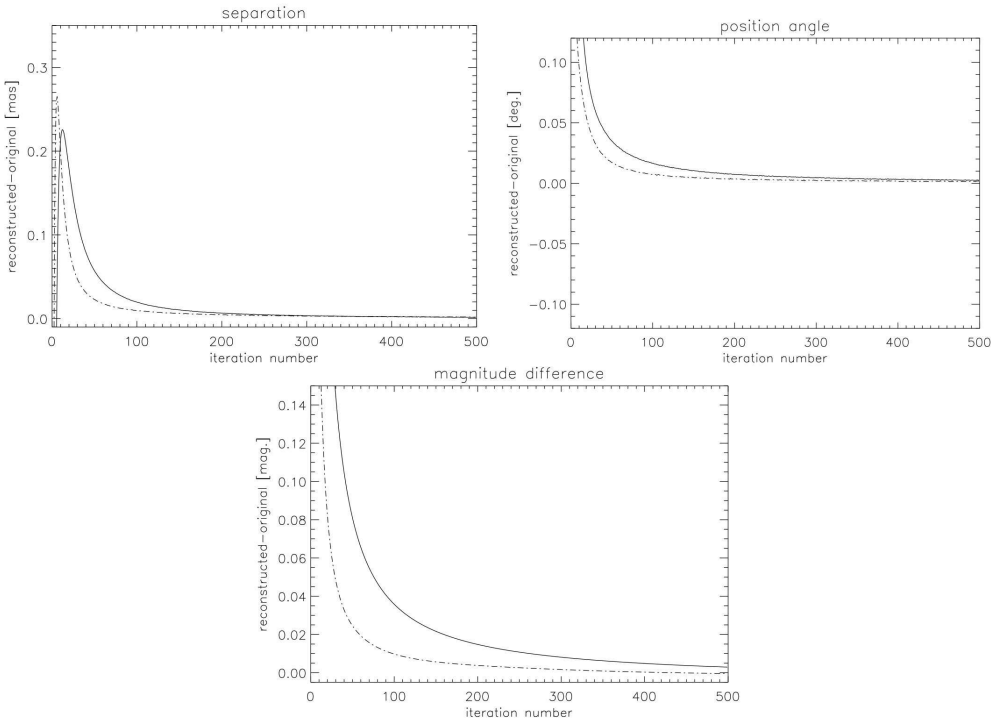

Fig. 12. Restoration of the binary parameters – uniform MCAO case: error plots for the separation ρ, position angle PA, and magnitude difference Δm, as functions of the number of OS-EM iterations for the two SR cases. Continuous line is for $SR = 0.53$, while dashed-dotted line is for $SR = 0.94$.

5. Summary and concluding remarks

In this paper we have applied the first release of the Software Package AIRY (Astronomical Image Restoration in interferometrY) to the case-study of the LBT interferometer. In order to test the interferometric imaging capabilities of LBT we have considered a realistic object: a young binary star surrounded by a faint circumbinary ring. In such a case we have investigated the effect of limited angular coverage and time-averaging smearing on the restored image. Next we have considered the effect of partial AO correction in both cases of general AO and uniform MCAO.

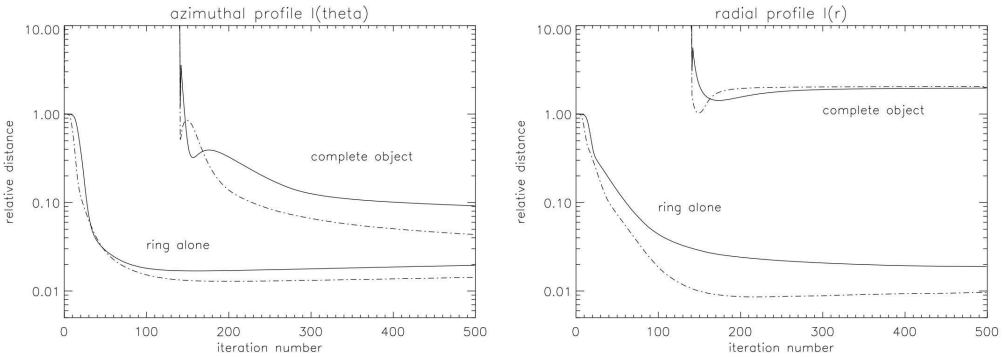

Fig. 13. Restoration of the circumbinary ring parameters – uniform MCAO case: logarithmic plots of the relative restoration error on the azimuthal profile $I_r(\theta)$ (left) and on the radial profile $I_\theta(r)$ (right), for the two SR cases. Continuous line is for $SR = 0.53$, while dashed-dotted line is for $SR = 0.94$. Two sets of results are represented: the upper set corresponds to the deconvolution of the data of the complete object, while the bottom set corresponds to the deconvolution of the ring data.

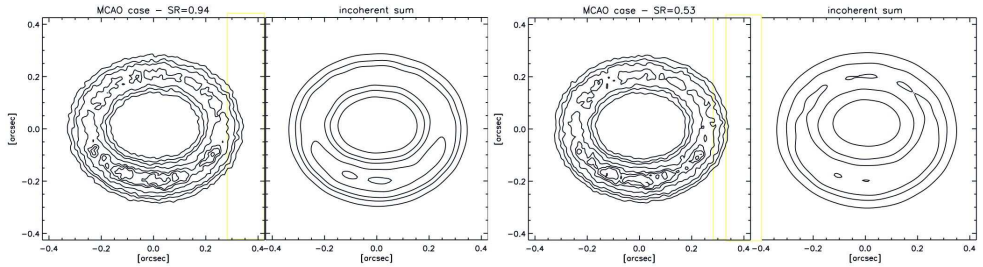

Fig. 14. Restoration of the circumbinary ring – uniform MCAO case. From left to right: the result obtained for $SR = 0.94$ and the corresponding incoherent sum; the result obtained for $SR = 0.53$ and the corresponding incoherent sum. The level lines correspond to 0.1, 0.2, 0.3, 0.5, 0.7, 0.8 and 0.9 of the maximum value of the model, and therefore are equivalent to the level lines of Fig. 1.

We have found that the method intrinsically allows for high-dynamic range imaging. The angular coverage and smearing seems, at the light of the simulations performed, not to affect significantly the large structure of the image nor the parameters of the binary, but only the convergence rate of the iterative method.

For what concerns general AO, we identify a possible direction of investigation in order to overcome the problem of PSF calibration, namely the development and testing of blind deconvolution methods. On the other hand, we have shown that the stability of the PSFs is a main issue for this observational technique, even at the cost of a lower average SR, at least for the field of application we have considered.

Such a condition, which may be satisfied by an MCAO system, is also required by the model of image formation assumed in the deconvolution method (see Paper I, Eq. (1)) and implies that the PSF obtained from a reference star provides a good approximation of the PSF which must be used in the process of image restoration. In addition our results show that, even in the case of relatively low SR, the AO-corrected PSF provides sufficient information at the higher angular frequencies which are accessible in the u–v plane.

Acknowledgements. All the work presented in this paper was done with the help of the Software Package AIRY, version 1.0, and the Software Package CAOS, version 3.0. The Software Package AIRY is obtainable under request and subscription to its dedicated mailing-list by visiting the web site `http://dirac.disi.unige.it`. The Software Package CAOS is obtainable under request and subscription to its dedicated mailing-list by visiting the web site `http://www.arcetri.astro.it/caos`. Both software packages are delivered together with the CAOS Application Builder (version 3.0): the IDL-based graphical environment within which they were developed.

We thank Piero Ranfagni for his help in astrometry, Piero Salinari for several stimulating discussions, Elena Masciadri for useful comments on the manuscript, and Luca Fini for the graphical tools of AIRY and CAOS. This work was also partially funded by CNAA (Consorzio Nazionale per l'Astronomia e l'Astrofisica) under the contract No. 16/97.

References

Bello, D., Conan, R., Le Roux, B., et al. 2001, in ESO Proc. Beyond Conventional Adaptive Optics, ed. É. Vernet, R. Ragazzoni, S. Esposito, & N. Hubin

Bertero, M., & Boccacci, P. 1998, Introduction to Inverse Problems in Imaging (IOP Publishing, Bristol)

Bertero, M., & Boccacci, P. 2000a, A&AS, 144, 181

Bertero, M., & Boccacci, P. 2000b, A&AS, 147, 323

Carbillet, M., Correia, S., Femenía, B., & Riccardi, A. 2000, in SPIE Conf. Ser. 4007, Adaptive Optical Systems Technology, ed. P. L. Wizinowich, 155

Carbillet, M., Fini, L., Femenía, B., et al. 2001a, in ASP Conf. Ser. ADASS X, ed. F. A. Primini, & F. R. Harnden, 249

Carbillet, M., Femenía, B., Esposito, S., Brusa, G., & Correia, S. 2001b, in ESO Proc. Beyond Conventional Adaptive Optics, ed. É. Vernet, R. Ragazzoni, S. Esposito, & N. Hubin

Correia, S., Carbillet, M., Richichi, A., Bertero, M., & Boccacci, P. 2000, in SPIE Proc. 4006, Interferometry in Optical Astronomy, ed. P. J. Léna, & A. Quirrenbach, 650

Correia, S., Carbillet, M., Fini, et al. 2001, in ASP Conf. Ser. ADASS X, ed. F. A. Primini, & F. R. Harnden, 404

Correia, S., Carbillet, M., Boccacci, P., & Bertero, M. 2002, A&A, 387, 733

Esposito, S., Riccardi, A., & Femenía, B. 2000, A&A, 353, L29

Femenía, B., Carbillet, M., Esposito, S., & Riccardi, A. 2000, in SPIE Proc. 4006, Interferometry in Optical Astronomy, ed. P. J. Léna, & A. Quirrenbach, 1116

Fini, L., Carbillet, M., & Riccardi, A. 2001, in ASP Conf. Ser. ADASS X, ed. F. A. Primini, & F. R. Harnden, 253

Fusco, T., Véran, J. P., Conan, J. M., & Mugnier, L. M. 1999, A&AS, 134, 193

Ghez, A. M., White, R. S., & Simon, M. 1997, ApJ, 490, 353

Jefferies, S. M., & Christou, J. C. 1993, ApJ, 415, 862

Krist, J. E., Stapelfeldt, K. R., Menard, F., Padgett, D. L., & Burrows, C. J. 2000, ApJ, 538, 793

Lanteri, H., Soummer, R., & Aime, C. 1999, A&AS, 140, 235

Lanteri, H., Roche, M., Cuevas, O., & Aime, C. 1999, in SPIE Proc. 3866, Optics in Atmospheric Propagation & Adaptive Systems III, ed. A. Kohle, & J. D. Gonglewski, 144

Roddier, C., Roddier, F., Northcott, M. J., Graves, J. E., & Jim, K. 1996, ApJ, 463, 326

Shepp, L. A., & Vardi, Y. 1982, IEEE Trans. Med. Imaging MI-1, 113

White R. L. 1994, in The Restoration of HST Images and Spectra II. Space Telescope Science Institute, ed. R. J. Hanish, & R. L. White, 104

Wood, K., Crosas, M., & Ghez, A. 1999, ApJ, 516, 335

3.2.2 Études successives

L'article reproduit à la Sous-sec. 1.2.3 présentait l'outil `AIRY`, avec une étude sur les limites intrinsèques de la méthode OSEM, dans le cas de l'objet le plus simple qui soit du point de vue de l'imagerie : une étoile binaire résolue (mais aux composantes non-résolues), ainsi que dans le cas d'un objet étendu/diffus. La possibilité de super-résoudre y était également démontrée.

Cette possibilité sera par la suite étudiée en détail dans Anconelli et al. [79] dans le cadre de sa thèse, sur des données simulées d'images partiellement corrigées d'objets compacts (des étoiles doubles/multiples aux séparations non-résolues par le télescope cette fois-ci) et avec une attention particulière aux limites atteignables en séparation angulaire et en différence de magnitude. La super-résolution sera un sujet repris lors de son application à des données post-OA réelles à la Sec. 3.3.

L'article présenté à la sous-section précédente était quant à lui dédié à l'étude des limitations dues à la couverture angulaire et à la correction OA partielles. Les articles qui en ont suivi se sont attaqués d'une part à la recherche d'accélérations ultérieures possibles [78], dans le but de proposer des méthodes d'imagerie rapides à utiliser en temps réel ou presque, mais non-optimisées pour un problème particulier. D'autre part, différentes régularisations ont été également considérées, permettant soit une réduction des effets de bord [87], soit la déconvolution d'images d'objets possédant une très haute dynamique [88, 102]. L'application de la déconvolution aveugle, déjà évoquée dans l'étude de la Sous-sec.3.2.1 pour le cas de l'imagerie grand champ, est mise en place dans Desiderà et al. [94]. Enfin, l'utilisation d'une contrainte de Strehl dans ce dernier cas de déconvolution aveugle est proposée dans Desiderà & Carbillet [119].

Cette dernière proposition, issue du travail de thèse de G. Desiderà durant son séjour à Nice en 2009, est détaillée, et l'article correspondant reproduit, à la Sec. 3.4).

Une introduction au problème général abordé a également été publié [124], ainsi qu'un article de revue [143] faisant le point sur l'ensemble des méthodes développées jusqu'alors et listant les questions restées ouvertes malgré tout.

3.3 Super-résolution par déconvolution

3.3.1 *Deconvolution-based super-resolution for post-adaptive-optics data*

L'algorithme de super-résolution proposé a été largement décrit par Anconelli et al. [79], et même déjà abordé par Correia et al. [58]), et est illustré ici à la Fig. 3.3. Cette figure montre bien le type de séparation qui peut être espérée pour un objet multiple dont chacune des séparations est inférieure à l'élément de résolution du télescope en question.

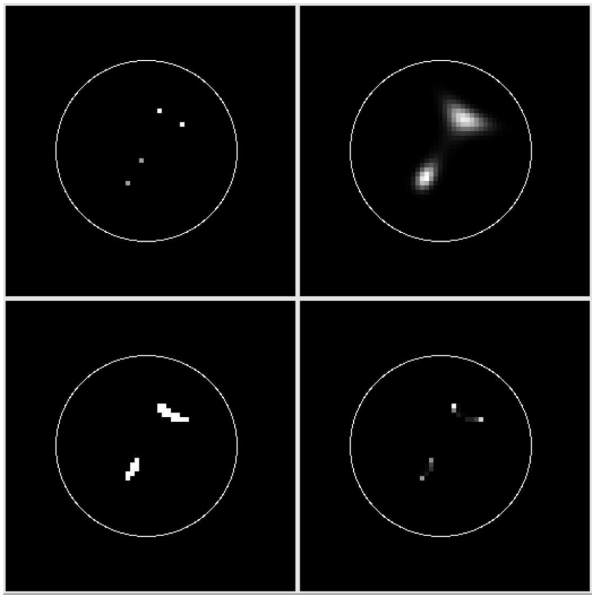

FIGURE 3.3: De gauche à droite et de haut en bas : l'objet (une étoile quadruple), la reconstruction obtenue après 1000 itérations d'un premier passage de déconvolution classique (Lucy-Richardson), le masque construit grâce à un seuil de 50% de la valeur maximum de la reconstruction précédente, la reconstruction après le deuxième passage de Lucy-Richardson. Le diamètre du cercle montré correspond à l'élément de résolution du télescope (ici du LBT en mode interférométrique). *(Figure tirée de Anconelli et al. [79].)*

Une première application de cet algorithme a été récemment effectuée sur des données réelles obtenues sur NACO/VLT et est détaillée dans l'article présenté à la conférence « Adaptive Optics for Extremely Large Telescopes #3 » à Florence en mai 2013, reproduit ci-après. Une détection de binaire serrée (à $\sim$30 mas en bande K, soit seulement $\sim$2 px, i.e. à peine plus d'un demi-élément de résolution sur le VLT) est confirmée par des observations interférométriques à l'aide d'AMBER/VLTI.

La méthode SGP (pour *Scaled Gradient Projection*) y est également testée en tant qu'accélération, ce qui devrait se révéler utile avec les données largement sur-échantillonnées que réclamerait idéalement la méthode.

DECONVOLUTION-BASED SUPER-RESOLUTION FOR POST-ADAPTIVE-OPTICS DATA

Marcel Carbillet[1a], Andrea La Camera[2b], Olivier Chesneau[3], Florentin Millour[3], Julien H. V. Girard[4], and Marco Prato[5]

[1] UMR 7293 Lagrange (Université de Nice Sophia-Antipolis/CNRS/Observatoire de la Côte d'Azur), Parc Valrose, 06100 Nice, France
[2] Dipartimento di Informatica, Bioingegneria, Robotica e Ingegneria dei Sistemi (Università di Genova), Via Dodecaneso 35, 16145 Genova, Italia
[3] UMR 7293 Lagrange (Université de Nice Sophia-Antipolis/CNRS/Observatoire de la Côte d'Azur), Boulevard de l'Observatoire, BP 4229, 06300 Nice, France
[4] European Southern Observatory, Casilla 19001, Vitacura, Santiago, Chile
[5] Dipartimento di Scienze Fisiche, Informatiche e Matematiche (Università di Modena e Reggio Emilia), Via Campi 213/b, 41125 Modena, Italia

Abstract. This article presents preliminary results on NACO/VLT images of close binary stars obtained by means of a Richardson-Lucy-based algorithm of super-resolution, where down to roughly a half-resolution element is attained, and with confirmation from VLTI observations in one of the cases treated. A new gradient method, the scaled gradient projection (SGP), permitting the acceleration of the used method, is also tested with the same scope.

1 Introduction

Super-resolution is a term which classically refers to methods aiming at going beyond the diffraction limit of an optical instrument such as a telescope. In our case, which is actually not relevant to a specific type of instrument but to the post-processing of the data obtained, we would rather use the term *computational super-resolution* (CSR). It is worthwhile to immediately note that CSR is not feasible in all situations/observational conditions, and, when it is possible, it is never unlimited [1].

The ideal angular resolution of a circular telescope is usually approximated by λ/D (where λ is the observing wavelength and D the diameter of the entrance pupil of the telescope, and forgetting for now about all the internal and atmospherically-induced aberrations which would dramatically enlarge it), which is roughly the full width at half-maximum (FWHM) of the Airy disc and (hence!) the empirical Dawes' limit, practically much rather used than the (somehow conservative) Rayleigh criterion, $1.22\,\lambda/D$.

CSR aims at breaking (when possible) this λ/D resolution limit by means in the present paper of deconvolution which, in addition to pretend to correct for the various residual aberrations due to the turbulent atmosphere, the adaptive optics (AO) system trying to correct from the effects of the latter, the telescope, and the imaging instrument, also pretends here to correct from the degradation due to diffraction.

[a] marcel.carbillet@unice.fr
[b] andrea.lacamera@unige.it

This basically translates into extrapolation of the Fourier spectrum of the image outside of the transmission band of the global imaging system (atmosphere⊕telescope⊕instrument), i.e. beyond the limiting angular frequency D/λ. See again Bertero & Boccacci [1] for a complete description of this out-of-band process.

In the case of post-AO astronomical imaging, it has been demonstrated (although by means of numerical simulations) that, in case of relatively high signal-to-noise ratio and relatively good AO correction, a gain of a factor 4 to 5 in resolution can be achieved [6]. A necessary condition anyway is also the fact that the object must be compact, with an angular size of the order of, or smaller than, λ/D.

Here, with real data and no particular careful pre-processing of it, and a very low angular sampling (e.g. large pixel size) with respect to the scopes of the method, we reach roughly half a resolution element, which can be considered as an encouraging starting point.

The paper is organised as follows. Next section, Sec. 2, presents the Richardson-Lucy (RL) method and its origins. Then, Sec. 3 exposes the CSR algorithm based on the RL method itself, and Sec. 4 proposes an alternative version of it, accelerated by means of the scaled gradient projection (SGP) method. Then, Sec. 5 shows and comments on the preliminary results obtained from VLT/NACO data of close binary stars in the wavebands K_s and L. Finally, Sec. 6 draws up a summary of the work performed up to now and gives our conclusions and perpectives for the next future.

2 Richardson-Lucy deconvolution method

Let us define $\mathbf{f}$ as the scientific target, $\mathbf{g}$ the acquired image to be deconvolved, $\mathbf{b}$ the sky background, and A the imaging matrix given by $A\mathbf{f} = \mathbf{K} * \mathbf{f}$, where $*$ is the convolution operator and K is the point-spread function (PSF), normalized to a unit volume. In the case of Poisson noise, the general approach to the deconvolution methods follows the minimization of the Kullback-Leibler (KL) divergence given by:

$$J_0(\mathbf{f};\mathbf{g}) = \sum_{\mathbf{m}\in S}\left\{\mathbf{g}(\mathbf{m})\ln\frac{\mathbf{g}(\mathbf{m})}{(A\mathbf{f})(\mathbf{m})+\mathbf{b}(\mathbf{m})} + (A\mathbf{f})(\mathbf{m})+\mathbf{b}(\mathbf{m})-\mathbf{g}(\mathbf{m})\right\}. \tag{1}$$

From well-known properties of this functional, it follows that J_0 is *non-negative*, *convex*, and *coercive*. So that absolute minimizers of this function exist: the so-called *maximum likelihood* solutions of the image reconstruction problem. The RL method [2,3] follows from the computation of the gradient of J_0 and the application of the Karush-Kuhn-Tucker conditions. It is described in Algorithm 1.

Algorithm 1 RL method

Choose the starting point $\mathbf{f}^{(0)} \geq 0$

For $k = 0, 1, 2, \ldots$ compute:

$$\mathbf{f}^{(k+1)} = \mathbf{f}^{(k)} A^T \frac{\mathbf{g}}{A\mathbf{f}^{(k)}+\mathbf{b}}$$

End

3 Richardson-Lucy-based super-resolution

The global method used in this paper is based on the well-known property of RL which allows CSR [4,5,1]. It consists in the following two steps, as described in Anconelli et al. [6]

- STEP 1 – Compute a large number of RL iterations, assuming a constant array as initial guess of the algorithm. We denote the result of this step by $\mathbf{f_1}$.
- STEP 2 – Define the (compact) support $\mathcal{S}$ of the object as the pixels where the flux of $\mathbf{f_1}$ is greater than a selected threshold, or alternatively an area of angular dimension of the order of the resolution element of the data, λ/D. Next, initialize the algorithm using the mask with pixels set to one inside and to zero outside the domain $\mathcal{S}$. Then, compute again a large number of RL iterations, obtaining the final reconstructed image $\mathbf{f_2}$.

The CSR method described above and used in the following is implemented within the last distributed versions of the `Software Package AIRY` [7,8], developed within the `CAOS` problem-solving environment (`PSE`) [9,10], and used in the following of the paper.

4 Scaled gradient projection acceleration

The RL algorithm can be seen as a particular case of a scaled gradient method. Indeed, since

$$\mathbf{f}^{(k+1)} = \mathbf{f}^{(k)} - \mathbf{f}^{(k)}\left(\mathbf{1} - A^T\frac{\mathbf{g}}{A\mathbf{f}^{(k)}+\mathbf{b}}\right) = \mathbf{f}^{(k)} - \mathbf{f}^{(k)}\nabla J_0(\mathbf{f}^{(k)};\mathbf{g}) \,, \tag{2}$$

it follows that the RL iteration can be obtained from the general scaled gradient algorithm:

$$\mathbf{f}^{(k+1)} = \mathbf{f}^{(k)} - \lambda_k(P_+(\mathbf{f}^{(k)} - \alpha_k D_k \nabla J_0(\mathbf{f}^{(k)};\mathbf{g})) - \mathbf{f}^{(k)}) \,, \tag{3}$$

by choosing the constant steplengths $\lambda_k = \alpha_k = 1$, the scaling matrix $D_k = \mathrm{diag}(\mathbf{f}^{(k)})$, and by remarking that for RL the projection P_+ on the non-negative pixels can be avoided since it is automatically satisfied by the iteration.

The choice of constant steplengths makes RL not very efficient and several acceleration schemes have been proposed in the literature to improve its convergence rate. The SGP method [11] is an optimization method for the minimization of the KL divergence that uses the scaling of the gradient suggested by RL, but exploits an adaptive strategy for the steplength parameters. For this reason, SGP can be considered as a more efficient version of RL.

The SGP scheme is described in Algorithm 2. For a general version of the algorithm and, in particular, for the computation of the steplength parameter α_k, we refer to Bonettini et al. [11] and Prato et al. [12]

Algorithm 2 SGP method

Choose the starting point $\mathbf{f}^{(0)} \geq 0$ and set the parameters $\beta, \theta \in (0,1)$, $0 < \alpha_{min} < \alpha_{max}$.

FOR $k = 0, 1, 2, \ldots$ DO THE FOLLOWING STEPS:

STEP 1. Choose the parameter $\alpha_k \in [\alpha_{min}, \alpha_{max}]$ and the scaling matrix D_k;

STEP 2. Projection:

$$\mathbf{y}^{(k)} = P_+(\mathbf{f}^{(k)} - \alpha_k D_k \nabla J_0(\mathbf{f}^{(k)}; \mathbf{g}));$$

STEP 3. Descent direction: $\mathbf{d}^{(k)} = \mathbf{y}^{(k)} - \mathbf{f}^{(k)}$;

STEP 4. Set $\lambda_k = 1$;

STEP 5. Backtracking loop:

IF $J_0(\mathbf{f}^{(k)} + \lambda_k \mathbf{d}^{(k)}; \mathbf{g}) \leq J_0(\mathbf{f}^{(k)}; \mathbf{g}) + \beta \lambda_k \nabla J_0(\mathbf{f}^{(k)}; \mathbf{g})^T \mathbf{d}^{(k)}$

THEN go to step 6;

ELSE set $\lambda_k = \theta \lambda_k$ and go to step 5.

ENDIF

STEP 6. Set $\mathbf{f}^{(k+1)} = \mathbf{f}^{(k)} + \lambda_k \mathbf{d}^{(k)}$.

END

The acceleration of the CSR can be obtained applying the same scheme described in previous section, replacing RL with SGP. The SGP method will be implemented in the next distributed version of the `Software Package AIRY`.

We apply in the following the two methods described to NACO/VLT data of very close binary stars, but in the case of SGP we push the algorithm to convergence, i.e. we compute the *objective function* $J_0(\mathbf{f}^{(k)}; \mathbf{g})$ at each iteration and we stop the iteration when this function is (almost) constant — i.e., according to a given tolerance ϵ, when

$$|J_0(\mathbf{f}^{(k)}; \mathbf{g}) - J_0(\mathbf{f}^{(k-1)}; \mathbf{g})| < \epsilon \cdot J_0(\mathbf{f}^{(k)}; \mathbf{g}) \, . \tag{4}$$

5 Preliminary results on NACO/VLT data

The data presented in this section were obtained by using the NACO adaptive optics camera (NAos adaptive optics system combined with the COnica camera, see Rousset et al. [13]) attached to the telescope UT 4 of the Very Large Telescope (VLT).

HD 87643

The data considered here are K_s-band data (2.18-μm) obtained with NACO/VLT and already analyzed by Millour et al. [14] together with VLTI observations of the same object: HD 87643. A first deconvolution of the NACO/VLT data has already also been presented in Le Bouquin et al. [15], but in both cases the (very close) binary star could not have been resolved. At the opposite, in Millour et al. [14], the observations of the same object using the interferometric instrument AMBER onboard the VLTI (the VLT long-baseline interferometer) clearly showed the binarity of the source.

The data analyzed here were taken with an atmospheric seeing of $\sim$0.″9, a total exposure time of $\sim$90 s, and by using camera mode S 13, with a pixel size of 13 mas and a 14″×14″ field of view. The Strehl ratio associated to these data is estimated to be 0.43±0.04, which is somehow limited with respect to the limitations expected for this method (see Sec. 1).

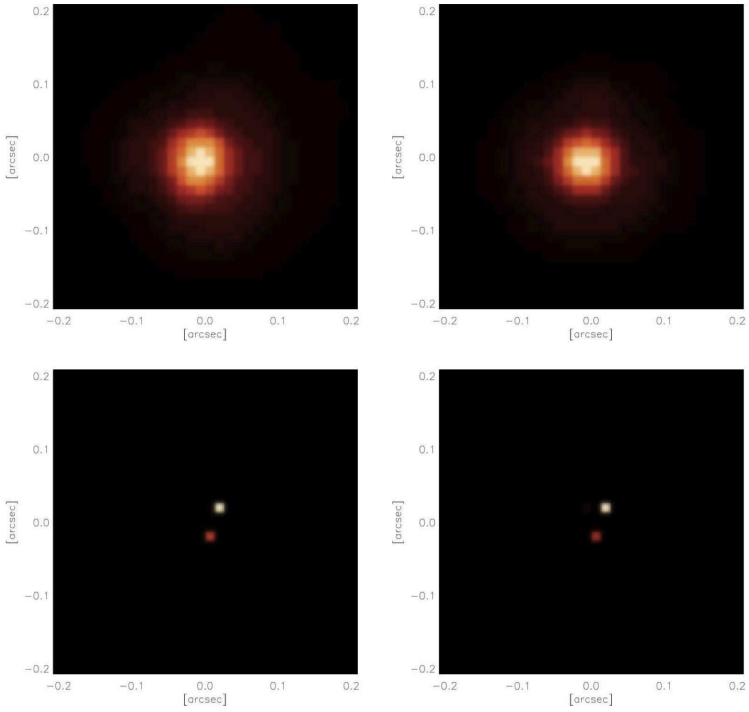

Fig. 1. From left to right and from top to bottom: post-NACO image of HD 87643, corresponding PSF, RL-based CSR reconstruction, RL-based SGP-accelerated CSR reconstruction. The resolution element is here $\lambda/D \simeq 56$ mas, corresponding to (a little bit more than) 4.3 px, the pixel size being of 13 mas. The binary separation found is $\rho \simeq 32$ mas $\simeq 2.45$ px $\simeq 0.57\,\lambda/D$.

The data pre-processing performed removed bad pixels, applied a flat-field correction, and also subtracted the sky background. Moreover, the PSF (estimated from images of the unresolved star HD 296986) was not exactly diffraction-limited since its FWHM was found to be 75 mas (see Millour et al. [14] for more details on these pre-processing points).

Figure 1 shows the results obtained by applying both our deconvolution-based CSR methods to our HD 87643 observations. A second set of data was also processed, giving fully similar results. Both results are also similar to the result obtained with the AMBER/VLTI data published in Millour et al. [14] Hence we can conclude that we have here fully validated our approach(es) of CSR.

HIP 113010 (HD 216405)

The data considered here are L'-band data (3.8-μm) obtained again with NACO/VLT. The resolution element is $\lambda/D \simeq 98$ mas, corresponding to (a little bit less than) 3.6 px, the pixel size being of $\simeq 27.2$ mas.

The observational conditions were good ones, leading to a Strehl ratio $\gtrsim 0.8$ in the observing waveband. Figure 2 shows the (pre-processed) image obtained. Component B (upper part of the image) was used as the PSF in order to deconvolve components AC (lower part of the image). In the same figure the results obtained with both methods employed are also shown and commented.

Although in this latter case the task is easier than previously because the binarity of the object could already be recognized in the pre-processed data (elongated shape clearly distinguishable from the PSF centro-symmetric shape), these results are also a matter for super-resolution.

Discussion

With the RL-based CSR algorithm 5000 iterations were performed for the first step and 1000 iterations for the second step. With in addition the SGP acceleration, the number of iterations were between ∼140 and ∼590 for the first step, and between ∼43 and ∼150 for the second step. The results are very similar in both cases.

Although the computational cost is heavier with SGP, we have at the end a resulting global speed-up between ∼7.5 and ∼24 when SGP is employed. In any case, and with such tiny regions of interest (in terms of number of pixels concerned by the object reconstruction process), computational times were in both cases quite small: between 14 s and 50 s for RL, and between 0.6 s and 6.7 s for SGP, on an Intel Core 2 Duo at 2.4 GHz. It is nevertheless worthwhile to note that, with a dedicated camera, with much more pixels per resolution element in order to fully take advantage from the CSR method, or simply by considering post-observational over-sampling of the data before applying our two CSR methods, this computational time gain would begin to be more interesting.

A last point concerns the photometric accuracy. No particular effort was made here, but our next-to-come step is to implement the third step of the procedure described in Anconelli et al. [6] and apply it to the data presented, permitting an a priori better reconstruction of the objects, and hopefully a quantitative comparison between the accuracies permitted with RL and SGP.

6 Summary and perspectives

In this paper we have presented a simple algorithm of CSR based on the very well known RL deconvolution method. An acceleration of it, based on the SGP method, is also presented in complement of the main one for possible acceleration of the reconstruction process. Both methods were tested and gave very encouraging results on two close binary stars observed with VLT/NACO in the wavebands K_s (for HD 87643) and L (for HIP 113010/HD 216405).

In the case of HD 87643, it has also been observed using the interferometric instrument AMBER onboard the VLTI and its binarity (half of the resolution limit of the VLT in band K_s) was clearly established with very similar results concerning the angular separation of the binary star, validating so our CSR approach in practice.

Further work on these data will concern first of all a careful pre-processing, with an estimation of the background to be used afterwards within the deconvolution method (rather than subtraction of it before deconvolution), then an over-sampling of the data before applying the CSR method(s), and, last but not least, an implementation of the third step of the

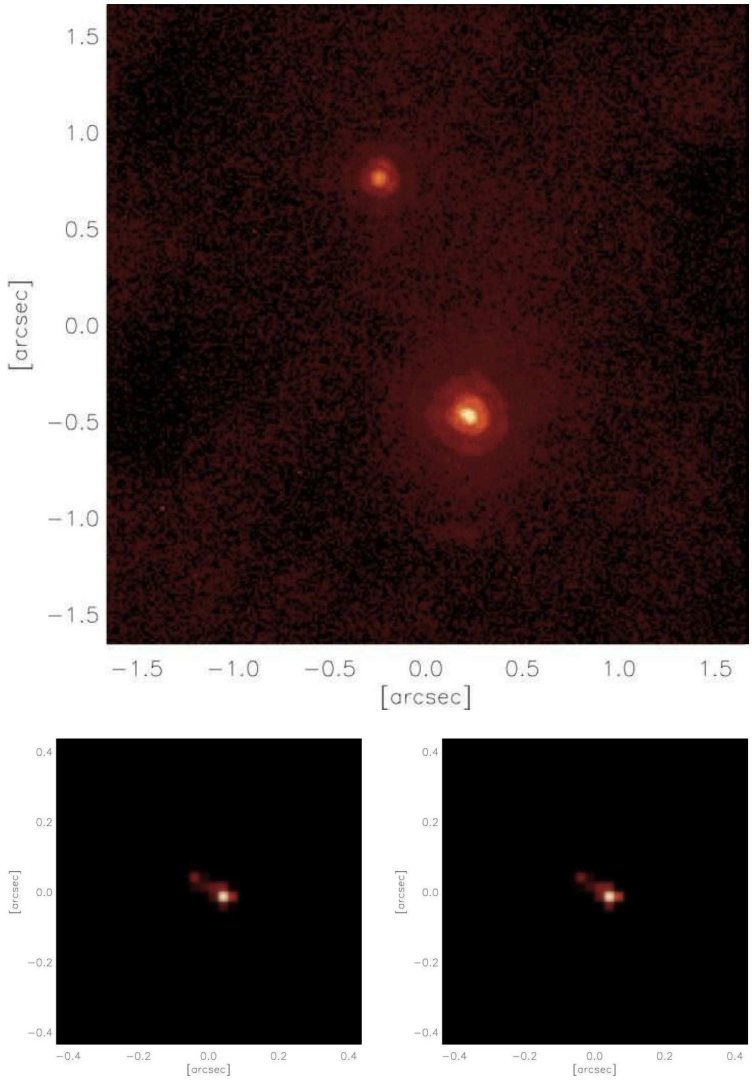

Fig. 2. From left to right and from top to bottom: post-NACO image of HIP 113010 (HD 216405), RL-based CSR reconstruction, RL-based SGP-accelerated CSR reconstruction. The binary separation found is $\rho \simeq 84$ mas $\simeq 3.0$ px $\simeq 0.86\,\lambda/D$.

method described in detail in Anconelli et al. [6] and permitting an a priori better reconstruction of the objects and hence a better quantitative comparison between the accelerated SGP method and the original RL one.

Finally note that this study has been performed by using the `Software Package AIRY` (see `http://airyproject.eu` for more details), developed within the `CAOS PSE` (see `http://lagrange.oca.eu/caos` for more details and to possibly freely download the last versions of both the `CAOS PSE` and the `Software Package AIRY`).

References

1. M. Bertero & P. Boccacci, *Micron* **34**, (2003) 265–273.
2. W. H. Richardson, J. Opt. Soc. Am. **62 (1)**, (1972) 55–59.
3. L. B. Lucy, Astron. J. **79**, (1974) 745–754.
4. M. Bertero & C. De Mol, *Progress in Optics XXXVI* (E. Wolf Ed., Elsevier, Amsterdam 1996) Chap. III.
5. M. Bertero & P. Boccacci, *Introduction to inverse problems in imaging* (IoP Publishing, Bristol 1998).
6. B. Anconelli, M. Bertero, P. Boccacci, M. Carbillet, Astron. Astrophys. **431**, (2005) 747–756.
7. S. Correia, M. Carbillet, P. Boccacci, M. Bertero, L. Fini, Astron. Astrophys. **387 (2)**, (2002) 733–743.
8. A. La Camera, M. Carbillet, C. Olivieri, P. Boccacci, M. Bertero, SPIE Proc. **8445**, (2012) 84453E–84453E-14.
9. M. Carbillet, C. Vérinaud, M. Guarracino, L. Fini, O. Lardière, B. Le Roux, A. T. Puglisi, B. Femenía, A. Riccardi, B. Anconelli, S. Correia, M. Bertero, P. Boccacci, SPIE Proc. **5490**, (2004) 550–559.
10. M. Carbillet, G. Desiderà, E. Augier, A. La Camera, A. Riccardi, A. Boccaletti, L. Jolissaint, D. Ab Kadir, SPIE Proc. **7736**, (2010) 773644–773644-8.
11. S. Bonettini, R. Zanella, L. Zanni, Inverse Prob. **25(1)**, (2009) 015002.
12. M. Prato, R. Cavicchioli, L. Zanni, P. Boccacci, M. Bertero, Astron. Astrophys. **539**, (2012) A133.
13. G. Rousset, F. Lacombe, P. Puget, N. N. Hubin, É. Gendron, T. Fusco, R. Arsenault, J. Charton, P. Feautrier, P. Gigan, P. Y. Kern, A.-M. Lagrange, P.-Y. Madec, D. Mouillet, D. Rabaud, P. Rabou, É. Stadler, G. Zins, SPIE Proc. **4839**, (2003) 140–149.
14. F. Millour, O. Chesneau, M. Borges Fernandes, A. Meilland, G. Mars, C. Benoist, É. Thiébaut, P. Stee, K.-H. Hofmann, F. Baron, J. Young, P. Bendjoya, A. Carciofi, A. Domiciano de Souza, T. Driebe, S. Jankov, P. Kervella, R. G. Petrov, S. Robbe-Dubois, F. Vakili, L. B. F. M. Waters, G. Weigelt, Astron. Astrophys. **507**, (2009) 317–326.
15. J.-B. Le Bouquin, F. Millour, A. Meilland, The Messenger **137**, (2009) 25–29.

3.3.2 Études en cours et perspectives d'application

Cet algorithme nécessite d'être testé en fonction du rapport de Strehl et du rapport signal-à-bruit caractérisant les données post-OA considérées. En effet, on s'attend déjà à ce que ces deux facteurs limitent sensiblement son domaine d'application, mais une étude complète et détaillée en ce sens doit être effectuée afin de quantifier ces limitations. L'implémentation de la troisième étape décrite dans Anconelli et al. [79], devant permettre une meilleure reconstruction photométrique de l'objet, fait également partie des nécessités immédiates concernant cet algorithme du `Software Package AIRY`. Un retraitement des données, incluant évaluation soignée du fond de ciel (pris en compte par la suite dans l'algorithme de reconstruction), sur-échantillonage numérique (à défaut d'optique) et application de la troisième étape de l'algorithme originellement proposé de super-résolution, devrait suivre rapidement.

Mais l'idée motrice pour cet algorithme est de le proposer par la suite pour des observations avec SPHERE sur le VLT et LUCIFER sur le LBT, pour les télescopes de la classe 8 mètres, à cause de la capacité de leurs systèmes d'OA de produire des rapports de Strehl relativement élevés, mais également le LBT en mode interférométrique, et, plus avant, l'E-ELT pour lequel la limite en magnitude des objets pourra être logiquement encore repoussée.

3.4 Déconvolution sous contrainte de Strehl

3.4.1 *Strehl-constrained iterative blind deconvolution for post-adaptive-optics data*

Les potentialités de la contrainte de Strehl sont illustrées dans l'article présenté ici, publié par *Astronomy & Astrophysics* en 2009. L'erreur de reconstruction y est tracée en fonction du rapport de Strehl caractérisant les données, tant pour ce qui est de la PSF que de l'objet. Le gain obtenu par l'application de la contrainte de Strehl atteint jusqu'à un facteur $\sim$10 pour le rapport de Strehl le plus faible ($\sim$0.17 ici). Mais aussi, l'erreur de reconstruction reste pratiquement constante (de quelques pourcents ici) quelque soit le rapport de Strehl caractérisant les données (dans la gamme 0.17–0.68).

Un gain en termes de stabilité de la reconstruction en fonction des nombres d'itérations (d'une part pour la reconstruction de l'objet et d'autre part pour celle de la PSF) se manifeste également. Du point-de-vue de l'utilisateur (observateur/« traiteur » des données), ce deuxième point est encore plus intéressant. Il permet en effet de diminuer de manière drastique les risques liés au choix du nombre d'itérations pour la reconstruction : on passe dans les exemples pris de quelques pourcents à $\sim$100% d'erreur ou plus en se trompant d'un ordre de grandeur sur les nombres d'itérations sans utiliser la contrainte de Strehl, mais seulement de quelques pourcents à un peu plus de 10% si l'on applique cette contrainte.

A&A 507, 1759–1762 (2009)
DOI: 10.1051/0004-6361/200912913

Astronomy & Astrophysics

Strehl-constrained iterative blind deconvolution for post-adaptive-optics data

G. Desiderà[1,2] and M. Carbillet[2]

[1] DISI, Università di Genova, Via Dodecaneso 35, 16146 Genova, Italy
e-mail: desidera@disi.unige.it
[2] UMR 6525 H. Fizeau, Université de Nice Sophia Antipolis/CNRS/Observatoire de la Côte d'Azur, Parc Valrose, 06108 Nice Cedex 2, France
e-mail: marcel.carbillet@unice.fr

Received 17 July 2009 / Accepted 4 September 2009

ABSTRACT

Aims. We aim to improve blind deconvolution applied to post-adaptive-optics (AO) data by taking into account one of their basic characteristics, resulting from the necessarily partial AO correction: the Strehl ratio.
Methods. We apply a Strehl constraint in the framework of iterative blind deconvolution (IBD) of post-AO near-infrared images simulated in a detailed end-to-end manner and considering a case that is as realistic as possible.
Results. The results obtained clearly show the advantage of using such a constraint, from the point of view of both performance and stability, especially for poorly AO-corrected data. The proposed algorithm has been implemented in the freely-distributed and CAOS-based Software Package AIRY.

Key words. methods: data analysis – methods: numerical – techniques: image processing

1. Introduction

Blind deconvolution is well suited for post-adaptive-optics (AO) data when the associated point-spread function (PSF) is poorly known, hence not permitting a satisfactory deconvolution and a subsequent optimal astrophysical interpretation from the reconstructed object. To improve PSF reconstruction (and hence the whole blind deconvolution process in order to obtain better reconstructed objects), one possibility is to use a priori information about the physical features of the PSF (Bertero & Boccacci 1998). For this purpose we propose to simply consider one of the basic characteristic of modern optical telescope data, which is the Strehl ratio (SR, Strehl 1902), as a new constraint applied during PSF reconstruction. The SR is nowadays used in optical astronomy in order to characterize the image quality that is obtained after AO correction of the images (the higher the SR, the closer to the ideal PSF), and an estimation of it is commonly delivered together with the data obtained at suitably equipped telescopes.

In a previous paper (Desiderà et al. 2006), we developed iterative blind deconvolution (IBD) of multiple images with application to the Fizeau interferometer of the Large Binocular Telescope (LBT). The corresponding code has also been integrated within the Software Package AIRY (Astronomical Image Reconstruction in interferometrY, see Correia et al. 2002, and http://www.airyproject.eu)[1], which can be used to reconstruct either Fizeau interferometric multiple images (Carbillet et al. 2002; Anconelli et al. 2005a,b, 2006a,b, 2007; La Camera et al. 2007) or standard mono-pupil data (Habart et al. 2004; Domiciano et al. 2008).

[1] Implemented within the CAOS (Code for Adaptive Optics Systems) problem-solving environment (see Carbillet et al. 2004a, and http://fizeau.unice.fr/caos).

In this paper, we propose a Strehl constraint to extend the IBD algorithm and apply this method to the reconstruction of 8m-class telescope images, which represents a current and generic case. Nevertheless, and in order to consider data that is as realistic as possible, we consider, as an example, the precise case of LUCIFER (Lbt near-infrared spectroscopic Utility with Camera and Integral-Field unit for Extragalactic Research) images, with a detailed end-to-end numerical simulation of the associated AO system.

The paper is organized as follows. In Sect. 2 we briefly describe the structure of the IBD used in our simulations and its implementation. In Sect. 3 we describe the motivations behind the introduction of the SR constraint and its integration within the IBD algorithm. Then we give the results of our numerical experiments, involving a detailed modeling of the AO system, in Sect. 4. Finally Sect. 5 consists of a discussion of the method proposed and the results obtained.

2. IBD structure and limitations

2.1. IBD structure

As described in Desiderà et al. (2006), the IBD method used in this study restores the object and the PSF separately in an iterative form: within each global iteration, which we will call a "cycle", either the object or the PSF is kept fixed while the other is updated. Therefore the output of each cycle updates both the object (within the so-called *object box*) and the PSF (within the *PSF box*), as provided by the previous one. Both in the *object box* and in the *PSF box* we use the Richardson-Lucy (RL) algorithm to perform the reconstruction. To briefly formalize the problem we use bold letters to denote $N \times N$ arrays, whose pixels

are indexed by a multi-index $\boldsymbol{n} = \{n_1, n_2\}$, and we consider the following model of image formation (Snyder et al. 1993):

$$\boldsymbol{g}(\boldsymbol{n}) = (\boldsymbol{H} * \boldsymbol{f})(\boldsymbol{n}) + \boldsymbol{b}(\boldsymbol{n}) + \boldsymbol{w}(\boldsymbol{n}), \tag{1}$$

where $\boldsymbol{g}$ is the detected image, $\boldsymbol{H}$ the corresponding PSF, $\boldsymbol{f}$ is the object array, $\boldsymbol{b}$ is the background, and $\boldsymbol{w}$ represents the noise term including read-out noise (RON). Moreover, we assume that the PSF is normalized to unit volume. The data of the problem are then $\boldsymbol{g}$ and $\boldsymbol{b}$, and the goal is to obtain an estimate of both $\boldsymbol{H}$ and $\boldsymbol{f}$.

We introduce an index k characterizing the IBD global cycles. If $\{\boldsymbol{H}^{(k-1)}; \boldsymbol{f}^{(k-1)}\}$ is the output of the cycle $k-1$ (or the initial estimate in the case $k = 1$), then for each cycle k the function of both the *PSF box* and the object box consists of the application of the reconstruction algorithm to provide the updates $\boldsymbol{f}^{(k)}$ and $\boldsymbol{H}^{(k)}$ of the object and the PSF, respectively.

Regarding the reconstruction algorithm, since the index k is used to characterize the IDB cycle, a different index, let us say l, will be used for the iterations of RL internal to the *object box* or the *PSF box*. Accordingly, the result of the lth iteration of RL inside the cycle k will be denoted by $\boldsymbol{f}^{(k,l)}$ and $\boldsymbol{H}^{(k,l)}$. Note that the maximum number of iterations is a priori different for the object and the PSF reconstructions ($l_{\rm obj} \neq l_{\rm psf}$).

Inside the *object box* the processing step consists of the following instructions:

– For $l = 0, ..., l_{\rm obj} - 1$, given $\boldsymbol{f}^{(k,l)}$, compute:

$$\tilde{\boldsymbol{f}}^{(k,l+1)} = \boldsymbol{f}^{(k,l)}[\boldsymbol{H}^{(k-1)}]^T * \frac{\boldsymbol{g}}{\boldsymbol{H}^{(k-1)} * \boldsymbol{f}^{(k,l)} + \boldsymbol{b}}, \tag{2}$$
$$\tilde{c}^{(k,l+1)} = \sum_{\boldsymbol{n}} \tilde{\boldsymbol{f}}^{(k,l+1)}(\boldsymbol{n}).$$

– Set:

$$\boldsymbol{f}^{(k,l+1)} = \tilde{\boldsymbol{f}}^{(k,l+1)} \frac{c}{\tilde{c}^{(k,l+1)}}, \tag{3}$$

where $c = \sum_{\boldsymbol{n}} \{\boldsymbol{g}(\boldsymbol{n}) - \boldsymbol{b}(\boldsymbol{n})\}$ represents the estimated flux of the object and $l_{\rm obj}$ is the number of RL iterations. The output of this box is the array $\boldsymbol{f}^{(k)} = \boldsymbol{f}^{(k,l_{\rm obj})}$, part of the output of the global cycle.

Analogously, for the *PSF box* we only need to exchange $\boldsymbol{f}$ and $\boldsymbol{H}$ within the previous equations, with $l_{\rm psf}$ the number of RL iterations, and where the normalization of the solution is calculated to obtain a PSF with a unit volume.

We use a pure IBD without any kind of additional constraint but that on the SR, in order to study here the gain due to the proposed method.

2.2. IBD limitations

IBD contains several parameters the choice of which can be critical for the final object reconstruction, such as the number of iterations within the *object* and *PSF boxes* ($l_{\rm obj}$ and $l_{\rm psf}$ respectively), and also the total number of IBD cycles to be performed ($k_{\rm max}$). In particular, a bad choice for $l_{\rm obj}$ or $l_{\rm psf}$ can compromise the result of the deconvolution for both the object and the PSF. For example, for what concerns $l_{\rm psf}$, performing too many iterations can overfit the peak of the reconstructed PSF with respect to that of the unknown one. On the other hand, choosing a too small number of iterations could be insufficient to improve the reconstructed PSF.

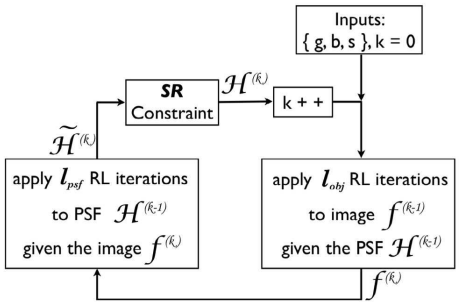

Fig. 1. General structure of the Strehl-constrained IBD.

3. The Strehl constraint

In particular, in order to circumvent the risk of choosing too high a value for $l_{\rm psf}$, we introduce a new constraint on the PSF reconstruction with the idea of taking into account the main physical feature of the PSF to be reconstructed, namely its SR. We will see that with this constraint the IBD is much less sensible to the value of $l_{\rm psf}$. The constraint is applied to the output of the *PSF box* $\boldsymbol{H}^{(k)}$ and essentially consists of blurring it when its SR exceeds the estimated one s, in order to reach the desired SR. The blurring process is performed in an iterative manner with a Gaussian function $\boldsymbol{G}$, with a small *rms* σ in order to make the peak of the PSF lower by following a slower process. $\boldsymbol{G}$ being normalized to the unit volume, the result of the convolution with $\boldsymbol{H}^{(k)}$ preserves the unit volume itself, while the band remains essentially the same. The processing steps to perform after the *PSF box* are then:

– initialize with $\boldsymbol{H}^{(k)}$ and compute its SR $\tilde{s}$:

$$\tilde{s} = \frac{\max(\boldsymbol{H}^{(k)})}{\max(\boldsymbol{H}_{\rm ideal})}; \tag{4}$$

– while $\tilde{s} \geq s$ compute:

$$\tilde{\boldsymbol{H}}^{(k)} = \boldsymbol{G} * \tilde{\boldsymbol{H}}^{(k)}; \tag{5}$$

$$\tilde{s} = \frac{\max(\tilde{\boldsymbol{H}}^{(k)})}{\max(\boldsymbol{H}_{\rm ideal})} \tag{6}$$

– set:

$$\boldsymbol{H}^{(k)} = \tilde{\boldsymbol{H}}^{(k)} \tag{7}$$

where the output of the *PSF box* is $\boldsymbol{H}^{(k)} = \boldsymbol{H}^{(k,l_{\rm psf})}$, the update of the PSF provided by the cycle k. A pictorial representation of the general structure of the Strehl-constrained IBD is given in Fig. 1.

4. Numerical experiments

In our numerical experiments we consider objects represented by 256×256 pixels arrays and we assume that they are observed in H band ($\lambda = 1.65$ μm) with a pixel size of 15 mas. Since we are interested in studying the behaviour of the IBD introducing the SR constraint, we consider a set of different AO-corrected PSFs with increasing SR. The five PSFs used here (with SR from 0.17 to 0.68) have been obtained by means of the `Software Package CAOS` (Carbillet et al. 2005), according to

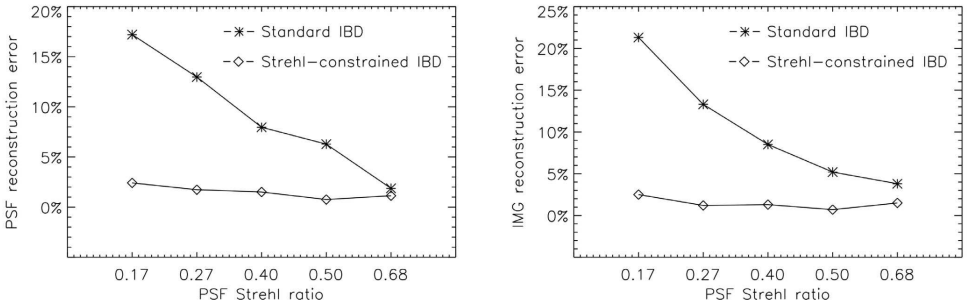

Fig. 2. *Left*: final error on the reconstruction of the PSF. *Right*: final error on the reconstruction of the object. Both plots are made as a function of the SR of the image data and comparing the simple IBD (rhombuses) to the Strehl-constrained IBD (asterisks). A gain of up to a factor ∼10 is achieved for the poorer SR.

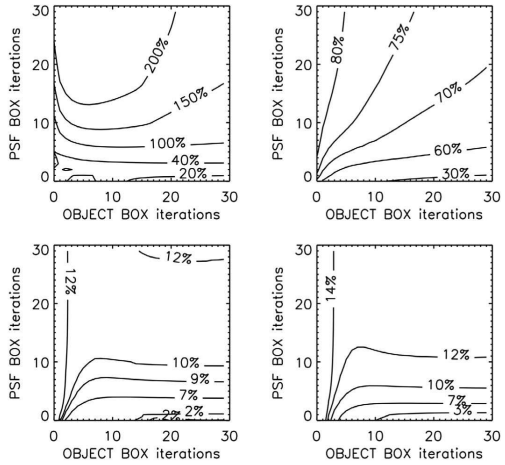

Fig. 3. Final error map (relative to the case of SR = 0.27) as a function of the iterations within the *object box* and the *PSF box*. *Left*: PSF reconstruction. *Right*: object reconstruction. *Top*: simple IBD. *Bottom*: Strehl-constrained IBD.

Table 1. Main parameters describing the PSF simulation.

turbulent atmosphere	
Fried parameter (at 500 nm)	15 cm
ground layer velocity	∼8 m/s
ground layer turbulence profile ratio	0.7
high layer velocity	∼16.5 m/s
high layer turbulence profile ratio	0.3
wavefront outer-scale	20 m
telescope & AO system	
telescope effective diameter D	8.22 m
telescope obstruction ratio	0.11
AO guide star spectral type	K5
AO guide star R-magnitude	12–16
number of actuators	672
number of modes reconstructed	up to 672
time filter type	pure integration
sensing central wavelength	750 nm
sensing bandwidth	300 nm
total sensing average transmission	0.41
number of equivalent sub-apertures	10×10, 15×15
sensing exposure time [ms]	1.67–5
sensing RON [e^- rms]	3.5–5.8

a precise model of the first-light AO system of LBT and the near-infrared camera LUCIFER described in a previous paper (Carbillet et al. 2004b). The main parameters associated with these simulations are reported in Table 1.

For the object, we have chosen a binary system, since it represents the elementary object to be reconstructed. We assume that the two components are of magnitude 12 and the angular separation is 285 mas (19 pixels), i.e. ∼7 times larger than the diffraction limit (∼40 mas). For each PSF, the images have been simulated according to Eq. (1), using a time exposure of 1200 s, with a total transmission of 0.3 and considering a CCD RON of 10 e^- rms.

In order to test the performance of the Strehl constraint, we have designed and run a large number of IBD simulations using a different number of iterations to be used within the *object* and *PSF boxes*. $l_{\rm obj}$ and $l_{\rm psf}$ range from 1 to 30 while the total number of cycles remain the same, fixed to 100 iterations. In this way, for each set of PSFs we computed 30×30 IBD projects with and without application of the Strehl constraint. For each project and for each PSF we then computed the error on the reconstructed PSF and on the collected flux (on 3×3 pixels which roughly correspond to λ/D) of the two stars at each global iteration. Doing so, we can give the behaviour of the minimum error achievable with respect to the asymmetry[2] of the IBD.

Figure 2 shows the error on both the PSF reconstruction and the object reconstruction as a function of the SR characterizing the data processed, with and without the Strehl constraint. The improvement is clear if we compare the behaviour of the error in the two cases, behavior which becomes remarkably low, and moreover flat, with the application of the Strehl constraint. Figure 3 also shows the corresponding maps as a function of the iterations within the *object box* and the *PSF box*. We can observe here how it can be important to choose the right number of iterations in order to avoid a high divergence in the

[2] I.e. the fact that optimal values of $l_{\rm psf}$ and $l_{\rm obj}$ will be a priori such that $l_{\rm psf} \neq l_{\rm obj}$.

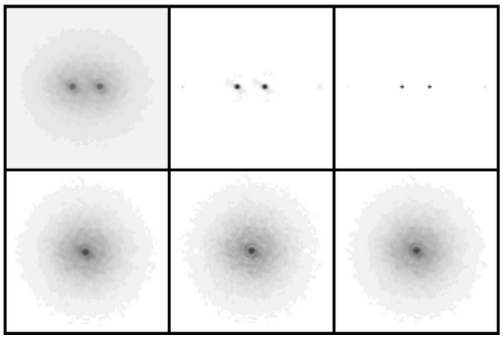

Fig. 4. *From top to bottom* and *from left to right*: observed image (SR = 0.27), reconstructed object with the simple IBD, reconstructed object with the Strehl-constrained IBD, PSF corresponding to the observed image, reconstructed PSF with the simple IBD, reconstructed PSF with the Strehl-constrained IBD. A logarithmic scale is used.

reconstruction process, in the case of a standard IBD. On the contrary, this limitation vanishes when considering the use of the Strehl-constrained IBD. In addition, the errors remain contained in a smaller range, which is reassuring with respect to the choice of the right iteration numbers for a given reconstruction.

5. Conclusions

In this paper, we introduced a new constraint on the reconstructed PSF in order to circumvent the well-know limitations of an IBD algorithm. The constraint forces the reconstructed PSF to fit the SR as much as possible, a feature which is strictly related to the observation conditions.

IBD algorithms (such as the one described in this paper) mainly suffer from the asymmetry between the iteration numbers adopted in the two reconstruction boxes (the so-called *PSF box* and *object box*). This limitation makes it difficult to calibrate all the parameters in order to obtain the best results. The application of the Strehl constraint seems to regularize the blind algorithm making it more robust, even in the case of a non-optimal choice of the parameters. In addition, the solutions themselves are characterized by a smaller error with respect to the standard IBD.

The gain of the proposed method essentially concerns the photometry of the object to be reconstructed, an example is given in Fig. 4 in which both the reconstructed object and the reconstructed PSF, using the Strehl constraint or not, are shown. The improvement obtained in the reconstructed PSF reflects an optimized reconstruction of the object, in which it is possible to collect the flux closer to the real position of the two unknown spots.

The mathematical application of the constraint, which can be seen as a projection in the set of the admissible PSFs, is easy to use. The constraint is applied before the reconstruction algorithm used to update the PSF, so that it can be used together with others constraints (an example is the constraint on the Fourier support of the PSF given in Desiderà et al. 2006) and/or within different kind of blind deconvolution algorithms (Jefferies & Christou 1993; Ayers 1988; Holmes 1992; Tsumuraya et al. 1994; Fisch et al. 1995; Biggs & Andrews 1998).

The implementation of the proposed algorithm is included in the ad hoc module `CBD` (Constrained Blind Deconvolution) of the freely-distributed and `CAOS`-based `Software Package AIRY`.

Acknowledgements. The authors would like to thank Prof. Mario Bertero and Prof. Henri Lanteri for interesting discussions on the subject.

References

Anconelli, B., Bertero, M., Boccacci, P., et al. 2005a, A&A, 430, 731
Anconelli, B., Bertero, M., Boccacci, P., & Carbillet, M. 2005b, A&A, 431, 747
Anconelli, B., Bertero, M., Boccacci, P., et al. 2006a, A&A, 448, 1217
Anconelli, B., Bertero, M., Boccacci, P., et al. 2006b, A&A, 460, 349
Anconelli, B., Bertero, M., Boccacci, P., et al. 2007, J. Comp. Appl. Math., 198, 321
Ayers, G. R., & Dainty, J. C. 1988, Opt. Lett., 13, 547
Bertero, M., & Boccacci, P. 1998, in Introduction to Inverse Problems in Imaging (Bristol: IOP Publishing)
Biggs D. S. C., & Andrews, M. 1998, SPIE Proc., 3461, 33
Carbillet, M., Correia, S., Boccacci, P., et al. 2002, A&A, 387, 743
Carbillet, M. C., Vérinaud, C., Guarracino, M., et al. 2004a, SPIE Proc., 5490, 550
Carbillet, M., Riccardi, A., & Esposito, S. 2004b, SPIE Proc., 5490, 721
Carbillet, M., Vérinaud, C., Femenía, B., et al. 2005, MNRAS, 356, 1263
Correia, S., Carbillet, M., Boccacci, P., et al. 2002, A&A, 387, 733
Desiderà, G., Anconelli, B., Bertero, M., et al. 2006, A&A, 452, 727
Domiciano de Souza, A., Kervella, P., Bendjoya, Ph., & Niccolini, G. 2008, A&A, 480, L29
Fish D. A., Brinicombe, A. M., & Pike, E. R. 1995, JOSA A, 12, 58
Habart, É., Testi, L., Natta, A., & Carbillet, M. 2004, ApJ, 614, L129
Holmes, T. J. 1992, JOSA, A9, 1052
Jefferies, S. M., & Christou, J. C. 1993, ApJ, 415, 862
La Camera, A., Desiderà, G., Arcidiacono, C., et al. 2007, A&A, 471, 1091
Snyder, D. L., Hammoud, A. M., & White, R. L. 1993, J. Opt. Soc. Am. A, 10, 1014
Strehl, K. 1902, Zeit. Instrumenkde, 22, 213
Tsumuraya, F., Miura, N., & Baba, N. 1994, A&A, 282, 699

3.4.2 Perspectives d'application

Il s'agit maintenant de proposer cette méthode et de l'appliquer à des données post-OA réelles et a priori de toute sorte (images, spectres), afin de la tester largement et de tenter d'optimiser le rendement scientifique des données ainsi traitées, surtout lorsque le rapport de Strehl lié à l'objet observé n'est pas particulièrement élevé et/ou qu'une PSF suffisamment semblable (c'est-à-dire présente dans le champ isoplanétique et enregistrée de manière simultanée ou presque) n'est pas disponible pour une déconvolution simple.

De plus, cette méthode a fait très récemment l'objet d'un renfort théorique qui devrait permettre de meilleures performances encore [159]. C'est cette nouvelle version, en phase d'être implémentée au sein de l'outil `AIRY` à l'occasion d'une nouvelle version (6.1) en train d'être mise au point avec A. La Camera du groupe de l'Université de Genova, que je prévois d'appliquer par exemple au cas d'observations spectroscopiques avec NACO (VLT) de disques proto-planétaires d'étoiles Herbig Ae/Be, dans le cadre cette fois-ci d'une collaboration avec É. Habart (Institut d'Astrophysique Spatiale, Université Paris Sud).

Des données d'une première campagne d'observation, des résultats encourageants ont été obtenus sur HD 97048, en appliquant une déconvolution classique à l'aide d'une PSF obtenue dans les mêmes conditions atmosphériques et les mêmes conditions physiques du système d'OA mais pas simultanément [73]. Les données de six autres objets obtenues lors d'une deuxième campagne ont également donné lieu à publication [95, 96]. Les données d'une troisième campagne, avec de nouveaux objets, doivent toujours être traitées. Pour certains de ces objets, plusieurs directions de la fente du spectromètre ont même été utilisées, pouvant ainsi en permettre une véritable cartographie.

3.5 Imagerie à très haute dynamique

3.5.1 Ça va SPHERE !

Depuis la découverte en 1995 de la première exoplanète orbitant autour d'une étoile de type solaire par Mayor & Queloz [26], beaucoup d'efforts ont été fournis afin de développer la détection directe et la caractérisation spectrale d'exoplanètes. Quelques détections directes ont déjà été possibles avec l'instrumentation existante [82, 83] ; mais une instrumentation dédiée intégrant notamment un système d'OA extrême et ce que la coronographie stellaire peut offrir de plus performant, le tout accompagné d'algorithmes de détection ad hoc, doit permettre un nombre bien plus important et systématique de ces découvertes. C'est avec cette ambition en ligne de mire que l'instrument SPHERE [90] pour le VLT a été conçu et développé, tout comme son concurrent direct GPI [98] pour Gemini, et devrait finalement voir sa première lumière en 2014.

SPHERE est équipé en amont de son système d'OA extrême, SAXO (Sphere Adaptive optics for eXoplanets Observations) [111], composé notamment d'un SH 40×40 filtré spatialement (voir Sec. 2.3) et desservant un canal proche-infrarouge avec un coronographe commun à deux des trois sous-instruments : IRDIS (InfraRed Dual Imager and Spectrograph) [107] et IFS (Integral Field Spectrograph) [106]. Le troisième sous-instrument, ZIMPOL (Zürich IMaging POLarimeter) [115], se trouve quant à lui dans le canal visible, partageant la lumière avec le SH de SAXO.

L'intégralité de cet instrument, complexe s'il en est, a été modélisé selon un niveau de détail très poussé au sein du `Software Package SPHERE` [105]. Après une phase de mise en place, a suivi une phase d'exploitation en termes de simulations de type « système » pour les études préliminaires concernant le coronographe de Lyot apodisé [2] (voir la sous-section suivante), ainsi que le coronographe quatre-quadrants, mais également et par exemple les performances du mode DBI (pour *Double Band Imaging*) d'IRDIS [104] ou celles du polarimètre imageur ZIMPOL [115].

Grâce à sa dernière version (3.0), un ensemble de données typiques a été élaboré pour l'observation d'exoplanètes avec le sous-instrument IRDIS, puis mis à disposition du consortium afin de pouvoir tester les algorithmes appropriés d'extraction du signal pour la détection d'exoplanètes avec SPHERE (sujet qui a d'ailleurs pour ma part fait l'objet de la thèse d'I. Smith co-encadrée avec A. Ferrari).

Ces données, à la différence des simulations « système » effectuées auparavant et en parallèle (voir par exemple à la sous-section suivante), tiennent compte de l'évolution temporelle du seeing, de la vitesse du vent dans les couches turbulentes et de plusieurs aberrations instrumentales, et ceci tout le long d'une observation globale de 4 hr (144 poses longues de 100 s, chacune composée de 100 réalisations indépendantes des fronts d'onde partiellement corrigés par SAXO).

La simulation de ces données de test a été mise en place en collaboration étroite avec D. Mouillet (IPAG) et A. Boccaletti (LESIA), et le détail de leur élaboration a été publié dans Smith et al. [113]. La Fig. 3.4 montre l'évolution de la PSF qui en résulte en fonction du temps. Plusieurs travaux ont par la suite été effectués à partir de ces données [113, 114, 123, 136, 118, 131, 139, 140, 141].

L' outil dévelloppé est également, et actuellement, utilisé pour la préparations des observations d'objets astrophysiques autres que les exoplanètes avec l'instrument SPHERE, comme nous le verrons plus en détails à la sous-section 3.5.3.

2. Coronographe duquel le laboratoire (LUAN aux prémices, Fizeau ensuite, Lagrange maintenant) est responsable au sein du consortium de l'instrument SPHERE.

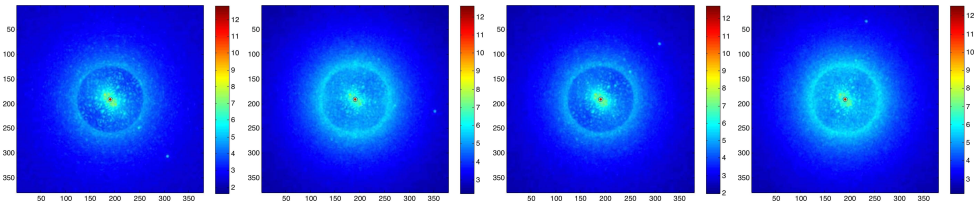

FIGURE 3.4: Données de test élaborées pour le sous-instrument IRDIS de SPHERE, constituées de 144 images longues poses de 100 s consécutives, pour une observation globale de 4 hr. De gauche à droite : pose longue n° 1, 50, 100 et 144, toutes représentées à la puissance 0.2. Le pixel mesure ici 12.2 mas et le champ de vue est d'environ $4\farcs5 \times 4\farcs5$.

3.5.2 *Apodized Lyot coronagraph for SPHERE/VLT – I. Detailed numerical study*

L'article suivant, publié par *Experimental Astronomy* en 2011, présente l'étude numérique détaillée effectuée pour le coronographe de Lyot apodisé de l'instrument de seconde génération du VLT SPHERE, dédié à l'imagerie à très haut contraste (avec pour objectif scientifique principal la détection d'exoplanètes et leur caractérisation). Cette étude est, au sens de la modélisation, très proche de l'instrument, puisque cette dernière inclue même ici des résultats de mesure en laboratoire optique des composantes de l'instrument, notamment en ce qui concerne les aberrations instrumentales.

Les résultats avancés dans cet article ont permis de finaliser le dessin optique de l'instrument avant ses tests de performance en laboratoire [146], mais sont également intéressants pour la conception d'autres instruments qui pourraient en découler dans la perspective des ELT. En tout premier lieu, le coronographe de Lyot apodisé y est optimisé par rapport au contraste, selon un critère défini dans l'article, montrant un net optimum pour un masque de diamètre $4\frac{\lambda}{D}$ (et l'apodiseur correspondant). Un certain nombre de points critiques sont ensuite étudiés : défauts possibles de l'apodiseur, menant à la définition d'un profil de tolérance et à la préconisation d'un resserrement du stop de Lyot afin de prévenir les effets des défauts de phase ; analyse de *ghosts* ; décentrage de l'apodiseur et du masque focal ; décentrage et rotation du stop de Lyot.

Exp Astron
DOI 10.1007/s10686-011-9219-4

ORIGINAL ARTICLE

Apodized Lyot coronagraph for SPHERE/VLT

I. Detailed numerical study

Marcel Carbillet · Philippe Bendjoya · Lyu Abe · Géraldine Guerri · Anthony Boccaletti · Jean-Baptiste Daban · Kjetil Dohlen · André Ferrari · Sylvie Robbe-Dubois · Richard Douet · Farrokh Vakili

Received: 29 September 2010 / Accepted: 4 March 2011

Abstract SPHERE (which stands for Spectro-Polarimetric High-contrast Exoplanet REsearch) is a second-generation Very Large Telescope (VLT) instrument dedicated to high-contrast direct imaging of exoplanets which first-light is scheduled for 2011. Within this complex instrument one of the central components is the apodized Lyot coronagraph (ALC). The present paper reports on the most interesting aspects and results of the whole numerical study made during the design of the ALC for SPHERE/VLT. The method followed for this study is purely numerical, but with an end-to-end approach which is largely fed by a number of instrumental feedbacks. The results obtained and presented in this paper firstly permit to finalize the optical design before

M. Carbillet (✉) · P. Bendjoya · L. Abe · G. Guerri · J.-B. Daban · A. Ferrari · S. Robbe-Dubois · R. Douet · F. Vakili
UMR 6525 H. Fizeau, Université de Nice Sophia Antipolis/CNRS/Observatoire de la Côte d'Azur, Parc Valrose, 06108 Nice cedex 2, France
e-mail: marcel.carbillet@unice.fr

A. Boccaletti
UMR 8109 LESIA, Observatoire de Meudon/CNRS, 5 Pl. J. Janssen, 92195 Meudon, France

K. Dohlen
UMR 6110 LAM, Observatoire Astrophysique de Marseille-Provence, Université de Provence/CNRS, 13388 Marseille cedex 13, France

Present Address:
G. Guerri
Département d'Astrophysique, Géophysique et Océanographie, Centre Spatial de Liège, Avenue Pré-Aily, 4031 Angleur, Belgium

Published online: 24 March 2011

laboratory performance testing of the ALC being built for SPHERE/VLT (see paper II "Laboratory tests and performances"), but will also hopefully help conceiving future other instruments alike, for example within the very promising extremely large telescope perspective.

Keywords Stellar coronagraphy · Apodized Lyot coronagraph · SPHERE · Numerical simulations

1 Introduction

Since 1995 and the discovery of the first extrasolar planet of a solar-type star by Mayor and Queloz [1], direct detection and spectral characterization of exoplanets has become one of the most exciting challenge in optical astronomy. In this context the second-generation Very Large Telescope (VLT) instrument SPHERE (Spectro-Polarimetric High-contrast Exoplanet REsearch [2]) main goal is to achieve direct imaging of exoplanets with a possible first spectral characterization. In order to achieve this goal, coronagraphy is, as far as we know, mandatory. A number of concepts have been proposed these last years of very exciting developments in the field of stellar coronagraphy. In the framework of SPHERE and as a result of its preliminary study, the four-quadrant phase mask (4QPM) [3] in one hand and the apodized Lyot coronagraph (ALC [4]) in the other hand have been chosen (in addition to the classical Lyot coronagraph).

In this paper we underline the most interesting aspects and results of the whole end-to-end numerical study we have achieved during the design of the ALC for SPHERE/VLT. A second article, subtitled "Laboratory tests and performances" [5], reports on the laboratory experiments and tests performed for the ALC for SPHERE/VLT.

The present paper is organized as follows. In Section 2 we describe the computation of the transmission function that characterizes the apodized entrance pupil of the coronagraph. Section 3 focalizes then on the detailed physical modeling that has been used for the complete end-to-end numerical simulations that permitted to achieve the study presented here. Section 4 is then dedicated to the optimization of the ALC within the framework of SPHERE/VLT. A number of identified critical points are afterwards studied in details in Section 5. Finally, a conclusion is derived in Section 6.

2 Apodization computation

The main point in considering an ALC [4] is its apodized entrance pupil which aim is to reduce the diffraction wings with respect to a standard Lyot

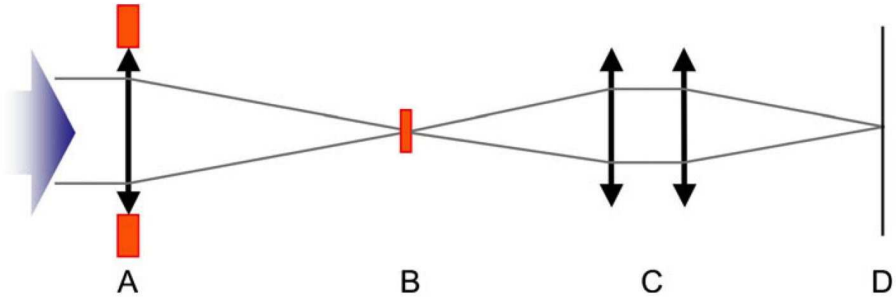

Fig. 1 Typical optical setup corresponding to an ALC. The first pupil plane (*plane A*) is apodized. An opaque mask is placed in the first focal plane (*plane B*), while a Lyot stop can be placed in the second pupil plane (*plane C*), and the coronagraphic image is formed in the final focal plane (*plane D*)

coronagraph [6, 7].[1] Together with it there is also the advantage of a smaller focal opaque mask, reducing hence the inner-working angle (IWA) of potential planet detection and characterization. In addition, there is theoretically no need for an undersized Lyot stop when apodizing the entrance pupil, a reproduction of the latter being sufficient (and optimal). But this last point becomes invalid when the manufacturing of the apodizer itself implies the undesired introduction of phase effects that needs therefore to be eliminated by undersizing the Lyot stop again (see Section 5.2).

It has been demonstrated in the literature, in the case of a rectangular aperture first [4], and then for a circular aperture [8], that when prolate spheroidal functions are considered for apodization of the entrance pupil, an optimal star-light extinction can be reached. As a consequence, a solution of this optimization can be found for any mask diameter—keeping in mind that the larger the mask, the lower the residual star light, but also that the stronger the apodization, the lower the transmission, and hence the lower the number of photons from the planet. In this section we are hence only determining a series of couples mask⊕apodizer for which the apodizer is the optimal one for a given mask diameter, i.e. the apodizer for which the proportion of star light diffracted outside the mask is minimum. Although a complete sketch of the optical setup can already be found in the literature [9–14], we reproduce it in Fig. 1 for sake of clarity. The usual approximations of paraxial optics are made. Moreover, it is also assumed that there is a simple Fourier transform relationship between each successive plane.

In order to compute these couples mask⊕apodizer, we have to face the fact that analytical expressions (series expansion) of the prolate solutions evoked here before only apply to unobscured apertures. In the case of obscured apertures like the VLT one, a numerical approach is necessary, following the

[1] But at the cost of a slight loss of angular resolution, following the rule of thumb "less foot, more shoulder" (Ricort, private communication, 2007).

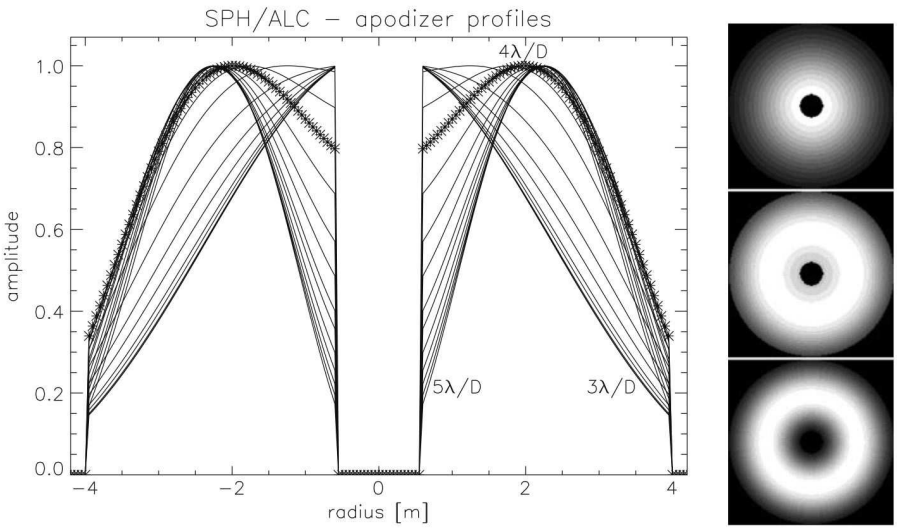

Fig. 2 *Left:* profiles of the computed apodizers for a mask of $3\lambda/D$ to $5\lambda/D$, with a step of $0.1\lambda/D$. The apodizer computed for $4\lambda/D$ is highlighted. *Right:* bidimensional representation of three of the computed apodizers, $3\lambda/D$ (*top*), $4\lambda/D$ (*middle*), and $5\lambda/D$ (*bottom*)

iterative algorithm of Guyon and Roddier [15] which efficiency in the ALC case has been proven [16]. Note that specific solutions for circular apertures with a central obscuration have also been studied [17].

Figure 2 shows the apodizers obtained for different mask diameters ranging from $3\lambda/D$ to $5\lambda/D$ (corresponding to an approximate range of 0″.12–0″.21 in band H, centered on 1.65 μm). One can notice the evolution, as the mask diameter increases, from a "bell" shape, typical of a weak obstruction, to a "bagel" shape, typical of a strong obstruction.

In Section 4 we use the resulting couples mask⊕apodizer in order to find the optimal one (i.e. the best trade-off between a small mask diameter and a high coronagraphic effect) with respect to the rest of the characteristics of the telescope and the instrument. Next section hence details the physical modeling considered for this optimization and the whole ensemble of tests performed within this paper.

3 Instrument physical and numerical modeling

A dedicated numerical tool has been developed for the whole instrument SPHERE, whilling to have a common basis from system studies to data simulation for data reduction and science cases testing. Hence it has been used to carry out a thorough system analysis and address critical points in the instrument opto-mechanical concept, to provide typical images delivered by the instrument in order to develop appropriate algorithms relevant to exoplanet

detection, and finally to evaluate the performance of the instrument for some realistic astrophysical targets. The resulting tool, the `Software Package SPHERE`, is `IDL`-based, was developed under the `CAOS` problem-solving environment [18], and includes modeling of the extreme adaptive optics (AO) system SAXO (SPHERE Adaptive optics for eXoplanet Observations [19]), the common optical path of the instrument and the three sub-instruments IRDIS (InfraRed Dual Imager and Spectrograph [20]), IFS (Integral Field Spectrometer [21]), and ZIMPOL (Zurich IMaging POLarimeter [22]). A detailed description of the tool can be found in Carbillet et al. [23].

The whole simulation code is based on Fourier analysis: both phase screens and amplitude masks are introduced in the successive pupil and focal planes where they respectively occur along the global propagation from the entrance pupil to the final coronagraphic image onto the science detector. The physical modeling of the common optical path aims at generating static aberrations upstream the coronagraph (from the telescope to the instrument) from the power spectral densities resulting from the global system study performed for the instrument. Table 1 resumes the *rms* values considered and corresponding to each of the different types of aberration identified and taken into account for the simulations presented within this paper.

The first error reported comes from the maps of the telescope aberrations at the level of the three consecutive VLT mirrors M_1, M_2, and M_3, for which low frequencies were removed in order to take into account the filtering performed by the AO system SAXO. The following two errors directly come from the system analysis aforesaid. The fourth error is due to the fact that the Fresnel propagation of defects not located in a pupil plane is chromatic and hence cannot be properly corrected, the wavefront sensing wavelength range (visible) differing from the observing wavelength (near-infrared). The fifth error is a remaining wavefront error coming from the fact that, because of atmospheric differential refraction, a beam shift occurs before its correction by the atmospheric dispersion corrector (ADC) and hence the AO system does

Table 1 Instrument static aberrations, main characteristics of the turbulent atmosphere, and other AO-related characteristics considered for the present end-to-end simulations

Static aberrations *rms*	
VLT mirrors M_1, M_2, M_3 (means)	11.9 nm, 11.9 nm, 16.6 nm
Instrument	34.5 nm
AO calibration	7.4 nm
Fresnel propagation	4.7 nm
Beam shift	8.0 nm
Turbulent atmosphere characteristics	
Seeing	0.″85
Wavefront outerscale	25 m
Turbulent layers altitude	0 m, 1000 m, 10000 m
Corresponding strength ratio	0.2, 0.6, 0.2
Corresponding wind speed	12.5 m/s, 12.5 m/s, 12.5 m/s
Corresponding wind direction	0°, 45°, 90°
Other related characteristics	
Guide star magnitude	8
Zenith angle	30°
Instrumental jitter	3 mas

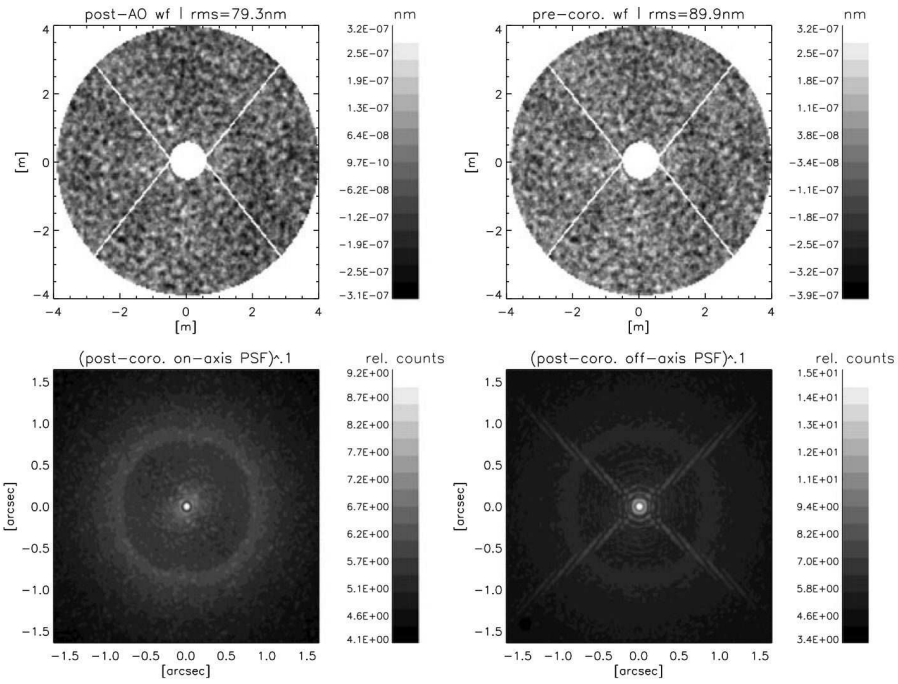

Fig. 3 From *left to right* and from *top to bottom*: example of instantaneous wavefront including atmospheric and post-AO aberrations; the same wavefront after common-optical-path aberrations and just before entering the coronagraph; resulting on-axis post-coronagraph PSF; example of resulting off-axis post-coronagraph. Note on the post-coronagraph PSFs the characteristic post-AO annulus at a radius of $\frac{1}{2}\lambda/d$ (where the $d = D/40$ for SAXO). For sake of clarity, PSFs were raised to the power of 0.1 before grey-scale representation

not correct from the exact wavefront aberration. A more detailed description of the various system aberrations considered along the end-to-end numerical simulations performed for the instrument can be found in Boccaletti et al. [24].

Table 1 also reports on the physical characteristics of the turbulent atmosphere considered above the telescope, and Fig. 3 shows an example of instantaneous post-AO wavefront, the subsequent pre-coronagraph wavefront (including the static aberrations in addition to the post-AO ones), and the resulting on- and off-axis PSFs.

4 Apodizer optimization for SPHERE/VLT

Optimizing the apodizer consists here in making full simulations of the system, with possibly instrument static aberrations, atmospheric turbulence and subsequent AO correction, and then computing the contrast obtained in the final focal plane in function of the separation of the candidate planet from the

central star. Moreover, this has to be evaluated for each couple mask⊕apodizer characterized by the mask diameter s, in order to determine the optimal one.

The relevant signal is here given by the core of the planet post-coronagraph PSF, for a planet at a separation ρ (sufficiently off axis not to be affected by the focal plane mask, although obviously still affected by the pupil plane apodizer). This signal has then to be detected over the residual light due to the wings of the central-star post-coronagraph PSF, clearly affected by both the pupil plane apodizer and the focal plane mask. Hence, for each mask diameter value s the relevant contrast K in the final focal plane can be practically computed as the ratio between the average value of the off-axis post-coronagraph PSF (apodized but not masked) over a disk of diameter λ/D (centered at a position ρ), and the average value of the on-axis post-coronagraph PSF (apodized and masked) over a ring of radius ρ and width λ/D:

$$K_{\rho_0}(s) = \frac{\langle I_s^{\rho_0}(\rho,\theta) \times \mathrm{disk}_{\lambda/D}^{\rho_0}(\rho,\theta)\rangle_{\rho,\theta}}{\langle I_s(\rho,\theta) \times \mathrm{ring}_{\lambda/D}^{\rho_0}(\rho,\theta)\rangle_{\rho,\theta}}\,, \tag{1}$$

where $I_s(\rho,\theta)$ is the star PSF obtained with a mask diameter s, $I_s^{\rho_0}(\rho,\theta)$ is the planet PSF obtained with the same mask diameter s and for a particular off-axis position ρ_0 of the planet, and $\langle\,\rangle_{\rho,\theta}$ is an average value over the whole range of values of ρ and θ, the polar coordinates within the final focal plane where these PSFs form. In addition, the PSF morphology can be taken into account when computing the contrast throughout the field by multiplying $K_{\rho_0}(s)$ by the maximum intensity of the apodized PSF. This is directly inspired from the metrics adopted by Martinez et al. [13], where actually the ratio of the maximum of the apodized PSF to the maximum of the standard PSF is considered for taking into account both the PSF morphology modifications when changing the apodizer profile, and the throughput. Here we have simplified this quantity by considering only the maximum of the apodized PSF, since the maximum of the standard PSF is indeed constant. One so obtains a *modified* contrast K' such as:

$$K'_{\rho_0}(s) = K_{\rho_0}(s) \times \max\left(I_s^{\rho_0}(\rho,\theta)\right). \tag{2}$$

At this point, one has to choose for which particular values of ρ_0 the contrasts have to be computed. For this purpose, rather than choosing a set of particularly interesting values, we found more interesting to adapt this computation to the peculiar morphology of the post-coronagraph post-XAO PSF formed. Figure 4 (top-left part) shows in background the typical post-XAO morphology of this post-coronagraph on-axis PSF, mainly characterized by the clear separation between an inner AO-cleaned area, for values of $\rho \leq \frac{1}{2}\lambda/d$, and an outer area where the AO system has roughly no effect. As a consequence, it seems very natural to consider both an average value of the contrasts obtained inside a disk of diameter λ/d, where the XAO system SAXO actually acts, and an average value of the contrasts obtained out of this AO-cleaned area. The resulting criterion is very close to the ALC optimization

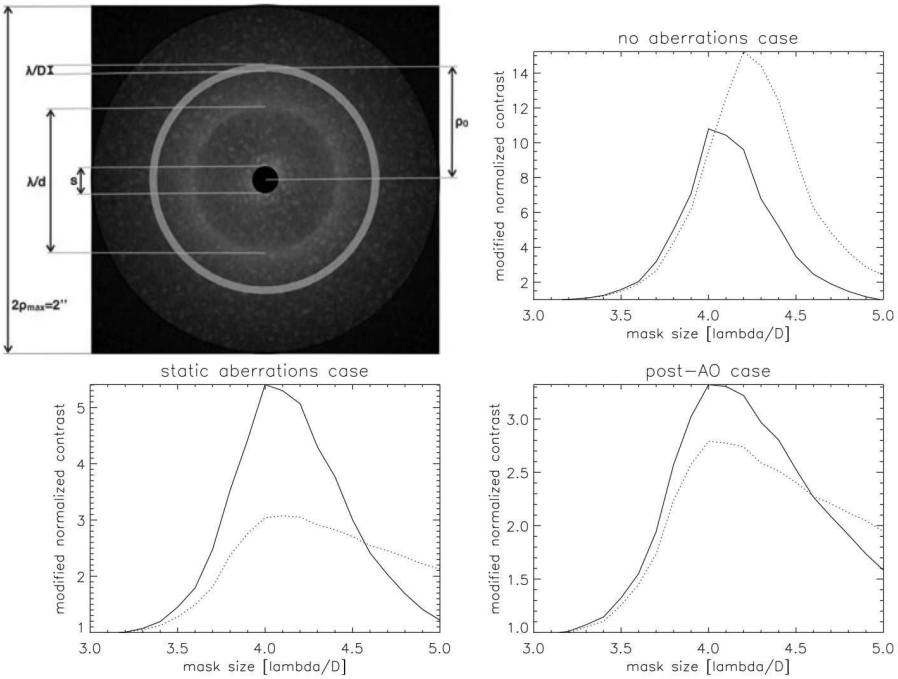

Fig. 4 *Top left:* definition of the areas considered for the different contrasts calculation. *Top right:* contrast $K'_{\rho_0}(s)$ of the ALC as a function of the mask diameter s, for both $\rho \leq \frac{1}{2}\lambda/d$ (*solid line*) and $\rho \geq \frac{1}{2}\lambda/d$ (*dotted line*), and for the aberration-free case. For sake of clarity and better comparison each contrast curve is also actually normalized with respect to its first computed value $K'_{\rho_0}(3\,\lambda/D)$. *Bottom left:* same two curves but with the instrument static aberrations. *Bottom right:* same two curves again but for the post-AO case (including indeed also the static aberrations)

criterion chosen in a similar paper for the general case of extremely large telescopes by Martinez et al. [13], at the main difference that the *modified* contrast computed here is not averaged over a whole range of off-axis distances but considered inside and outside the AO-cleaned disk of diameter λ/d.

Although the region of major interest for exoplanet searching (the main goal of SPHERE) is the inner one (within the disk of diameter λ/d), the outer region (outside the disk of diameter λ/d) is also considered for sake of completeness. In fact, the ALC is not here optimized for finding the maximum number of exoplanets—which goes much beyond the scope of this paper, and would requier dedicated subsequent studies—but only for having the best possible contrast. As it can be easily remarked from Fig. 4, this optimal contrast is clearly obtained for a mask diameter s of $\sim 4\,\lambda/D$.

Hence, it has been decided to optimize for the larger wavelength of our priority-goal broad band H, i.e. for $\lambda_{\max}$=1.78 μm, following so the conclusion of Soummer [17] concerning broad-band optimization for the ALC. As a consequence, the apodizer to be manufactured in our case is computed for $4\,\lambda_{\max}/D \simeq 4.3\,\lambda_0/D$, where λ_0 is the central wavelength of band H.

It is worth to finally remark that we chose not to discuss the IWA at this point since the 4QPM is a priori more adapted for close-in sources than the ALC. Nevertheless, and since the 4QPM is also more sensitive to low orders, we have chosen redundancy, having both within SPHERE in order also to reduce possible failure risks. As a consequence, the IWA issue for the ALC is discussed more in details in the laboratory-measures-based paper II [5].

5 Critical-points studies

In this section we focus on different points that can potentially be identified as critical for the performance of the ALC, and particularly for the apodizer itself.

5.1 Defects of the apodizer profile

Whatever the technique used to manufacture the apodizer, some imperfections will appear. At what extent these imperfections can be neglected, considering the whole set of other imperfections coming from the various optical components of the system? This is the point we are tackling in this subsection.

Several apodizers with different defects were hence computed and then considered into our numerical modeling of the whole system in order to capture the resulting effects on the coronagraphic performances. Benefitting from our previous experience in the prototyping of apodizers (see e.g. Guerri et al. [25]), we have considered realistic defect sources such as:

- the presence of a plateau close to the location of the maximum of the transmission mimicking an over-deposition in this critical region of the apodizer,
- a discrepancy from the ideal transmission profile due to an excess or a lack of material deposition,
- the presence of a bump at different locations along the profile due to a possible non-linearity in the deposition process (testing then the influence of the radial position of such a bump),
- the presence of roughness simulating a non-smooth deposition.

Figure 5 shows an illustation of these four simulated generic defects. In order to quantify the influence of these defects on the performance of the ALC, we have introduced these anomalous apodizers in our numerical simulations. The corresponding coronagraphic performances have then been evaluated by considering the PSF contrast inside and outside the AO-cleaned area of the PSF (see previous section).

We have considered that the presence of a defect would be acceptable if its computed coronagraphic contrast would be equivalent to the contrast obtained with an ideal apodizer with a maximum loss of 10%.

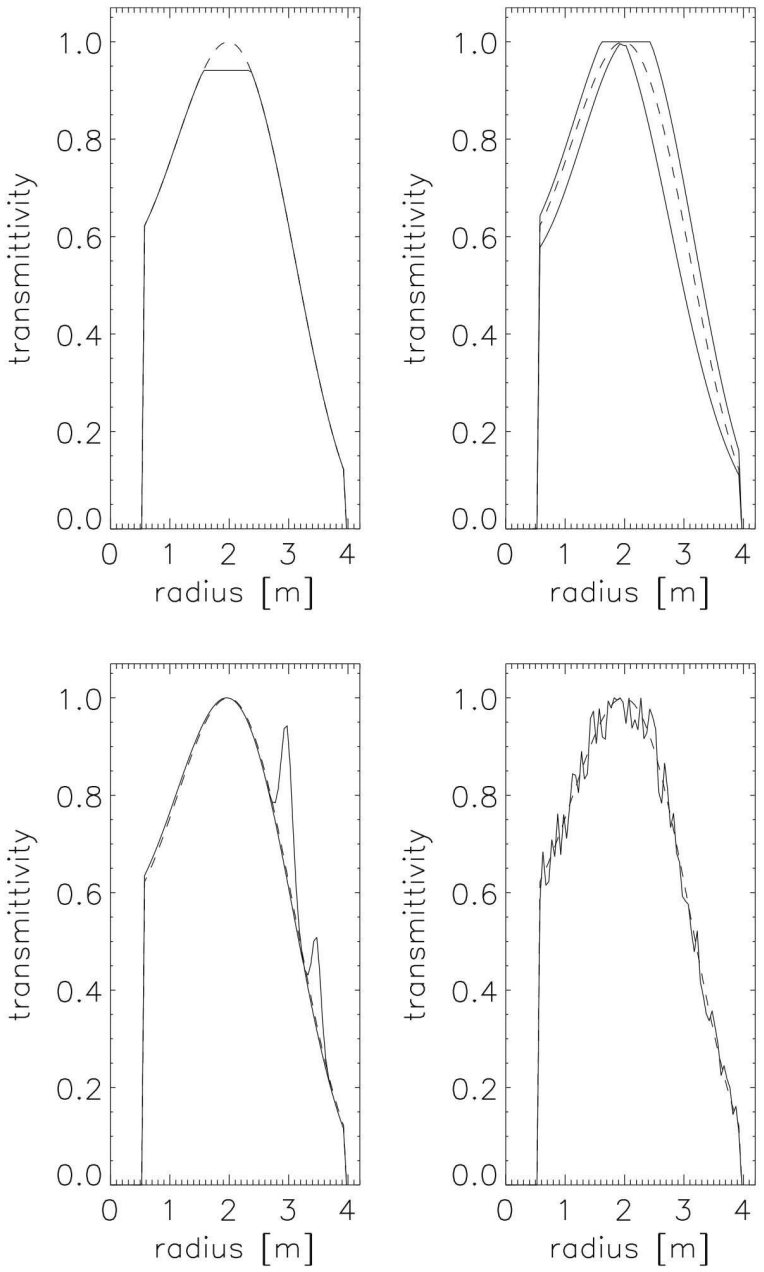

Fig. 5 Simulated generic defects. From *left to right* and from *top to bottom*: ideal $4\lambda/D$ apodizer transmission profile (*dashed line*), together with a profile with a plateau at the maximum transmission location (*solid line*); two profiles mimicking an excess and a lack of material deposition; simulation of the presence of a bump at two different locations; simulation of roughness in the transmission profile

In order to qualify an importance degree for each defect, we have generated anomalous apodiser with the same *rms* value for the relative discrepancies $\delta(r)$, where $\delta(r)$ is a function of the radius r of the apodizer and is defined as:

$$\delta(r) = \left| 1 - \frac{\text{ideal apodizer (r)}}{\text{anomalous apodizer (r)}} \right| , \tag{3}$$

where it is important to note that $\delta(r)$ has radial (not bidimensional) *rms* values.

As an illustration of this quantitative study of the influence of apodizer defects on the ALC performance, we propose in Fig. 6 a sample of contrast degradations due to the defects superimposed to the ideal case for a sample of apodizers with a *rms* value for $\delta(r)$ equal to 8%, roughly corresponding to what was expected from the manufacturer. From this figure, it clearly appears that the most critical defect is the presence of a bump over the profile, and that a bump located in the middle has a worse effect than a bump located at the edge.

For each generic case, we have simulated several amplitudes of the considered defect so as to provide tolerance specifications for the apodizer transmission profile. We conclude that two major effects contribute to a significant degradation of the coronagraphic PSF image: the first is the smoothness of the apodizer profile, especially at mid frequencies. Indeed, large amplitude bumps

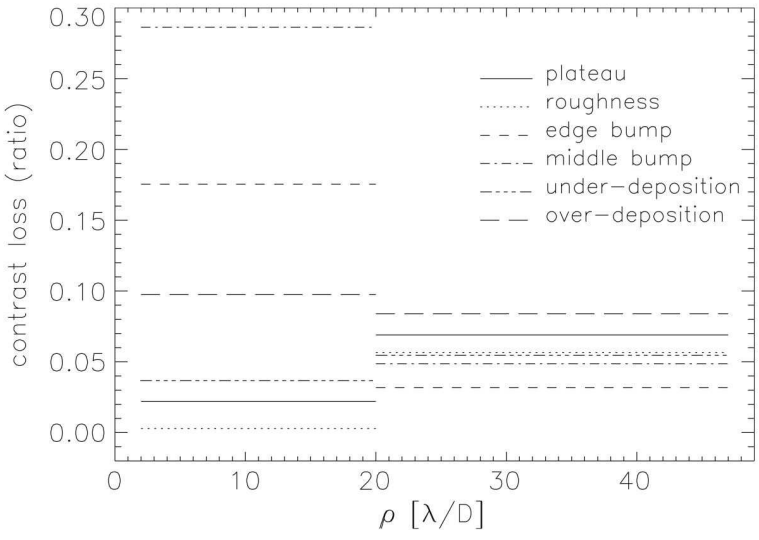

Fig. 6 Contrast loss $\Delta(\rho) = \left| 1 - \frac{\text{ideal PSF}(\rho)}{\text{anomalous PSF}(\rho)} \right|$ computed, for the different defects of the apodizer profile defined in the text, inside and outside the AO-cleaned area. The first zone (inside the AO-cleaned area) corresponding here to values of ρ between $2\lambda/D$ (0.″085 at 1.65 μm) and $20\lambda/D$ (0.″85 at 1.65 μm), the second zone (outside the AO-cleaned area) being then considered here until $47\lambda/D$ (2″ at 1.65 μm)

(middle bump or edge bump in Fig. 6) produce most significant degradation. Note that higher frequency defects (which we call "roughness") naturally affect the coronagraphic image in the outer zone, as shown in Fig. 6 (dotted line has a more degrading effect in the outer zone). This roughness is rather uniform over the whole apodizer map, and tends to produce an averaging effect so the degradation is not so high compared to localized defects. The second effect that significantly hampers the coronagraphic performance is the conformity of the realized profile to the theoretical one toward the external region.

We have hence deduced the upper and lower tolerance bounds for the apodizer transmission profile, which are shown in Fig. 7. The manufacturing specifications also include conditions on the smoothness of the profile (as explained previously) that can not be presented on that type of figure. Moreover, this figure also shows the distribution of the relative dicrepancies $\delta(r)$ of the apodizer for both tolerance profiles. These curves have been given to the manufacturer of the apodizer, together with an additional specification concerning the bumps (lower than 2–3% for $\delta(r)$ at the edges and 1–2% in the middle).

5.2 Phase defects effect

Let us consider the apodizer being manufactured by evaporation of a radially variable thin layer of metal (Inconel 600) on a fused silica substrate. In addition to providing the required apodizer transmitivity, it is crucial to determine the

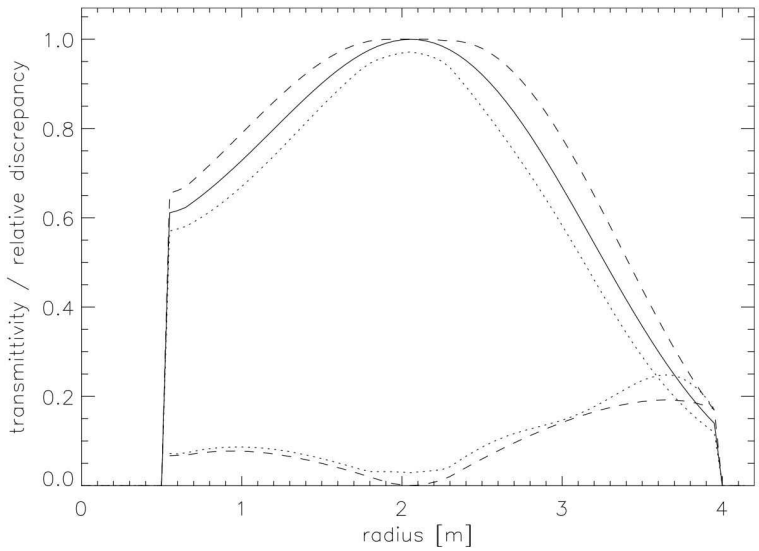

Fig. 7 *Top:* upper and lower limits of the acceptable transmission profile. *Bottom:* relative discrepancy $\delta(r)$ for both the upper and the lower limiting profiles

reflectivity of the apodizer, as well as the wavefront error introduced by this optical component.

Using thin film theory equations described by Born and Wolf [26], we can calculate the optical constants of the apodizer Inconel 600 coating (considering the case of normal incidence to simplify equations). These features can be conveniently expressed in terms of the reflection and transmission coefficients at the interface between a medium i and a medium j. One of these features particularly interesting for us here, is the phase error that the apodizer introduces in the wavefront.

The global configuration we are here considering is very simple: light is coming from air (refraction index $n_1 = 1$), passes through the Inconel layer (refraction index $n_2 + \imath k_2$), then through the substrate (refraction index n_3), and then comes out to air again. The expression of the phase change $\delta_t(r)$ introduced in transmission by the apodizer is hence determined from:[2]

$$\delta_t(r) = \arctan\left(\frac{\exp(2k_2\eta)\ \sin(2n_2\eta) - \rho_{12}\ \rho_{23}\ \sin(\phi_{12}+\phi_{23})}{\exp(2k_2\eta)\ \cos(2n_2\eta) - \rho_{12}\ \rho_{23}\ \cos(\phi_{12}+\phi_{23})}\right) + \chi_{12} + \chi_{23} - n_2\eta, \tag{4}$$

where: χ_{ij} is the phase of the transmission coefficient, $\rho_{ij}\exp(\imath\phi_{ij})$ is the reflection coefficient, $\eta = \frac{2\pi}{\lambda}e(r)$, λ is the operating wavelength, and $e(r)$ is the thickness of the Inconel 600 layer which is preliminary determined by minimizing an error function obtained from the desired transmission profile. Note that for sake of clarity we have omitted the dependency in λ of the various terms.

These calculations are possible if we know the values of the real and imaginary parts of the refractive index of the Inconel 600 (n_2 and k_2) over the whole spectral domain. These data were extracted from Goodell et al. [27], and confirmed by Reynard Corp., who manufactured the apodizer.

Simulations were then carried out in order to analyze the effect of the apodizer wavefront error on the coronagraphic performance. From the calculus of the phase defects profiles, we modeled an apodizer with a modulus transmission term and a phase transmission term. This apodizer was then used for numerical simulations in order to calculate the corresponding coronagraphed PSF. Figure 8 shows the resulting coronagraphed PSFs. We can deduce from it that the apodizer wavefront error reduces significantly the contrast when the Lyot stop is equivalent to the pupil. However, this effect can be cancelled out by reducing the Lyot stop diameter by a factor of 0.98. Nevertheless, a factor

[2]Note that since the substrate is supposed infinitely thin, we are not considering interference and diffraction effects for this layer.

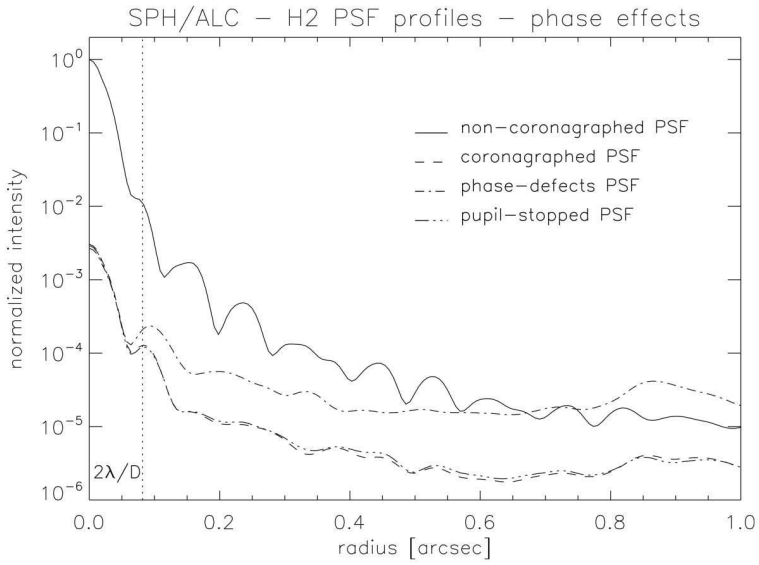

Fig. 8 Profile of the post-coronagraph PSF with phase defects and pupil stop

of 0.96 has been chosen for the final ALC component in order to also take into account a possible additional stop-centering inaccuracy.

5.3 Ghost analysis

This paragraph deals with the ghosts created by reflection on the back face of the substrate and on the Inconel coated face. The calculation of the ghost pupil consists in multiplying the apodizer transmission, the back-face reflection and the apodizer reflection. This is illustrated in Fig. 9 (left part), where are roughly represented, as a function of the radial coordinate r, the transmission profile T_a and the reflection profile R_a of the Inconel coating. R_t is the reflectivity of the anti-reflection (AR) coated back face, expected to be $< 1\%$ in bands Y, J, H, and K (and hopefully $< 0.5\%$ in bands Y, J, and H). As an illustration, the right part of Fig. 9 shows the AR coating of the prototype apodizer back face.

The absolute intensity $I_{GP}(r)$ in the ghost pupil is approximated by:

$$I_{GP}(r) = T_a(r)\ R_t\ R_a(r), \tag{5}$$

where $R_a(r)$, the reflective profile of the apodizer, can be calculated using the same notations as in section 5.2:

$$R_a(r) = \left| \frac{\rho_{12} \exp(\imath\phi_{12}) + \rho_{23} \exp(-2k_2\eta) \exp(\imath(\phi_{23} + 2n_2\eta))}{1 + \rho_{12}\ \rho_{23} \exp(-2k_2\eta) \exp(\imath(\phi_{12} + \phi_{23} + 2n_2\eta))} \right|^2 . \tag{6}$$

Calculations of the reflective profiles were made at different wavelengths within Y, J, H, K bands and resulted in very similar profiles, confirming the

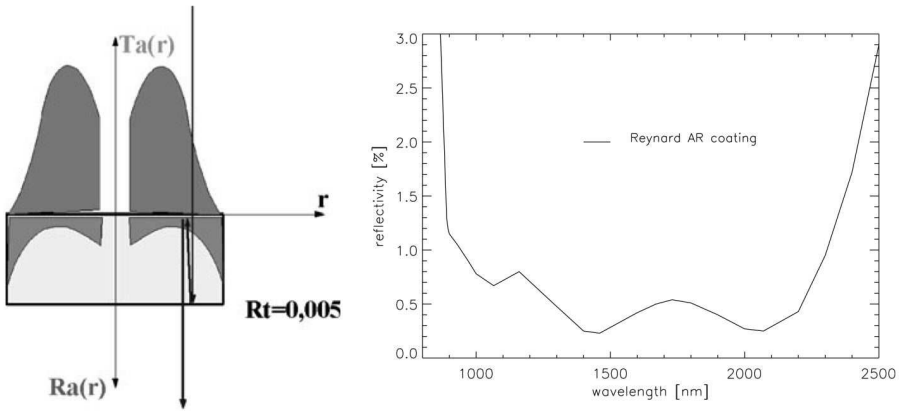

Fig. 9 *Left:* first-generation ghost produced by back reflection on the Inconel coated front face (see text for explanations). *Right:* AR coating values versus wavelength provided by the apodizer manufacturer

apodizer relative achromaticity. The calculations also show that the global reflection rate of this Inconel coating is 16%. Given that the global transmission of the coating is about 60%, the absorption is about 24%, value similar from Y to K within 1%.

From the reflective profile calculated above, and through Eq. 5, the ghost pupil can be obtained. Figure 10 (top part) shows its intensity profile (considering $R_t = 0.5\%$). This ghost pupil is then used for numerical simulations in order to calculate the PSF corresponding to the ghost at the end of the whole coronagraphic chain. Simulations were carried out in different cases of de-centering of the ghost image with respect to the coronagraphic mask: ghost perfectly coronagraphed, ghost partially coronagraphed, and ghost slightly out of the mask. In Fig. 10 (middle and bottom parts) ghost PSF profiles are shifted along the abscissa following two different cases of ghost de-centering.

These simulations lead to conclude that, if the ghost misalignment with respect to the coronagraphic mask is less than $0.4\,R_{\text{mask}}$, the ghost intensity is attenuated enough so that it does not reduce the contrast, even with an AR coating of 1%.

Considering the refractive index of the substrate (1.43) we deduce from this study that the substrate parallelism should be performed with a tolerance angle better than 5″. This constraint is easily reachable by technology, hence degradations of the performances due to the ghosts are not to be considered with a deeper priority. Note that secondary reflexions even if not coronagraphed will contribute in a ratio as less as 10^{-6} in intensity and are negligible.

5.4 De-centering of the ALC components

The contrast loss due to apodizer de-centering, focal mask de-centering, and Lyot stop de-centering is studied in this paragraph, and Fig. 11 shows the

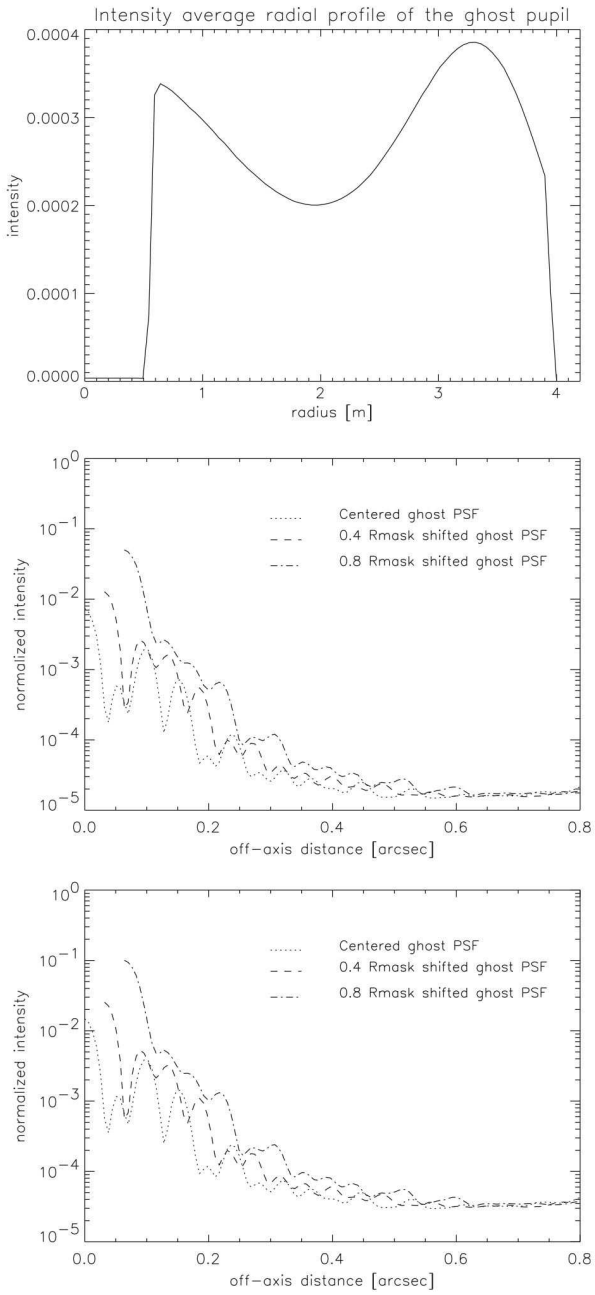

Fig. 10 *Top:* the ghost pupil in H band. *Middle:* ghost PSF for an AR coating of 0.5%. *Bottom:* ghost PSF for an AR coating of 1%

results of the simulation performed concerning these three items (together with the item approached in next sub-section).

As it can be seen from Fig. 11, and for what concerns apodizer de-centering, 10% of contrast loss is obtained for a de-centering of $0.015\,D$ inside the

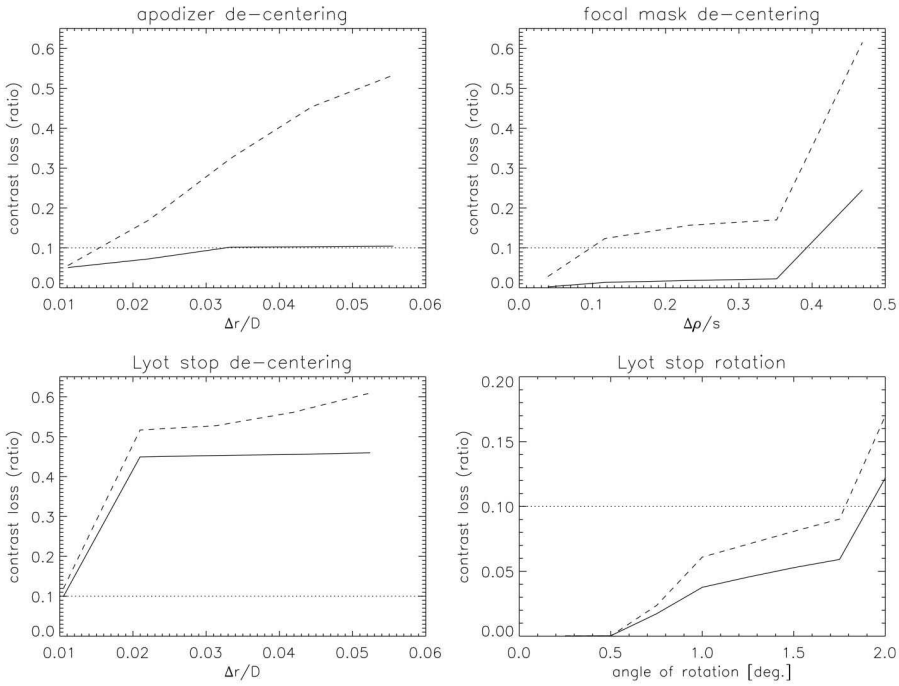

Fig. 11 Contrast losses for both $\rho \leq \frac{1}{2}\lambda/d$ (*dashed line*) and $\rho \geq \frac{1}{2}\lambda/d$ line). *Top left:* contrast loss due to apodizer de-centering (from $\Delta r = 0$ to $\Delta r = 1$ mm, with respect to an actual apodizer diameter $D = 18$ mm). *Top right:* contrast loss due to focal mask de-centering (from $\Delta\rho = 0$ to $\Delta\rho = 120\,\mu$m, with respect to an actual focal mask diameter $s = 264\,\mu$m). *Bottom left:* contrast loss due to Lyot stop de-centering (from $\Delta r = 0$ to $\Delta r = 0.5$ mm, with respect to an actual Lyot stop diameter $D = 9.54$ mm). *Bottom right:* contrast loss due to Lyot stop rotation (from 0 to 2°). The 10% level contrast loss is given by the straight *dotted line*

AO-cleaned area, and of 0.03 D out of this area. This corresponds to absolute de-centerings of ∼0.27 mm to ∼0.54 mm, which are very reasonable values.

Focal mask de-centering also is more critical in the case of small ρ's (inside the AO-cleaned area) than in the case of large ρ's (outside the AO-cleaned area), with de-centerings of, respectively, $\sim 0.1\,s$ and $\sim 0.4\,s$, which corresponds at the scale of SPHERE to $\sim 25\,\mu$m and $\sim 100\,\mu$m, respectively.

A Lyot stop de-centering of 0.01 D provokes in both cases to lose 10% of contrast. This corresponds to 95 μm at the scale of SPHERE, which is reasonable here again.

5.5 Lyot stop rotation

Lyot stop rotation provokes a loss of 10% of contrast for an angle value of almost 2° in both cases, as it can be seen on the last plot of Fig. 11.

6 Summary and concluding remarks

We have reported here on the most interesting aspects and results of the whole end-to-end numerical study achieved during the design of the ALC for SPHERE/VLT, using a dedicated numerical tool and considering wavefront errors coming from a detailed optical aberrations analysis. First of all, the apodizer was optimized with respect to an ad hoc *modified* contrast, showing a very clear optimum for a mask diameter of $\sim 4\,\lambda/D$ (and its corresponding apodization). A number of critical points were then studied. The results obtained after the simulation of different classes of apodizer profile defects drove to the deduction of an upper and a lower tolerance profiles, together with specifications on possible bumps that could occur during the manufacturing of the apodizer. Afterwards the effects of the expected phase defects were simulated too, leading to a dramatic reduction of the coronagraphic performances, but we also found that a slight reduction of the Lyot stop diameter is sufficient to cancel out this effect. A ghost analysis was also performed, leading to a very reasonable specification on the ghost misalignment. De-centering of the apodizer, the focal mask, and the Lyot stop were then performed, leading here again to reasonable specifications on the needed precision on the position of the three main optical components of the ALC. Finally, we also tackled the problem of Lyot stop rotation and found an identical result.

In the second paper we analyze the results obtained during our laboratory experiments and compare it to the results presented here.

Acknowledgements The authors wish to thank A. Domiciano de Souza for a pertinent remark. Thanks are also due to Th. Fusco for providing the code permitting to simulate the XAO system SAXO, and to an anonymous referee for his comments that permitted to clarify some important points of the paper. G. Guerri is grateful to the CNRS (*Centre National de la Recherche Scientifique*, France), the *Région Provence Alpes Côte d'Azur* (France), and *Sud-Est Optique de Précision* (France) for having supported her PhD thesis. SPHERE is an instrument designed and built by a consortium consisting of LAOG (*Laboratoire d'Astrophysique de Grenoble*, France), MPIA (*Max-Planck-Institute für Astronomie*, Heidelberg, Germany), LAM (*Laboratoire d'Astrophysique de Marseille*, France), LESIA (*Laboratoire d'Études Spatiales et d'Instrumentation en Astrophysique*, Meudon, France), Laboratoire H. Fizeau (Nice, France), INAF–OAPD (*Istituto Nazionale di AstroFisica–Osservatorio Astrofisico di Padova*, Italy), Observatoire de Genève (Switzerland), ETH (*Eidgenössische Technische Hochschule*, Zürich, Switzerland), NOVA (*Nederlandse Onderzoekschool voor de Astronomie*, Leiden, The Netherlands), ONERA (*Office National d'Études et de Recherches Aérospatiales*, Châtillon, France), and ASTRON (Dwingeloo, The Netherlands), in collaboration with ESO (*European Southern Observatory*, Garching-bei-München, Germany).

References

1. Mayor, M., Queloz, D.: A Jupiter-mass companion to a solar-type star. Nature **378**, 355 (1995)
2. Beuzit, J.-L., Feldt, M., Dohlen, K., et al.: SPHERE: a planet finder instrument for the VLT. The Messenger **125**, 29 (2006)
3. Rouan, D., Riaud, P., Boccaletti, A., et al.: The four-quadrant phase-mask coronagraph. I. Principle. PASP **112**, 1479 (2000)

4. Aime, C., Soummer, R., Ferrari, A.: Total coronagraphic extinction of rectangular apertures using linear prolate apodization. A&A **389**, 334 (2002)
5. Guerri, G., Daban, J.-B., Robbe-Dubois, S., et al.: Apodized Lyot coronagraph for SPHERE/VLT: II. Laboratory tests and performances. Exp. Astron. (2011, accepted)
6. Lyot, B.: La couronne solaire étudiée en dehors des éclipses. C. R. Acad. Sci. Paris **4860**, 171 (1930)
7. Lyot, B.: The study of the solar corona and prominences without eclipses. MNRAS **4860**, 171 (1939)
8. Soummer, R., Aime, C., Falloon, P.: Stellar coronagraphy with prolate apodized circular apertures. A&A **397**, 1161 (2003)
9. Aime, C., Soummer, R.: Introduction to stellar coronagraphy with entrance pupil apodization. In: Aime, C., Soummer, R. (eds.) Astronomy with High Contrast Imaging: From Planetary Systems to Active Galactic Nuclei. EAS Pub. Series 8, 79 (2002)
10. Abe, L.: Numerical simulations in coronagraphy. Part I. In: Aime, C., Soummer, R. (eds.) Astronomy with High Contrast Imaging II: Instrumentation for Coronagraphy and Nulling Interferometry. EAS Pub. Series 12, 157 (2004)
11. Boccaletti, A.: Numerical simulations in coronagraphy. Part II. In: Aime, C., Soummer, R. (eds.) Astronomy with High Contrast Imaging II: Instrumentation for Coronagraphy and Nulling Interferometry. EAS Pub. Series 12, 165 (2004)
12. Ferrari, A., Soummer, R., Aime, C.: An introduction to stellar coronagraphy. C. R. Phys. **8**(3–4), 277 (2007)
13. Martinez, P., Boccaletti, A., Kasper, M., et al.: Optimization of apodized pupil Lyot coronagraph for ELTs. A&A **474**(2), 671 (2007)
14. Soummer, R., Pueyo, L., Sivaramakrishnan, A., Vanderbei, R.J.: Fast computation of Lyot-style coronagraph propagation. Opt. Express **15**(24), 15935 (2007)
15. Guyon, O., Roddier, F.: Direct exoplanet imaging possibilities of the nulling stellar coronagraph. In: Léna, P.J., Quirrenbach, A. (eds.) Interferometry in Optical Astronomy. SPIE Proc. 4006, 377 (2000)
16. Soummer, R., Aime, C., Falloon, P.: Prolate apodized coronagraphy: numerical simulations for circular apertures. In: Aime, C., Soummer, R. (eds.) Astronomy with High Contrast Imaging: From Planetary Systems to Active Galactic Nuclei. EAS Pub. Series 8, 93 (2003)
17. Soummer, R.: Apodized pupil Lyot coronagraphs for arbitrary telescope apertures. ApJ **618**, L161 (2005)
18. Carbillet, M., Vérinaud, C., Guarracino, M., et al.: CAOS - a numerical simulation tool for astronomical adaptive optics (and beyond). In: Bonaccini, D., Ellerbroek, B., Ragazzoni, R. (eds.) Adaptive Optics Systems, SPIE Proc. 5490(2), 550 (2004)
19. Petit, C., Fusco, Th., Charton, J., et al.: The SPHERE XAO system: design and performance. In: Hubin, N., Max, C.E., Wizinowich, P.L. (eds.) Advancements in Adaptive Optics. SPIE Proc. 7015, 70151D (2008)
20. Dohlen, K., Langlois, M., Saisse, M., et al.: The infra-red dual imaging and spectrograph for SPHERE: design and performance. In: McLean, I.S., Casali, M.M. (eds.) Ground-based and Airborne Instrumentation. SPIE Proc. 7014, 70143L (2008)
21. Claudi, R., Turatto, M., Gratton, R., et al.: SPHERE IFS: the spectro differential imager of the VLT for exoplanets search. In: McLean, I.S., Casali, M.M. (eds.) Ground-based and Airborne Instrumentation. SPIE Proc. 7014, 70143E (2008)
22. Thalmann, Ch., Schmid, H.M., Boccaletti, A., et al.: SPHERE ZIMPOL: overview and performance simulation. In: McLean, I.S., Casali, M.M. (eds.) Ground-based and Airborne Instrumentation. SPIE Proc. 7014, 70143F (2008)
23. Carbillet, M., Boccaletti, A., Thalmann, Ch., et al.: The software package SPHERE: a CAOS-based numerical tool for end-to-end simulations of SPHERE/VLT. In: Hubin, N., Max, C.E., Wizinowich, P.L. (eds.) Advancements in Adaptive Optics. SPIE Proc. 7015, 70156Z (2008)
24. Boccaletti, A., Carbillet, M., Fusco, Th., et al.: End to end simulation of AO-assisted coronagraphic differential imaging: estimation of performance for SPHERE. In: Hubin, N., Max, C.E., Wizinowich, P.L. (eds.) Advancements in Adaptive Optics. SPIE Proc. 7015, 70156E (2008)
25. Guerri, G., Robbe-Dubois, S., Daban, J.-B., et al.: Apodized Lyot coronagraph for VLT-SPHERE: laboratory tests and performances of a first prototype in the visible. In: McLean,

I.S., Casali, M.M. (eds.) Ground-based and Airborne Instrumentation II. SPIE Proc. 7014, 70143J (2008)
26. Born, M., Wolf, E.: Principles of Optics, 7th edn. Cambridge University Press, 499 (1979)
27. Goodell, W.V., Coulter, J.K., Johnson, P.B.: Optical constants of Inconel alloy films. J. Opt. Soc. Am. **63**, 85 (1973)

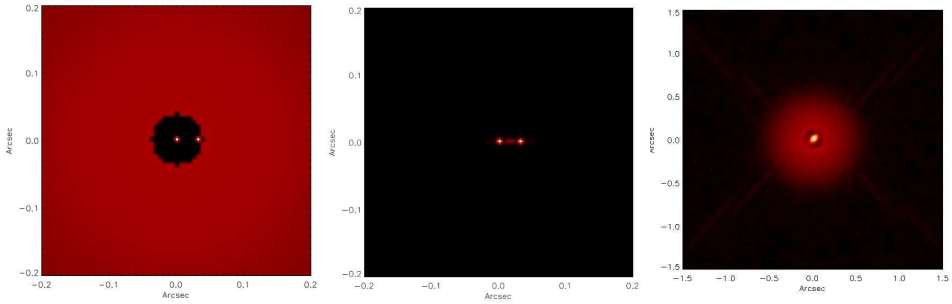

FIGURE 3.5: Exemple de binaire séparée de $0.5\,\lambda/D$ (un demi-élément de résolution du télescope donc) et munie d'un environnement faible (à gauche), observée sans coronographe à l'aide de SPHERE puis déconvoluée en suivant l'algorithme de super-résolution proposé (milieu), et observée avec le coronographe de Lyot apodisé de SPHERE puis déconvoluée de manière « standard » de manière à faire apparaître l'environnement circumbinaire.

3.5.3 Autres études effectuées dans le cadre de SPHERE

Passées les saisons de simulations « système » et de test des algorithmes de détection d'exoplanètes, le `Software Package SPHERE` a pu également être exploité en alliance avec le `Software Package AIRY` afin de préparer les observations des autres objets scientifiques visés, et notamment en ce qui concerne l'OCA de ceux relevant de la partie *Other Science* du groupe *Science* du consortium SPHERE.

Ceci a été initié, dans le cadre du stage de Master 2 d'I. Belokogne [142] co-encadré avec O. Chesneau, sur des objets binaires dont la séparation est en-dessous de la limite de diffraction du télescope et qui sont pourvus d'un environnement circumstellaire faible, avec donc à la fois une application de l'algorithme de super-résolution décrit précédemment et des premiers essais de déconvolution concernant l'environnement circumstellaire. Une des conclusions préliminaires intéressantes de ce travail est qu'une double observation (sans coronographe pour le côté super-résolution, puis avec coronographe pour l'imagerie circumbinaire) est toute indiquée pour ce type d'objets doublement ardus.

D'un point de vue technique, un premier problème se présente en phase même de simulation, pour l'obtention des images post-coronographe d'objets étendus. En effet, dans ce cas-là la PSF n'est pas uniforme dans le champ et dépend fortement de la distance hors-axe. Le temps et la puissance de calcul étant par ailleurs limités, dans certains cas (objets assez étendus) la solution adoptée pour l'heure a été de considérer une convolution de type « par parties », ce qui par contre devrait se révéler insatisfaisant dans le cas d'objets peu étendus [134].

Un second problème plus intéressant concerne la déconvolution de ces images post-coronographe devant permettre la reconstruction de l'environnement circumbinaire. En effet, et pour la même raison que précédemment (*space-variance* de la PSF), une déconvolution au sens propre n'est pas, comme nous pouvons le constater à la Fig. 3.5, totalement satisfaisante (alors que la super-résolution de la binaire centrale apparaît très clairement performante). Il faut sans doute, à présent et dans ce cas, étudier la possibilité de mettre en place un algorithme de pseudo-déconvolution de ces données.

3.6 Conclusion

Nous avons dans ce chapitre vu l'essentiel des travaux d'imagerie post-OA auxquels je me suis intéressé depuis ma thèse de doctorat, autant du point de vue de l'application de méthodes de déconvolution (pour l'instrument LN/LBT au départ, puis selon une portée plus générale), que de la coronographie de l'instrument SPHERE/VLT (en partant du coronographe lui-même et de la modélisation globale de l'instrument, pour arriver à la détection d'exoplanètes et à l'imagerie possible d'autres objets).

Concernant l'application de méthodes de déconvolution, j'ai tout d'abord, fort de l'outil `AIRY` présenté à la Sous-Sec. 1.2.3, abordé la reconstruction d'objets observés en mode interférométrique de Fizeau avec le LBT à la Sec. 3.2, reconstruction de type déconvolution multiple, à travers l'étude de deux limitations physiques importantes : la couverture angulaire permise par la position de l'objet, et la correction adaptative obtenue pour les données. Un résultat concernant l'imagerie à grand champ (et donc par extension l'OAMC prévue pour cet instrument) est également formulé : l'uniformité de la correction de l'OA sur le champ de vue peut se révéler plus importante que la qualité globale des images.

Les études de la même veine d'application principale à LN/LBT, et effectuées à la suite des deux premiers articles reproduits dans cette thèse, ont été ensuite évoquées : algorithme de super-résolution, recherche d'accélérations ultérieures, application de régularisations permettant soit de diminuer les effets de bord, soit de traiter la reconstruction d'objets à très forte dynamique, application d'un algorithme de déconvolution aveugle, proposition de déconvolution aveugle avec contrainte de Strehl.

Les deux applications auxquelles je me suis particulièrement intéressé par la suite ont été la super-résolution par déconvolution d'une part (à la Sec. 3.3) et la déconvolution aveugle avec contrainte de Strehl d'autre part (à la Sec. 3.4).

La super-résolution fait l'objet de la première application à des données réelles d'étoiles binaires particulièrement serrées, avec confirmation du résultat trouvé par des observations AMBER/VLTI, et proposition d'accélération par ailleurs. Les perspectives énoncées pour cette application sont dans l'immédiat liées à ses améliorations possibles, puis, à une échelle temporelle plus grande,

à une application espérée très large sur les plus grands télescopes équipés des meilleurs système d'OA (VLT, LBT, E-ELT).

La déconvolution aveugle avec contrainte de Strehl est ensuite proposée et ses performances attendues sont présentées. Un renfort théorique ayant été effectué récemment concernant cette méthode, la nouvelle version qui en découle pour le `Software Package AIRY` doit bientôt être proposée à la communauté. Elle sera ensuite appliquée à des données réelles obtenues avec NAOS/VLT.

Les travaux effectués dans le cadre de l'instrument SPHERE sont présentés à la Sec. 3.5. L'outil ad hoc développé (le `Software Package SPHERE`, déjà présenté à la Sous-sec. 1.2.4), a été utilisé, entre autres choses, pour l'étude détaillée du coronographe de Lyot apodisé, étude à l'issue de laquelle le diamètre du masque focal du coronographe a été déterminé (et de manière associée l'apodiseur correspondant) par optimisation d'un critère de contraste redéfini au passage. Le `Software Package SPHERE` a également été très largement utilisé dans le cadre de la mise en place d'algorithmes de détection d'exoplanètes pour l'instrument. Finalement, l'application de stratégies d'observation ad hoc (avec coronographe pour le milieu circumbinaire, sans coronographe pour la binaire centrale) et de méthodes d'imagerie tout aussi ad hoc (super-résolution pour la binaire centrale, pseudo-déconvolution encore à mettre en place pour le milieu circumbinaire) est également présentée pour un objet alternatif aux exoplanètes mais particulièrement intéressant et stimulant pour un instrument tel que SPHERE.

Chapitre 4

Bilan et perspectives

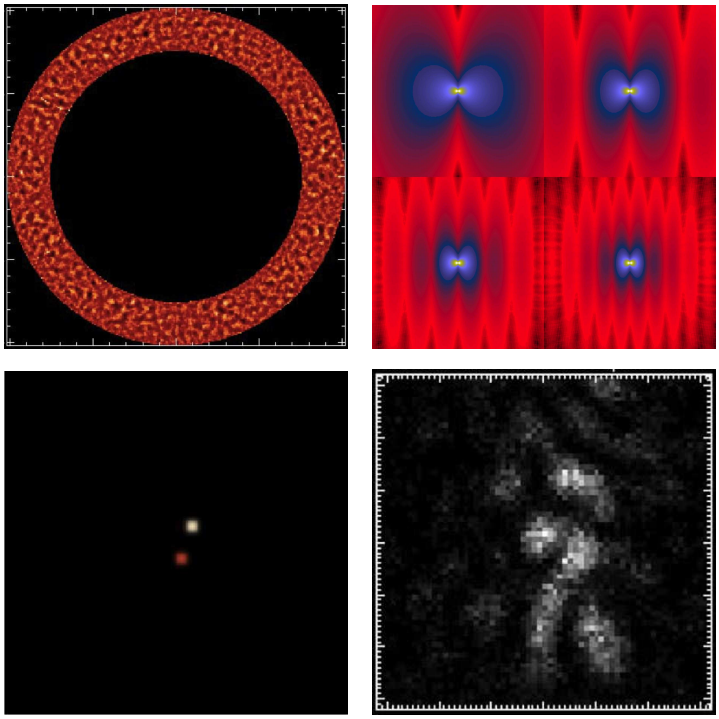

La vérité ne se possède pas, elle se cherche.
Albert Jacquart, in *Petite philosophie à l'usage des non-philosophes*,
Calmann-Lévy (Livre de poche), 1997.

4.1 Sommaire

Le sommaire qui suit a pour ambition, plutôt que de simplement passer en revue les thématiques scientifiques exposées dans la thèse, de les situer au sein de l'ensemble constituant mon parcours professionnel depuis l'obtention de ma thèse de doctorat en décembre 1996 – parcours fait de thématiques scientifiques, mais aussi de responsabilités et de collaborations.

Modélisation numérique d'OA La modélisation numérique des composantes physiques des système d'OA a été tout d'abord directement liée à la responsabilité que j'ai revêtu au sein du groupe d'OA de l'INAF–OAA pour les études numériques nécessaires à la conception du système d'OA de première lumière du LBT. Ces études numériques ont tout d'abord nécessité la mise en place de l'outil de simulation `CAOS` (vu en détail à la Sous-sec. 1.2.2 et devenu avec le temps un des *software packages* du `PSE` homonyme de portée et d'utilisation plus générales). Cette activité de modélisation a tout d'abord eu comme objectif la caractérisation complète d'un système particulièrement innovant, puisque basé sur un ASO pyramidal et un miroir secondaire adaptatif, dont le résultat final en termes de performances attendues avec l'instrumentation scientifique en aval est matérialisé par la Sous-sec. 2.5.1. Les études engendrées ont auparavant concerné différentes questions aussi bien sur le plan de la modélisation de l'atmosphère turbulente (voir à la Sous-sec. 2.2.1), que sur celui du système lui-même : le type d'ASO à considérer et ses configurations (voir Sous-sec. 2.3.1), l'éventualité d'un analyseur spécifique au basculement atmosphérique (voir l'étude traitée au sein de la publication présentée à la Sous-sec. 1.2.2), l'éventualité d'un EMCCD pour l'ASO (voir le résultat publié à la Sous-sec. 2.3.2) – question finalement encore d'actualité pour le système FLAO [157], etc.

Ces différents développements numériques au sein de l'outil, outil dont il a fallu également assurer la maintenance et la bonne distribution (voir à ce sujet le site consacré `http://lagrange.oca.eu/caos`), ont bénéficié des apports de nombreux intervenants qu'il a fallu coordonner. Cette dynamique a permis un certain nombre de collaborations fructueuses :

- ⋆ Certaines ont perdurées après mon séjour à l'INAF–OAA. La collaboration avec C. Vérinaud concernant l'OA à très haute dynamique est évoquée à la Sous-sec. 2.3.1. La Sous-sec. 2.2.1 et la Sous-sec. 2.3.2 s'articulent quant à elles autour de la collaboration avec A. Riccardi concernant la finalisation de quelques points de modélisation (sous forme de publications consultables et de codes distribués au sein du `Software Package CAOS`).
- ⋆ D'autres ont été engagées par la suite. La Sec. 2.4 fait état de la collaboration avec A. Riccardi concernant les études numériques nécessaires pour le miroir M4 de l'E-ELT. La Sous-sec. 2.5.3 s'intéresse notamment à la collaboration avec É. Aristidi et à l'encadrement de différents tra-

vaux (stage de C. Giordano et al. [120], stage d'A.-L. Maire [121], une partie de la thèse de C. Giordano co-dirigée avec J. Vernin) concernant les conclusions à tirer des mesures atmosphériques effectuées au Dôme C pour un système d'OA à éventuellement y installer. La Sous-sec. 2.5.2 présente la collaboration avec L. Jolissaint concernant la comparaison et la recherche de compromis entre modélisation analytique « à la `PAOLA` » et modélisation end-to-end « à la `CAOS` ».

D'autres efforts de modélisation qui n'ont pas été détaillés dans cette thèse ont concerné la commande en OA (collaboration tout d'abord avec B. Le Roux découlant également de mon séjour à l'INAF–OAA, collaboration plus récente avec J.-P. Folcher et A. Ferrari autour de la thèse d'A. Abelli [153]), la caractérisation du site accueillant le télescope sud-africain SALT et le dimensionnement d'un système d'OA le concernant (collaboration avec A. Ziad autour de la thèse de L. Catala), ou encore la correction apportée par MACAO dans le cadre des mesures interférométriques (au sens de Michelson cette fois) effectuées par AMBER au VLTI (collaboration avec notamment S. Robbe-Dubois).

Imagerie post-OA L'imagerie post-OA [1] a également été liée à une responsabilité que j'ai revêtu, celle au sein de l'INAF–OAA qui concernait les tests et la recherche d'algorithmes de reconstruction pour le mode interférométrique du LBT et qui a inclus la co-direction de la thèse de S. Correia [57]. Plus tard, la continuation de la collaboration me liant à mes collègues de l'Università di Genova m'a tout naturellement impliqué dans le co-encadrement de plusieurs autres thèses [86, 132, 147]. Cette collaboration, à laquelle est consacré le site `http://airyproject.eu`, a par ailleurs été porteuse de nombreuses publications, de l'évolution toujours vive du `Software Package AIRY` depuis une douzaine d'années, du `Software Package AIRY-LN` délivré au sein du consortium développant l'instrument LN. Les thématiques scientifiques concernées ont couvert tout d'abord la proposition d'un algorithme de déconvolution multiple pour les images interférométriques de LN/LBT (dès la Sous-sec. 1.2.3), les études concernant les limites en termes de couverture angulaire et de correction d'OA pour la reconstruction d'objet avec LN/LBT (voir Sous-sec. 3.2.1), la proposition, l'étude et l'application d'une part d'un (simple) algorithme de super-résolution par déconvolution (à la Sec. 3.3) et d'autre part de la considération d'une contrainte de Strehl dans le cadre de la déconvolution aveugle (à la Sec. 3.4), puis un ensemble d'autres propositions d'accélérations et de régularisations permettant notamment de diminuer les effets de bord ou de traiter la reconstruction d'objets à très forte dynamique (listées à la Sous-sec. 3.2.2).

1. Dans laquelle j'inclus autant l'application de méthodes de déconvolution dédiées à certains cas observationnels intéressants (interférométrie de Fizeau avec LN/LBT, super-résolution par déconvolution, déconvolution aveugle avec contrainte de Strehl), que la coronographie stellaire autour de l'instrument SPHERE (définition du coronographe de Lyot apodisé, modélisation de l'instrument dans son ensemble, détection d'exoplanètes, imagerie d'autres cibles astrophysiques).

La proposition de super-résolution par déconvolution a été appliquée à des données post-OA impliquant des données issues du système NAOS et de la caméra proche-infrarouge CONICA (ou NACO pour marier les deux) du VLT, d'une part dans le cadre d'une collaboration avec J. Girard, responsable à l'ESO de NACO, et d'autre part avec O. Chesneau et F. Millour. La proposition de contrainte de Strehl, quant à elle, a été développée dans le cadre du séjour de G. Desiderà à Nice en 2009 pendant la préparation de sa thèse de doctorat.

À mon arrivée à Nice, fin 2004, j'ai pris la responsabilité des activités du laboratoire au sein du consortium SPHERE, activités qui concernaient déjà les développements instrumentaux autour du coronographe de Lyot apodisé, mais également et par la suite la mise en place de l'outil de modélisation très détaillé du point de vue instrumental, le `Software Package SPHERE`, d'une part, ainsi que la mise en route des études autour de l'extraction de signal/détection d'exoplanètes, notamment dans le cadre de la thèse d'I. Smith co-dirigée avec A. Ferrari [138] – ce même sujet, mêlant intimement modélisation physique et modélisation statistique, avait par ailleurs déjà concerné les stages de niveau Master 2 de E. Serradell [99], F. Allouche [85] et A. Ambros [101]. Plus récemment, les activités locales autour de l'instrument SPHERE ont dérivé vers la préparation des observations d'objets alternatifs au sujet phare de l'instrument (les exoplanètes) [156, 158], activités développées notamment autour du stage de Master 2 d'I. Belokogne [142], que j'ai co-dirigé avec O. Chesneau, et de la thèse actuellement préparée par Z. Khorrami, co-dirigée par O. Chesneau et F. Vakili et pour laquelle je participe à la partie modélisation instrumentale.

4.2 Perspectives

Il existe une part importante de maintenance et développement du `PSE CAOS` dans la partie « bilan » précédente qui se retrouve transmise intégralement à cette partie « perspectives »... Il est en effet, à mon sens, fondamental de faire l'effort de maintenir à disposition de la communauté un ensemble d'outils de référence dans les domaines de la modélisation numérique en OA (et même plus généralement en optique astronomique) d'une part, et des méthodes de traitement des données post-OA et post-instrumentation (recombinaison de Fizeau, coronographie, autres) d'autre part. Ceci ne constitue pas en soit une perspective très excitante, mais il s'agit là d'entretenir un écrin pouvant permettre à de nouvelles perspectives plus intéressantes d'éclore...

Les (autres) perspectives scientifiques liées à cette thèse d'HDR ont déjà été en partie semées tout au long du document. Je vais ici en rappeler l'essentiel en tentant de le placer dans un contexte pratique.

Modélisation numérique d'OA Il s'agit dans ce cadre tout d'abord d'améliorer la représentation utilisée couramment aujourd'hui de l'atmosphère tur-

bulente en optique astronomique. Cette représentation considère souvent, du moins au sein du `Software Package CAOS`, une propagation à travers les couches turbulentes simplement géométrique, ne prenant donc aucunement en compte son caractère naturellement « de Fresnel » (et donc, notamment, ne pouvant tenir compte du phénomène de scintillation). De la même manière, l'échelle externe de la turbulence $\mathcal{L}_0$ n'est considérée que par sa valeur intégrée et non par son profil (contrairement à la situation physique réelle où à chaque couche turbulente correspond une échelle externe, comme c'est le cas pour r_0 et $\vec{v}$), et l'hypothèse de Taylor est communément embrassée (voir Sous-sec. 2.2.2). Il ne s'agit pas a priori d'appliquer ces points aveuglément et systématiquement (propagation de Fresnel, profil de $\mathcal{L}_0$, alternative à l'hypothèse de Taylor) mais de jauger de leur utilité au vu des mesures atmosphériques les plus récentes, voire même spécialement effectuées pour l'occasion, et de pouvoir les avoir à disposition si et quand la nécessité scientifique le réclamera. D'un point de vue pratique, ces différents développements de modélisation atmosphériques se feront (sont déjà en train de se mettre en place) dans le cadre d'une collaboration avec A. Ziad, collègue avec lequel je collabore déjà dans le cadre de la thèse de doctorat (et avant du stage de Master 2) [145] de L. Catala pour les études liées au télescope sud-africain SALT.

Un second point concerne les études menées en collaboration avec A. Riccardi sur le miroir adaptatif M4 pour l'E-ELT. Les résultats obtenus jusqu'ici et reportés à la Sous-sec. 2.4.2 l'ont été en considérant une configuration optique, et donc une série de fonctions d'influence (FI), maintenant obsolète. Il s'agit ici de déterminer précisément quel actionneur du miroir M4 (pour ceux externes à la projection en axe de la pupille qui a notablement diminuée) est finalement à considérer comme slave « forcé » ou slave « non-forcé »... En effet, un grand nombre d'entre eux se retrouvent à présent suffisamment loin de la projection en axe de la pupille pour produire une mauvaise inversion numérique lors de la projection du front d'onde d'entrée sur la base des FI définissant le miroir. La solution optimale finale impliquera probablement une classification des actionneurs en trois classes au lieu des deux considérées auparavant, dans un soucis d'optimisation de l'erreur de sous-échantillonnage spatial, ainsi que de la considération d'une base de modes, déduite de celle des FI, plus adaptée au problème physique que celle qui découle de la pseudo-inversion calculée lors de phase de reconstruction du front d'onde. Par la suite, les performances du miroir devront être évaluées également en considérant un modèle physique complet de l'ASO (et pour être clair et précis le modèle de pyramide au sein du `Software Package CAOS`), grâce au modèle réduit du miroir (pour les raisons évoquées précédemment), modèle dont la validité a déjà été testée lors des simulations avec le modèle impliquant la pupille précédente de 42 m (au lieu des 39 m actuels).

Les perspectives relatives au travail de comparaison et de recherche de compromis entre modélisation OA analytique et end-to-end, mené de concert avec L. Jolissaint, ont été déjà énoncées en conclusion de la Sous-sec. 2.5.2.

Pour rappel, il s'agit ici de faire converger du mieux possible les deux approches en comprenant mieux leurs différences, au niveau par exemple des modes choisis pour le miroir déformable (l'équivalent de fonctions *sinc* sous `PAOLA`, des modèles plus proches des miroirs existants sous `CAOS`) et en vérifiant de manière plus poussée la validité du modèle de bruit de mesure analytique dans certains cas limite. D'autres améliorations sont possibles aussi du côté du code end-to-end pour les futures comparaisons, comme le nombre de réalisations indépendantes (peut-être trop faible jusqu'ici) d'une part et une recherche d'optima plus systématique pour les paramètres caractérisant la boucle d'autre part (à comparer aux optima calculés a priori avec le code analytique, optima sur lesquels nous nous sommes basés précédemment). C'est un travail minutieux d'accordage qu'il s'agit de tenir ici, soulevant parfois des questions plus fondamentales, et qui devrait mener à un compromis intéressant pour les modélisations gourmandes en temps de calcul et/ou en mémoire vive.

Un premier domaine d'application, moins radicalement demandeur que les applications ELT, pourrait concerner l'OA à grand champ pour le dôme C. Comme il a été expliqué à la Sous-sec. 2.5.3, il s'agit ici de tirer au mieux partie des dernières mesures disponibles concernant la statistique de la couche limite de turbulence (plus d'évènements, plus de résolution spatiale) afin qu'une conclusion puisse être donnée, indiquant quel est le meilleur système adaptatif à prévoir et dans quelles conditions de fonctionnement – hauteur de la tour recevant le télescope, pourcentage de temps dédié à l'astronomie grand champ et performance correspondantes, etc. Ce travail est à mener en collaboration avec (notamment) É. Aristidi et C. Giordano, pour ce dernier dans le cadre de sa thèse de doctorat. Ces modélisations ont également été inscrites au programme de la récente demande ANR ANGISS menée par M. Langlois à Lyon et pour lequel je suis responsable du *work package* en charge de la définition du « concept » d'OA et d'instrumentation focale.

Imagerie post-OA Les deux algorithmes proposés plus tôt (super-résolution d'une part et contrainte de Strehl d'autre part) sont porteurs de perspectives d'application à des données réelles, (au moins !) dans le cadre d'une collaboration avec J. Girard, responsable du système NACO/VLT, pour ce qui est de la super-résolution, et dans le cadre d'une collaboration avec É. Habart pour ce qui est de la contrainte de Strehl. Ces deux applications, couplées aux avancées/implémentations correspondantes au sein de l'outil `AIRY`, seront également effectuées en collaboration avec A. La Camera. Un sujet de stage de Master 2 a été déposé récemment concernant le traitement des données et les tests par simulation nécessaires déjà évoqués à la Sous-sec. 3.4.2 (limites en rapport de Strehl et rapport signal-à-bruit notamment). Le but ultime est bien entendu de proposer ces algorithmes à un ensemble vaste de données de télescopes optiques équipés de système d'OA, présents et futurs.

Le volet de préparation des observations avec SPHERE doit continuer sur le chemin actuel au niveau modélisation instrumentale, avec la possibilité d'application des deux algorithmes pré-cités, comme déjà précisé à la Sous-sec. 3.5.3 notamment pour ce qui est de la super-résolution. Le développement d'une procédure de pseudo-déconvolution des images post-coronographe d'objets étendus serait également à mettre en œuvre.

Un dernier volet de perspectives concerne la mise en place de techniques d'imagerie à la frontière entre déconvolution et imagerie speckle, afin d' « étendre le domaine de la lutte » de l'imagerie post-OA vers le visible, domaine spectral où la correction est (tout particulièrement) partielle. Il s'agit ici de parvenir à la proposition de méthodes d'imagerie (acquisition des données, traitements des données) adaptées à chaque niveau de correction atteint par un système d'OA, en focalisant particulièrement sur les basses corrections et en considérant des techniques allant de la déconvolution aveugle avec contrainte de Strehl pour les régimes de correction plus cléments, à des techniques speckle avancées (e.g. inter-corrélation [35], densité de probabilité d'ordre supérieur [36]), en passant par la technique dite de *Lucky Imaging*.

Cette recherche pourra profiter d'une part du système d'OA ODISSEE actuellement en phase d'adaptation sur le télescope de 1.54 m MéO (pour Métrologie Optique) de l'Observatoire de Calern, système développé par ailleurs par l'ONERA (Office National d'Études et de Recherches Aérospatiales) en collaboration avec l'OCA, en y installant une caméra rapide de type EMCCD dédiée à ce type d'observations. Ceci fait l'objet d'un *work package* dédié dont je suis responsable au sein de la demande ANR ILIOS menée par T. Fusco de l'ONERA. Une demande CPER-FEDER 2014–2020 dont je suis le porteur (la demande AOC – pour *Adaptive Optics at Calern*) propose également cette thématique de recherche, avec en sus un équipement de mesure des paramètres de la turbulence atmosphérique à installer sur le site de Calern (afin de pouvoir recueillir en temps réel ces informations directement liées à la qualité de l'image finale), ainsi que l'installation d'un second système d'OA afin d'en équiper le télescope C2PU voisin.

Bibliographie

[1] "Über Luftschlieren und Zonenfehler, Zeitschrift für Instrumentenkunde", K. Strehl, *Zeitschrift für Instrumentenkunde* **22**, 213–217 (1902).

[2] "The local structure of turbulence in incompressible viscous fluids at very large Reynolds numbers", A. N. Kolmogorov, *Dokl. Akad. Nauk. SSSR* **30(4)**, 299 (1941).
(Reprinted in *Proc. R. Soc. London A* **434**, 9 (1991)).

[3] V. I. Tatarski, *Wave Propagation In A Turbulent Medium*, Translated by R. A. Silverman, McGraw-Hill, New York (1961).

[4] "Optical Resolution Through a Randomly Inhomogeneous Medium for Very Long and Very Short Exposures", D. L. Fried, *J. Opt. Soc. Am.* **56**, 1372 (1966).

[5] "Attainment of diffraction-limited resolution in large telescopes by Fourier analysing speckle patterns in star images", A. Labeyrie, *Astron. Astrophys.* **6**, 85 (1970).

[6] "Reconstructed images of Alpha Orionis using stellar speckle interferometry", S. P. Worden, C. R. Lynds, J. W. Harvey, *J. Opt. Soc. Am.* **66**, 1243 (1976).

[7] "Modified astronomical speckle interferometry 'speckle masking' ", G. P. Weigelt, *Opt. Commun.* **21**, 55 (1977).

[8] "The universe at faint magnitudes. I - Models for the Galaxy and the predicted star counts", J. N. Bahcall & R. M. Soneira, *Astroph. J. Supp. Ser.* **44**, 73 (1980).

[9] "The effects of atmospheric turbulence in optical astronomy", F. Roddier, *Progress in Optics* **XIX**, 281, E. Wolf Ed., North-Holland Pub. Co. (1981).

[10] F. Roddier, *Distributions et transformation de Fourier*, McGraw-Hill (1981).

[11] "On the isoplanatic patch size in stellar speckle interferometry.", F. Roddier, J. M. Gilli, J. Vernin, *J. Optics (Paris)* **13**, 63 (1982).

[12] "On the origin of speckle boiling and its effects in stellar speckle interferometry", F. Roddier, J.-M. Gilli, G. Lund, *J. Opt.* **13**, 263 (1982).

[13] "Feasibility of adaptive telescope with laser probe", R. Foy & A. Labeyrie, *Astron. Astrophys.* **152 (2)**, L29 (1985).

[14] "Contribution to the space-time study of stellar speckle patterns", C. Aime, J. Borgnino, F. Martin, R. G. Petrov, G. Ricort, S. Kadiri, *J. Opt. Soc. Am. A* **3**, 1001 (1986).

[15] "Proposition of speckle probability imaging for stellar systems", C. Aime, *J. Optics (Paris)* **10**, 318 (1987).

[16] "Curvature sensing and compensation : a new concept in adaptive optics", F. Roddier, *Appl. Opt.* **27**, 1223 (1988).

[17] "Estimation of the spatial coherence outer scale relevant to long baseline interferometry and imaging in optical astronomy", J. Borgnino, *Appl. Opt.*, **29**, 1863 (1990)

[18] "First diffraction-limited astronomical images with adaptive optics", G. Rousset,J.-C. Fontanella, P. Kern, P. Gigan, F. Rigaut, P. Léna, C. Boyer, P. Jagourel, J.-P. Gaffard, F. Merkle, *Astron. Astrosphys.* **230**, L29 (1990).

[19] A. Acker, *Astronomie — Introduction*, Coll. De Caelo, Éd. Masson (1992).

[20] "Simulation of a Kolmogorov phase screen", R. G. Lane, A. Glindeman, J. C. Dainty, *Waves in Random Media* **2**, 209 (1992).

[21] J. S. Levine, in *The Astronomy And Astrophysics Encyclopedia*, S. P. Moran Ed., Cambridge University Press, 176 (1992).

[22] "Laser guide star in adaptive optics – The tilt determination problem", F. Rigaut & É. Gendron, *Astron. Astrophys.*, **261**, 677 (1992).

[23] "Estimation des échelles limites de cohérence spatiale des fronts d'onde et optimisation des observations à haute résolution angulaire en astronomie", A. Ziad, Thèse de Doctorat, Université de Nice–Sophia Antipolis (1993).

[24] "GSM : une expérience dédiée à la mesure des paramètres de cohérence des fronts d'onde en Haute Résolution Angulaire", A. Agabi, Thèse de Doctorat, Université de Nice–Sophia Antipolis (1994).

[25] "Contribution à l'étude de l'apparition de la turbulence optique dans les couches minces. Concept du Scidar généralisé", A. Fuchs, Thèse de Doctorat, Université de Nice–Sophia Antipolis (1995).

[26] "A Jupiter-mass companion to a solar-type star", M. Mayor & D. Queloz, 1995, Nature, 378, 355 (1995).

[27] "Theoretical spatiotemporal analysis of angle of arrival induced by atmospheric turbulence as observed with the grating scale monitor experiment", R. Avila, A. Ziad, J. Borgnino, F. Martin, A. Agabi, A. Tokovinin, *J. Opt. Soc. Am. A* **14 (11)** (1996).

[28] "Techniques probabilistes : application à l'imagerie à haute résolution angulaire en astrophysique", M. Carbillet, Thèse de Doctorat, Université de Nice–Sophia Antipolis (1996).

[29] "Probability imaging of a few double stars from near-infrared one-dimensional speckle data", M. Carbillet, G. Ricort, C. Aime, Ch. Perrier, *Astron. Astrophys.* 310, 508 (1996).

[30] "Discovery of a new bright close double star" (*Research Note*), M. Carbillet, B. Lopez, É. Aristidi, Y. Bresson, C. Aime, G. Ricort, J.-L. Prieur, L. Koechlin, G. Helmer, J. Lefèvre, P. Cruzalèbes, *Astron. Astrophys.* **314**, 122 (1996).

[31] P. Léna (avec le concours de F. Lebrun & F. Mignard) : *Astrophysique – Méthodes physiques de l'observation*, 2me Éd., Coll. Savoirs Actuels, InterÉd./CNRS Éd. (1996).

[32] "Pupil plane wavefront sensing with an oscillating prism", R. Ragazzoni, *Journal of Modern Optics* **43 (2)**, 289 (1996).

[33] "Adaptive Optics Imaging of GG Tauri : Optical Detection of the Circumbinary Ring", C. Roddier, F. Roddier, M. J. Northcott, J. E. Graves, K. Jim, *Astroph. J.* **463**, 326 (1996).

[34] "Site atmospheric characterization", M. Sarrazin, in *ESO Conf. and Workshop Proc. (Topical Meeting held October 2–6, 1995)*, M. Cullum Ed., 439 (1996).

[35] "Imaging binary stars by the cross-correlation technique", É. Aristidi, M. Carbillet, J.-F. Lyon, C. Aime, *Astron. Astrophys. Suppl. Ser.* **125**, 139 (1997).

[36] "Speckle imaging of binary stars : use of ratios of twofold probability density functions", M. Carbillet, C. Aime, É. Aristidi, G. Ricort, *Astron. Astrophys. Suppl. Ser.* **127**, 569 (1998).

[37] "Laser guide stars for 8-m class telescopes", F. Delplancke, M. Carbillet, N. Hubin, S. Esposito, F. Rigaut, E. Marchetti, A. Riccardi, É. Viard, R. Ragazzoni, M. Le Louarn, L. Fini, in *Adaptive Optical System Technologies*, D. Bonaccini & R. K. Tyson Eds., *SPIE Proc.* **3353**, 371 (1998).

[38] "Performance analysis of and compensation for aspect-ratio of fast-Fourier-transform-based simulations of large atmospheric wavefronts", G. Sedmak, *App. Opt.* **37** (21), 4605 (1998).

[39] "LA^{3}OS^2 : a software package for laser guide star adaptive optics systems", M. Carbillet, B. Femenía, F. Delplancke, S. Esposito, L. Fini, A. Riccardi, É. Viard, N. Hubin, F. Rigaut, in *Adaptive Optics Systems and Technology*, R. K. Tyson & R. Q. Fugate Eds., *SPIE Proc.* **3762**, 378 (1999).

[40] "Preliminary results of simulations for the adaptive optics system of the Large Binocular Telescope", M. Carbillet, A. Riccardi, B. Femenía, L. Fini, S. Esposito, in *Telescopes, instruments and data processing for astronomy in the year 2000*, *Mem. Soc. Astr. It./AstroTech Journal* **2 (2)** (1999).

[41] "Sentivity of a pyramidic wavefront sensor in closed-loop adaptive optics", R. Ragazzoni & J. Farinato, *Astron. Astrophys.* **350**, L23 (1999).

[42] "Imaging through the atmosphere", F. Roddier, in *Adaptive Optics for Astronomy*, F. Roddier Ed. (Cambridge University Press), 16 (1999).

[43] "Wave-front sensors", G. Rousset, in *Adaptive Optics for Astronomy*, F. Roddier Ed. (Cambridge University Press), 91 (1999).

[44] "Application of the OS-EM method to the restoration of LBT images", M. Bertero & P. Boccacci, *Astron. Astrophys. Suppl. Ser.* **144**, 181 (2000).

[45] "Image restoration methods for the Large Binocular Telescope (LBT)", M. Bertero & P. Boccacci, *Astron. Astrophys. Suppl. Ser.* **147**, 323 (2000).

[46] "A study for a multi-conjugate adaptive optics system for 8-m class telescopes", G. Brusa, A. Riccardi, S. Esposito, B. Femenía, M. Carbillet, in *Adaptive Optics Technology*, T. D. Steiner & P. H. Merritt Eds, *SPIE Proc.* **4034**, 190 (2000).

[47] "Adaptive optics simulations for imaging with the Large Binocular Telescope interferometer : a first application", M. Carbillet, S. Correia, B. Femenía, A. Riccardi, in *Adaptive Optical Systems Technology*, P. L. Wizinowich Ed., *SPIE Proc.* **4007**, 155 (2000).

[48] "Large Binocular Telescope image restoration using simulated adaptively corrected point-spread functions", S. Correia, M. Carbillet, A. Richichi, M. Bertero, P. Boccacci, in *Interferometry in Optical Astronomy*, P. J. Léna & A. Quirrenbach Eds., *SPIE Proc.* **4006**, 650 (2000).

[49] "Diffraction-limited 800 nm imaging with the 2.56 m Nordic Optical Telescope", J. E. Baldwin, R. N. Tubbs, C. D. Mackay, R. W. Wilson, M. I. Andersen, *Astron.& Astrophys.* **368**, L1 (2001).

[50] "CAOS Simulation Package 3.0 – an IDL-based tool for adaptive optics systems design and simulations", M. Carbillet, L. Fini, B. Femenía, A. Riccardi, S. Esposito, É. Viard, F. Delplancke, N. Hubin, in *Astronomical Data Analysis Software And Systems X*, F. R. Harnden, Jr., F. A. Primini, H. E. Payne, Eds., *ASP Conf. Series* **238**, 249 (2001).

[51] "AIRY – Astronomical Image Restoration in interferometrY", S. Correia, M. Carbillet, L. Fini, P. Boccacci, M. Bertero, A. Vallenari, A. Richichi, M. Barbati, in *Astronomical Data Analysis Software And Systems X*, F. R. Harnden, Jr., F. A. Primini, H. E. Payne, Eds., *ASP Conf. Series* **238**, 404 (2001).

[52] "Pyramid wavefront sensor behavior in partial correction adaptive optics systems", S. Esposito & A. Riccardi, *Astron. Astrophys.* **369**, L9 (2001).

[53] "Numerical simulations of MCAO modal systems in open-loop and closed-loop operation", B. Femenía, M. Carbillet, S. Esposito, G. Brusa, in *Adaptive Optics Systems and Technology II*, R. K. Tyson & D. Bonaccini Eds., *SPIE Proc.* **4494**, 132 (2001).

[54] "The CAOS Application Builder", L. Fini, M. Carbillet, A. Riccardi, in *Astronomical Data Analysis Software And Systems X*, F. R. Harnden, Jr., F. A. Primini, H. E. Payne, Eds., *ASP Conf. Series* **238**, 253 (2001).

[55] "Total coronagraphic extinctions of rectangular apretures using linear prolate apodization", C. Aime, R. Soummer, A. Ferrari, *Astron. Astrophys.* **389**, 334 (2002).

[56] "Restoration of interferometric images : II. The case-study of the Large Binocular Telescope", M. Carbillet, S. Correia, P. Boccacci, M. Bertero, *Astron. Astrophys.* **387** (2), 743 (2002).

[57] "Haute résolution angulaire et interférométrie optique en astrophysique : applications au Large Binocular Telescope et au Very Large Telescope Interferometer", S. Correia, Thèse de doctorat, Université de Nice–Sophia Antipolis (2002).

[58] "Restoration of interferometric images : I. The software package AIRY", S. Correia, M. Carbillet, P. Boccacci, M. Bertero, L. Fini, *Astron. Astrophys.* **387** (2), 733 (2002).

[59] "High angular resolution observations of late-type stars", J.-L. Prieur, É. Aristidi, B. Lopez, M. Scardia, F. Mignard, M. Carbillet, *Ap. J. Suppl.* **139**, 249–258 (2002).

[60] "Comparison of different 3D wavefront sensing and reconstruction techniques for MCAO", D. Bello, C. Vérinaud, J.-M. Conan, M. Carbillet, in *Adaptive Optical Systems Technology*, P. L. Wizinovich & D. Bonaccini Eds., *SPIE Proc.* **4839**, 554 (2003).

[61] "Closed loop performance of a modal MCAO system using real star configurations : the young open cluster NGC 2362 as seen by MAD", M. Carbillet, B. Femenía, S. Esposito, G. Brusa, S. Correia, in *Beyond conventional adaptive optics*, É. Vernet-Viard, R. Ragazzoni, S. Esposito, N. Hubin, Eds., *ESO Conference & Workshop Proc.* **58**, 259 (2003).

[62] "Performance of the first-light AO system of LBT by means of CAOS simulations", M. Carbillet, C. Vérinaud, S. Esposito, A. Riccardi, A. Puglisi, B. Femenía, L. Fini, in *Adaptive optical systems technology*, P. L. Wizinovich & D. Bonaccini Eds., *SPIE Proc.* **4839**, 131 (2003).

[63] "Performance of the restoration of LBT interferometric images – the effect of angular coverage and partial adaptive optics correction", M. Carbillet, S. Correia, P. Boccacci, M. Bertero, in *Interferometry for Optical Astronomy II*, W. A. Traub Ed., *SPIE Proc.* **4838**, 444 (2003).

[64] "Development of a Generalized SCIDAR at UNAM", D. X. Cruz, F. Angeles, R. Avila, S. Cuevas, A. Farah, S. I. González, A. Iriarte, L. A. Martínez, M. Martínez, B. Sánchez, L. J. Sánchez, in *San Pedro Mártir : Astronomical Site Evaluation*, I. Cruz-González, R. Avila, M. Tapia, Eds., *Rev. Mex. Astron. Astrofis. (Conf. Ser.)* **19**, 44 (2003).

[65] "Efficient distribution of computational load on a beowoulf-like cluster", L. Fini & M. Carbillet, in *Astronomical Data Analysis Software And Systems XII*, H. E. Payne, R. I. Jedrzejewski, R. N. Hook, Eds., *ASP Conf. Series* **295**, 347 (2003).

[66] "Adaptive optics simulations with CAOS : application to exoplanets detection", C. Vérinaud & M. Carbillet, in *Astronomy with High Contrast Imaging : From Planetary Systems to Active Galactic Nuclei*, C. Aime & R. Soummer Eds., *EAS Publications Series* **8**, 209 (2003).

[67] "Layer-Oriented Multi-Conjugate Adaptive Optics systems : performance analysis by numerical simulations", C. Vérinaud, C. Arcidiacono, M. Carbillet, E. Diolaiti, R. Ragazzoni, É. Vernet-Viard, in *Adaptive Optical Systems Technology*, P. L. Wizinovich & D. Bonaccini Eds., *SPIE Proc.* **4839**, 524 (2003).

[68] "Deconvolution methods for LINC/NIRVANA data reduction", B. Anconelli, M. Carbillet, M. Bertero, P. Boccacci, in *New frontiers in Stellar Interferometry*, W. A. Traub Ed., *SPIE Proc.* **5491** (2), 932 (2004).

[69] "The Large Binocular Telescope : challenging problems in image restoration", M. Bertero, B. Anconelli, P. Boccacci, M. Carbillet, H. Lantéri, C. Theys, in *Astronomical Data Analysis III Conference*, http://ewic.bcs.org/conferences/2004/ada_iii/session3/paper6.htm (2004).

[70] "Adaptive optics for very high-contrast imaging : numerical simulations", M. Carbillet, in *Astronomy with High Contrast Imaging II : instrumentation for coronagraphy and nulling interferometry*, C. Aime & R. Soummer Eds., *EAS Publications Series* **12**, 137 (2004).

[71] "CAOS – a numerical simulation tool for astronomical adaptive optics (and beyond)", M. Carbillet, C. Vérinaud, M. Guarracino, L. Fini, O. Lardière, B. Le Roux, A. T. Puglisi, B. Femenía, A. Riccardi, B. Anconelli, M. Bertero, P. Boccacci, in *Advancements in Adaptive Optics*, D. Bonaccini, B. Ellerbroek, R. Ragazzoni, Eds., *SPIE Proc.* **5490** (2), 550 (2004).

[72] "Numerical simulations studies for the first-light adaptive optics system of the Large Binocular Telescope", M. Carbillet, A. Riccardi, S. Esposito, in *Advancements in Adaptive Optics*, D. Bonaccini, B. Ellerbroek, R. Ragazzoni, Eds., *SPIE Proc.* **5490** (2), 721 (2004).

[73] "Diamonds in HD 97048 : a closer look" (*Letter*), É. Habart, L. Testi, A. Natta, M. Carbillet, *Ap. J.* **614** (2), L129 (2004).

[74] "Adaptive optics and site requirements for the search of earth-like planets with ELTs", O. Lardière, P. Salinari, L. Jolissaint, M. Carbillet, A. Riccardi, S. Esposito, in *Emerging Optoelectronic Applications'* (2nd Bäckaskog Workshop on ELTs), G. E. Jabbour & J. T. Rantala Eds., *SPIE Proc.* **5382**, 550 (2004).

[75] "Improvement of Shack-Hartmann wave-front sensor measurement for extreme adaptive optics", M. Nicolle, T. Fusco, G. Rousset, V. Michau, *Opt. Lett.* **29**, 2743 (2004).

[76] "Spatially filtered wave-front sensor for high-order adaptive optics", R. Poyneer & J. Machintosh, *J. Opt. Soc. Am. A* **350**, L23 (2004).

[77] "Implementation of fast-Fourier-transform-based simulations of extra-large atmospheric phase and scintillation screens", G. Sedmak, *App. Opt.* **43** (23), 4527 (2004).

[78] "Restoration of interferometric images : III. Efficient Richardson-Lucy methods for LINC-NIRVANA data reduction", B. Anconelli, M. Bertero, P. Boccacci, M. Carbillet, H. Lantéri, *Astron. Astrophys.* **430**, 731 (2005).

[79] "Restoration of interferometric images : IV. An algorithm for super-resolution of binary systems", B. Anconelli, M. Bertero, P. Boccacci, M. Carbillet, *Astron. Astrophys.* **431**, 747 (2005).

[80] "Iterative methods for the reconstruction of LINC-NIRVANA images", B. Anconelli, M. Bertero, P. Boccacci, M. Carbillet, H. Lantéri, in *Signal Recovery and Synthesis 2005*, Technical Digest (Opt. Soc. Am.), paper SMC1, http://www.opticsinfobase.org/DirectPDFAccess/35E44855-BDB9-137E-C38FF56D977DB072_99482.pdf?da=1&id=99482&seq=0&CFID=15889613&CFTOKEN=28616749 (2005).

[81] "Modelling astronomical adaptive optics : I. The software package CAOS", M. Carbillet, C. Vérinaud, B. Femenía, A. Riccardi, L. Fini, *Mon. Not. R. Astron. Soc.* **356** (4), 1263 (2005).

[82] "Giant planet companion to 2MASSW J1207334-393254", G. Chauvin, A.-M. Lagrange, C. Dumas, B. Zuckerman, D. Mouillet, I. Song, J.-L. Beuzit, P. Lowrance, *Astron. Astrophys.* **438**, 25 (2005).

[83] "Evidence for a co-moving sub-stellar companion of GQ Lup", R. Neuhäuser, E. W. Guenther, G. Wuchterl, M. Mugrauer, A. Bedalov, P. H. Hauschildt, *Astron. Astrophys.* **435**, 13 (2005).

[84] "Adaptive optics for high-contrast imaging : pyramid sensor versus Shack-Hartmann sensor" (*Letter*), C. Vérinaud, M. Le Louarn, V. Korkiakoski, M. Carbillet, *Mon. Not. R. Astron. Soc.* **357** (1), L26 (2005).

[85] "Traitement statistique de données pour la détection des exoplanètes par imagerie directe", F. Allouche, Rapport de stage de Master 2 OMEGA, Université de Nice–Sophia Antipolis (2006).

[86] "Multiple image deconvolution : methods, software and application to the Large Binocular Telescope", B. Anconelli, Thèse de doctorat, *Università di Genova* (2006).

[87] "Reduction of boundary effects in multiple image deconvolution with an application to LBT LINC-NIRVANA", B. Anconelli, M. Bertero, P. Boccacci, M. Carbillet, H. Lantéri, *Astron. Astrophys.* **448** (3), 1217 (2006).

[88] "Deconvolution of multiple images with high dynamic range and an application to LBT LINC-NIRVANA", B. Anconelli, M. Bertero, P. Boccacci, G. Desiderà, M. Carbillet, H. Lantéri, *Astron. Astrophys.* **460**, 349 (2006).

[89] "High-resolution image reconstruction : the case of the Large Binocular Telescope (LBT)", M. Bertero, B. Anconelli, P. Boccacci, G. Desiderà, M. Carbillet, H. Lantéri, in *Astronomy with High Contrast Imaging III : Instrumentation and data processing*, M. Carbillet, C. Aime, A. Ferrari, Eds., *EAS Publications Series* **22**, 35 (2006).

[90] "SPHERE : a planet finder instrument for the VLT", J.-L. Beuzit, M. Feldt, K. Dohlen, D. Mouillet, P. Puget, J. Antichi, A. Baruffolo, P. Baudoz, A. Berton, A. Boccaletti, M. Carbillet, J. Charton, R. Claudi, M. Downing, P. Feautrier, E. Fedrigo, T. Fusco, R. Gratton, N. Hubin, M. Kasper, M. Langlois, C. Moutou, L. M. Mugnier, J. Pragt, P. Rabou, M. Saisse, H.-M. Schmid, E. Stadler, M. Turatto, S. Udry, R. Waters, F. Wildi, *ESO Messenger* **125**, 29 (2006).

[91] "Wavefront sensing : from historical roots to the state-of-the-art", H. I. Campbell & A. H. Greenaway, in *Astronomy with High Contrast Imaging III*, M. Carbillet, A. Ferrari & C. Aime Eds., *EAS Publ. Ser.* **22**, 165 (2006).

[92] "Astronomical adaptive optics for high contrast imaging", M. Carbillet, in *Astronomy with High Contrast Imaging III : instrumentation and data processing*, M. Carbillet, C. Aime, A. Ferrari, Eds., *EAS Publications Series* **22**, 121 (2006).

[93] "CAOS, a "problem solving environment" for adaptive optics and adaptive-optics-aided astronomy", M. Carbillet, C. Vérinaud, L. Fini, A. Riccardi, B. Le Roux, B. Femenía, B. Anconelli, G. Desiderà, P. Boccacci, M. Bertero, S. Correia, O. Lardière, in *SF2A - Scientific Highlights 2005'*, F. Casoli, T. Contini, J.-M. Hameury, L. Pagani, Eds., *EDP Sciences - Conference Series*, 275 (2006).

[94] "Application of iterative blind deconvolution to the reconstruction of LBT LINC-NIRVANA images", G. Desiderà, B. Anconelli, M. Bertero, P. Boccacci, M. Carbillet, *Astron. Astrophys.* **452**, 727 (2006).

[95] "Spatially resolved PAH emission in the inner disks of Herbig Ae/Be stars", É. Habart, A. Natta, L. Testi, M. Carbillet, *Astron. Astrophys.* **449** (3), 1067 (2006).

[96] "Small carbon grains in circumstellar disks", É. Habart, A. Natta, L. Testi, M. Carbillet, in *SF2A - Scientific Highlights 2005*, F. Casoli, T. Contini, J.-M. Hameury, L. Pagani, Eds., *EDP Sciences - Conference Series*, 421 (2006).

[97] "Analytical modelling of adaptive optics : foundations of the phase spatial power spectrum approach", L. Jolissaint, J.-P. Véran, R. Conan, *J. Opt. Soc. Am. A* **23 (2)**, 382 (2006).

[98] "The Gemini Planet Imager", B. Macintosh, J. Graham, D. Palmer, R. Doyon, D. Gavel, J. Larkin, B. Oppenheimer, L. Saddlemyer, J. K. Wallace, B. Bauman, J. Evans, D. Erikson, K. Morzinski, D. Phillion, L. Poyneer, A. Sivaramakrishnan, R. Soummer, S. Thibault, J.-P. Véran, *Proc. SPIE* **6272**, 18 (2006).

[99] "Analyse statistique pour la détection de planètes par imagerie directe", E. Serradell Domingo, Rapport de projet de fin d'étude, Universitat Politècnica de Catalunya (2006).

[100] "Simulation de systèmes d'observation astronomique : exploitation de la fonctionnalité « Virtual Machine » d'IDL et modélisation des bruits de CCD et L3CCD", D. Ab Kadir, Rapport de stage d'IUT, Université de Nice–Sophia Antipolis (2007).

[101] "Analyse d'une méthode statistique de détection de planètes par imagerie directe", A. Ambrós Descarega, Rapport de projet de fin d'étude, Universitat Politècnica de Catalunya (2007).

[102] "Iterative methods for the reconstruction of astronomical images with high-dynamic range", B. Anconelli, M. Bertero, P. Boccacci, M. Carbillet, H. Lantéri, *J. Comp. Appl. Math.* **198**, 321 (2007).

[103] "Modelling the optical turbulence boiling and its effect on finite-exposure differential image motion", A. Berdja, J. Borgnino, *Mon. Not. R. Astron. Soc.* **378 (3)**, 1177 (2007).

[104] "End-to-End Simulation of AO-assisted coronagraphic differential imaging : estimation of performance for SPHERE", A. Boccaletti, M. Carbillet, Th. Fusco, D. Mouillet, M. Langlois, C. Moutou, K. Dohlen, in *Adaptive Optics Systems*, N. Hubin, C. E. Max, P. L. Wizinowich, Eds., *SPIE Proc.* **7015**, 70156E (2008).

[105] "The Software Package SPHERE : a CAOS-based numerical tool for end-to-end simulations of SPHERE/VLT", M. Carbillet, A. Boccaletti, Ch. Thalmann, Th. Fusco, A. Vigan, I. Smith, D. Mouillet, K. Dohlen, Ph. Bendjoya, A. Ferrari, in *Adaptive Optics Systems*, N. Hubin, C. E. Max, P. L. Wizinowich, Eds., *SPIE Proc.* **7015**, 70156Z (2008).

[106] "SPHERE IFS : the spectro differential imager of the VLT for exoplanets search", R. Claudi, M. Turatto, R. Gratton, J. Antichi, M. Bonavita, P. Bruno, E. Cascone, V. De Caprio, S. Desiderà, E. Giro, D. Mesa, S. Scuderi, K. Dohlen, KJ.-L. Beuzit, P. Puget, in *Ground-based and Airborne Instrumentation for Astronomy II*, I. S. McLean & M. M. Casali Eds., *SPIE Proc.* **7014**, 70143E (2008).

[107] "The infra-red dual imaging and spectrograph for SPHERE : design and performance", K. Dohlen, M. Langlois, M. Saisse, L. Hill, A. Origne, M. Jacquet, C. Fabron, J.-C. Blanc, M. Llored, M. Carle, C. Moutou, A. Vigan, A. Boccaletti, M. Carbillet, D. Mouillet, J.-L. Beuzit, in *Ground-based and Airborne Instrumentation for Astronomy II*, I. S. McLean & M. M. Casali Eds., *SPIE Proc.* **7014**, 70143L (2008).

[108] "AIRY-LN : an ad-hoc numerical tool for deconvolution of images from the LBT instrument LINC-NIRVANA", G. Desiderà, A. La Camera, P. Boccacci, M. Bertero, M. Carbillet, in *Optical and Infrared Interferometry*, M. Schoeller, W. C. Danchi, F. Delplancke, Eds., *SPIE Proc.* **7013**, 701340 (2008).

[109] "Comparison between atmospheric turbulence models by angle-of-arrival covariance measurements", J. Maire, A. Ziad, J. Borgnino, F. Martin, *Mon. Not. R. Astron. Soc.* **386 (2)**, 1064 (2008).

[110] "TOE : The Onduline Experiment - A new kind of WaveFront Sensor to characterize astronomical sites for Extremely Large Telescopes", C. Metti, G. Gentile, M. Dima, J. Farinato, C. Arcidiacono, A. Baruffolo, V. Viotto, E Diolaiti, R. Ragazzoni, *Ground-based and Airborne Telescopes II*, L. M. Stepp & R. Gilmozzi Eds, *SPIE Proc.* **7012**, 701247 (2008).

[111] "The SPHERE XAO system : design and performance", C. Petit, Th. Fusco, J. Charton, D. Mouillet, P. Rabou, T. Buey, G. Rousset, J.-F. Sauvage, P. Baudoz, P. Gigan, M. Kasper, E. Fedrigo, N. Hubin, P. Feautrier, J.-L. Beuzit, P. Puget, in *Advancements in Adaptive Optics*, N. Hubin, C. E. Max, P. L. Wizinowich, Eds., *SPIE Proc.* **7015**, 70151D (2008).

[112] "Adaptive secondary mirror for the Large Binocular Telescope : results of acceptance laboratory test", A. Riccardi, M. Xompero, D. Zanotti, L. Busoni, C. Del Vecchio, P. Salinari, P. Ranfagni, G. Brusa Zappellini, R. Biasi, M. Andrighettoni, D. Gallieni, E. Anaclerio, H. M. Martin, S. M. Miller, in *Adaptive Optics Systems*, *Adaptive Optics Systems*, N. Hubin, C. Max, P. L. Winizowich, Eds., *SPIE Proc.* **7015**, 701512 (2008).

[113] "Simulation of moving exoplanets detection using the VLT instrument SPHERE/IRDIS", I. Smith, M. Carbillet, A. Ferrari, D. Mouillet, A. Boccaletti, K. Dohlen, in *Adaptive Optics Systems*, N. Hubin, C. E. Max, P. L. Wizinowich, Eds., *SPIE Proc.* **7015**, 70156F (2008).

[114] "Detection and performance analysis for a moving point source in speckle noise, application to exoplanet detection by direct imaging", I. Smith, A. Ferrari, M. Carbillet, in *Proceedings of the IEEE International Conference on Acoustics, Speech and Signal Processing (ICASSP'08)* (2008).

[115] "SPHERE ZIMPOL : Design and performance simulation", Ch. Thalmann, H.-M. Schmid, A. Boccaletti, D. Mouillet, K. Dohlen, R. Roelfsema, M. Carbillet, D. Gisler, J.-L. Beuzit, M. Feldt, R. Gratton, F. Joos, Ch. U. Keller, J. Kragt, J. H. Pragt, P. Puget, F. Rigal, F. Snik, R. Waters, F. Wildi, in *Ground-based and Airborne Instrumentation for Astronomy II*, I. S. McLean, M. M. Casali, Eds., *SPIE Proc.* **7014**, 70143F (2008).

[116] "Nighttime optical turbulence vertical structure above Dome C in Antarctica", H. Trinquet, A. Agabi, J. Vernin, M. Azouit, É. Aristidi, É. Fossat, *Pub. Astr. Soc. Pac.* **120 (864)**, 203 (2008).

[117] "Dome C site testing : surface layer, free atmosphere seeing, and isoplanatic angle statistics", É. Aristidi, É. Fossat, A. Agabi, D. Mékarnia, F. Jeanneaux, E. Bondoux, Z. Challita, A. Ziad, J. Vernin, H. Trinquet, *Astron. Astrophys.* **499** (3), 955 (2009).

[118] "Méthode de type maximum de vraisemblance pour la détection d'exoplanètes par imagerie différentielle spectrale et angulaire", A. Cornia, L. M. Mugnier, J.-F. Sauvage, N. Védrenne, M. Carbillet, A. Boccaletti, G. Rousset, Th. Fusco, (http://documents.irevues.inist.fr/handle/2042/29158), *22me Colloque sur le Traitement du Signal et des Images*, GRETSI'09 (2009).

[119] "Strehl-constrained iterative blind deconvolution for post-adaptive-optics data", G. Desiderà & M. Carbillet, *Astron. Astrophys.* **507** (3), 1759 (2009).

[120] "Caractérisation de la turbulence atmosphérique et étude d'un système d'optique adaptative à grand champ pour le Dôme C (Antarctique)", Ch. Giordano, O. Pasqueron de Fommervault, J. Gautier, Rapport de stage de Licence 3 de Physique, Université de Nice–Sophia Antipolis (2009).

[121] "Étude de systèmes d'optique adaptative grand champ pour le Dôme C", A.-L. Maire, Rapport de stage de Master 2 OMEGA, Université de Nice–Sophia Antipolis (2009).

[122] "Study of the atmospheric refraction in a single mode instrument - Application to AMBER/VLTI", S. Robbe-Dubois, S. Lagarde, Y. Bresson, R. G. Petrov, M. Carbillet, E. Lecoarer, F. Rantakyro, I. Tallon-Bosc, M. Vannier, P. Antonelli, G. Martinot-Lagarde, A. Roussel, D. Tasso, *Mon. Not. R. Astron. Soc.* **395** (2), 991 (2009).

[123] "Detection of a moving source in speckle noise : application to exoplanet detection", I. Smith, A. Ferrari, M. Carbillet, *IEEE Trans. on Signal Processing* **57** (3), 904 (2009)

[124] "Imaging with LINC-NIRVANA (An introduction to deconvolution methods and their capability)", M. Bertero, P. Boccacci, G. Desiderà, A. La Camera, M. Carbillet, H. Lantéri, *IEEE Signal Processing Magazine* **27** (1) *(Special Section on Astronomy and Cosmology)*, 110 (2010).

[125] "The CAOS problem-solving environment : recent developments", M. Carbillet, G. Desiderà, E. Augier, A. La Camera, A. Riccardi, A. Boccaletti, L. Jolissaint, D. Ab Kadir, in *Adaptive Optics Systems II*, B. L. Ellerbroek, M. Hart, N. Hubin, P. L. Wizinowich, Eds., *SPIE Proc.* **7736**, 773644 (2010).

[126] "The Software Package PAOLAC : an embedment of the analytical code PAOLA within the CAOS problem-solving environment", M. Carbillet, L. Jolissaint, A.-L. Maire, *1st AO4ELT (Adaptive Optics for Extremely Large Telescopes) conf.*, Y. Clénet, J.-M. Conan, Th. Fusco, G. Rousset, Eds., EDP Sciences (ao4elt.edpsciences.org), 03006 (2010).

[127] "The CAOS problem-solving environment : last news", M. Carbillet, G. Desiderà, E. Augier, A. La Camera, A. Riccardi, A. Boccaletti, L. Jolissaint, D. Ab Kadir, in *SF2A-2010 : Proceedings of the Annual meeting of t/he French Society of Astronomy and Astrophysics*, S. Boissier, M. Heydari-Malayeri, R. Samadi, D. Valls-Gabaud, Eds., 61 (http://sf2a.cesr.fr/2010/2010sf2a.conf..0061C.pdf) (2010).

[128] "Adaptive optics (AO) and ground-layer AO for Dome C : numerical simulation results", M. Carbillet, A.-L. Maire, B. Le Roux, É. Aristidi, Ch. Giordano, O. Pasqueron de Fommervault, J. Gautier, H. Trinquet, 3rd ARENA Conference on *"An astronomical Observatory at CONCORDIA (Dome C, Antarctica)"*, L. Spinoglio & N. Epchtein Eds., *EAS Publications Series* **40**, 157 (2010).

[129] "Numerical modeling of atmospherically perturbed phase screens : new solutions for classical fast Fourier transform and Zernike methods", M. Carbillet & A. Riccardi, *App. Opt.* **49** (31) *(JOSA A/App. Opt. Joint Feature Issue on Adaptive Optics)*, G47–G52 (2010).

[130] "Low-ligh-level CCDs for wave-front sensing : what actual gain ?", M. Carbillet & A. Riccardi, *App. Opt.* **49** (31) *(JOSA A/App. Opt. Joint Feature Issue on Adaptive Optics)*, G167–G173 (2010).

[131] "Optimal method for exoplanet detection by spectral and angular differential imaging", A. Cornia, L. M. Mugnier, D. Mouillet, A. Vigan, A. Eggenberger, G. Rousset, A. Boccaletti, M. Carbillet, K. Dohlen, Th. Fusco, J. Carson, G. Montagnier, in *Adaptive Optics Systems II*, B. L. Ellerbroek, M. Hart, N. Hubin, P. L. Wizinowich, Eds., *SPIE Proc.* **7736**, 77361E12 (2010).

[132] "The AIRY-LN software package for the LINC-NIRVANA interferometer of the Large Binocular Telescope (LBT) : image reconstruction methods and simulations", G. Desiderà, Thèse de doctorat, *Università di Genova* (2010).

[133] "First-light AO (FLAO) system for LBT : final integration, acceptance test in Europe, and preliminary on-sky commissioning results", S. Esposito, A. Riccardi, L. Fini, A. T. Puglisi, E. Pinna, M. Xompero, R. Briguglio, F. Quirós Pacheco, P. Stefanini, J. C. Guerra, L. Busoni, A. Tozzi, F. Pieralli, G. Agapito, G. Brusa-Zappellini, R. Demers, J. Brynnel, C. Arcidiacono, P. Salinari, in *Adaptive Optics Systems II*, B. L. Ellerbroek, M. Hart, N. Hubin, P. L. Winizowich, Eds., *SPIE Proc.* **7736**, 773609 (2010).

[134] "Analytical computation of the Lyot coronagraph response to an extended source", A. Ferrari, C. Aime, R. Soummer, *The Astrophysical Journal* **708 (1)**, 218 (2010).

[135] "Synthetic modeling of closed loop astronomical adaptive optics", L. Jolissaint, J. Europ. Opt. Soc. Rap. Public. **5**, 10055 (2010).

[136] "Parallelization of exoplanets detection algorithms based on field rotation ; example of the MOODS algorithm for SPHERE", D. Mattei, I. Smith, A. Ferrari, M. Carbillet, in *In the spirit of Lyot 2010*, A. Boccaletti Ed., http://lyot2010.lesia.obspm.fr/sites/lyot2010/IMG/pdf/Lyot2010proc_s7_poster_MatteiD.pdf (2010).

[137] "The adaptive secondary mirror for the Large Binocular Telescope : optical acceptance test and preliminary on-sky commissioning results", A. Riccardi, M. Xompero, R. Briguglio, F. Quirós Pacheco, L. Busoni, L. Fini, A. T. Puglisi, S. Esposito, C. Arcidiacono, E. Pinna, P. Ranfagni, P. Salinari, G. Brusa-Zappelini, R. Demers, R. Biasi, D. Gallieni, in *Adaptive Optics Systems II*, B. L. Ellerbroek, M. Hart, N. Hubin, P. L. Winizowich, Eds., *Proc. SPIE* **7736**, 77362C (2010).

[138] "Détection d'une source faible : modèles et méthodes statistiques. Application à la détection d'exoplanètes par imagerie directe", I. Smith, Thèse de Doctorat, Université de Nice–Sophia Antipolis (2010).

[139] "Photometric exoplanet characterization using angular and spectral differential imaging", A. Vigan, C. Moutou, M. Langlois, F. Allard, A. Boccaletti, M. Carbillet, D. Mouillet, I. Smith, *Mon. Not. R. Astron. Soc.* **407** (1), 71–82 (2010).

[140] "Comparison of Methods for Detection and Characterization of Exoplanets wih SPHERE/IRDIS", A. Vigan, C. Moutou, M. Langlois, D. Mouillet, K. Dohlen, A. Boccaletti, M. Carbillet, I. Smith, A. Ferrari, L. M. Mugnier, Ch. Thalmann, in *Ground-based and Airborne Instrumentation for Astronomy III*, I. S. McLean, S. K. Ramsay, H. Takami, Eds., *SPIE Proc.* **7735**, 77352X (2010).

[141] "Photometric characterization of exoplanet using angular and spectral differential imaging in SPHERE/IRDIS", A. Vigan, C. Moutou, M. Langlois, F. Allard, A. Boccaletti, M. Carbillet, D. Mouillet, I. Smith, in *In the spirit of Lyot 2010*, A. Boccaletti Ed., http://lyot2010.lesia.obspm.fr/sites/lyot2010/IMG/PDF/Lyot2010proc_s7_talk_ViganA.pdf (2010).

[142] "How to push the limits of evolved stars observations with SPHERE/VLT", I. Belokogne, Rapport de stage de Master 2 OMEGA, Université de Nice–Sophia Antipolis (2011).

[143] "Imaging with LINC-NIRVANA, the Fizeau interferometer of the Large Binocular Telescope : state of the art and open problems", M. Bertero, P. Boccacci, G. Desiderà, A. La Camera, C. Olivieri, M. Carbillet, *Inverse Problems* **27**, 113001 (2011).

[144] "Apodized Lyot coronagraph for SPHERE/VLT : I. Detailed numerical study", M. Carbillet, Ph. Bendjoya, L. Abe, G. Guerri, A. Boccaletti, J.-B. Daban, K. Dohlen, A. Ferrari, S. Robbe-Dubois, R. Douet, F. Vakili, *Exp. Astronomy* **30 (1)**, 39 (2011).

[145] "Atmospheric turbulence characterization and adaptive optics modelling for the Southern African Large Telescope", L. Catala, Rapport de stage de Master 2 OMEGA, Université de Nice–Sophia Antipolis (2011).

[146] "Apodized Lyot coronagraph for SPHERE/VLT : II. Laboratory tests and performances", G. Guerri, J.-B. Daban, S. Robbe-Dubois, R. Douet, L. Abe, J. Baudrand, P. Riaud, M. Carbillet, A. Boccaletti, Ph. Bendjoya, C. Gouvret, F. Vakili, *Exp. Astronomy* **30 (1)**, 59 (2011).

[147] "Advanced methods for astronomical image reconstruction : analysis, validation and implementation in the Software Packages AIRY and AIRY-LN", A. La Camera, Thèse de doctorat, *Università di Genova* (2011).

[148] "Analytical vs. end-to-end numerical modeling of adaptive optics systems : comparison between the `PAOLA` code and the Software Package `CAOS`", M. Carbillet & L. Jolissaint, in *2nd AO4ELT (Adaptive Optics for Extremely Large Telescopes) conf.*, J.-P. Véran, Th. Fusco, Y. Clénet, Eds., http://ao4elt2.lesia.obspm.fr/sites/ao4elt2/IMG/pdf/061carbillet.pdf (2012).

[149] "Dimensioning and performances of an AO system for the SALT", L. Catala, M. Carbillet, L. Jolissaint, T. Pickering, S. Crawford, *Adaptive Optics Systems III*, B. L. Ellerbroek, E. Marchetti, J.-P. Véran, Eds., SPIE Proc. **8447**, 84473W (2012).

[150] "Dome C site characterization in 2006 with Single-Star SCIDAR", C. Giordano, J. Vernin, M. Chadid, É. Aristidi, A. Agabi, *Pub. Astr. Soc. Pac.* **124**, 494 (2012).

[151] "AIRY : A complete tool for the simulation and the reconstruction of Fizeau interferometric images", A. La Camera, M. Carbillet, Ch. Olivieri, P. Boccacci, M. Bertero, in *Optical and Infrared Interferometry III*, F. Delplancke, J. K. Rajagopal, F. Malbet, Eds., *SPIE Proc.* **8445**, 84453E (2012).

[152] "AOLI : Adaptive Optics Lucky Imager : diffraction limited imaging in the visible on large ground-based telescopes", C. D. Mackay, R. Rebolo-López, B. Femenía Castellá, J. Crass, D. L. King, L. Labadie, P. Aisher, A. Pérez Garrido, M. Balcells, A. Díaz Sánchez, J. Jimenez Fuensalida, R. L. Lopez, A. Oscoz, J. A. Pérez Prieto, L. F. Rodríguez Ramos, I. Villó, *SPIE Proc.* **8446**, 844672 (2012).

[153] "Adaptive Optics Control Design : from the linear to the nonlinear case", A. Abelli, Thèse de Doctorat, Université de Nice–Sophia Antipolis et *Università La Sapienza–Roma* (2013).

[154] "Astronomical imaging... Atmospheric turbulence ? Adaptive optics !", M. Carbillet, in *New Concepts in Imaging : Optical and Statistical Models"*, D. Mary, C. Theys, and C. Aime, Eds., *EAS Publications Series* **59**, 59 (2013).

[155] "Deconvolution-based super-resolution for post-adaptive optics data", M. Carbillet, A. La Camera, O. Chesneau, F. Millour, J. Girard, M. Prato, presented at *3rd AO4ELT (Adaptive Optics for Extremely Large Telescopes) conf.*, Florence (Italy), 26th–31st May 2013 (2013).

[156] "The SPHERE view of Betelgeuse", O. Chesneau, H.-M. Schmidt, M. Carbillet, A. Chiavassa, L. Abe, D. Mouillet, in *Betelgeuse Workshop 2012 – The Physics of Red Supergiants : Recent Advances and Open Questions*, P. Kervella , T. Le Bertre, G. Perrin, Eds., *EAS Publication Series* **60**, 261 (2013).

[157] S. Esposito, Communication privée (2013).

[158] "High spatial resolution of the compact starburst cluster R136 at 50 to 10 mass and beyond", Z. Khorrami, F. Vakili, O. Chesneau, M. Carbillet, D. Mekarnia, presented at *EELT 2013 - Shaping E-ELT Science and Instrumentation*, Garching-bei-Muenchen (Germany), 25th February–1st March 2013 (2013).

[159] "A convergent blind deconvolution method for post-adaptive-optics astronomical imaging", M. Prato, A. La Camera, S. Bonettini, M. Bertero, *Inverse Problems* **29 (6)**, 0605017 (2013).

[160] "First results of the PML monitor of atmospheric turbulence profile with high vertical resolution", A. Ziad, F. Blary, J. Borgnino, Y. Fanteï-Caujolle, É. Aristidi, F. Martin, H. Lantéri, R. Douet, É. Bondoux, D. Mékarnia, *Astron. Astrophys.* **559**, L6 (2013).

Annexes

Annexe A

Observations astronomiques et turbulence atmosphérique

[« La nuit étoilée », Vincent Van Gogh, 1889, MoMA, New York.]

E poi non sapevo più cosa guardare e guardai il cielo.
(Et puis je ne savais plus quoi regarder et je regardai le ciel.)
Italo Calvino, in *Gli amori difficili* (Les amours difficiles), 1971.

Introduction Les observations astronomiques depuis le sol s'effectuent naturellement au travers d'un milieu qui n'est ni transparent, ni homogène, ni stationnaire : l'atmosphère terrestre. Celle-ci débute à la surface du globe et se termine là où commence le milieu interplanétaire. La structure physique moyenne ainsi que l'organisation en couches successives de notre atmosphère sont déterminées par les lois de température, de pression et de densité en fonction de l'altitude. Cette structure est donc verticale, et 99% de sa masse totale se trouve confinée dans ses deux premières couches géophysiques : la troposphère et la stratosphère [21].

Cet ensemble structuré de gaz neutres, particules ionisées et autres va se comporter comme un écran naturel protégeant la Terre, mais limitant également nos possibilités d'observation vers l'extérieur. Cette limitation due à l'atmosphère se manifeste de diverses manières (pour un exposé exhaustif, voir l'ouvrage de Pierre Léna [31]). Tout d'abord de par son *opacité* toutes les ondes électromagnétiques ne s'y propagent pas de la même façon : elles y sont plus ou moins absorbées. En examinant l'absorption du rayonnement électromagnétique par les couches atmosphériques terrestres en fonction de la longueur d'onde (voir par exemple [19]), nous remarquons immédiatement que bien qu'elle soit totale pour les très grandes ondes et l'ultraviolet, elle laisse libres deux fenêtres notoires : celle des ondes visibles, et celles des ondes radios. C'est à la première que nous nous intéressons tout particulièrement ici, ainsi qu'à celles successives qui se profilent dans le proche infrarouge.

L'observation au sol est également gênée par la *diffusion atmosphérique* qui, bien que nous offrant parfois un magnifique ciel bleu, nous interdit toute observation stellaire diurne dans le visible et favorise la pollution lumineuse nocturne. La *dispersion* (ou *réfraction*) écarte quant à elle la direction apparente d'un astre de sa position véritable. Les observations dans l'infrarouge sont également contaminées par l'*émission thermique* de l'atmosphère. Enfin, la *turbulence atmosphérique* dégrade considérablement la qualité des images obtenues au foyer d'un grand télescope. C'est ce dernier phénomène qui, déformant aléatoirement les fronts d'onde nous parvenant des astres observés, limite leur résolution angulaire et donc le discernement de détails fins les concernant.

La turbulence atmosphérique L'atmosphère présente naturellement un gradient thermique, et est le siège de mouvements d'air qui sont presque toujours complètement turbulents. Cette turbulence se traduit par un mélange des couches thermiques en volumes d'air de différentes températures et pressions. Les fluctuations de température qui en découlent vont elles-mêmes provoquer des fluctuations de l'indice de réfraction de l'air. Ce sont elles qui vont perturber la propagation optique au travers de l'atmosphère.

Les travaux théoriques de Kolmogorov publiés en 1941 [2] ont jeté les bases de l'étude des propriétés statistiques de la turbulence. Il y est notamment montré comment, dans un milieu à turbulence pleinement développée, l'énergie

cinétique injectée des mouvements à grande échelle se transfère (depuis une échelle dite *externe* L_0) à des mouvements d'échelle de plus en plus petite jusqu'à une échelle l_0 (dite *interne*) où l'énergie se dissipe en chaleur par frottement visqueux. C'est la théorie des cascades, dans laquelle le transfert s'effectue en régime inertiel entre les deux valeurs $\frac{2\pi}{L_0}$ et $\frac{2\pi}{l_0}$ du nombre d'onde $k = \frac{2\pi}{\lambda}$ (où λ représente la longueur d'onde) et selon une loi en puissance $-\frac{5}{3}$ de k.

L'influence de cette turbulence sur la propagation de la lumière a été étudiée par Tatarski dès 1961 [3], nous allons en retenir que le spectre de puissance des fluctuations de température, et par conséquent le spectre de puissance tridimensionnel des fluctuations de l'indice de réfraction n s'écrit :

$$\Phi_n(\vec{k}) = 0.033\ C_n^2\ k^{-\frac{11}{3}}, \tag{A.1}$$

où C_n^2 est la constante de structure des fluctuations d'indice qui exprime l'intensité de la contribution optique de la turbulence atmosphérique et se mesure en $\mathrm{m}^{-\frac{2}{3}}$.

Cette constante de structure est absolument dépendante de l'altitude, et sa mesure (ou celle équivalente de la constante de structure des fluctuations de température T, C_T^2) fait apparaître assez nettement le fait que l'atmosphère est en réalité stratifiée en fines couches turbulentes [25]. Il apparaît également que les deux échelles l_0 et L_0 évoquées plus haut sont des paramètres géophysiques locaux caractéristiques de chacune de ces fines couches turbulentes [23, 24, 27]. Les paramètres qui vont quant à eux directement influencer l'observation au sol sont des paramètres optiques intégrés déduits des deux précédents : les échelles de cohérence spatiale ℓ_0 et $\mathcal{L}_0$ [17]. $\mathcal{L}_0$ caractérise la distance sur laquelle le front d'onde conserve sa cohérence spatiale, ℓ_0 chiffre la plus petite structure présente dans le front d'onde.

Dégradations de l'image formée Comme nous l'avons vu précédemment, les fluctuations de T, et donc de n, perturbent la propagation des ondes électromagnétiques, ce qui affecte la qualité des images. De la traversée de l'atmosphère turbulente par l'onde (les derniers 10–20 km traversée par la lumière provenant de l'astre observé) vont résulter plusieurs conséquences néfastes pour l'image obtenue au foyer d'un grand télescope :

- ⋆ *Scintilation* : il s'agit de la fluctuation de l'éclat observé et donc de l'énergie reçue par la pupille, ce qui correspond à un étalement ou une concentration de l'énergie du front d'onde sur cette même pupille.
- ⋆ *Agitation* : il s'agit de la variation de position du photocentre de l'image d'un point-source observé au plan focal du télescope. Cette position dépend du basculement global du front d'onde sur la pupille d'entrée du télescope. Elle est donc forte pour un petit télescope et de plus en plus réduite pour un télescope de grand diamètre, du fait de la plus importante intégration des fluctuations locales.

⋆ *Étalement* : la dimension des images est largement supérieure à celle qu'imposerait la diffraction, ce qui correspond à une perte de cohérence spatiale sur la pupille.

Une analyse complète de ces effets de la turbulence sur la formation des images en astronomie optique fut présentée par Roddier en 1981 [9], nous allons dans ce qui suit en rappeler les résultats principaux et utiles pour la suite, i.e. les paramètres observationnels qui vont directement caractériser l'image obtenue.

Nous avons vu que l'atmosphère est un milieu à indice de réfraction aléatoire : $n(\vec{r},t)$. Considérons le processus stochastique correspondant comme ergodique (moyenne dans le temps = moyenne d'ensemble = espérance mathématique) et stationnaire (les propriétés statistiques de $n(\vec{r},t)$ ne dépendent pas de t). Considérons maintenant une onde plane monochromatique unité provenant de l'infini ($\Psi_\infty = 1$) et traversant une couche turbulente située à l'altitude z et d'épaisseur Δz petite. L'onde à la sortie s'écrit :

$$\Psi_z(\vec{r}) = \exp\{i\ \phi_z(\vec{r})\}\,, \tag{A.2}$$

avec ϕ_z une variable aléatoire dont la statistique spatiale se déduit de celle de n par :

$$\phi_z(\vec{r}) = k\int_z^{z+\Delta z} n(\vec{r},z)dz\ . \tag{A.3}$$

La moyenne et le moment du second ordre associés sont :

$$\begin{cases} \langle\Psi_z(\vec{r})\rangle = 0, \\ \\ \langle\Psi_z(\vec{r})\ \Psi_z^*(\vec{r}+\vec{\rho})\rangle = \langle\exp\{i\,[\phi_z(\vec{r}) - \phi_z(\vec{r}+\vec{\rho})]\}\rangle = B_z(\vec{\rho})\ , \end{cases} \tag{A.4}$$

où $B_z(\vec{\rho})$ représente la covariance de l'onde et $\langle\bullet\rangle$ la moyenne d'ensemble de $\bullet$. Nous avons donc là déterminé la covariance de l'onde après traversée d'une couche mince. Après la traversée d'une grande quantité de celles-ci, la perturbation de phase en un point sera donc la somme d'un grand nombre de perturbations élémentaires indépendantes. La distribution de ϕ_z peut donc être considérée comme gaussienne, par application du théorème de la limite centrale. Nous avons par conséquent :

$$B_z(\vec{\rho}) = \exp\left\{-\frac{1}{2}\ \langle|\phi_z(\vec{r}) - \phi_z(\vec{r}+\vec{\rho})|^2\rangle\right\} = \exp\left\{-\frac{1}{2}\ D_\phi(\vec{\rho})\right\}, \tag{A.5}$$

où $D_\phi(\vec{\rho})$ représente la fonction de structure de la phase. Sous l'hypothèse d'une turbulence homogène et isotrope, cette fonction peut s'exprimer comme :

$$D_\phi(\vec{\rho}) = 2.91\ k^2\ C_n^2\ \Delta h\ \rho^{\frac{5}{3}}. \tag{A.6}$$

Nous pouvons alors en déduire l'expression de $B_z(\vec{\rho})$, et comme de plus $B_z(\vec{\rho})$ est invariant par diffraction de Fresnel, nous avons :

$$B_0(\vec{\rho}) = B_z(\vec{\rho}) = \exp\left\{-1.45\ k^2\ C_n^2\ \Delta h\ \rho^{\frac{5}{3}}\right\}. \tag{A.7}$$

Nous pouvons déjà en déduire qu'à faible distance derrière la couche, seule la phase est perturbée, il n'y a donc pas de scintillation dans ce cas-là. À plus grande distance, la scintillation apparaît puisque phase *et* amplitude sont perturbées, nous négligeons cependant cet effet, ce qui est légitime lorsque la turbulence n'est pas trop importante. Puisque la turbulence s'étend sur plusieurs couches correspondant à toute l'épaisseur de l'atmosphère, et vu que les calculs restent valides dans ce cas-là à condition de remplacer le terme $C_n^2\ \Delta h$ par $\int_0^\infty C_n^2(z)\ dz$, nous avons, en tenant également compte de l'écart angulaire au zénith γ :

$$B(\vec{\rho}) = \exp\left\{-3.44\ \left(\frac{\rho}{r_0}\right)^{\frac{5}{3}}\right\} = \exp\left\{-3.44\ \left(\frac{\lambda f}{r_0}\right)^{\frac{5}{3}}\right\} = B(\lambda f)\ , \tag{A.8}$$

avec :

$$r_0 = \left[0.423\ k^2\,(\cos\gamma)^{-1}\int_0^\infty C_n^2(z)\ dz\right]^{-\frac{3}{5}} = 0.185\ \lambda^{\frac{6}{5}}\,(\cos\gamma)^{\frac{3}{5}}\ \left[\int_0^\infty C_n^2(z)\ dz\right]^{-\frac{3}{5}}\ , \tag{A.9}$$

où r_0 est le paramètre défini par Fried en 1966 [4], f est une fréquence angulaire et B n'est autre que la fonction de transfert de l'atmosphère.

Paramètre de Fried r_0 et *seeing* ϵ Le paramètre de Fried r_0, directement lié au profil de la turbulence, est celui qui va caractériser de manière pratique la qualité de l'image instantanée obtenue au foyer d'un télescope. Il peut être défini comme le diamètre d'un télescope qui, en l'absence de turbulence, donnerait la même résolution qu'un télescope de diamètre infini dans les conditions de turbulence en question. Dans les équations A.9 et A.8, il apparaît comme une longueur de cohérence pour laquelle la fonction de transfert $B(\lambda f)$ chute pratiquement à zéro. C'est aussi le diamètre de la surface sur laquelle la variance de phase est égale à 1.03 rd^2. Il a une dépendance en longueur d'onde qui varie comme la puissance $\frac{6}{5}$ de celle-ci et varie naturellement dans le temps de la même façon que la turbulence. Typiquement, et pour un site astronomique d'assez bonne qualité, sa valeur moyenne s'échelonne entre 5 cm et 20 cm dans le visible.

Il est directement relié au seeing ϵ, qui est défini comme la largeur angulaire à mi-hauteur de l'image pose-longue obtenue au foyer du télescope :

$$\epsilon = 0.98\ \frac{\lambda}{r_0} \simeq \frac{\lambda}{r_0}. \tag{A.10}$$

Cette notion de seeing est communément utilisée pour caractériser la dégradation de l'image due à l'état de la turbulence lors d'une observation, particulièrement facile à manipuler puisqu'il suffit d'examiner l'image obtenue pour l'estimer, au moins qualitativement. Le seeing est peu dépendant de λ. Pour une valeur du r_0 de 10 cm à une longueur d'onde d'observation de 500 nm, sa valeur est d'environ $1''$. Ceci va donner un r_0 de 30 cm en bande J (à 1.25 μm) et de 59 cm en bande K (à 2.2 μm), et qui va correspondre à un seeing de $\sim 0''.86$ en bande J et de $\sim 0''.77$ en bande K.

L'image obtenue au foyer d'un grand télescope se décrit globalement selon les points 2 et 3 du début du paragraphe précédent : agitation et étalement (nous négligeons, comme nous l'avons déjà remarqué, la scintillation). Ce qui est obtenu est appelée *figure de tavelures*, ou *figure de speckles*, qui est composée d'une myriade bouillonnante de taches de diffraction dues au télescope (les speckles) et d'une taille angulaire équivalente :

$$s \simeq \frac{\lambda}{D} \ . \tag{A.11}$$

Durée de vie des speckles τ_0 Étant donné la variabilité temporelle de la turbulence, et donc des images, il convient également de définir la durée de vie des speckles τ_0, qui est finalement le temps durant lequel la figure de speckles a suffisament peu évolué pour pouvoir considérer que la turbulence est gelée. Dans le cadre de modèles simples, elle s'exprime comme [12] :

$$\tau_0 = 0.31 \ \frac{r_0}{v} \ , \tag{A.12}$$

où v représente l'écart-type de la distribution de vitesse du vent pondéré par l'intégrale du profil de turbulence. Son expression a été également donnée par Aime et al. [14] comme :

$$\tau_0 = 0.47 \ \frac{r_0}{v} \ . \tag{A.13}$$

Typiquement, en considérant la première équation, légèrement plus pessimiste, et pour un vent de 10 m/s, τ_0 vaut $\sim$3 ms à 500 nm, $\sim$9 ms en bande J et $\sim$18 ms en bande K.

Angle d'isoplanétisme θ_0 L'angle d'isoplanétisme sous lequel nous pouvons considérer que le front d'onde reste cohérent spatialement (hypothèse de *champ homogène*) s'exprime quant à lui [11] :

$$\theta_0 = 0.36 \ \frac{r_0}{h}, \tag{A.14}$$

où h est l'écart-type de la distribution d'altitude des couches turbulentes pondéré par l'intégrale du profil de turbulence. Pour une valeur typique pour h de 5000 m, nous parvenons, toujours avec $r_0 \simeq 10$ cm à 500 nm, à un angle d'isoplanétisme d'environ $1''.5$ ($4''.5$ en J, pratiquement $9''$ en K).

FIGURE A.1: Exemple de PSFs perturbées par la turbulence atmosphérique et observées au foyer d'un grand télescope au sol. De gauche à droite : tache d'Airy (cas idéal), PSF longue-pose observée, PSF courte-pose observée. Cet exemple illustratif a été réalisé à partir de simulations mettant notamment en jeu un télescope de 4 m, une longueur d'onde de 660 nm et un r_0 de 20 cm. (*Figure tirée de Carbillet [28].*)

Tache d'Airy — image longue-pose — image instantanée La Fig. A.1 montre un exemple de réponse impulsionnelle [1] perturbée par la turbulence atmosphérique telle qu'elle peut être enregistrée au foyer d'un télescope au sol.

La différence entre la tache d'Airy attendue, correspondant au cas idéal, la PSF longue-pose et celle courte-pose – une image scintillante, agitée et étalée, i.e. formée de speckles, est manifeste. La tache d'Airy montre un cœur de largeur à mi-hauteur [2] λ/D. D'un autre côté, la PSF longue-pose est caractérisée par un cœur beaucoup plus grand : λ/r_0 de larguer à mi-hauteur. Finalement, la PSF courte-pose est formée quant à elle de cette fameuse figure de speckles, figure qui change extrêmement rapidement avec le temps.

Front d'onde La phase ϕ, perturbée par l'atmosphère turbulente, possède une densité spectrale classiquement modélisée par (au sein du modèle de Kolmogorov/von Kármán) :

$$\Phi_\phi(\vec{f}) = 0.0228\ r_0^{-\frac{5}{3}} \left(f^2 + \frac{1}{\mathcal{L}_0^2} \right)^{-\frac{11}{6}} \quad , \tag{A.15}$$

où f est la fréquence spatiale et $\mathcal{L}_0$ est l'échelle externe de la turbulence (avec une valeur typique médiane de 20–30 m pour des sites de latitude moyenne). Concernant cette notion de phase, on lui préfèrera souvent celle de *front d'onde*, achromatique [3], mesuré en mètres (ϕ l'est naturellement en radians) et qui est, par définition, lié à la phase par un facteur $\frac{\lambda}{2\pi}$.

1. Que l'on peut estimer en faisant l'image d'un point-source, i.e. d'un astre non-résolue par le télescope. On utilise aussi beaucoup l'acronyme PSF, de *point-spread function* en anglais.
2. FWHM pour *Full-Width at Half-Maximum* en anglais.
3. Aux variations de l'indice de réfraction près en fonction de λ.

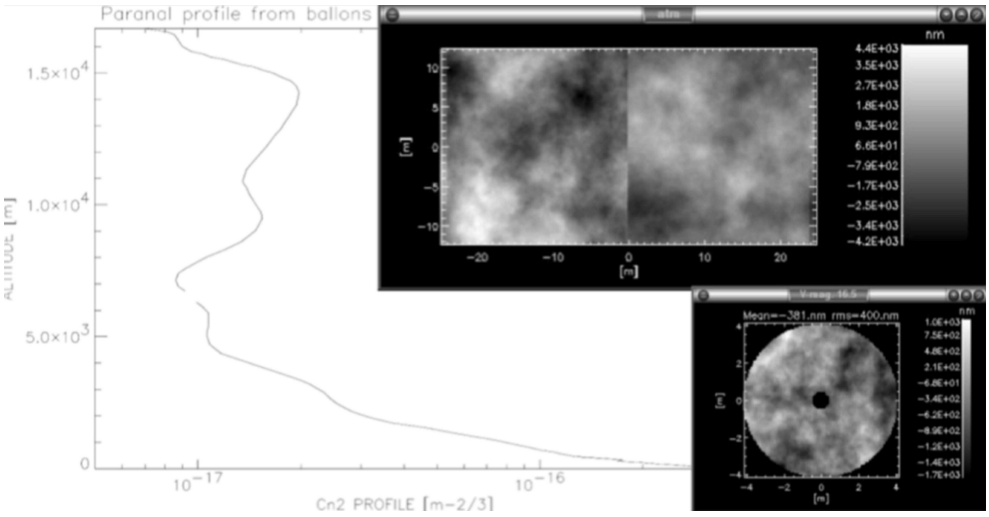

FIGURE A.2: Turbulence atmosphérique. À gauche : profile de turbulence typique correspondant à une campagne de caractérisation du site du Mont Paranal au Chili [34]. En haut à droite : deux couches de 24 m×24 m. En bas à droite : front d'onde résultant de la propagation à travers ces couches turbulentes et jusqu'à un télescope de la classe 8 mètres. (*Figure tirée de Carbillet [92].*)

La Fig. A.2 montre un profil typique de turbulence atmosphérique, où les couches sont clairement identifiables, accompagné de la représentation de deux couches turbulentes suivant une statistique de Kolmogorov/von Kármán, ainsi que le front d'onde résultant de la propagation à travers ces couches turbulentes jusqu'à la pupille d'entrée du télescope.

Formation de l'image La relation objet-image qui lie l'éclairement $I(\vec{\alpha})$, dans le plan image (i.e. au foyer du télescope), où $\vec{\alpha}$ est le vecteur angulaire bidimensionnel décrivant la direction de visée, à la luminance $O(\vec{\alpha})$ de l'objet céleste, est une relation de convolution impliquant la réponse impulsionnelle $S(\vec{\alpha})$ de l'ensemble télescope⊕atmosphère :

$$I(\vec{\alpha}) = O(\vec{\alpha}) * S(\vec{\alpha}) \ . \tag{A.16}$$

où $*$ symbolise la relation de convolution selon $\vec{\alpha}$. Cette relation présuppose que nous soyons bien en éclairage incohérent et est valable notamment à la condition que le système soit invariant par translation, i.e. que « tout se passe » à l'intérieur du domaine d'isoplanétisme [4]...

4. À ceci il faut ajouter, pour être rigoureux, le fond de ciel (et éventuellement instrumental). L'image non-bruitée et le fond ajouté sont ensuite « photonisés » (bruit de Poisson dû au fait-même que l'on observe une source délivrant un nombre fini de photons). Enfin,

Par transformation de Fourier [10], l'équation A.16 devient une relation de filtrage linéaire :

$$\hat{I}(\vec{f}) = \hat{O}(\vec{f})\ \hat{S}(\vec{f}), \tag{A.17}$$

où $\hat{S}(\vec{f})$ est appelée la fonction de transfert optique (FTO) et $\vec{f}$ est le vecteur de fréquence angulaire.

Si on en revient aux trois perturbations énoncées en début de cette section (scintillation, agitation et étalement), on peut tout d'abord préciser que la scintillation n'affecte que marginalement les images dans le (proche) infrarouge, domaine de prédilection de l'astronomie assistée par OA actuelle (puisque les deux autres perturbations citées y sont elles aussi amoindries, due à la dépendance en longueur d'onde mise en évidence dans les équations précédentes).

Précisons également que dans le cas particulier des images obtenues par une pupille diluée (le cas le plus simple étant celui d'un interféromètre formé de deux ouvertures), il y a deux types d'agitation à considérer :

- ⋆ Celle de la figure de franges, agitée le long de l'axe de la base entre les deux ouvertures. Ceci est dû au piston différentiel entre les deux ouvertures,
- ⋆ Celle de chacune des taches d'Airy de chacune des ouvertures (dans le cas d'ouvertures circulaire) qui provoque une mauvaise superposition des taches déformant l'enveloppe résultante des franges de la PSF interférométrique. Ce deuxième point est dû au basculement différentiel entre les deux ouvertures.

Imagerie speckle et Lucky imaging Pour en revenir au cas monopupille, l'agitation peut y être formellement corrigée par une technique post-détection de type *shift-and-add* (un simple recentrage avant addition des différentes images courte-pose enregistrées) [6]. Mais un problème sérieux de sensibilité, comme dans le cas de toutes les techniques speckle, reste présent. La plupart de ces techniques speckle sont plus élaborées que le shift-and-add, telle que la technique pionière d'interférométrie des speckles de Labeyrie [5], utilisant la densité spectrale, transformée de Fourier inverse de l'autocorrélation des images, ou celle de Weigelt [7] utilisant le bispectre, transformée de Fourier de la triple corrélation des images, ou bien encore celle d'imagerie probabiliste, proposée par Aime [15] et utilisant des densités de probabilité d'ordres supérieurs.

Dans le cas de la densité spectrale, on effectue une analyse statistique en deux points des images obtenues, tandis que dans le celui du bispectre, en

le bruit dû à l'appareil effectuant la détection, habituellement un CCD, composé principalement d'un bruit de lecture (bruit additif suivant une distribution de Gauss) et d'un courant d'obscurité (poissonien), doit être également considéré.

trois points. Une alternative en deux points, en calculant une intercorrélation des images et de leurs carrés, a aussi été proposée et appliquée sur des données d'étoiles binaires [35]. Dans le cas de l'imagerie probabiliste les applications ont également été surtout effectuées en deux points [29, 30, 36]. Mais toutes ces opérations sont effectuées après la détection, et les détecteurs possèdent un bruit de lecture important (important au regard des exigences astrophysiques), bruit qui limite donc fortement les observations.

Les détecteurs EMCCD, apparus plus récemment, n'en sont par contre pas entachés, ils permettent alors d'appliquer la technique d'imagerie speckle de Labeyrie encore plus simplement : sans même avoir besoin de calculer un invariant statistique tel que l'autocorrélation, l'intercorrélation, la triple-corrélation ou une densité de probabilité d'ordre deux ou plus, calculé à partir d'image où la turbulence a été « gelée » (i.e. à partir d'images dont le temps de pose est inférieur ou de l'ordre de τ_0). Il s'agit de la technique dite de *Lucky Imaging* [49], considérée aussi dans le cas de correction partielle en OA [152] – ce qui est particulièrement pertinent dans le contexte actuel pour des données à obtenir dans le visible.

Ordres de grandeur pour un système d'OA Le système d'OA adapté à un site donné (caractérisé *in primis* par sa turbulence atmosphérique), un télescope donné (diamètre) et une gamme de longueur d'onde donnée correspond à des ordres de grandeur de ses composantes premières (taille des sous-ouvertures de l'analyseur de surface d'ondes, ASO, et distance inter-actuateurs, temps de pose de l'ASO, temps de réponse global de la boucle OA) que nous pouvons tout-de-suite évalué grâce aux informations précédentes sur les ordres de grandeur concernant la turbulence atmosphérique.

La taille typique d de chaque élément de mesure de l'ASO (ou de manière équivalente la distance inter-actuateur typique du miroir déformable) peut suivre intuitivement la loi $d \simeq r_0$, ce qui se traduit instantanément par un nombre approximatif d'éléments (un peu moins de $(D/r_0)^2$) de l'ordre de 7500 pour un télescope (de pupille circulaire) de diamètre 10 m et un r_0 de 10 cm dans le visible, ou (de l'ordre de) 200 en bande K. Côté aspects temporels, et si l'on prétend par exemple échantilloner la turbulence à quelques fractions de τ_0, on doit considérer des fréquences de l'ordre du kHz.

La Fig. A.3 schématise l'opération effectuée par un système d'OA : un front d'onde perturbé se présente en entrée du télescope, est réfléchi par un miroir déformable, puis envoyé à un séparateur de faisceaux qui partage la lumière entre l'instrument d'observation (un CCD, un spectromètre, autre chose) et l'ASO, ASO à partir duquel l'information collectée (e.g. les signaux de la pyramide permettant de calculer les pentes locales) est envoyée au reconstructeur (de front d'onde) / contrôleur (de commandes envoyées au miroir déformable) qui va élaborer, justement, les commandes à envoyer au miroir.

La Fig. A.4 montre le résultat de la correction OA, avec différents niveaux

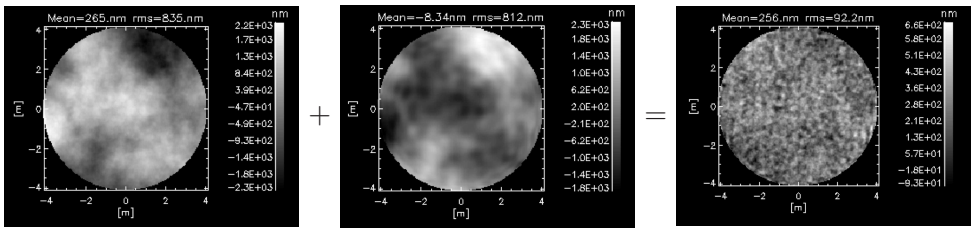

FIGURE A.3: Principe d'un système d'OA. À gauche : le front d'onde incident. Au centre : la forme du miroir déformable, résultante des commandes envoyées par le reconstructeur après analyse des informations collectées par l'ASO. À droite : front d'onde résultant, après réflection du front d'onde incident sur le miroir déformé. (*Figure tirée de Carbillet [92].*)

de qualité, aussi bien pour un télescope monopupille que pour un interféromètre de Fizeau tel que le LBT. Les paramètre principaux des simulations menées avec le `Software Package CAOS` pour cet exemple sont ceux du LBT et de FLAO, avec pour l'atmosphère et l'étoile guide : r_0=15 cm à 500 nm, vitesse moyenne = 15 m/s, $\mathcal{L}_0$=20 m, seeing$\sim$0.″5, magnitude de l'étoile guide en bande R = 13. Avec une telle magnitude, il s'agit ici de la configuration 15×15 de l'ASO, avec un temps de pose de 1.67 ms et 150 modes corrigés [62].

La Fig. A.5 montre quant à elle ce même résultat de la correction partielle d'OA répercutée sur la formation de l'image (et donc après convolution de la PSF avec un objet céleste composite) pour un télescope monopupille (ici encore, le LBT à un œil, un très bon exemple de la classe 8 m) et pour différents niveaux de qualité de la correction de l'OA. Les deux niveaux de correction considérés ici correspondent à des rapports de Strehl de 0.07 et 0.93. La différence visuelle dans le rendu de l'image est évidente, ce qui tend à montrer l'efficacité du rapport de Strehl en tant qu'indicateur de la qualité d'une image astronomique obtenue en dépit de la turbulence atmosphérique. Il conviendrait cependant parfois d'utiliser d'autres indicateurs, tels que :

- ⋆ la FWHM effectivement atteinte dans l'image (dans les cas observationnels où la résolution angulaire est au centre des préoccupations) ;
- ⋆ l'énergie encerclée, ou bien contenue dans la fente du spectrographe en question (quand il en est question) ;
- ⋆ ou par exemple le niveau des « ailes » de la PSF post-OA post-coronographe dans le cas à très haut contraste (la question étant ici la détection et éventuelle caractérisation du compagnon faible –la potentielle planète– normalement noyé dans la lumière résiduelle de l'étoile centrale).

D'autres critères (encore plus raffinés et plus ou moins aisés à établir) peuvent être définis, comme par exemple le rapport signal-à-bruit atteignable pour un problème de détection, ou la capacité de retrouver les paramètres astrophysiques d'intérêt dans l'objet observé. Dans ce dernier cas il sera nécessaire de considérer *toute* la chaîne d'obtention de l'image/des données

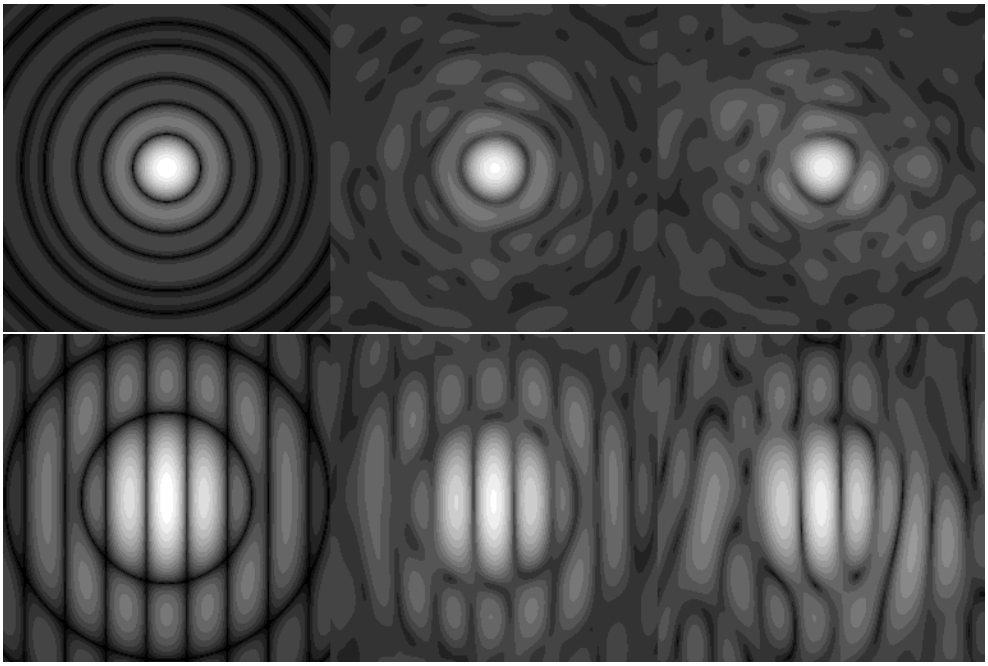

FIGURE A.4: PSF simulées en bande K pour le LBT « à un œil » (en haut) et « à deux yeux » (en bas). De gauche à droite : cas idéal, cas en axe, cas 15″ hors-axe. Les rapports de Strehl correspondant sont, de gauche à droite et de haut en bas : 1, 0.79, 0.67, 1, 0.77, 0.66 (une –ici légère– erreur de piston différentiel est additionnellement présente dans les données interférométriques). En haut, le champ de vue est de 0.″64×0.″64, en bas de 0.″256×0.″256. (*Figures tirées de Anconelli et al. [79].*)

(télescope⊕système d'OA⊕instrument d'acquisition des données⊕traitements des données).

Une grande variété de « concepts » OA Les systèmes d'OA n'accomplissent pas de miracle. Le premier facteur limitant est le nombre de photons nécessaire à l'analyse du front d'onde incident. La fréquence temporelle de l'analyse étant forcément élevée, comme nous venons de le voir, des étoiles très brillantes sont nécessaires afin de pouvoir contre-carrer les bruits induits par le manque de photons au niveau des détecteurs utilisés pour l'analyse. Ceci va limiter la portion de ciel observable avec une qualité de correction donnée par un système d'OA donné[5].

Une première solution, permettant en principe une couverture du ciel de 100%, consiste à venir à bout de cette limitation en utilisant des étoiles laser artificielles opportunément disposés dans la direction céleste visée [13]. Ces

5. On parle alors de couverture du ciel.

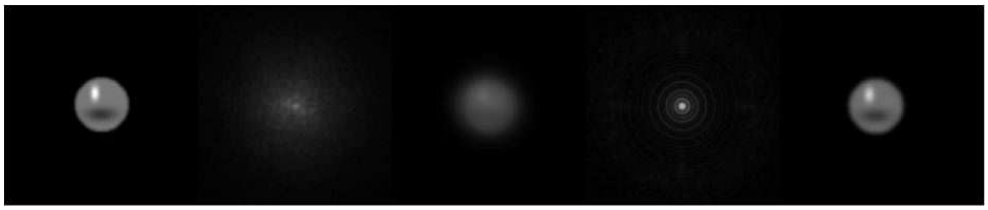

FIGURE A.5: De gauche à droite : objet, PSF avec un rapport de Strehl de 0.07, image résultante, PSF avec un rapport de Strehl de 0.93, image résultante. (*Figure tirée de Carbillet [154].*)

étoiles laser artificielles sont formées soit par rétro-diffusion de la couche de Sodium située à 90–100 km d'altitude, soit par diffusion Rayleigh (surtout sur les 10–15 premiers kilomètres). Cette technique présente cependant un certain nombre de problèmes additionnels, de la grande puissance requise pour le laser utilisé, aux effets liés au fait que l'étoile guide est formée à une distance finie du télescope (effet de cône, qui empire avec D croissant), qu'elle a une étendue malheureusement non-négligeable, que la couche de Sodium sollicitée pour la rétro-diffusion est le siège de fluctuations entrainant une défocalisation, et que le basculement du front d'onde n'en est pas directement mesurable (le même basculement étant rencontré lors de la propagation vers le haut puis lors de celle vers le bas : on parle d'indétermination du basculement). Une étoile naturelle additionnelle (de magnitude même élevée) peut déjà enlever une belle épine du pied, rendant la mesure du basculement possible (et éventuellement de la défocalisation).

Un second problème important est celui lié à l'anisoplanétisme, anisoplanétisme qui entraine un champ de correction très limité autour de l'étoile guide OA. Afin de limiter cette erreur et permettre de mieux observer des objets faibles, une solution consiste à considérer plusieurs étoiles guides autour de l'astre voulu, et donc de considérer des systèmes d'OA multi-références. De tels systèmes doivent ainsi permettre de mesurer un volume de turbulence plus grand. On parle alors de tomographie appliquée à l'OA, ou d'OA tomographique. Ces systèmes d'OA peuvent être à leur tour déclinés selon quatre catégories aux caractéristiques différentes :

- ⋆ OA par tomographie laser (ou LTAO en anglais) : système à plusieurs étoiles guides laser et un seul miroir déformable qui fixe surtout le problème d'effet de cône inévitable si on n'utilise qu'une seule étoile laser (dans la direction de l'objet visé). Le champ de vue corrigé en résultant reste serré.
- ⋆ OA multi-conjuguée (MCAO) : système à plusieurs étoiles *et* plusieurs miroirs déformables, chacun conjugué optiquement à une couche turbulente. Le champ de vue corrigé en résultant est plus large (typiquement $1'$), celui (ou ceux, dans le cas où il y aurait différentiation entre étoiles

lasers et étoiles naturelles) d'analyse encore plus (2′–3′, voire plus). Il en existe deux concepts : *star-oriented* (un ASO par étoile guide) et *layer-oriented* (un ASO conjugué sur chaque couche turbulente visée).

- ⋆ OA multi-objets (MOAO) : système corrigeant plusieurs objets dans différentes directions du champ séparément. Chacun des champs corrigés individuellement reste serré, mais l'ensemble se distribue sur un grand champ global.
- ⋆ OA couche-limite (GLAO) : système qui ne prétend corriger que la couche limite. La correction est modeste mais effective sur un très grand champ.

Finalement, le besoin d'observer à très haut contraste, en plus qu'à HRA, mène aux systèmes d'OA extrême (ou XAO en anglais). Ces systèmes sont identique en tout point à celui d'un système standard, à la différence près que chaque composant matériel est poussé dans ses ultimes retranchements technologiques, tant et si bien que le système global a besoin de briser un certain nombre de barrières conceptuellles et technologiques.

De plus, une classe d'objets astrophysiques donnée a ses propres priorités observationnelles. Dans le cas des exoplanètes ceci peut se traduire par le besoin premier de directement détecter ces objets, et, éventuellement, de les caractériser spectralement, ou dans le cas de galaxies lointaines par la nécessité d'obtenir leurs morphologies précises. Ceci porte à considérer la/les erreur(s) OA dominante(s) pour chaque cas : l'anisoplanétisme dans le cas des galaxies lointaines, tout sauf l'anisoplanétisme dans celui des exoplanètes, et par conséquent à considérer des concepts OA ad hoc.

Sans parler des applications aux observations du Soleil qui ne diffèrent que sur quelques points techniques tel que la mesure du front d'onde (effectuée avec un SH mais à partir du calcul d'intercorrélations au lieu de photocentres), d'autres types d'applications de l'OA sont développées : l'observation de satellites basse orbite (une situation somme toute assez proche de celle astronomique standard), les communications optiques (le réseau radio arrivant semble-t-il à saturation, ceci devrait permettre le transfert massif demandé des données des satellites vers le sol), sans oublier l'ophtalmologie (avec, pour commencer, l'imagerie du fond de l'œil – une technique conceptuellement voisine de l'AO assistée d'étoiles laser en astronomie).

Annexe B

Curriculum vitæ

Marcel Carbillet

Maître de Conférence, Classe Normale
34^e section du CNU, Université de Nice–Sophia Antipolis (UNS)

UMR 7293 Joseph-Louis Lagrange (UNS/CNRS/Observatoire de la Côte d'Azur),
Bâtiment Hyppolite Fizeau, Parc Valrose, 06100 Nice
Tél. : +33 (0)4 92 07 63 28 (Fax : 21) – Mél : `marcel.carbillet@unice.fr`
URL : `http://lagrange.oca.eu/marcel` – `skype` : `marcel.carbillet`

1 Activités de recherche/Fonctions exercées

Depuis Septembre 2004

Maître de Conférence à l'UMR 7293 Lagrange [1], Université de Nice Sophia Antipolis (UNS) / Centre National de la Recherche Scientifique (CNRS) / Observatoire de la Côte d'Azur (OCA).
→ [Année universitaire 2013—2014] Congé pour Recherche au titre du contingent UNS (mi-temps).
→ [Années civiles 2010–2011, 2012–2013] *Associato* (Associé) à l'*Istituto Nazionale di AstroFisica* (INAF) auprès du groupe d'optique adaptative de l'*Osservatorio Astrofisico di Arcetri* (OAA) (Florence, Italie).
→ [Années universitaires 2010—2011, 2011–2012 et 2012–2013] Délégation à mi-temps au CNRS.
→ [Année universitaire 2006—2007] Congé pour Recherche au titre du contingent UNS (mi-temps).
→ [2005–2008] Responsable *Local Project Control and Administration* du LUAN au sein du consortium européen conduisant le projet SPHERE (Spectro-Polarimetric High-contrast Exoplanet REsearch).
→ [2004–∞] Responsable du projet logiciel CAOS (Code for Adaptive Optics Systems).

Juin 2001–Août 2004

Contrat de recherche à durée déterminée à l'Osservatorio Astrofisico di Arcetri (OAA, Florence, Italie), dans le cadre du projet LBT (Large Binocular Telescope).
→ Responsable de la partie modélisation physique et simulations numériques pour l'instrument d'optique adaptative (OA) de première lumière FLAO du LBT, ainsi que pour les stratégies de reconstruction d'images en mode interférométrique.

Octobre 2000–Juin 2001

Contrat de recherche post-doctoral de l'OAA, dans le cadre du projet LBT.
→ Modélisation physique et simulations numériques des systèmes d'OA et interférométriques du LBT, reconstruction d'images interférométriques post-OA pour le LBT, développement des paquets logiciel correspondants.

Octobre 1997–Septembre 2000

Bourse post-doctorale dans le cadre du programme Européen *Training & Mobility of Researchers*, réseau "Laser Guide Stars for 8-m Class Telescopes", à l'OAA, groupe LBT.
→ Études des systèmes d'OA pour les télescopes de la classe 8 m, simulations numériques détaillées incluant l'étoile laser. Développement du paquet logiciel correspondant. Encadrant : S. Esposito.

Janvier 1997–Septembre 1997

Bourse post-doctorale dans le cadre de la "Communauté de Travail des Alpes Occidentales", à l'Université de Genève, équipe LIDAR du Groupe de Physique Appliquée.
→ Modélisation de la réponse LIDAR en présence de turbulence atmosphérique. Encadrant : C. Flesia.

1. Initialement à l'UMR 6525 LUAN (UNS/CNRS, avant 2008), englobée par la suite dans l'UMR 6525 Fizeau (UNS/CNRS/OCA, 2008–2011), elle-même englobée depuis janvier 2012 dans l'actuelle UMR 7293 Lagrange.

Décembre 1993–Novembre 1996

Allocataire de recherche MENRT, au sein de l'équipe d'Imagerie Probabiliste, Département d'Astrophysique de l'Université de Nice–Sophia Antipolis.
→ Développement des techniques d'imagerie probabiliste et observations speckle-interférométriques d'étoiles doubles/multiple application au proche-infrarouge et au visible. Directeur de thèse : C. Aime.

Juillet 1995–Novembre 1995

Stage pré-doctoral dans le cadre du programme Européen *Human Capital & Mobility*, à l'*Applied Optics Group, Blackett Laboratory, Imperial College, Londres*.
→ Imagerie probabiliste d'étoiles doubles/multiples : extension au problème bidimensionelle et traitement de données obtenues au télescope William Hershel Telescope (4 m) dans le visible. Encadrant : J. C. Dainty.

Mars 1993–Juillet 1993

Stage de DEA *"Détermination des paramètres orbitaux d'étoiles doubles en infrarouge"*, au Département d'Astrophysique, Université de Nice–Sophia Antipolis, Nice. Encadrant : G. Ricort.

2 Activités d'encadrement/Animation de la recherche

Encadrement de thèses

Co-encadrement de la thèse de doctorat de Zeinab Khorrami

Doctorat de l'UNS en cours débuté en septembre 2012. Co-encadrement de la thèse dirigée par F. Vakili et O. Chesneau (Lagrange, UNS/CNRS/OCA). Cette thèse porte sur l'étude de l'amas d'étoiles R 136 dans la nébuleuse 30 Doradus du Grand Nuage de Magellan. Encadrement de ma part : ∼10%. 1 publication commune.

Co-direction de la thèse de doctorat de Laure Catala

Doctorat de l'Université du Cap en cours débuté en février 2012. Co-direction de thèse en collaboration avec A. Ziad (Lagrange, UNS/CNRS/OCA) et S. Crawford (*South African Astronomical Observatory*). Cette thèse porte sur la caractérisation du site et le développement d'une OA pour le grand télescope sud-africain SALT. Encadrement de ma part : ∼20%. 2 publications communes.

Co-direction de la thèse de doctorat de Christophe Giordano

Doctorat de l'UNS en cours débuté en septembre 2011. Co-direction de thèse en collaboration avec J. Vernin (Lagrange, UNS/CNRS/OCA). Le travail doctoral porte sur l'optique atmosphérique et ses liens vers l'observation assistée d'un système d'OA à travers la prévision de *seeing* d'une part et l'évaluation de performance de site d'autre part. Encadrement de ma part : ∼25%. 1 publication commune.

Co-encadrement de la thèse de doctorat de Andrea Abelli

Doctorat de l'Université Franco-Italienne/Università Italo-Française, qui s'est déroulée entre l'UNS et L'Università di Roma–La Sapienza (Rome, Italie) et a été obtenue en avril 2013. Co-encadrement de la thèse dirigée localement par A. Ferrari et J.-P. Folcher (Lagrange, UNS/CNRS/OCA). Cette thèse a porté sur la commande linéaire et non-linéaire avec application à l'OA. Encadrement de ma part : ∼10%. 4 publications communes.

Co-encadrement de la thèse de doctorat d'Andrea La Camera

Doctorat de l'Università di Genova (UG) obtenu en mai 2011. Co-encadrement de la thèse dirigée par M. Bertero et P. Boccacci (Dipartimento di Fisica, UG). Ce travail doctoral, tout comme celui précédent de Gabriele Desiderà (voir plus loin) mais selon une approche moins informatique/plus physique, a porté sur la reconstruction/déconvolution d'image dans le cas spécifique de l'instrument interférométrique imageur LINC-NIRVANA (LN) du LBT. Encadrement de ma part : ∼25%. 7 publications communes.

Co-direction de la thèse de doctorat de Isabelle Smith

Doctorat de l'UNS obtenu en octobre 2010. Co-direction de thèse en collaboration avec A. Ferrari (Fizeau, UNS/OCA/CNRS). Le travail doctoral a eu pour cadre le traitement des données qui seront issues de l'instrument SPHERE, et notamment de sa caméra proche-infrarouge IRDIS (InfraRed Dual-Beam Imager and Spectrometer), post-OA extrême et post-coronographe. Encadrement de ma part : ∼30%. 10 publications communes.

Co-encadrement de la thèse de doctorat de Gabriele Desiderà

Doctorat de l'UG obtenu en mai 2010. Co-encadrement de la thèse dirigée par M. Bertero et P. Boccacci (Dipartimento di Fisica, UG). Le travail doctoral a porté sur la reconstruction/déconvolution d'image dans le cas spécifique de l'instrument interférométrique imageur LN du LBT mais aussi d'un point de vue plus général de l'imagerie post-OA. Encadrement de ma part : ∼30%. 10 publications communes.

Co-encadrement de la thèse de doctorat de Barbara Anconelli

Doctorat de l'UG obtenu en mai 2006. Co-encadrement de la thèse dirigée par M. Bertero et P. Boccacci (Dipartimento di Fisica, UG). Le travail doctoral a porté sur le traitement des données interférométriques qui seront issues de l'instrument focal LINC-NIRVANA du LBT. Encadrement de ma part : ∼10%. 15 publications communes.

Co-direction de la thèse de doctorat de Serge Correia

Doctorat de l'UNS obtenu en décembre 2002. Co-direction de thèse en collaboration avec H. Lantéri (LUAN, UNS/CNRS). Le travail doctoral s'est effectué principalement à l'observatoire d'Arcetri et a eu pour titre "Haute résolution angulaire et interférométrie optique en Astrophysique : Applications au *Large Binocular Telescope* et au *Very Large Telescope Interferometer*". Encadrement de ma part : ∼90%. 10 publications communes.

Encadrement de stages de Master 2 (et similia)

Co-direction du stage d'Ivan Belokogne

Stage de Master 2 Omega (parcours "Astronomie & Astrophysique") de l'UNS. Co-direction en collaboration avec O. Chesneau (Fizeau, UNS/OCA/CNRS). Le stage a porté sur l'application de méthodes de déconvolution extrêmes appliquées aux données simulées d'observations avec l'instrument SPHERE d'étoiles évoluées et leur environnement, avec et sans coronographe : super-résolution de la binaire centrale à partir de données à haut Strehl et reconstuction de l'environnement circumbinaire à partir de données à haut Strehl *et* haut contraste, de février 2011 à juin 2011. Encadrement de ma part : ∼60%.

Co-direction du stage de Laure Catala

Stage de Master 2 Omega (parcours "Astronomie & Astrophysique") de l'UNS. Co-directionen collaboration avec A. Ziad (Fizeau, UNS/CNRS/OCA) et S. Crawford (SALT). Le stage a porté sur la caractérisation de la turbulence atmosphérique au-dessus du SALT et la modélisation du système d'OA qui pourrait permettre d'améliorer la qualité des images obtenues dans le proche infrarouge, de février 2011 à juin 2011 Encadrement de ma part : ∼30%. Publications communes : voir thèse de doctorat ci-avant.

Direction du stage d'Anne-Lise Maire

Stage de Master 2 Omega (parcours "Astronomie & Astrophysique") de l'UNS sur l'étude d'un système d'OA de type "ground-layer" (GLAO) pour le futur site du dôme C (Antarctique), selon une approche détaillée de l'analyse et de la correction d'OA sur un télescope de la classe 2m, de février 2009 à juin 2009. Encadrement de ma part : 100%. 3 publications communes.

Co-direction du stage d'Albert Ambros

Stage de cinquième année de l'Universitat Politècnica de Catalunya. Co-direction en collaboration avec A. Ferrari (LUAN, UNS/CNRS). Le stage a porté sur l'étude du phénomène de "pinned speckles" en imagerie à très haut contraste, de novembre 2006 à juin 2007 dans le cadre d'un programme Erasmus. Encadrement de ma part : ∼40%.

Co-direction du stage de Fatmé Allouche

Stage de Master 2 Omega (parcours "Astronomie & Astrophysique") de l'UNS. Co-direction avec A. Ferrari (LUAN., UNS/OCA/CNRS). Le stage a porté sur le traitement statistique de données pour la détection des exoplanètes par imagerie directe, de mars 2006 à juin 2006. Encadrement de ma part : ∼40%.

Co-direction du stage d'Eduard Serradell

Stage de cinquième année de l'Universitat Politècnica de Catalunya. Co-direction avec A. Ferrari (LUAN, UNS/CNRS). Le stage a porté sur le traitement de données en imagerie à très haut contraste dans la perspective du futur "planet finder" du VLT (à l'époque VLT-PF et maintenant SPHERE), de novembre 2005 à juin 2006 dans le cadre d'un programme Erasmus. Encadrement de ma part : ∼40%.

Co-direction de la "tesi di laurea" de Barbara Anconelli

Stage de cinquième année universitaire de l'UG. Co-direction en collaboration avec M. Bertero et P. Boccacci (Dipartimento di Fisica, UG). La *tesi di laurea* a porté sur le traitement des données interférométriques dans le cadre de l'instrument focal LINC-NIRVANA du LBT, de novembre 2001 à juillet 2002. Encadrement de ma part : ∼10%. Publications communes : voir thèse de doctorat.

Encadrement de stages de niveau Licence

Direction du stage de Diyana Ab Kadir

Stage de dernière année d'IUT de l'UNS sur la simulation numérique de systèmes d'observation astronomique par le biais du "problem-solving environment" CAOS, de mars 2007 à juin 2007. Encadrement de ma part : 100%. 1 publication commune.

Co-direction du stage de Christophe Giordano, Olivier Pasqueron de Fommervault et Jean Gautier

Stage de Licence 3 Physique de l'UNS. Co-direction avec É. Aristidi (Fizeau, UNS/OCA/CNRS). Le stage a porté sur l'étude d'un système d'OA pour le futur site du dôme C (Antarctique), selon une approche purement atmosphérique d'un système parfait d'OA, de février 2009 à juin 2009. Encadrement de ma part : ∼50%. 1 publication commune.

Coordination de projets

Spectro-Polarimetric High-contrast Exoplanet REsearch — SPHERE

- ⋆ De janvier 2005 à janvier 2008 : Responsable LPCA pour le LUAN/Fizeau au sein du consortium européen (France, Italie, Allemagne, Suisse, Hollande) construisant l'instrument SPHERE pour le *Very Large Telescope* (VLT) de l'*European Southern Observatory* (ESO). Ce qui s'est traduit par la responsabilité vis-à-vis du consortium SPHERE (13 instituts) de toutes les activités menées par le LUAN/Fizeau pour cet instrument.
- ⋆ De janvier 2005 à courant 2011 : Au sein du même projet SPHERE j'ai continué à revêtir également le rôle de *simulation expert* dans l'organigramme du consortium. J'ai continué de plus à participer au développement de la partie de l'instrument mise au point au LUAN/Fizeau : le coronographe de Lyot apodisé, ainsi qu'à l'élaboration du traitement des donnés qui devra permettre d'atteindre l'objectif scientifique principal de SPHERE : la détection directe d'exoplanètes géantes et leur caractérisation à basse résolution spectrale.
- ⋆ À ce jour, je ne participe "plus que" à la mise en place du programme d'observation astrophysique de SPHERE, notamment en ce qui concerne la partie "Other Science".

Code for Adaptive Optics Systems — CAOS

Coordination, maintenance et développement des différentes composantes du projet logiciel CAOS, utilisées par une centaine de chercheurs à travers le monde : le *CAOS Problem Solving Environment*, structure et interface globale, le *Software Package CAOS* (version 5.2 actuellement), ensemble de modules pour la simulation de systèmes d'OA, le *Software Package AIRY* (version 6.0 actuellement), pour la déconvolution/reconstruction d'images, le *Software Package AIRY-LN* (version 1.3 actuellement), sa version spécialement adaptée aux données issues de l'instrument LINC-NIRVANA du LBT, le *Software Package MAOS* (version β actuellement), pour la modélisation de systèmes d'OA multi-référence, ainsi que le *Software Package PAOLAC* (version 1.0 actuellement), adaptation sous CAOS du

package PAOLA de modélisation semi-analytique de systèmes d'OA, et le *Software Package SPHERE* (version 3.0 finale), outil de simulation *end-to-end* pour l'instrument SPHERE du VLT. Les parties publiques et actuellement distribuées du projet CAOS sont documentées en détail à partir de l'adresse `http://lagrange.oca.eu/caos`. Le `Software Package SPHERE` et le `Software Package AIRY-LN` ne sont distribués qu'au sein des projets respectifs SPHERE et LINC-NIRVANA.

Organisation de colloques et écoles thématiques

École d'été "Atmospheric Characterization & Adaptive Optics in Astronomy"

Participation à l'organisation de la première école d'été "Atmospheric Characterization & Adaptive Optics in Astronomy", destinée aux jeunes chercheurs des pays africains, Sutherland, Afrique du Sud, décembre 2012 (voir `http://amao.saao.ac.za`).

Colloque IAU "Direct Imaging of Exoplanets : Science & Techniques"

Participation à l'organisation du colloque n. 200 de l'Union Astronomique Internationale (UAI–IAU) "Direct Imaging of Exoplanets : Science & Techniques", Villefranche-sur-mer, France, octobre 2005.

École thématique du CNRS "Astronomie à très haute dynamique"

Co-organisation, avec C. Aime et A. Ferrari du LUAN, de la troisième école thématique "Astronomie à très haute dynamique", Nice et Fréjus, France, 16–19 mai 2005 (voir `http://www-luan.unice.fr/Jithde/`). Co-édition des actes (volume 22 des *EAS Publications Series*, novembre 2006).

Autres écoles et colloques

- ⋆ Supercomputing meeting : 2 jours de rencontre entre spécialistes de la modélisation numérique de systèmes d'OA à di Napoli), Firenze, juillet 2003.
- ⋆ CAOS Software Tutorial #2 : 2 jours de cours et exercices sur l'utilisation du paquet software CAOS, pour les jeunes chercheurs du réseau Européen "Training & Mobility of Researchers" sur le thème de la "Laser guide-star for 8-m class telescopes", ESO, Garching-bei-München, octobre 2000.
- ⋆ CAOS Software Tutorial #1 : 2 jours de cours et exercices sur l'utilisation du paquet software CAOS, pour les jeunes chercheurs du réseau Européen "Training & Mobility of Researchers" sur le thème de la "Laser guide-star for 8-m class telescopes", ESO, Garching-bei-München, mai 1999.
- ⋆ Physique en Herbe 1995 : trésorier du bureau organisateur du congrès "Physique en Herbe 1995 – PeH 95", 12ième colloque européen destiné aux jeunes chercheurs en physique. 5 jours, ∼300 participants du monde entier, 500 kFF de budget.

Cours dans des écoles thématiques (et similia)

- ⋆ Cours & exercices sur machine "(Introduction to) The CAOS Problem-Solving Environment & The Software Package CAOS ⊕ Adaptive Optics Simulations...", en collaboration avec Laure Catala (SALT), école d'été "Atmospheric Characterization & Adaptive Optics in Astronomy", Sutherland, 3–7 décembre 2012.
- ⋆ Cours "Optique astronomique... Turbulence atmosphérique ? Optique adaptative !", école thématique du CNRS "Reconstruction d'image - Applications astronomiques", Nice et Fréjus, 18–22 juin 2012.
- ⋆ Cours "Optique adaptative pour l'imagerie à très haute dynamique", troisième école thématique du CNRS "Astronomie à très haute dynamique", Nice et Fréjus, 16–19 mai 2005.
- ⋆ Cours "Optique adaptative : simulations numériques", deuxième école thématique du CNRS "Astronomie à très haute dynamique", Nice, 6–10 octobre 2003.
- ⋆ Cours "Essentials of the software system CAOS and extension to MCAO for ELTs", "Mini-school on Multi-Conjugate Adaptive Optics for ELTs" (école du RTN "AO for ELTs"), Munich, 19–21 février 2003.
- ⋆ Cours "Interferometric (Fizeau) imaging : numerical simulations", "Scuola Nazionale di Tecnologie Astronomiche" (école d'été nationale italienne), Naples, 23–28 septembre 2002.
- ⋆ Cours & exercices sur machine d'utilisation du paquet software CAOS, "CAOS Software Tutorial #2" (école du TMR "Laser guide-star for 8-m class telescopes"), ESO, Garching-bei-München, octobre 2000.
- ⋆ Cours & exercices sur machine d'utilisation du paquet software CAOS, "CAOS Software Tutorial #1 (école du TMR "Laser guide-star for 8-m class telescopes"), ESO, Garching-bei-München, mai 1999.

3 Enseignements supérieur & secondaire

Auxiliaire du secondaire

⋆ Auxiliaire d'enseignement en Mathématiques : Terminale D, Lycée Rousseau (Nice), 1992–1993,
⋆ Maitre-auxiliaire en Mathématiques : 1ère B et 5ème, Lycée Stanislas-Masséna (Nice), 1991–1992.

Vacataire du supérieur (UNS)

⋆ TD "Propriétés de la Matière" (mécanique quantique et physique du solide) : Lic. EEA, 1995–1996.
⋆ TP "Ondes et Vibrations" (optique et acoustique) : Licence de Physique, 1995–1996.
⋆ TP "Physique" (optique et électrostatique) : DEUG A "SPI", 1994–1995.
⋆ Tutorat en DEUG A Sciences Physiques pour l'Ingénieur (SPI), 1992–1993.

Maître de Conférence (UNS)

⋆ Cours-TP "Optique adaptative extrême" : Master 2 "Optique", 2013–2014.
⋆ Cours-TP "Optique adaptative" : Master 2 "Optique", 2013–2014.
⋆ Cours-TP "Imagerie à travers l'atmosphère turbulente" : Master 1 "IMAG2E", 2012–2014.
⋆ Cours-TD "Mécanique" : Licence 1 "Sciences de la Terre et Environnement", 2005–2014.
⋆ TP "Optique" : Lic. 1 "Mathématiques et Physique" et "Sciences de la Matière", 2004–2010, puis 2012–2014.
⋆ Cours-TD "Optique Adaptative" : Master 2 Omega "Astronomie & Astrophysique", 2006—2012.
⋆ Cours-TP "Imagerie à travers l'atmosphère" : Master 2 Omega "IMMEN", 2009—2012.
⋆ Cours-TP "Imagerie" : Licence 3 "Sciences de la Terre et Environnement", 2008—2012.
⋆ TP "Optique Cohérente" : Master 1 Omega "Astronomie & Astrophysique", 2005—2011.
⋆ Cours-TP "Transformée de Fourier" : Lic. 3 "Physique" et Lic. 3 "Physique-Chimie", 2005—2009.
⋆ TD "Mécanique" : Lic. 1 "Mathématiques et Physique" et "Sciences de la Matière", 2004—2009.
⋆ Cours-TD "Informatique Disciplinaire" (Maple) : Lic. 2 "Mathématiques et Physique", 2005—2008.
⋆ TD "Informatique" (langage C) : Master 2 "Génie Bio-Médical", 2004—2006.
⋆ TP "Électronique" : préparation à l'agrégation de Physique, 2004—2005.
⋆ TP "Optique" : préparation à l'agrégation de Physique, 2004—2005.

4 Autres

Autres activités en matière d'administration et de responsabilités collectives

⋆ 2009–2010 : Membre de la mission Projets évaluant/organisant les projets instrumentaux au sein de Fizeau.
⋆ 2007–2008 : Membre de la Commission de Spécialistes de la Section 34 au sein de l'UNS.
⋆ 2006–2007 : Membre du Conseil du LUAN ⊕ commission des locaux.
⋆ 2002–2003 : Membre de diverse commissions d'attribution (de marché, de bourses) au sein de l'OAA.
⋆ 1992–1996, UNS (en tant qu'étudiant) : Commission Avenir et Formation des Jeunes-Chercheurs du Département d'Astrophysique (1996), représentant des jeunes-chercheurs au Conseil du Département d'Astrophysique (1994), membre élu du Conseil Scientifique et membre de la commission d'attribution des équivalences de DEA (1993–1995) de l'UNS, membre élu du Conseil de Gestion de l'UFR Sciences et membre de la commission de gestion du foyer étudiant (1992–1994).

Autres expériences professionnelles

Cantonier (commune de Crolles, Isère), nettoyeur de chantier (entreprise de peinture GPS, Nice), transport et magazinier (entreprise de mobilier, Nice), vendeur électroménager (Philips/Rowenta, Alpes Maritimes), etc.

Langues lues, parlées et écrites / Languages de programmation pratiqués

Français (courant), Italien (courant), Anglais (un peu plus que professionnel), Espagnol (un peu plus que scolaire).
IDL, et plus occasionellement : Maple, C, Fortran, Mathematica, Matlab.

Annexe C

Liste des publications

Liste des Publications

Marcel Carbillet

[Au 15 octobre 2013]

(163 références, dont 31 articles dans des journaux scientifiques, 8 communications en tant qu'invité, 86 autres articles de conférence, 14 autres communications publiées, 6 posters non publiées, 15 rapports et thèse, 2 circulaires IAU et 1 catalogue stellaire)

— Revues à comité de lecture

(26 articles, 2 lettres, 1 research note*, 1* erratum*)*

1. "Probability imaging of a few double stars from near-infrared one-dimensional speckle data", M. Carbillet, G. Ricort, C. Aime, Ch. Perrier, *Astron. Astrophys.* **310**, 508 (1996).
2. "Discovery of a new bright close double star" (*Research Note*), M. Carbillet, B. Lopez, É. Aristidi, Y. Bresson, C. Aime, G. Ricort, J.-L. Prieur, L. Koechlin, G. Helmer, J. Lefèvre, P. Cruzalèbes, *Astron. Astrophys.* **314**, 122 (1996).
3. "Imaging binary stars by the cross-correlation technique", É. Aristidi, M. Carbillet, J.-F. Lyon, C. Aime, *Astron. Astrophys. Suppl. Ser.* **125**, 139 (1997).
4. "ICCD speckle observations of binary stars : measurements during 1994–1995", É. Aristidi, M. Carbillet, J.-L. Prieur, B. Lopez, Y. Bresson, L. Koechlin, *Astron. Astrophys. Suppl. Ser.* **126**, 555 (1997).
5. "Discovery of a new bright close double star" (*Erratum*), M. Carbillet, B. Lopez, É. Aristidi, Y. Bresson, C. Aime, G. Ricort, J.-L. Prieur, L. Koechlin, G. Helmer, J. Lefèvre, P. Cruzalèbes, *Astron. Astrophys.* **329**, 1172 (1998).
6. "Speckle imaging of binary stars : use of ratios of twofold probability density functions", M. Carbillet, C. Aime, É. Aristidi, G. Ricort, *Astron. Astrophys. Suppl. Ser.* **127**, 569 (1998).
7. "Speckle observations of double and multiple stars at Pic du Midi : measurements during 1995 and 1997 and new orbits", É. Aristidi, J.-L. Prieur, M. Scardia, L. Koechlin, R. Avila, M. Carbillet, B. Lopez, Y. Rabbia, P. Nisenson, D. Gezari, *Astron. Astrophys. Suppl. Ser.* **134**, 545 (1999).
8. "High angular resolution observations of late-type stars", J.-L. Prieur, É. Aristidi, B. Lopez, M. Scardia, F. Mignard, M. Carbillet, *Ap. J. Suppl.* **139**, 249–258 (2002).
9. "Restoration of interferometric images : I. The software package AIRY", S. Correia, M. Carbillet, P. Boccacci, M. Bertero, L. Fini, *Astron. Astrophys.* **387** (2), 733 (2002).
10. "Restoration of interferometric images : II. The case-study of the Large Binocular Telescope", M. Carbillet, S. Correia, P. Boccacci, M. Bertero, *Astron. Astrophys.* **387** (2), 743 (2002).
11. "Diamonds in HD 97048 : a closer look" (*Letter*), É. Habart, L. Testi, A. Natta, M. Carbillet, *Ap. J.* **614** (2), L129 (2004).
12. "Restoration of interferometric images : III. Efficient Richardson-Lucy methods for LINC-NIRVANA data reduction", B. Anconelli, M. Bertero, P. Boccacci, M. Carbillet, H. Lantéri, *Astron. Astrophys.* **430**, 731 (2005).
13. "Restoration of interferometric images : IV. An algorithm for super-resolution of binary systems", B. Anconelli, M. Bertero, P. Boccacci, M. Carbillet, *Astron. Astrophys.* **431**, 747 (2005).
14. "Modelling astronomical adaptive optics : I. The software package CAOS", M. Carbillet, C. Vérinaud, B. Femenía, A. Riccardi, L. Fini, *Mon. Not. R. Astron. Soc.* **356** (4), 1263 (2005).
15. "Adaptive optics for high-contrast imaging : pyramid sensor versus Shack-Hartmann sensor" (*Letter*), C. Vérinaud, M. Le Louarn, V. Korkiakoski, M. Carbillet, *Mon. Not. R. Astron. Soc.* **357** (1), L26 (2005).

16. "Reduction of boundary effects in multiple image deconvolution with an application to LBT LINC-NIRVANA", B. Anconelli, M. Bertero, P. Boccacci, M. Carbillet, H. Lantéri, *Astron. Astrophys.* **448** (3), 1217 (2006).
17. "Spatially resolved PAH emission in the inner disks of Herbig Ae/Be stars", É. Habart, A. Natta, L. Testi, M. Carbillet, *Astron. Astrophys.* **449** (3), 1067 (2006).
18. "Application of iterative blind deconvolution to the reconstruction of LBT LINC-NIRVANA images", G. Desiderà, B. Anconelli, M. Bertero, P. Boccacci, M. Carbillet, *Astron. Astrophys.* **452**, 727 (2006).
19. "Deconvolution of multiple images with high dynamic range and an application to LBT LINC-NIRVANA", B. Anconelli, M. Bertero, P. Boccacci, G. Desiderà, M. Carbillet, H. Lantéri, *Astron. Astrophys.* **460**, 349 (2006).
20. "Iterative methods for the reconstruction of astronomical images with high-dynamic range", B. Anconelli, M. Bertero, P. Boccacci, M. Carbillet, H. Lantéri, *J. Comp. Appl. Math.* **198**, 321 (2007).
21. "Detection of a moving source in speckle noise : application to exoplanet detection", I. Smith, A. Ferrari, M. Carbillet, *IEEE Trans. on Signal Processing* **57** (3), 904 (2009)
22. "Study of the atmospheric refraction in a single mode instrument - Application to AMBER/VLTI", S. Robbe-Dubois, S. Lagarde, Y. Bresson, R. G. Petrov, M. Carbillet, E. Lecoarer, F. Rantakyro, I. Tallon-Bosc, M. Vannier, P. Antonelli, G. Martinot-Lagarde, A. Roussel, D. Tasso, *Mon. Not. R. Astron. Soc.* **395** (2), 991 (2009).
23. "Strehl-constrained iterative blind deconvolution for post-adaptive-optics data", G. Desiderà & M. Carbillet, *Astron. Astrophys.* **507** (3), 1759 (2009).
24. "Imaging with LINC-NIRVANA (An introduction to deconvolution methods and their capability)", M. Bertero, P. Boccacci, G. Desiderà, A. La Camera, M. Carbillet, H. Lantéri, *IEEE Signal Processing Magazine* **27** (1) *(Special Section on Astronomy and Cosmology)*, 110 (2010).
25. "Photometric exoplanet characterization using angular and spectral differential imaging", A. Vigan, C. Moutou, M. Langlois, F. Allard, A. Boccaletti, M. Carbillet, D. Mouillet, I. Smith, *Mon. Not. R. Astron. Soc.* **407** (1), 71–82 (2010).
26. "Numerical modeling of atmospherically perturbed phase screens : new solutions for classical fast Fourier transform and Zernike methods", M. Carbillet & A. Riccardi, *App. Opt.* **49** (31) *(JOSA A/App. Opt. Joint Feature Issue on Adaptive Optics)*, G47–G52 (2010).
27. "Low-ligh-level CCDs for wave-front sensing : what actual gain ?", M. Carbillet & A. Riccardi, *App. Opt.* **49** (31) *(JOSA A/App. Opt. Joint Feature Issue on Adaptive Optics)*, G167–G173 (2010).
28. "Apodized Lyot coronagraph for SPHERE/VLT : I. Detailed numerical study", M. Carbillet, Ph. Bendjoya, L. Abe, G. Guerri, A. Boccaletti, J.-B. Daban, K. Dohlen, A. Ferrari, S. Robbe-Dubois, R. Douet, F. Vakili, *Exp. Astronomy* 30 (1), 39–58 (2011).
29. "Apodized Lyot coronagraph for SPHERE/VLT : II. Laboratory tests and performances", G. Guerri, J.-B. Daban, S. Robbe-Dubois, R. Douet, L. Abe, J. Baudrand, P. Riaud, M. Carbillet, A. Boccaletti, Ph. Bendjoya, C. Gouvret, F. Vakili, *Exp. Astronomy* 30 (1), 59–81 (2011).
30. "Imaging with LINC-NIRVANA, the Fizeau interferometer of the Large Binocular Telescope : state of the art and open problems", M. Bertero, P. Boccacci, G. Desiderà, A. La Camera, C. Olivieri, M. Carbillet, *Inverse Problems* 27, 113001 (2011).

— Autres revues
(1 article)

31. "SPHERE : a planet finder instrument for the VLT", J.-L. Beuzit, M. Feldt, K. Dohlen, D. Mouillet, P. Puget, J. Antichi, A. Baruffolo, P. Baudoz, A. Berton, A. Boccaletti, M. Carbillet, J. Charton, R. Claudi, M. Downing, P. Feautrier, E. Fedrigo, T. Fusco, R. Gratton, N. Hubin, M. Kasper, M. Langlois, C. Moutou, L. M. Mugnier, J. Pragt, P. Rabou, M. Saisse, H.-M. Schmid, E. Stadler, M. Turatto, S. Udry, R. Waters, F. Wildi, *ESO Messenger* **125**, 29 (2006).

— Communications à des conférences / Invité
(3 articles, 1 talk*, 4 résumés)*

32. "Restoration of interferometric images from the Large Binocular Telescope", M. Carbillet, S. Correia, M. Bertero, P. Boccacci, *abstract* paru dans les actes du Symposium "Imaging problems for the new generation telescopes", *VI Congresso della Società Italiana di Matematica Applicata e Industriale" (SIMAI 2002)*, Chia-Laguna, Sardègne, Italie (2002).
33. "Adaptive optics for ground-based large telescopes", C. Vérinaud, E. Diolaiti, M. Carbillet, C. Arcidiacono, R. Ragazzoni, *abstract* paru dans les actes du Symposium "Imaging problems for the new generation telescopes", *VI Congresso della Società Italiana di Matematica Applicata e Industriale" (SIMAI 2002)*, Chia-Laguna, Sardègne, Italie (2002).
34. "CAOS (Code for Adaptive Optics Systems) : a problem-solving environment in high-angular-resolution astronomy", M. Carbillet, *abstract* paru dans les actes de la Session "Scientific Computing Environment for Imaging in Science", *2004 International Conference on Computational Science and its Applications" (ICCSA 2004)*, Santa Maria degli Angeli, Assisi, Italie (2004).
35. "Numerical simulations in astronomical adaptive optics – the CAOS system", M. Carbillet, *abstract* paru dans les actes de *OCS 2005 - Optical Complex Systems*, Marseille, France (2005).
36. "Astronomical adaptive optics for high contrast imaging", M. Carbillet, in "Astronomy with High Contrast Imaging III : instrumentation and data processing", M. Carbillet, C. Aime, A. Ferrari, Eds., *EAS Publications Series* **22**, 121–138 (2006).
37. "Astronomical imaging... Atmospheric turbulence ? Adaptive optics !", M. Carbillet, in "New Concepts in Imaging : Optical and Statistical Models", D. Mary, C. Theys, and C. Aime, Eds., *EAS Publications Series* **59**, 59–76 (2013).
38. "Adaptive optics feedback control", J.-P. Folcher, M. Carbillet, A. Ferrari, A. Abelli, in "New Concepts in Imaging : Optical and Statistical Models", D. Mary, C. Theys, and C. Aime, Eds., *EAS Publications Series* **59**, 93–130 (2013).
39. "(Introduction to) The CAOS Problem-Solving Environment & The Software Package CAOS ⊕ Adaptive Optics Simulations...", L. Catala & M. Carbillet, Cours et exercices sur machine présentés à l'école d'été "Atmospheric Characterization and Adaptive Optics in Astronomy" (Sutherland, Afrique du Sud, décembre 2012), `http://amao.saao.ac.za/wp-content/uploads/2013/05/Introduction-to-CAOS.pdf` (2012).

— Communications à des conférences / Autres articles publiés
(86 articles)

40. "Probability imaging of binary stars from infrared speckle observations", M. Carbillet, É. Aristidi, G. Ricort, C. Aime, in "International Conference on Holography and Correlation Optics", O. V. Angelsky Ed., *SPIE Proc.* **2647**, 422–432 (1995).
41. "Speckle observations of late-type post-Hipparcos double stars", É. Aristidi, B. Lopez, M. Carbillet, P. Cruzalèbes, F. Mignard, Y. Bresson, G. Helmer, in "Science with the VLT interferometer", F. Paresce Ed., *ESO Astrophysics Symposia*, 351–352 (1997).
42. "High-resolution measurements of close binary stars and the probability imaging technique", M. Carbillet, C. Aime, É. Aristidi, G. Ricort, in "Science with the VLT interferometer", F. Paresce Ed., *ESO Astrophysics Symposia*, 361–362 (1997).
43. "Laser guide stars for 8-m class telescopes", F. Delplancke, M. Carbillet, N. Hubin, S. Esposito, F. Rigaut, E. Marchetti, A. Riccardi, É. Viard, R. Ragazzoni, M. Le Louarn, L. Fini, in "Adaptive Optical System Technologies", D. Bonaccini & R. K. Tyson Eds., *SPIE Proc.* **3353**, 371–382 (1998).
44. "From adaptive secondary mirrors to extra-thin extra-large adaptive primary mirrors", G. Brusa, A. Riccardi, M. Accardo, V. Biliotti, M. Carbillet, C. Del Vecchio, S. Esposito, B. Femenía, O. Feeney, L. Fini, S. Gennari, L. Miglietta, P. Salinari, P. Stefanini, in "Proceedings of the Backaskög workshop on extremely large telescopes", T. Andersen, A. Ardeberg & R. Gilmozzi, Eds., *ESO Conference & Workshop Proc.* **57**, 181–201 (1999).
45. "LA^{3}OS^2 : a software package for laser guide star adaptive optics systems", M. Carbillet, B. Femenía, F. Delplancke, S. Esposito, L. Fini, A. Riccardi, É. Viard, N. Hubin, F. Rigaut, in "Adaptive Optics Systems and Technology", R. K. Tyson & R. Q. Fugate Eds., *SPIE Proc.* **3762, 378–389** (1999).

46. "Preliminary results of simulations for the adaptive optics system of the Large Binocular Telescope", M. Carbillet, A. Riccardi, B. Femenía, L. Fini, S. Esposito, in "Telescopes, instruments and data processing for astronomy in the year 2000", *Mem. Soc. Astr. It./AstroTech Journal* **2 (2)** (1999).

47. "Large Binocular Telescope image restoration using simulated adaptively corrected point-spread functions", S. Correia, M. Carbillet, A. Richichi, M. Bertero, P. Boccacci, in "Interferometry in Optical Astronomy", P. J. Léna & A. Quirrenbach Eds., *SPIE Proc.* **4006**, 650–658 (2000).

48. "Considerations about the differential piston for adaptive optics interferometry", B. Femenía, M. Carbillet, S. Esposito, A. Riccardi, in "Interferometry in Optical Astronomy", P. J. Léna & A. Quirrenbach Eds., *SPIE Proc.* **4006**, 1116–1127 (2000).

49. "Adaptive optics simulations for imaging with the Large Binocular Telescope interferometer : a first application", M. Carbillet, S. Correia, B. Femenía, A. Riccardi, in "Adaptive Optical Systems Technology", P. L. Wizinowich Ed., *SPIE Proc.* **4007**, 155–166 (2000).

50. "A study for a multi-conjugate adaptive optics system for 8-m class telescopes", G. Brusa, A. Riccardi, S. Esposito, B. Femenía, M. Carbillet, in "Adaptive Optics Technology", T. D. Steiner, P. H. Merritt, Eds, *SPIE Proc.* **4034**, 190–200 (2000).

51. "Atmospheric OPD implications for adaptive IR and optical interferometry", B. Femenía, M. Carbillet, S. Esposito, A. Riccardi, in "School on space and ground based optical/infrared interferometry", *Proc. of the NOVA/LEIDEN/NEVE workshop*, 295–301 (2000).

52. "CAOS Simulation Package 3.0 – an IDL-based tool for adaptive optics systems design and simulations", M. Carbillet, L. Fini, B. Femenía, A. Riccardi, S. Esposito, É. Viard, F. Delplancke, N. Hubin, in "Astronomical Data Analysis Software And Systems X", F. R. Harnden, Jr., F. A. Primini, H. E. Payne, Eds., *ASP Conf. Series* **238**, 249–252 (2001).

53. "The CAOS Application Builder", L. Fini, M. Carbillet, A. Riccardi, in "Astronomical Data Analysis Software And Systems X", F. R. Harnden, Jr., F. A. Primini, and H. E. Payne, Eds., *ASP Conf. Series* **238**, 253–256 (2001).

54. "AIRY — Astronomical Image Restoration in interferometrY", S. Correia, M. Carbillet, L. Fini, P. Boccacci, M. Bertero, A. Vallenari, A. Richichi, M. Barbati, in "Astronomical Data Analysis Software And Systems X", F. R. Harnden, Jr., F. A. Primini, and H. E. Payne Eds., *ASP Conf. Series* **238**, 404–407 (2001).

55. "Numerical simulations of MCAO modal systems in open-loop and closed-loop operation", B. Femenía, M. Carbillet, S. Esposito, G. Brusa, in "Adaptive Optics Systems and Technology II", R. K. Tyson & D. Bonaccini Eds., *SPIE Proc.* **4494**, 132–143 (2001).

56. "Closed loop performance of a modal MCAO system using real star configurations : the young open cluster NGC 2362 as seen by MAD", M. Carbillet, B. Femenía, S. Esposito, G. Brusa, S. Correia, in "Beyond conventional adaptive optics", É. Vernet-Viard, R. Ragazzoni, S. Esposito, N. Hubin, Eds., *ESO Conference & Workshop Proc.* **58**, 259–266 (2003).

57. "Specifications and optical budget for the layer-oriented wavefront sensor for MAD", R. Ragazzoni, S. Esposito, É. Vernet-Viard, A. Baruffolo, M. Carbillet, E. Diolaiti, R. Falomo, J. Farinato, E. Fedrigo, E. Marchetti, M. Tordi, in "Beyond conventional adaptive optics", É. Vernet-Viard, R. Ragazzoni, S. Esposito, & N. Hubin Eds., *ESO Conference & Workshop Proc.* **58**, 421–426 (2003).

58. "Performance of the restoration of LBT interferometric images – the effect of angular coverage and partial adaptive optics correction", M. Carbillet, S. Correia, P. Boccacci, M. Bertero, in "Interferometry for Optical Astronomy II", W. A. Traub Ed., *SPIE Proc.* **4838**, 444–455 (2003).

59. "Performance of the first-light AO system of LBT by means of CAOS simulations", M. Carbillet, C. Vérinaud, S. Esposito, A. Riccardi, A. Puglisi, B. Femenía, L. Fini, in "Adaptive Optical Systems Technology", P. L. Wizinovich & D. Bonaccini Eds., *SPIE Proc.* **4839**, 131–139 (2003).

60. "The first-light AO system of LBT", S. Esposito, A. Tozzi, D. Feruzzi, M. Carbillet, A. Riccardi, L. Fini, C. Vérinaud, M. Accardo, G. Brusa, D. Gallieni, R. Biasi, C. Baffa, V. Biliotti, I. Foppiani, A. Puglisi, R. Ragazzoni, P. Ranfagni, P. Stefanini, P. Salinari, W. Seifert, J. Storm, in "Adaptive Optical Systems Technology", P. L. Wizinovich & D. Bonaccini Eds., *SPIE Proc.* **4839**, 164–173 (2003).

61. "Is there any need of any modulation in the pyramid wavefront sensor ?", J. Buechler Costa, R. Ragazzoni, A. Ghedina, M. Carbillet, C. Vérinaud, M. Feldt, S. Esposito, E. Puga, J. Farinato, in "Adaptive Optical Systems Technology", P. L. Wizinovich & D. Bonaccini Eds., *SPIE Proc.* **4839**, 288–298 (2003).

62. "Layer-Oriented wavefront sensor for MAD : status and progress", É. Vernet-Viard, R. Ragazzoni, C. Arcidiacono, A. Baruffolo, E. Diolaiti, J. Farinato, E. Fedrigo, E. Marchetti, R. Falomo, S. Esposito, M. Carbillet, C. Vérinaud, in "Adaptive Optical Systems Technology", P. L. Wizinovich & D. Bonaccini Eds., *SPIE Proc.* **4839**, 344–353 (2003).
63. "Layer-Oriented Multi-Conjugate Adaptive Optics systems : performance analysis by numerical simulations", C. Vérinaud, C. Arcidiacono, M. Carbillet, E. Diolaiti, R. Ragazzoni, É. Vernet-Viard, in "Adaptive Optical Systems Technology", P. L. Wizinovich & D. Bonaccini Eds., *SPIE Proc.* **4839**, 524–535 (2003).
64. "Comparison of different 3D wavefront sensing and reconstruction techniques for MCAO", D. Bello, C. Vérinaud, J.-M. Conan, M. Carbillet, in "Adaptive Optical Systems Technology", P. L. Wizinovich & D. Bonaccini Eds., *SPIE Proc.* **4839**, 554–565 (2003).
65. "Adaptive optics simulations with CAOS : application to exoplanets detection", C. Vérinaud & M. Carbillet, in "Astronomy with High Contrast Imaging : From Planetary Systems to Active Galactic Nuclei", C. Aime & R. Soummer Eds., *EAS Publications Series* **8**, 209–219 (2003).
66. "Efficient distribution of computational load on a beowoulf-like cluster", L. Fini & M. Carbillet, in "Astronomical Data Analysis Software And Systems XII", H. E. Payne, R. I. Jedrzejewski, R. N. Hook, Eds., *ASP Conf. Series* **295**, 347–351 (2003).
67. "Adaptive optics and site requirements for the search of earth-like planets with ELTs", O. Lardière, P. Salinari, L. Jolissaint, M. Carbillet, A. Riccardi, S. Esposito, in "Emerging Optoelectronic Applications" (2nd Bäckaskog Workshop on ELTs), Jabbour, Ghassan, Rantala, Eds., *SPIE Proc.* **5382**, 550–559 (2004).
68. "Adaptive optics for very high-contrast imaging : numerical simulations", M. Carbillet, in "Astronomy with High Contrast Imaging II : instrumentation for coronagraphy and nulling interferometry", C. Aime & R. Soummer Eds., *EAS Publications Series* **12**, 137–156 (2004).
69. "CAOS – a numerical simulation tool for astronomical adaptive optics (and beyond)", M. Carbillet, C. Vérinaud, M. Guarracino, L. Fini, O. Lardière, B. Le Roux, A. T. Puglisi, B. Femenía, A. Riccardi, B. Anconelli, M. Bertero, P. Boccacci, in "Advancements in Adaptive Optics", D. Bonaccini, B. Ellerbroek, R. Ragazzoni, Eds., *SPIE Proc.* **5490** (2), 550–559 (2004).
70. "Numerical simulations studies for the first-light adaptive optics system of the Large Binocular Telescope", M. Carbillet, A. Riccardi, S. Esposito, in "Advancements in Adaptive Optics", D. Bonaccini, B. Ellerbroek, R. Ragazzoni, Eds., *SPIE Proc.* **5490** (2), 721–732 (2004).
71. "High-contrast imaging with Extremely Large Telescopes : effects of cophasing and adaptive optics residual errors on the point-spread function contrast", O. Lardière, M. Carbillet, A. Riccardi, P. Salinari, in "Advancements in Adaptive Optics", D. Bonaccini, B. Ellerbroek, R. Ragazzoni, Eds., *SPIE Proc.* **5490** (2), 516–526 (2004).
72. "VIDA, a hypertelescope on the VLTI : last instrument design studies and performance analysis", O. Lardière, D. Mourard, F. Patru, M. Carbillet, in "New frontiers in Stellar Interferometry", W. A. Traub Ed., *SPIE Proc.* **5491** (1), 415–423 (2004).
73. "Deconvolution methods for LINC/NIRVANA data reduction", B. Anconelli, M. Carbillet, M. Bertero, P. Boccacci, in "New frontiers in Stellar Interferometry", W. A. Traub Ed., *SPIE Proc.* **5491** (2), 932–943 (2004).
74. "The Large Binocular Telescope : challenging problems in image restoration", M. Bertero, B. Anconelli, P. Boccacci, M. Carbillet, H. Lantéri, C. Theys, in "Astronomical Data Analysis III Conference", `http://ewic.bcs.org/conference`s (2004).
75. "The Dome C : a unique site for high-contrast imaging and extrasolar planet searching with a large telescopes", O. Lardière, M. Carbillet, A. Riccardi, P. Salinari, C. Aime, in "Dome C Astronomy and Astrophysics Meeting", M. Giard, F. Casoli, F. Paletou, Eds., *EAS Publications Series* **14**, 291–296 (2005).
76. "LINC-NIRVANA : MCAO toward extremely large telescopes", W. Gaessler, C. Arcidiacono, S. Egner, T. M. Herbst, D. Andersen, H. Baumeister, P. Bizenberger, H. Boehnhardt, F. Briegel, M. Kuester, W. Laun, L. Mohr, B. Grimm, H.-W. Rix, R.-R. Rohloff, R. Soci, C. Stroz, W. Xu, R. Ragazzoni, P. Salinari, E. Diolaiti, J. Farinato, M. Carbillet, L. Schreiber, A. Eckart, T. Bertram, C. Strubmeier, Y. Wang, L. Zealouk, G. Weigelt, U. Beckmann, J. Behrend, T. Driebe, M. Heininger, K.-H. Hofmann, E. Nussbaum, D. Shertel, E. Masciadri, in "MCAO for very large telescopes/OAMC pour les très grands télescopes", J.-M. Conan & G. Rousset Eds., *C. R. Physique* **6**, 1129–1138 (2005).
77. "Optimal control law in state-space formalism for extreme adaptive optics", B. Le Roux & M. Carbillet, in *Adaptive Optics : Analysis and Methods 2005*, Technical Digest (Opt. Soc. Am.), paper AWC3, `http://www.opticsinfobase.org/DirectPDFAccess/35D8EC1C-BDB9-137E-C52F17A50F074616_9` (2005).

78. "Iterative methods for the reconstruction of LINC-NIRVANA images", B. Anconelli, M. Bertero, P. Boccacci, M. Carbillet, H. Lantéri, in *Signal Recovery and Synthesis 2005*, Technical Digest (Opt. Soc. Am.), paper SMC1, `http://www.opticsinfobase.org/DirectPDFAccess/35E44855-BDB9-137E-C38FF56D977DB072_99482.pdf?da=1&id=99482&seq=0&CFID=15889613&CFTOKEN=28616749` (2005).
79. "High dynamic range imaging experiments at LUAN : progress and future prospects", G. Guerri, J.-B. Daban, L. Abe, P. Bendjoya, F. Vakili, J. Sarry, S. Auroux, M. Carbillet, in "SF2A - Scientific Highlights 2005", F. Casoli, T. Contini, J.-M. Hameury, L. Pagani, Eds., *EDP Sciences - Conference Series*, 277–278 (2006).
80. "Small carbon grains in circumstellar disks", É. Habart, A. Natta, L. Testi, M. Carbillet, in "SF2A - Scientific Highlights 2005", F. Casoli, T. Contini, J.-M. Hameury, L. Pagani, Eds., *EDP Sciences - Conference Series*, 421–424 (2006).
81. "CAOS, a "problem solving environment" for adaptive optics and adaptive-optics-aided astronomy", M. Carbillet, C. Vérinaud, L. Fini, A. Riccardi, B. Le Roux, B. Femenía, B. Anconelli, G. Desiderà, P. Boccacci, M. Bertero, S. Correia, O. Lardière, in "SF2A - Scientific Highlights 2005", F. Casoli, T. Contini, J.-M. Hameury, L. Pagani, Eds., *EDP Sciences - Conference Series*, 275–276 (2006).
82. "Data processing for exoplanet detection using direct imaging", A. Ferrari, M. Carbillet, C. Aime, E. Serradel, R. Soummer, in "Direct Imaging of Exoplanets : Science & Techniques", C. Aime & F. Vakili Eds., *Proc. of the IAU Colloquium 200, Cambridge University Press*, 565–570 (2006).
83. "Speckle statistics in direct and coronagraphic imaging", R. Soummer, C. Aime, A. Ferrari, A. Sivaramakrishnan, L. Jolissaint, J. Lloyd, B. Oppenheimer, R. Makidon, M. Carbillet, in "Direct Imaging of Exoplanets : Science & Techniques", C. Aime & F. Vakili Eds., *Proc. of the IAU Colloquium 200, Cambridge University Press*, 581–586 (2006).
84. "Advantage of a predictive control law for extreme adaptive optics imaging", B. Le Roux & M. Carbillet, in "Direct Imaging of Exoplanets : Science & Techniques", C. Aime & F. Vakili Eds., *Proc. of the IAU Colloquium 200, Cambridge University Press*, 597–602 (2006).
85. "SPHERE : a planet finder instrument for the VLT", K. Dohlen, J.-L. Beuzit, M. Feldt, D. Mouillet, P. Puget, J. Antichi, A. Baruffolo, P. Baudoz, A. Berton, A. Boccaletti, M. Carbillet, J. Charton, R. Claudi, M. Downing, C. Fabron, P. Feautrier, E. Fedrigo, T. Fusco, J.-L. Gach, R. Gratton, N. Hubin, M. Kasper, M. Langlois, A. Longmore, C. Moutou, C. Petit, J. Pragt, P. Rabou, G. Rousset, M. Saisse, H.-M. Schmid, E. Stadler, D. Stamm, M. Turatto, R. Waters, F. Wildi, in "Ground-based and Airborne Instrumentation for Astronomy", I. S. McLean & M. Iye Eds., *SPIE Proc.* **6269**, 62690Q (2006).
86. "High-resolution image reconstruction : the case of the Large Binocular Telescope (LBT)", M. Bertero, B. Anconelli, P. Boccacci, G. Desiderà, M. Carbillet, H. Lantéri, in "Astronomy with High Contrast Imaging III : Instrumentation and data processing", M. Carbillet, C. Aime, A. Ferrari, Eds., *EAS Publications Series* **22**, 35–68 (2006).
87. "The SPHERE exoplanet imager : Status report at PDR", F. Wildi, J.-L. Beuzit, M. Feldt, D. Mouillet, K. Dohlen, P. Puget, A. Baruffolo, J. Charton, J. Antichi, P. Baudoz, A. Boccaletti, M. Carbillet, R. Claudi, Ph. Feautrier, E. Fedrigo, Th. Fusco, R. Gratton, N. Hubin, M. Kasper, M. Langlois, R. Lenzen, C. Moutou, A. Pavlov, C. Petit, J. Pragt, P. Rabou, R. Roelfsema, M. Saisse, H.-M. Schmid, E. Stadler, M. Turatto, S. Udry, R. Waters, Th. Henning , A.-M. Lagrange , F. Vakili, *SPIE Proc.* **6691**, 66910L (2007).
88. "An exoplanet detection algorithm for field-rotated coronagraphic images, and preliminary results for SPHERE", I. Smith, A. Ferrari, M. Carbillet, A. Boccaletti, T. Fusco, K. Dohlen, D. Mouillet, M. Langlois, in *SF2A 2007 - Semaine de l'Astrophysique Française*, J. Bouvier, A. Chalabaev, C. Charbonnel, Eds., 65 (2007).
89. "SPHERE : a planet finder instrument for the VLT", J.-L. Beuzit, M. Feldt, K. Dohlen, D. Mouillet, P. Puget, J. Antichi, P. Baudoz, A. Boccaletti, M. Carbillet, J. Charton, R. Claudi, T. Fusco, R. Gratton, T. Henning, N. Hubin, F. Joos, M. Kasper, M. Langlois, C. Moutou, J. Pragt, P. Rabou, M. Saisse, H.-M. Schmid, M. Turatto, S. Udry, F. Vakili, R. Waters, F. Wildi, in *In the spirit of Bernard Lyot : the direct detection of planets and circumstellar disks in the 21st century*, P. Kalas Ed. (2007).
90. "Ground-layer adaptive optics for Dome C : optimisation and performance", B. Le Roux, M. Langlois, M. Carbillet, T. Fusco, M. Ferrari, D. Burgarella, in *Adaptive Optics : Analysis and Methods 2007*, Technical Digest (Opt. Soc. Am.), paper AWA5, `http://www.opticsinfobase.org/DirectPDFAccess/35DC6324-BDB9-137E-C380027A58A2A9F2_139373.pdf?da=1&id=139373&seq=0&CFID=15889613&CFTOKEN=28616749`, (2007).
91. "Detection and performance analysis for a moving point source in speckle noise, application to exoplanet detection by direct imaging", I. Smith, A. Ferrari, M. Carbillet, in *Proceedings of the IEEE International Conference on Acoustics, Speech and Signal Processing (ICASSP'08)* (2008).

92. "Ground-layer AO for Dome C : the WHITE instrument", B. Le Roux, M. Carbillet, M. Langlois, H. Trinquet, D. Burgarella, M. Ferrari, F.-X. Schmider, in *Adaptive Optics Systems*, N. Hubin, C. E. Max, P. L. Wizinowich, Eds., *SPIE Proc.* **7015**, 70154G-70154G-8 (2008).
93. "AIRY-LN : an ad-hoc numerical tool for deconvolution of images from the LBT instrument LINC-NIRVANA", G. Desiderà, A. La Camera, P. Boccacci, M. Bertero, M. Carbillet, in *Optical and Infrared Interferometry*, M. Schoeller, W. C. Danchi, & F. Delplancke, Eds., *SPIE Proc.* **7013**, 701340-701340-12 (2008).
94. "Apodized Lyot Coronagraph for VLT-SPHERE : Laboratory tests and performances of a first prototype in the visible", G. Guerri, S. Robbe-Dubois, J.-B. Daban, L. Abe, R. Douet, Ph. Bendjoya, F. Vakili, M. Carbillet, J.-L. Beuzit, P. Puget, K. Dohlen, in *Ground-based and Airborne Instrumentation for Astronomy II*, I. S. McLean, M. M. Casali, Eds., *SPIE Proc.* **7014**, 70143J-70143J-12 (2008).
95. "End-to-End Simulation of AO-assisted coronagraphic differential imaging : estimation of performance for SPHERE", A. Boccaletti, M. Carbillet, Th. Fusco, D. Mouillet, M. Langlois, C. Moutou, K. Dohlen, in *Adaptive Optics Systems*, N. Hubin, C. E. Max, P. L. Wizinowich, Eds., *SPIE Proc.* **7015**, 70156E-70156E-11 (2008).
96. "Simulation of moving exoplanets detection using the VLT instrument SPHERE/IRDIS", I. Smith, M. Carbillet, A. Ferrari, D Mouillet, A. Boccaletti, K. Dohlen, in *Adaptive Optics Systems*, N. Hubin, C. E. Max, P. L. Wizinowich, Eds., *SPIE Proc.* **7015**, 70156F-70156F-12 (2008).
97. "The Software Package SPHERE : a CAOS-based numerical tool for end-to-end simulations of SPHERE/VLT", M. Carbillet, A. Boccaletti, Ch. Thalmann, Th. Fusco, A. Vigan, I. Smith, D. Mouillet, K. Dohlen, Ph. Bendjoya, A. Ferrari, in *Adaptive Optics Systems*, N. Hubin, C. E. Max, P. L. Wizinowich, Eds., *SPIE Proc.* **7015**, 70156Z-70156Z-12 (2008).
98. "SPHERE ZIMPOL : Design and performance simulation", Ch. Thalmann, H.-M. Schmid, A. Boccaletti, D. Mouillet, K. Dohlen, R. Roelfsema, M. Carbillet, D. Gisler, J.-L. Beuzit, M. Feldt, R. Gratton, F. Joos, Ch. U. Keller, J. Kragt, J. H. Pragt, P. Puget, F. Rigal, F. Snik, R. Waters, F. Wildi, in *Ground-based and Airborne Instrumentation for Astronomy II*, I. S. McLean, M. M. Casali, Eds., *SPIE Proc.* **7014**, 70143F-70143F-12 (2008).
99. "The infrared dual imaging and spectrograph (IRDIS) for SPHERE : design and performance", K. Dohlen, M. Langlois, M. Saisse, L. Hill, A. Origne, M. Jacquet, Ch. Fabron, J.-C. Blanc, M. Llored, M. Carle, C. Moutou, A. Vigan, A. Boccaletti, M. Carbillet, D. Mouillet, J.-L. Beuzit, in *Ground-based and Airborne Instrumentation for Astronomy II*, I. S. McLean, M. M. Casali, Eds., *SPIE Proc.* **7014**, 70143L-70143L-10 (2008).
100. "SPHERE : a planet finder instrument for the VLT", J.-L. Beuzit, M. Feldt, K. Dohlen, D. Mouillet, P. Puget, F. Wildi, L. Abe, J. Antichi, A. Baruffolo, P. Baudoz, A. Boccaletti, M. Carbillet, J. Charton, R. Claudi, M. Downing, Ch. Fabron, Ph. Feautrier, E. Fedrigo, Th. Fusco, J.-L. Gach, R. Gratton, Th. Henning, N. Hubin, F. Joos, M. Kasper, M. Langlois, R. Lenzen, C. Moutou, A. Pavlov, C. Petit, J. Pragt, P. Rabou, F. Rigal, R. Roelfsema, G. Rousset, M. Saisse, H.-M. Schmid, E. Stadler, Ch. Thalmann, M. Turatto, S. Udry, F. Vakili, R. Waters, in *Ground-based and Airborne Instrumentation for Astronomy II*, I. S. McLean, M. M. Casali, Eds., *SPIE Proc.* **7014**, 701418–701418-12 (2008).
101. "Méthode de type maximum de vraisemblance pour la détection d'exoplanètes par imagerie différentielle spectrale et angulaire", A. Cornia, L. M. Mugnier, J.-F. Sauvage, N. Védrenne, M. Carbillet, A. Boccaletti, G. Rousset, Th. Fusco, (`http://documents.irevues.inist.fr/handle/2042/29158`), *22ème Colloque sur le Traitement du Signal et des Images*, GRETSI'09 (2009).
102. "Adaptive optics (AO) and ground-layer AO for Dome C : numerical simulation results", M. Carbillet, A.-L. Maire, B. Le Roux, É. Aristidi, Ch. Giordano, O. Pasqueron de Fommervault, J. Gautier, H. Trinquet, 3rd ARENA Conference on *"An astronomical Observatory at CONCORDIA (Dome C, Antarctica)"*, L. Spinoglio & N. Epchtein Eds., EAS Publications Series **40**, 157 (2010).
103. "Direct detection of giant extrasolar planets with SPHERE on the VLT", J.-L. Beuzit, A. Boccaletti, M. Feldt, K. Dohlen, D. Mouillet, P. Puget, F. Wildi, L. Abe, J. Antichi, A. Baruffolo, P. Baudoz, M. Carbillet, J. Charton, R. Claudi, S. Desiderà, M. Downing, Ch. Fabron, Ph. Feautrier, E. Fedrigo, Th. Fusco, J.-L. Gach, E. Giro, R. Gratton, Th. Henning, N. Hubin, F. Joos, M. Kasper, A.-M. Lagrange, M. Langlois, R. Lenzen, C. Moutou, A. Pavlov, C. Petit, J. Pragt, P. Rabou, F. Rigal, S. Rochat, R. Roelfsema, G. Rousset, M. Saisse, H.-M. Schmid, E. Stadler, Ch. Thalmann, M. Turatto, S. Udry, F. Vakili, A. Vigan, R. Waters, in *Pathways towards habitable planets*, V. Coudé du Foresto, D. M. Gelino, I. Ribas, Eds., ASP Conf. Series **430**, 231 (2010).
104. "Optimal method for exoplanet detection by spectral and angular differential imaging", A. Cornia, L. M. Mugnier, M. Carbillet, J.-F. Sauvage, A. Boccaletti, N. Védrenne, D. Mouillet, G. Rousset, Th. Fusco, *1st AO4ELT (Adaptive Optics for Extremely Large Telescopes) conf.*, Y. Clénet, J.-M. Conan, Th. Fusco, G. Rousset, Eds., EDP Sciences (`ao4elt.edpsciences.org`), 03005 (2010).

105. "The Software Package PAOLAC : an embedment of the analytical code PAOLA within the CAOS problem-solving environment", M. Carbillet, L. Jolissaint, A.-L. Maire, *1st AO4ELT (Adaptive Optics for Extremely Large Telescopes) conf.*, Y. Clénet, J. -M. Conan, Th. Fusco, G. Rousset, Eds., EDP Sciences (`ao4elt.edpsciences.org`) 03006 (2010).

106. "The CAOS problem-solving environment : recent developments", M. Carbillet, G. Desiderà, E. Augier, A. La Camera, A. Riccardi, A. Boccaletti, L. Jolissaint, D. Ab Kadir, in *Adaptive Optics Systems II*, B. L. Ellerbroek, M. Hart, N. Hubin, P. L. Wizinowich, Eds., *SPIE Proc.* **7736**, 773644–773644-8 (2010).

107. "Classical adaptive optics : disturbance rejection control", J.-P. Folcher, A. Abelli, A. Ferrari, M. Carbillet, in *Adaptive Optics Systems II*, B. L. Ellerbroek, M. Hart, N. Hubin, P. L. Wizinowich, Eds., *SPIE Proc.* **7736**, 77364F–77364F-12 (2010).

108. "Optimal method for exoplanet detection by spectral and angular differential imaging", A. Cornia, L. M. Mugnier, D. Mouillet, A. Vigan, A. Eggenberger, G. Rousset, A. Boccaletti, M. Carbillet, K. Dohlen, Th. Fusco, J. Carson, G. Montagnier, in *Adaptive Optics Systems II*, B. L. Ellerbroek, M. Hart, N. Hubin, P. L. Wizinowich, Eds., *SPIE Proc.* **7736**, 77361E–77361E-12 (2010).

109. "Comparison of Methods for Detection and Characterization of Exoplanets wih SPHERE/IRDIS", A. Vigan, C. Moutou, M. Langlois, D. Mouillet, K. Dohlen, A. Boccaletti, M. Carbillet, I. Smith, A. Ferrari, L. M. Mugnier, Ch. Thalmann, in *Ground-based and Airborne Instrumentation for Astronomy III*, I. S. McLean, S. K. Ramsay, H. Takami, Eds., *SPIE Proc.* **7735**, 77352X–77352X-12 (2010).

110. "FOROS : Fresnel optical propagation code for SPHERE", N. Yaitskova, D. Kjetil, P. Rabou, A. Boccaletti, M. Carbillet, J.-L. Beuzit, M. Kasper, N. Hubin, in *Ground-based and Airborne Instrumentation for Astronomy III*, I. S. McLean, S. K. Ramsay, H. Takami, Eds., *SPIE Proc.* **7735**, 77352T–77352T-13 (2010).

111. "The CAOS problem-solving environment : last news", M. Carbillet, G. Desiderà, E. Augier, A. La Camera, A. Riccardi, A. Boccaletti, L. Jolissaint, D. Ab Kadir, in *SF2A-2010 : Proceedings of the Annual meeting of the French Society of Astronomy and Astrophysics*, S. Boissier, M. Heydari-Malayeri, R. Samadi, and D. Valls-Gabaud, Eds., 61 (`http://sf2a.cesr.fr/2010/2010sf2a.conf..0061C.pdf`) (2010).

112. "Some results on disturbance rejection control for an adaptive optics system", J.-P. Folcher, A. Abelli, A. Ferrari, M. Carbillet, in *SF2A-2010 : Proceedings of the Annual meeting of the French Society of Astronomy and Astrophysics*, S. Boissier, M. Heydari-Malayeri, R. Samadi, and D. Valls-Gabaud, Eds., 71 (`http://sf2a.cesr.fr/2010/2010sf2a.conf..0071F.pdf`) (2010).

113. "Exoplanet characterization using angular and spectral differential imaging", A. Vigan, C. Moutou, M. Langlois, F. Allard, A. Boccaletti, M. Carbillet, D. Mouillet, I. Smith, in *SF2A-2010 : Proceedings of the Annual meeting of the French Society of Astronomy and Astrophysics*, S. Boissier, M. Heydari-Malayeri, R. Samadi, and D. Valls-Gabaud, Eds., 93 (`http://sf2a.cesr.fr/2010/2010sf2a.conf..0093V.pdf`) (2010).

114. "Numerical atmospheric turbulence models and LQG control for adaptive optics system ", J.-P. Folcher & M. Carbillet, in *Optical Complex Systems : OCS11*, G. Berginc, Ed., *SPIE Proc.* **8172**, 81721C-81721C-8 (2011).

115. "Analytical vs. end-to-end numerical modeling of adaptive optics systems : comparison between the `PAOLA` code and the Software Package `CAOS`", M. Carbillet & L. Jolissaint, *2nd AO4ELT (Adaptive Optics for Extremely Large Telescopes) conf.*, J.-P. Véran, Th. Fusco, Y. Clénet, Eds., `http://ao4elt2.lesia.obspm.fr/sites/ao4elt2/IM` (2012).

116. "LQG control for adaptive optics systems using numerical atmospheric turbulence models", J.-P. Folcher & M. Carbillet, *2nd AO4ELT (Adaptive Optics for Extremely Large Telescopes) conf.*, J.-P. Véran, Th. Fusco, Y. Clénet, Eds., `http://ao4elt2.lesia.obspm.fr/sites/ao4elt2/IMG/pdf/060folcher.pdf` (2012).

117. "Numerical modeling and simulation study for the M4 adaptive mirror of the E-ELT", M. Carbillet, A. Riccardi, M. Xompero, *Adaptive Optics Systems III, SPIE Astronomical Telescopes and Instrumentation 2012*, B. L. Ellerbroek, E. Marchetti, J.-P. Véran, Eds., SPIE Proc. 8447, 844762–844762-7 (2012).

118. "AIRY : A complete tool for the simulation and the reconstruction of Fizeau interferometric images", A. La Camera, M. Carbillet, Ch. Olivieri, P. Boccacci, M. Bertero, *Optical and Infrared Interferometry III, SPIE Astronomical Telescopes and Instrumentation 2012*, F. Delplancke, J. K. Rajagopal, F. Malbet, Eds., SPIE Proc. 8445, 84453E–84453E-14 (2012).

119. "Performance of LQG-based control for adaptive optics : a numerical analysis", J.-P. Folcher, M. Carbillet, A. Abelli, A. Ferrari, *Adaptive Optics Systems III, SPIE Astronomical Telescopes and Instrumentation 2012*, B. L. Ellerbroek, E. Marchetti, J.-P. Véran, Eds., SPIE Proc. 8447, 84472Z–84472Z-8 (2012).

120. "Dimensioning and performances of an AO system for the SALT", L. Catala, M. Carbillet, L. Jolissaint, T. Pickering, S. Crawford, *Adaptive Optics Systems III, SPIE Astronomical Telescopes and Instrumentation 2012*, B. L. Ellerbroek, E. Marchetti, J.-P. Véran, Eds., SPIE Proc. 8447, 84473W–84473W-10 (2012).
121. "A European vision for a "Polar Large Telescope" project, and beyond", L. Abe, N. Epchtein, W. Ansorge, S. Argentini, M. C. B. Ashley, I. Bryson, M. G. Burton, M. Carbillet, G. Dalton, C. David, I. Esau, C. Genthon, T. Guillot, M. Langlois, J. S. Lawrence, T. Le Bertre, R. Lemrani, B. Le Roux, G. Marchiori, D. Mékarnia, J. Montnacher, G. Moretto, P. Prugniel, J.-P. Rivet, E. Ruch, J. W V. Storey, C. Tao, A. Tilquin, I. Vauglin, *IAUS 288 Ñ Astrophysics from Antarctica*, *XXVIII IAU General Assembly*, M. Burton, X. Cui, N. Tothill, Eds., Proc. of the IAU Symposium Series, to appear (2013).
122. "The SPHERE view of Betelgeuse", O. Chesneau, H.-M. Schmidt, M. Carbillet, A. Chiavassa, L. Abe, D. Mouillet, in *Betelgeuse Workshop 2012 – The Physics of Red Supergiants : Recent Advances and Open Questions*, P. Kervella , T. Le Bertre, G. Perrin, Eds., *EAS Publication Series* **60**, 261 (2013).
123. "Deconvolution-based super-resolution for post-adaptive optics data", M. Carbillet, A. La Camera, O. Chesneau, F. Millour, J. Girard, M. Prato, presented at *3rd AO4ELT (Adaptive Optics for Extremely Large Telescopes) conf.*, Florence (Italy), 26th–31st May 2013.
124. "DAM, a new high frequency optical filter for high contrast imaging", F. Patru, J. Antichi, M. Carbillet, D. Mawet, J. Girard, presented at *3rd AO4ELT (Adaptive Optics for Extremely Large Telescopes) conf.*, Florence (Italy), 26th–31st May 2013.
125. "ANGISS – A New Generation of Infrared Sky Survey for the E-ELT era", I. Vauglin, M. Langlois, G. Moretto, N. Epchtein, É. Aristidi, M. Carbillet, L. Abe, in *Proceedings of the annual meeting of the French Society of Astronomy & Astrophysics – SF2A 2013*, L. Cambrésy, F. Martins, E. Nuss, A. Palacios, Eds., `http://www.sf2a.eu`, `ProceedingsSF2A2013`, 37 (2013).

— Communications à des conférences / Autres résumés, *posters* ou *talks* publiés

(4 résumés, 7 posters*, 3* talks*)*

126. "Techniques probabilistes appliquées à l'imagerie de binaires en infrarouge", M. Carbillet, *abstract* paru dans les actes "14èmes journées scientifiques de la SFSA", Besançon, France (1994).
127. "Techniques d'imagerie probabiliste appliquées aux observations en Haute Résolution Angulaire d'étoiles doubles en infra-rouge", M. Carbillet, *abstract* paru dans les actes "Physique en Herbe 1994", Montpellier, France (1994).
128. "AIRY : a software package for the deconvolution of interferometric image", B. Anconelli, M. Bertero, P. Boccacci, M. Carbillet, S. Correia, *abstract* paru dans les actes du *VI Congresso della Società Italiana di Matematica Applicata e Industriale" (SIMAI 2004)*, Isola di San Servolo, Venise, Italie (2004).
129. "SPHERE/ZIMPOL : Simulating the direct detection of exoplanets by polarimetry", C. Thalmann, A. Boccaletti, D. Mouillet, K. Dohlen, M. Carbillet, H. M. Schmid, R. Roelfsema, J.-L. Beuzit, *abstract* paru dans les actes de *Extreme Solar Systems*, Santorini, Greece (2007).
130. "Development of coronagraphs for optics for exoplanet detection with SPHERE", A. Boccaletti, J. Baudrand, P. Riaud, P. Baudoz, G. Rousset, J.-B.. Daban, M. Carbillet, R. Douet, G. Guerri, S. Robbe-Dubois, Ph. Bendjoya, *talk* paru dans les actes de *In the spirit of Bernard Lyot : the direct detection of planets and circumstellar disks in the 21st century*, P. Kalas Ed., `http://www.lyot2007.org/Presentations/Boccaletti_Anthony_poster.pdf` (2007).
131. "SPHERE : a planet finder instrument for the VLT", J.-L. Beuzit, M. Feldt, K. Dohlen, D. Mouillet, P. Puget, J. Antichi, P. Baudoz, A. Boccaletti, M. Carbillet, J. Charton, R. Claudi, T. Fusco, R. Gratton, T. Henning, N. Hubin, F. Joos, M. Kasper, M. Langlois, C. Moutou, J. Pragt, P. Rabou, M. Saisse, H.-M. Schmid, M. Turatto, S. Udry, F. Vakili, R. Waters, F. Wildi, *talk* paru dans les actes de *In the spirit of Bernard Lyot : the direct detection of planets and circumstellar disks in the 21st century*, P. Kalas Ed., `http://www.lyot2007.org/Presentations/Beuzit_Jean-Luc.pdf` (2007).
132. "Characterizing extra-solar planets with long-slit spectroscopy", A. Vigan, M. Langlois, C. Moutou, K. Dohlen, A. Boccaletti, M. Carbillet, *poster* paru dans les actes de *In the spirit of Bernard Lyot : the direct detection of planets and circumstellar disks in the 21st century*, P. Kalas Ed., `http://www.lyot2007.org/Presentations/Vigan_Arthur_poster.pdf` (2007).

133. "Apodized Lyot coronagraph of SPHERE/VLT : numerical study and laboratory performance", M. Carbillet, S. Robbe-Dubois, G. Guerri, Ph. Bendjoya, R. Douet, J.-B. Daban, L. Abe, C. Gouvret, A. Boccaletti, K. Dohlen, J. Baudrand, A. Ferrari, F. Vakili, *poster* paru dans les actes de *In the spirit of Lyot 2010*, A. Boccaletti Ed., `http://lyot2010.lesia.obspm.fr/sites/lyot2010/IMG/pdf/Lyot2010proc_s7_poster_CarbilletM.pdf` (2010).
134. "FOROS : Fresnel optical propagation code for SPHERE", N. Yaitskova, K. Dohlen, P. Rabou, A. Boccaletti, M. Carbillet, J.-L. Beuzit, M. Kasper, N. Hubin, *poster* paru dans les actes de *In the spirit of Lyot 2010*, A. Boccaletti Ed., `http://lyot2010.lesia.obspm.fr/sites/lyot2010/IMG/pdf/Lyot2010proc_s7_poster_YaitskovaN.pdf` (2010).
135. "Parallelization of exoplanets detection algorithms based on field rotation ; example of the MOODS algorithm for SPHERE", D. Mattei, I. Smith, A. Ferrari, M. Carbillet, *poster* paru dans les actes de *In the spirit of Lyot 2010*, A. Boccaletti Ed., `http://lyot2010.lesia.obspm.fr/sites/lyot2010/IMG/pdf/Lyot2010proc_s7_poster_MatteiD.pdf` (2010).
136. "DAM (Densified Aperture Masking) : A preliminary design of a high contrast imager on VLT-NACO", F. Patru, J. Girard, S. Lacour, A. Shutz, M. Carbillet, D. Mary, D. Mourard, *poster* paru dans les actes de *In the spirit of Lyot 2010*, A. Boccaletti Ed., `http://lyot2010.lesia.obspm.fr/sites/lyot2010/IMG/pdf/Lyot2010proc_s8_poster_PatruF.pdf` (2010).
137. "Photometric characterization of exoplanet using angular and spectral differential imaging in SPHERE/IRDIS", A. Vigan, C. Moutou, M. Langlois, F. Allard, A. Boccaletti, M. Carbillet, D. Mouillet, I. Smith, *talk* paru dans les actes de *In the spirit of Lyot 2010*, A. Boccaletti Ed., `http://lyot2010.lesia.obspm.fr/sites/lyot2010/IMG/PDF/Lyot2010proc_s7_talk_ViganA.pdf` (2010).
138. "High spatial resolution of the compact starburst cluster R136 at 50 to 10 mass and beyond", Z. Khorrami, F. Vakili, O. Chesneau, M. Carbillet, D. Mekarnia, in *EELT 2013 - Shaping E-ELT Science and Instrumentation*, `http://www.eso.org/sci/meetings/2013/EELT2013/posters/Khorrami.pdf` (2013).
139. "A New Generation Infrared Sky Survey for the E-ELT era (an assessment study)", N. Epchtein, M. Langlois, G. Moretto, I. Vauglin, L. Abe, M. Carbillet, É. Aristidi, in *EELT 2013 - Shaping E-ELT Science and Instrumentation*, `http://www.eso.org/sci/meetings/2013/EELT2013/posters/Epchtein.pdf` (2013).

— Communications à des conférences / Présentations non publiées

(6 posters)

140. "Lidar and imaging through turbulence", M. Carbillet, *poster* présenté à l'*OTAN Summer School "Laser Guide Stars for Adaptive Optics"*, Carghjese, Corsica (1997).
141. "CAOS (Code for Adaptive Optics Systems) Software Package : New Developments", C. Vérinaud, M. Carbillet, B. Femenía, *poster* présenté à la conférence "SF2A 2002 - Semaine de l'Astrophysique Française", Paris, France (2002).
142. "First-ligth AO system for LBT", A. Tozzi, S. Esposito, D. Feruzzi, M. Carbillet, A. Riccardi, L. Fini, C. Vérinaud, M. Accardo, G. Brusa, D. Gallieni, R. Biasi, C. Baffa, V. Biliotti, I. Foppiani, A. Puglisi, R. Ragazzoni, P. Ranfagni, P. Stefanini, P. Salinari, W. Seifert, J. Storm, *poster* présenté à l'*OTAN Summer School "Astronomical Adaptice Optics"*, Carghjese, Corsica (2002).
143. "Wave-front sensing for extreme adaptive optics", C. Vérinaud, M. Le Louarn, V. Korkiakoski, M. Carbillet, *poster* présenté à la conférence "MCAO for very large telescopes/OAMC pour les très grands télescopes", Paris, France (2005).
144. "Study of an adaptive optics system for Dome C", A.-L. Maire & M. Carbillet, *poster* présenté à la "Formation optique adaptative JRIOA 2009", Marseille, France (2009).
145. "The Polar Large Telescope : a synoptic survey of the southern sky in the infrared", N. Epchtein, W. Ansorge, L. Abe, M. Langlois, I. Vauglin, B. Le Roux, M. Carbillet, S. Argentini, C. Genthon, R. Lemrani, T. Le Bertre, G. Marchiori, J. Montnacher, C. David, I. Esau, E. Ruch, I. Bryson, G. Dalton, M. Ashley, J. Storey, J. Lawrence, and the PLT consortium, *poster* présenté au "Colloque R&D INSU 2011", Grenoble, France (2011).

— Rapports & Thèse

(1 thèse, 14 rapports)

146. "Détermination des paramètres orbitaux d'étoiles doubles en infra-rouge", M. Carbillet, *rapport de DEA — Université de Nice–Sophia Antipolis* (1993).
147. "Probability imaging of double/multiple stars : extension to the two-dimensional problem", M. Carbillet, *rapport final de stage du réseau Européen HCM* (1995).
148. "Techniques probabilistes : application à l'imagerie à haute résolution angulaire en astrophysique", M. Carbillet, *Thèse de doctorat — Université de Nice–Sophia Antipolis* (1996).
149. "Mesures LIDAR et turbulence atmosphérique : étude sur la distribution d'intensité LIDAR", M. Carbillet, *rapport post-doctoral final COTRAO* (1997).
150. "Work-Package B Deliverable Report", M. Carbillet, F. Delplancke, B. Femenía, L. Fini, M. Le Louarn, A. Riccardi, É. Viard, S. Esposito, N. Hubin, *rapport du réseau Européen TMR Laser guide star for 8-m class telescopes* (1999).
151. "Work-Package B Mid-Term Report", M. Carbillet, F. Delplancke, B. Femenía, L. Fini, M. Le Louarn, A. Riccardi, É. Viard, S. Esposito, N. Hubin, *rapport du réseau Européen TMR Laser guide star for 8-m class telescopes* (2000).
152. "MAD Layer-Oriented WFS : Final Design", E. Diolaiti, J. Farinato, R. Ragazzoni, É. Vernet-Viard, A. Baruffolo, C. Arcidiacono, M. Carbillet, *ESO Internal Report* (2003).
153. "LLLCCD for the LBT first-light AO system : numerical simulations results", M. Carbillet, *rapport INAF-OAA* (2003).
154. "The Software Package AIRY - a tool for the reconstruction of LINC-NIRVANA images", B. Anconelli, M. Bertero, P. Boccacci, M. Carbillet, G. Desiderà, *LINC/NIRVANA Project Report* (2005).
155. "Simulations studies with AIRY", B. Anconelli, M. Bertero, P. Boccacci, M. Carbillet, G. Desiderà, *LINC/NIRVANA Project Report* (2005).
156. "SPHERE numerical simulations, v. 0.1", A. Boccaletti, M. Carbillet, Ph. Bendjoya, *SPHERE Internal Report* (2006).
157. "SPHERE IR coronagraph apodizer ghosts analysis, v. 1.1", R. Douet, Ph. Bendjoya, J.-B. Daban, G. Guerri, S. Robbe-Dubois, M. Carbillet, C. Gouvret, *SPHERE Internal Report* (2007).
158. "Simulation tool manual for Software Package SPHERE v. 2.1", A. Boccaletti, M. Carbillet, T. Fusco, C. Thalmann, *SPHERE PDR Documents/ESO doc. # VLT-MAN-SPH-14690-0230* (2007).
159. "IRDIS simulation and performance analysis report", M. Langlois, A. Boccaletti, A. Vigan, C. Moutou, J.-C. Augereau, M. Carbillet, *SPHERE PDR Documents/ESO doc. # VLT-TRE-SPH-14690-0195* (2007).
160. "Coronagraph design report", A. Boccaletti, J.-B. Daban, H.-M. Schmid, J. Baudrand, P. Riaud, Ph. Bendjoya, M. Carbillet, R. Douet, G. Guerri, S. Robbe-Dubois, C. Thalmann, *SPHERE PDR Documents/ESO doc. # VLT-TRE-SPH-14690-0229* (2007).

— Circulaire IAU & catalogue stellaire

(2 circulaires, 1 catalogue)

161. "New double star : Moaï 1 (SAO 12917)", É. Aristidi, Y. Bresson, M. Carbillet, B. Lopez, IAU Commission 26 (double stars) Information Circular 128 (1996).
162. "Double star measurements 1995–1997 (Aristidi+ 1999)", É. Aristidi, J.-L. Prieur, M. Scardia, L. Koechlin, R. Avila, M. Carbillet, B. Lopez, Y. Rabbia, P. Nisenson, D. Gezari, VizieR On-line Data Catalog : J/A+AS/134/545, (`http://vizier.u-strasbg.fr/viz-bin/VizieR?-source=J/A+AS/134/545`), (originally published in A&ASS 134, 545) (1999).
163. "New orbit for WDS 02193-0259", M. Scardia, J.-L. Prieur, É. Aristidi, B. Lopez, M. Carbillet, IAU Commission 26 (double stars) Information Circular 145 (2001).

Résumé

Cette thèse d'Habilitation à Diriger des Recherches s'articule autour de la modélisation d'optique adaptative (OA) et de l'imagerie post-OA, deux thématiques abordées à l'aide de différents développements de l'outil numérique `CAOS`, et dans le cadre de différents instruments ou projets instrumentaux.
Côté modélisation d'OA, je détaille plusieurs résultats, s'appuyant sur autant d'articles reproduits dans la thèse et concernant : la modélisation fine de l'atmosphère turbulente, le gain dû à l'utilisation de CCD de type *Electron Multiplying* pour l'analyse de surface d'onde, les performances du miroir *secondaire* adaptatif M4 pour l'*European Extremely Large Telescope* (EELT), et celles du système d'OA de première lumière (FLAO) du *Large Binocular Telescope* (LBT). Je compare ensuite modélisation analytique et modélisation *end-to-end*, et donne une première idée des performances d'un système d'OA au Dôme C (Antarctique).
Côté imagerie post-OA, j'étudie tout d'abord les limitations dues à la correction d'OA et à la couverture angulaire, partielles, dans le cadre de l'interféromètre de Fizeau LINC-NIRVANA (LN) du LBT. J'applique ensuite pour la première fois un algorithme de super-résolution par déconvolution sur des données post-AO réelles de l'instrument NACO du *Very Large Telescope* (VLT), puis je propose une méthode de déconvolution aveugle prenant explicitement en compte la qualité de la correction d'OA. Je présente également des études concernant l'instrument SPHERE pour le VLT et notamment son coronographe de Lyot apodisé.
Finalement, je dégage des perspectives concernant : la remise en question d'hypothèses convenues en modélisation atmosphérique, la continuation des études pour M4/EELT, la recherche de compromis déterminants entre modélisations analytique et *end-to-end*, la finalisation de l'étude d'un système d'OA au Dôme C, l'application étendue des algorithmes de super-résolution et de déconvolution sous contrainte de Strehl, la préparation des observations *Other Science* pour SPHERE/VLT, et la mise en place de techniques d'imagerie dédiées au domaine du visible, à la frontière entre déconvolution post-OA « classique » et imagerie *speckle*.

Abstract

This HDR (*Habilitation à Diriger des Recherches*) thesis is structured around adaptive optics (AO) modeling and post-AO imaging, two thematics tackled through different developments of the numerical tool `CAOS` and within the framework of different instruments or instrument projects.
From the AO modeling side, I detail various results, based on articles reproduced within the thesis and concerning : the detailed modeling of the turbulent atmosphere, the gain when using *Electron Multiplying* CCDs for wavefront sensing, the performances of the *secondary* mirror M4 for the European Extremely Large Telescope (EELT), and the performances of the first-light AO system (FLAO) of the Large Binocular Telescope (LBT). I then compare analytic modeling and end-to-end modeling, and give a first idea of the performances of an AO system at Dome C (Antarctica).
From the post-AO imaging side, I first study the limitations due to partial AO correction and partial angular coverage, in the framework of the Fizeau interferometer LINC-NIRVANA (LN) of LBT. Then I apply for the first time a deconvolution-based algorithm of super resolution on real post-AO data from the instrument NACO of the Very Large Telescope (VLT), and I propose a blind deconvolution method which explicitly takes into account the AO correction quality. I also present studies concerning the instrument SPHERE for the VLT, and in particular its apodized Lyot coronagraph.
Eventually, I reveal prospects concerning : the questioning of common assumptions in atmospheric modeling, the continuation of the studies for M4/EELT, the quest for decisive trade-offs between analytic modeling and end-to-end modeling, the finalization of the study for an AO system at Dome C, the extended application of both the super-resolution algorithm and the Strehl-constrained deconvolution, the preparation of "Other Science" observations with SPHERE/VLT, and the setting up of imaging techniques dedicated to the visible domain, at the boundary between "classical" post-AO deconvolution and speckle imaging.